

**Improved calculation of
offshore
meteorological parameters
for applications in
wind energy**

Inaugural-Dissertation

zur
Erlangung des Doktorgrades
der Mathematisch-Naturwissenschaftlichen Fakultät
der Universität zu Köln

vorgelegt von

Richard J. Foreman

aus Adelaide

Köln
im Januar 2012

Berichterstatter: Prof. Dr. Stefan Emeis
Prof. Dr. Michael Kerschgens

Tag der mündlichen Prüfung: 03.04.2012

Abstract

Work presented in this thesis demonstrates an improved calculation of offshore meteorological parameters, in particular the wind speed and turbulence intensity, relevant for wind energy applications. An alternative offshore drag law is proposed that anticipates drag coefficients at intermediate wind speeds expected in applications for wind energy, but is also consistent with the functional behaviour of drag coefficients as a function of wind speed expected at tropical cyclone wind speeds. The law is compared with measurements recorded at the FINO1 platform in the North Sea and with those reported in the literature, where differences are attributed to the nature of the water wave field. A correlation equation connecting the air side drag coefficients and water side wave steepnesses is then proposed which can also anticipate drag coefficients expected at tropical cyclone wind speeds using measurements from a buoy recorded during hurricane Rita (2005). The correlation equation interpolates between two hypothesised asymptotic regimes: One whereby drag coefficients scale with the squared wave steepness and the other whereby drag coefficients are constant. At wind speeds relevant for wind energy purposes, two distinctive wave steepness scaling regimes were detected in measurements recorded at FINO1, which are also evident in results reported in the literature. A higher order correlation attempted here, but left open for further development in the future, finds that the unsteady orientation of the wind with the wave direction is likely a further important parameter. This is found by analysing a stable internal boundary layer detected at FINO1 for a period of about a week, which resulted in a diurnal cycle of offshore meteorological parameters including the wind direction. An oscillation was correspondingly found in buoy measurements of wave steepnesses during this period, and hence in drag coefficients. It is demonstrated if higher order wave field effects can be correctly accounted for, an enhanced calculation in the wind speed will result.

The nature of the stable internal boundary layer then facilitated investigation throughout a large portion of the boundary layer by the 100 m high FINO1 tower, due to the relatively shallow ($O(100)$ m) height of the internal layer. Comparison with numerical simulations using the Mellor-Yamada-Janjić planetary boundary layer parametrization within the Weather Research and Forecasting model showed contrasting vertical profiles of turbulent kinetic energy compared with the measurements. This consequently resulted in an overprediction of turbulence intensities as calculated by the model compared with FINO1 measurements at 80 m above the sea surface, and an underprediction of turbulence closer to the surface as inferred from previously reported work in the literature. It is shown here that an improved calculation of turbulence is possible by making changes to the selection of the closure constants and the surface length scale.

Comparison with more conventional, less stably stratified periods at FINO1 showed the current Mellor-Yamada-Janjić parametrization underpredicted the 80 m high turbulence intensity during these periods, whereas the changes proposed here showed an improved calculation of hub height turbulence intensity.

Zusammenfassung

Die vorliegende Doktorarbeit präsentiert eine verbesserte Berechnung meteorologischer Parameter in der marinen atmosphärischen Grenzschicht, insbesondere der Windgeschwindigkeit und der Turbulenzintensität, geeignet für Windenergieanwendungen. Es wird ein alternatives Widerstandsgesetz vorgeschlagen, das den Luftwiderstandsbeiwert bei mittleren Windgeschwindigkeiten gut wiedergibt, und das auch dem praktischen Verhältnis zwischen dem Widerstandsbeiwert und der Windgeschwindigkeit bei tropischen Wirbelstürmen entspricht. Das Gesetz wird mit Messungen der FINO1 Messplattform in der Nordsee und vorhandenen Messungen in der Literatur verglichen. Die gefundenen Unterschiede in den Messungen werden dem Charakter des Wasser-Wellenfelds zugeschrieben.

Es wird eine Korrelationsgleichung vorgeschlagen, die den Luftwiderstandsbeiwert und die Wellensteilheit verbindet und die erwarteten Luftwiderstandsbeiwerte während Wirbelsturms Rita (2005) berechnen kann. Die Korrelationsgleichung interpoliert zwischen zwei vorausgesetzten asymptotischen Regimen: In einem Regime entspricht der Luftwiderstandsbeiwert dem Quadrat der Wellensteilheit und im anderen ist der Luftwiderstandsbeiwert konstant. Bei Windgeschwindigkeiten, die für Windenergieerzeugung relevant sind, werden zwei charakteristische Wellensteilheitsregime in den Messungen von FINO1 entdeckt. Die gleichen Ergebnisse werden auch in der Literatur nachgewiesen.

Eine Korrelation höherer Ordnung zwischen Wind und Wellen wird ebenfalls untersucht, mit dem Ergebnis, dass auch die variable Orientierung der Windrichtung wichtig ist. Dieses Ergebnis wird bei einer Analyse einer Episode mit einer sehr stabilen Grenzschicht in den FINO1-Messungen gefunden, die eine Woche andauerte und einen deutlichen Tagesgang aufwies, einschließlich der Windrichtung. Entsprechend wurde in diesem Zeitraum auch bei den Bojen-Messungen zur Wellensteilheit eine Oszillation festgestellt, und demzufolge auch im Luftwiderstandsbeiwert. Es wird dargestellt, dass eine Berücksichtigung des Wind-Wellen Parameters höherer Ordnung, eine verbesserte Berechnung der Windgeschwindigkeit ermöglichen wird. Die weitere Auswertung und Entwicklung bleibt zukünftiger Forschung überlassen.

Weiterhin erlaubt die geringe Höhe der sehr stabilen Grenzschicht eine Untersuchung eines großen, vertikalen Teils dieser Grenzschicht aus den FINO1-Daten bis 100 m Höhe. Werden die gemessenen vertikalen Profile der turbulenten kinetischen Energie mit Ergebnissen der Grenzschichtparameterisierung von Mellor-Yamada-Janjić in numerischen Modellen wie dem Weather Research and Forecasting (WRF) Modell verglichen, zeigt sich ein deutlicher Unterschied zwischen Messungen und Modellen. Dies resultiert für die sehr stabile Schichtung in vom Modell zu hoch berechneten Turbulenzintensitäten in 80 m Höhe,

und in zu niedrig berechneten Turbulenzintensitäten in Oberflächennähe, was sich auf bereits in der Literatur publizierte Ergebnisse zurückführen lässt. Es wird hier dargestellt, dass eine verbesserte Berechnung der Turbulenz durch Veränderungen der Modellkonstanten und Oberflächenlängenskala möglich ist. Bei weniger stabilen Grenzschichten wird festgestellt, dass die vorgeschlagenen Veränderungen in der Turbulenzparametrisierung auch hier eine verbesserte Berechnung der Turbulenzintensität ermöglichen.

Acknowledgments

The following thesis originally arose from the idea of my supervisor Prof. Dr. Stefan Emeis concerning the possibility that there may be something unique about the nature of offshore turbulence to be subsequently included in numerical weather prediction models. I thus would like to thank Prof. Dr. Emeis for accepting me as his PhD student here at the Institute for Meteorology and Climate Research (IMK-IFU), Garmisch-Partenkirchen and providing much support and advice the last three years. I hope that the following thesis has gone some way to answering his question and is also useful for others wanting to further pursue work in this fascinating field.

In addition to Prof. Dr. Emeis, I would also like to thank the many people here at the IMK-IFU whose help I have received in some manner which has enabled this work to be carried out. In particular, I would like to mention the efforts of Drs. Johannes Werhahn and Peter Suppan.

The work in this thesis follows from the thesis of Dr. Matthias Türk, whom I thank for making his processed data available for use here. The original data comes courtesy of the German wind energy institute (DEWI) and the German maritime and hydrographic agency (BSH) which are also gratefully acknowledged. This thesis was done within the VERITAS project (work package 5 of OWEA) which is funded by the German Ministry of the Environment (BMU) via the PTJ (FKZ 0325060).

Many thanks to der Mathematisch-Naturwissenschaftlichen Fakultät der Universität zu Köln, in particular Prof. Dr. Michael Kerschgens, for giving me the opportunity to obtain my PhD from their institute whilst working from afar here in Garmisch-Partenkirchen.

On a personal note, I am deeply thankful for all the support I have received from Indra Lopez both leading up to and during this thesis. Back home, I would like to thank David and Martyn Foreman, as well as Dr. Zebb Prime for their long distance support.

Contents

Abstract	3
Zusammenfassung	5
Acknowledgments	7
Notation	11
List of Figures	14
List of Tables	23
1 Introduction	25
1.1 Introduction	25
1.2 Problem Definition	27
1.3 Methodology	30
1.4 Scope	31
2 Offshore surface roughness effects	35
2.1 Introduction	35
2.2 Surface roughness	36
2.2.1 Offshore roughness	36
2.2.2 Drag coefficient	38
2.2.3 Stratification effects	39
2.2.4 Froude number effects	41
2.3 FINO1	42
2.3.1 Data Description	42
2.3.2 January 2005	43
2.3.3 February 2005	48
2.3.4 November 2005	54
2.4 Tropical cyclone wind speeds	58
2.5 Conclusion	59
3 Offshore aspect ratio effects	61
3.1 Introduction	61
3.2 Scaling Analysis	62
3.2.1 Introduction	62
3.2.2 Toba's $\frac{3}{2}$ power law	64
3.2.3 Extension of Toba's $\frac{3}{2}$ power law	65

3.2.4	The aspect ratio	66
3.2.5	General correlating expression	69
3.3	Data analysis	70
3.3.1	FINO1	70
3.3.2	Literature	73
3.3.3	Tropical Cyclones	78
3.4	Conclusions	80
4	Air/Sea/Land interaction effects	83
4.1	Introduction	83
4.2	Results from previous analyses	85
4.3	General description of WRF and the Mellor-Yamada-Janjić Model	87
4.4	Results	89
4.4.1	Mean fields	89
4.4.2	Turbulent fields	95
4.4.3	Model results	99
4.5	Conclusions	107
5	Mellor-Yamada-Janjić model modifications	109
5.1	Introduction	109
5.2	Description of the MYJ model	110
5.3	Determination of the closure constants	114
5.3.1	Traditional approach	114
5.3.2	Alternative strategy to the traditional approach	116
5.4	Single Column Model Results	124
5.5	Conclusions	128
6	Applications for wind energy	131
6.1	Introduction	131
6.2	Results	134
6.2.1	May 2006	134
6.2.2	January 2005	141
6.2.3	February 2005	148
6.2.4	November, 2005	151
6.3	Conclusion	155
7	Conclusions	157
	Bibliography	160
	Erklärung	172

Notation

a	Constant
$a_{1,2}$	Regression constants
a_H	Model parameter
a_M	Model parameter
A	Wind turbine rotor cross sectional area (m^2)
A_1	Closure constant
A_2	Closure constant
b	Ellipse span (m)
b	Buoyancy parameter (ms^{-2})
B_1	Closure constant
B_2	Closure constant
c_p	Peak wave phase speed (ms^{-1})
C	Logarithmic velocity profile constant
C_1	Closure constant
C_D	Drag coefficient
C_{Dn}	Neutral drag coefficient
C_{D10n}	10 m neutral drag coefficient
C_f	Skin friction coefficient
C_p	Specific heat ($\text{Jkg}^{-1}\text{K}^{-1}$)
d	Water depth (m)
D	Wind turbine rotor diameter (m)
f	Arbitrary functional dependence
f_c	Coriolis parameter (s^{-1})
f_p	Peak wave frequency (s^{-1})
g	Gravitational acceleration (ms^{-2})
h	Internal boundary layer height (m)
H_s	Significant wave height (m)
k_s	Equivalent roughness height (m)
K_h	Heat exchange coefficient (m^2s^{-1})
K_m	Eddy viscosity (m^2s^{-1})
ℓ	Turbulent length scale (m)
ℓ	Ellipse length (m)
ℓ_o	Asymptotic length scale (m)
ℓ_s	Surface length scale (m)
L	Obukhov length (m)
L_L	Local Obukhov length (m)
n	Exponent
$\overline{p'w'}$	pressure-vertical velocity covariance ($\text{Nm}^{-1}\text{s}^{-1}$)
P	Atmospheric pressure (Nm^{-2})

P_o	Wind power (W)
Pr	Prandtl number
Re	Reynolds number
Re_δ	Reynolds number
Re_k	Roughness Reynolds number
Re_*	Aerodynamic roughness Reynolds number
Ri	Gradient Richardson number
Ri_c	Critical Richardson number
Ri_f	Flux Richardson number
S_q	Model constant
t	Time (s)
T	Averaging time (s)
$TKE = \frac{1}{2}q^2$	Turbulent Kinetic Energy (m^2s^{-2})
T_p	Peak wave period (s)
Ti	Turbulence intensity
u	Wind speed (ms^{-1})
u_L	Local friction velocity (ms^{-1})
u'	Fluctuating velocity (ms^{-1})
u_*	Friction velocity (ms^{-1})
$\overline{u'^2}$	Streamwise velocity variance (m^2s^{-2})
$\overline{u'w'}$	Streamwise Reynolds stress (m^2s^{-2})
$\overline{u'v'}$	Lateral Reynolds stress (m^2s^{-2})
$\overline{w'^2}$	Vertical velocity variance (m^2s^{-2})
$\overline{v'w'}$	Lateral Reynolds stress (m^2s^{-2})
$\overline{v'^2}$	Lateral velocity variance (m^2s^{-2})
$\overline{w'\theta'_v}$	Heat flux ($ms^{-1}K$)
U	Mean wind speed (ms^{-1})
U	Mean horizontal wind speed (ms^{-1})
U_∞	Free stream velocity (ms^{-1})
V_g	Geostrophic wind speed (ms^{-1})
X	Stability parameter
y	Correlating function
$y_{o,\infty}$	Asymptotic functions
Y	Asymptotic ratio
z	Vertical coordinate (m)
z_i	Boundary layer height (m)
z_o	Aerodynamic surface roughness (m)
z_+	Wall coordinate (m)
Z	Asymptotic ratio

Greek:

α	Charnock's constant
α	Model length scale constant
β	Stability parameter
γ_1	Model parameter
δ_{ij}	Kronecker delta
δ	Outer length scale (m)
ϵ_{ij3}	Alternating unit tensor

ϵ	Turbulent kinetic energy dissipation (m^2s^{-3})
ζ	Monin-Obukhov stability parameter
θ_ℓ	Potential temperature, land (K)
θ_s	Potential temperature, sea surface (K)
θ_v	Virtual potential temperature (K)
θ_*	Angle between u_* and V_g
θ_*	Heat flux normalised by u_*
κ	Von Karman's constant
λ_p	Peak wave length (m)
ν	Kinematic viscosity (m^2s^{-1})
Φ_m	Dimensionless wind shear
Π	Arbitrary dimensionless group
ρ	Air density (kgm^{-3})
σ	Water surface displacement standard deviation (ms^{-1})
σ_u	Streamwise velocity standard deviation (ms^{-1})
σ_v	Lateral velocity standard deviation (ms^{-1})
σ_w	Vertical velocity standard deviation (ms^{-1})
Ψ	Stability function

Acronyms:

BSH	German Maritime and Hydrographic Agency
DEWI	German Wind Energy Institute
FINO1	North Sea research platform
LLJ	Low level jet
MYJ	Mellor-Yamada-Janjić
NCEP	National Centers for Environmental Protection
WRF	Weather Research and Forecasting

List of Figures

1.1	Photograph of the FINO1 platform (source: bundesregierung.de).	26
1.2	The figure 2.2 from Stull (1988) as adapted from Van der Hoven (1957) showing the relative contributions to horizontal wind speed variations (“spectral intensity”) from synoptic and turbulent scales of motion.	27
1.3	Photograph of wake clouds generated by the Horns Rev wind farm. (Christian Steiness, 2008, Vattenfall)	27
1.4	The effect of turbulence intensity on the reduction in wind speed (% deficit) behind a given wind turbine at a certain wind speed as a function of the wind turbine rotor diameter, D (source: adapted from the figure 2 of Elliott (1991)).	28
2.1	Sea (ocean) surface drag coefficients at 10 m as a function of the 10 m neutral wind speed as reported by Merzi and Graf (1988), Janssen (1997) and Dobson et al. (1994). Also included is Charnock’s parametrization, eq. (2.12) for $\alpha = 0.018$.	41
2.2	Wind speeds at 80 m (top), wind direction at 90 m and 33 m (middle) and relative humidities at 90 and 33 m (bottom) as recored at FINO1 during January 4–10, 2005.	44
2.3	Friction velocities (top) and vertical standard deviations (middle) at 80 and 40 m, and Obukhov lengths as estimated from the 40 m sonic (bottom) as recorded at FINO1 during January, 4–10.	45
2.4	Top: Friction velocities (left) and drag coefficients (right) as a function of wind speed using u_* estimated from the 40 m sonic during January 4–10, 2005. Bottom: Measurements of drag coefficients (left) and friction velocities (right) as reported by Dobson et al. (1994). The solid line is Charnock’s law for $\alpha = 0.018$ and the dashed line is a regression in $u_* = f(U_{10m})$ space based on the FINO1 measurements (i.e., top left).	46
2.5	Average wind profiles during the 5th (top) and 7th (bottom) of January 2005 compared with equivalent neutral wind profiles assuming $\beta = 5$ (left) and $\beta = 10$ (right) in eq. (2.39).	47
2.6	Wind speeds at 80 m (top), wind direction at 90 m (middle) and relative humidities at 90 and 33 m (bottom) at FINO1 during February, 20–28, 2005.	49

2.7	Friction velocities (top) and vertical standard deviations (middle) at 80 and 40 m, and Obukhov lengths as estimated from the 40 m sonic (bottom) as recorded at FINO1 during February, 20–28, 2005.	50
2.8	Average wind speed profiles during the 23rd (left) and 25th (right) of February 2005 compared with equivalent neutral wind profiles (solid black curve) and the unstable profiles from Monin-Obukhov similarity theory based on the 40 m sonic and cup anemometers.	51
2.9	Top: Friction velocities (left) and drag coefficients (right) as a function of wind speed as measured at FINO1 between February 20-28, 2005. Middle: Measurements during this same period with no rain detected at the 20 m measurement (left) and with rain detected at the 20 m measurement (right). Bottom: For comparison are measurements of u_* and C_{D10n} as a function of wind speed in the Baltic as reported by Johnson et al. (1998). The solid line is Charnock's law for $\alpha = 0.018$, the dashed is a regression for $a_{1,2} = (0.042, -0.01)$ using all measurements.	52
2.10	Roughness Reynolds number (top) and C_{D10n} (bottom) as a function of wind speed during January 2005 (left) and February 2005 (right). The two solid lines (top) are for $Re_* = 300$ and 3. The solid line (bottom) is Charnock's parametrization for $\alpha = 0.018$. The dashed curves are eq. (2.36) for $a_{1,2} = (0.057, -0.26)$ (left) and $(0.042, -0.01)$ (right). The dotted line is eq. (2.40) after Amorochio and Devries (1980).	53
2.11	Wind speeds at 80 m (top), wind direction at 90 m (middle) and relative humidity at 90 and 33 m (bottom) at FINO1 during November, 9–15 2005.	55
2.12	Friction velocities (top) and vertical velocity standard deviations (middle) at 80 and 40 m and Obukhov lengths from the 40 m sonic (bottom).	56
2.13	Friction velocities (left) and drag coefficients (right) as a function of wind speed as measured at FINO1 between November 9–15, 2005 (top) and measurements reported by Anderson (1993) (bottom). The solid line is Charnock's law for $\alpha = 0.018$. The dashed curve is the linear regressions in $u_* = f(U_{10n})$ space for measurements in the top left figure.	57
2.14	Average wind speed profiles during the 11th (13:00 – 24:00) (left) and 14th (13:00 – 24:00) (right) of November 2005 compared with equivalent neutral wind profiles (solid black curve) and the stable (left, $\beta = 10$) and unstable (right) profiles from Monin-Obukhov similarity theory based on the 40 m sonic and cup anemometers.	58
2.15	The drag coefficient as a function of the 10 m wind speed according to Charnock (1955)'s parametrization for $\alpha = 0.018$ (solid line). The squares with error bars are the estimates of Powell et al. (2003) using radiosonde profiles in tropical cyclones. Gray dots are direct aircraft measurements reported by French et al. (2007). The curves corresponding with the January, February and November, 2005 measurements defined according to eq. (2.36) for the linear regression constants specified in the text.	59

- 3.1 Illustration of Toba's $\frac{3}{2}$ law showing the measurements at FINO1 during January 4–10, 2005 and February 20–28, 2005 and the line defined by eq. (3.7) for $B = 0.06$ 65
- 3.2 Left: The figure 9.19 from Munson et al. (2002) with some aspects removed showing the relationship between the drag coefficient and aspect ratio for an ellipse of length ℓ and height D . Right: The relationship between the offshore drag coefficient derived from eq. (3.16) (gray dashed line), a constant drag coefficient assuming $C_{D10n}^{1/2} = 0.03$ (dashed black line) and a correlation equation between these two (solid black line). 67
- 3.3 Eq. (3.22) on logarithmic axes for various exponents n (adapted from the figure 1 of Churchill and Usagi (1972)). 68
- 3.4 A working plot for correlation based using eqs. (3.22) and (3.23) (adapted from the figure 2 of Churchill and Usagi (1972)). 68
- 3.5 Y versus Z (left hand side) and $\frac{Y}{Z}$ versus $\frac{1}{Z}$ (right hand side) as calculated at FINO1 for the periods during January (top), February (middle) and November (bottom) 2005 as calculated for various n (1, 2, 3, 4 and ∞) based on eqs. (3.22) and (3.23). Here, $Y = \frac{C_{D10n}^{1/2}}{\frac{H_s}{\lambda_p}}$ and $Z = \frac{0.03}{\frac{H_s}{\lambda_p}}$ 71
- 3.6 Drag coefficients as a function of one-tenth aspect ratios during January and February 2005. The solid black, dashed gray and dashed gray lines are the correlation equation, eq. (3.27) the wave steepness asymptote (3.16) and the constant drag coefficient asymptote (3.19). The top figure shows bin averages and the bottom figure shows one hour means. 72
- 3.7 January 2005 (top), February 2005 (middle) and November 2005 (bottom): Drag coefficients as measured from the FINO1 tower compared with C_{D10n} inferred from buoy measurements according to the correlation eq. (3.27) (top), the asymptotic relations, eq. (3.28) and (3.29) (middle), and the correlation equation again (bottom). 74
- 3.8 Top: Phase diagram of C_{D10n} against $\frac{\lambda_p}{10H_s}$ from January 4–5th, 2005. A period within this period is indicated by black bullets for the 4th (14:00) to the 5th (5:00) illustrating the scaling with eq. (3.16) during this time. Bottom: Wind (33 m) and wave directions during the same period, also showing the black bullets corresponding with those in the phase diagram. 75
- 3.9 Y versus Z (left hand plots) and $\frac{Y}{Z}$ versus $\frac{1}{Z}$ (right hand plots) for $n = 1, 2, 3$ and 4 according to eqs. (3.22) and (3.23) where $Y = C_{D10n}^{1/2} / \frac{H_s}{\lambda_p}$ and $Z = 0.03 / \frac{H_s}{\lambda_p}$. Top: Measurements reported by Janssen (1997) in the North Sea and SCOPE measurements exposed to the open Pacific Ocean. Middle: Measurements reported by Dobson et al. (1994) in the North Atlantic. Bottom: Measurements reported by Merzi and Graf (1988) and Johnson et al. (1998) over Lake Geneva and in the Baltic Sea, respectively. 76

- 3.10 Top: Bin averaged (note the logarithmic x-axes scale) drag coefficients calculated from tabulated data provided by Merzi and Graf (1988), Dobson et al. (1994), Janssen (1997) and Johnson et al. (1998) and the online SCOPE (Grachev and Fairall, 2001) measurements, plotted as a function of one-tenth of the aspect ratio, $\frac{\lambda_p}{10H_s}$. Also included are functions corresponding to eq. (3.8) for $C_{D10n}^{1/2} = 0.03$ (gray dashed line), eq. (3.16) (black dashed line) and eq. (3.27) (solid black line) which is an interpolating function between the two asymptotes. Bottom: Same as the top figure but focused on the low aspect ratio region and the scale of both axes are linear. 77
- 3.11 Top: Estimates of C_{D10n} as a function of wind speed calculated using eq. (3.27) using measurements from buoys located in the Mexican gulf (stations 42001 (left) and 42035 (right)). For comparison are the estimates in tropical cyclones from Powell et al. (2003), Charnock's parametrization for $\alpha = 0.018$ and eq. (3.30) for $(a_{1,2} = (0.057, -0.26))$ (January, 2005 at FINO1). Bottom: The corresponding plots of friction velocities as a function of wind speed. Buoys 42001 and 42035 correspond with the periods 21–24 September and 23–25 September 2005, respectively. 79
- 4.1 The figures 1a and 1b from Garratt (1987) showing the growth of an internal boundary layer as warm continental air flows over a cold sea (a) and the corresponding vertical profiles of potential temperature over land (θ_l) and over sea (θ_s) (b). 84
- 4.2 Adapted from the figure 2 from Brooks and Rogers (2000) showing wind speed and virtual potential temperature profiles recorded by aircraft at two different locations over the Persian Gulf during the passage of a stable internal boundary layer. 86
- 4.3 The 151 x 151 (10 km resolution) domain centered on FINO1. . . 87
- 4.4 DWD surface pressure map (as archived by Wetter3.de) on indicative of the period 04/05/06 - 11/05/06 (here 07/05/06 6 UTC) showing a high over Scandinavia and low just east of Ireland (left). The estimated geostrophic wind at FINO1 for the entire period (right). 89
- 4.5 Wind speed according to the 80 m cup anemometer compared with the 80 m wind speed according to the WRF model (top). Wind direction at 90 and 33 m as measured by wind vanes at FINO1 (middle). Relative humidity as measured at 90, 50 and 33 m by hygrometers at FINO1 (bottom). 91
- 4.6 Time series of temperature at 100 m, 33 m and the sea surface (SST) at FINO1 in comparison with the modelled 2 m temperature over land directly east of FINO1 (top). The dashed line shows the modelled temperature shifted three hours forward. Potential temperature (middle) and wind speed profiles (bottom) during the 4th as shown every second hour (UTC). 92
- 4.7 Heat fluxes (top), turbulence intensities (middle) (eq. (4.19)) and local friction velocities (bottom) (eq. (4.17)) at 80, 60 and 40 m at FINO1. 97

4.8	Comparison between the TKE and streamwise variances as measured at 40 (left) and 60 m (right) during the period May 4-11, 2006.	98
4.9	TKE ₊ at FINO1 assuming TKE $\approx \overline{u'^2}$ and u_* from u_L interpolated to the surface using eq. (4.21) The scaling is compared with that performed by Caughey et al. (1979) (it is their solid curve from their figure 5 (top left)).	100
4.10	Scaled TKE during the 10th from 6:00 – 20:00 similar to that performed in Fig. 4.9, but concentrating on the 40 m measurement (top left). Also shown that are the times 12:00 and 18:00 indicating the departure from outer scaling. TKE ₊ as a function of the local Monin-Obukhov stability parameter indicating illustrating instability between 12:00 and 18:00 (top right). Wind speed profiles from 8:00 – 13:00 (bottom left) and from 14:00 – 19:00 (bottom right).	101
4.11	Drag coefficients as estimated from buoy measurements using eq. (4.26) compared with the MYJ model (top). Local friction velocities at 40 m (middle). Wind (33 m) and wave directions (bottom).	102
4.12	Time series of the difference between the rate of change of wind and wave direction (5 hour moving average) compared with 50 times the rate of change of the drag coefficient estimated from buoy measurements plus 9 hours in time (also a 5 hour moving average).	103
4.13	Scaled TKE (TKE ₊) as calculated by the MYJ model assuming TKE $\approx \overline{u'^2}$. The periods here correspond with those in Fig. 4.9 above.	104
4.14	Absolute TKE and turbulence intensity as measured at FINO1 and calculated by the MYJ model.	105
4.15	Velocity profiles at FINO1 during the 4th (top), 6th (middle) and 8th (bottom) at various times in comparison with the MYJ model and when using an extra 6 levels less than 100 m.	106
5.1	Left: Adapted from the figure 1 of Mellor and Yamada (1982) interpreting the measurements of scaled horizontal velocity fluctuations as reported by Perry and Abell (1975) (their figure 7) for different Reynolds numbers. The horizontal line corresponds with $\overline{u'^2}_+ = 4.49$. Right: Adapted from the figure 7 (top) of DeGraaff and Eaton (2000) showing measurements for a range of Reynolds numbers and a lack of an obvious choice for $\overline{u'^2}_+$	115
5.2	The figure 5 of Grant (1986) showing aircraft measurements of horizontal (a), lateral (b) and vertical (c) variances ($\sigma_{u,v,w}^2$) normalised by the friction velocity and plotted against the height, z which itself has been normalised by the boundary layer height, z_i . The “P” and “S” along the horizontal axis refer to the measurements of Panofsky et al. (1977) and Smith (1980), respectively. The solid lines are based on the aircraft measurements of Nicholls and Readings (1979).	115
5.3	Calculation of Φ_m and Φ_h in stable stratification according to eqs. (5.31) and (5.32) for various γ_1 and surface length scale, ℓ_s as defined in the text.	119

5.4	Calculation of Φ_m and Φ_h in unstable stable stratification according to eqs. (5.31) and (5.32) for various γ_1 and ℓ_s as defined in the text.	120
5.5	40 m lateral and vertical variances normalised by twice the TKE, q^2 for the year 2005 at FINO1 as a function of stability. The error bars are two standard deviation width. Comparison the LES results of Nakanishi (2001) are also included.	121
5.6	The relationship between Ri_c and B_1 as calculated from eq. (5.46) for a range of γ_1	123
5.7	Left column: Time series of 10 and 50 m wind speeds and TKE from single column model simulations using the current MYJ model, that defined in Mellor and Yamada (1982) (MY82), an example of physical unrealistic simulation where $\gamma_1 = 0.2$ and $B_1 = 26$ (MYJg1) and an alternative MYJ versions using $\gamma_1 = 0.27$ and $B_1 = 26$ (MYJv2). Right column: The same cases as the left column showing profiles of wind speed, TKE and K_m at 3:00 local time. The observations are those taken from the main tower during the CASES-99 experiment.	125
5.8	Left column: Time series of 10 and 50 m wind speeds and TKE from single column model simulations using $\gamma_1 = 0.27$. Right column: The same cases as the left column showing profiles of wind speed, TKE and K_m at 3:00 local time. The observations are those taken from the main tower during the CASES-99 experiment.	126
5.9	Left: The dependence of the maximum K_m throughout the boundary layer at 3:00 local time on Ri_c for MYJ, MY82 and MYJ (with $\gamma_1 = 0.27$, $B_1 = 26$ and $c = 2.7$). Right: The dependence on this same K_m on γ_1 and c at constant Ri_c	127
6.1	Vertical profiles of turbulent kinetic energy normalised by the friction velocity as calculated by MYJ and MY82 and compared with the curve of Caughey et al. (1979) as presented in their figure 5 (top left). The height, z has been normalised by the estimated internal boundary layer height (see Chapter 4).	135
6.2	Vertical profiles of turbulent kinetic energy normalised by the friction velocity as calculated by MYJ and g127b128 and compared with the curve of Caughey et al. (1979) as presented in their figure 5 (top left). The height, z has been normalised by the estimated internal boundary layer height (see Chapter 4).	136
6.3	Wind speed at 80 m as calculated by MYJ (top), MY82 (middle) and g127b128 (bottom) in comparison with both MYJ and FINO1 measurements.	137
6.4	Turbulence intensity as calculated by MYJ (top), MY82 (middle) and g127b128 (bottom) in comparison with both MYJ and FINO1 measurements.	138
6.5	Wind speed (left) and TKE (right) profiles on May 4th at 22:00 for different critical Richardson numbers, Ri_c	140
6.6	Wind speed and TKE (absolute) profiles on May 4th at 12:00 (left) and 22:00 (right) as calculated by MYJ, MY82 and g128b128 compared with FINO1 measurements.	142

6.7	Wind speed and TKE (absolute) profiles on May 6th at 15:00 (left) and 22:00 (right) as calculated by MYJ, MY82 and g128b128 compared with FINO1 measurements.	143
6.8	Wind speed and TKE (absolute) profiles on May 8th at 15:00 (left) and 22:00 (right) as calculated by MYJ, MY82 and g128b128 compared with FINO1 measurements.	144
6.9	Profiles of WRF calculated TKE_+ according to MYJ (left) and g127b128 (right) as a function of the height normalised by the boundary layer height, $\frac{z}{z_i}$ in comparison with the results of Caughey et al. (1979) and the FINO1 measured TKE_+ at 40, 60 and 80 m during January 4–10, 2005.	145
6.10	Hub height (80 m) wind speeds (left column) and turbulence intensity (right column) as measured by FINO1 in comparison with MYJ (top), MY82 (middle) and g127b128 (bottom).	146
6.11	Average profiles at FINO1 during January 5th (top left) and 7th (top right) compared with MYJ and g127b128. The drag coefficient as a function of the aspect ratio (bottom left) and wind speed (bottom right) at FINO1. Highlighted in these figures are the points corresponding with the 5th (circles) and the 7th (squares). Bottom left: Solid black line is eq. (6.6); dashed black line is eq. (6.7); dashed gray line is eq. (6.8). Bottom right: The solid black line is Charnock's parametrization and the solid gray line is eq. (6.10) for $a_{1,2} = (0.058, -0.28)$	147
6.12	Wind speeds at 80 m (top), Wind (33 m) and wave directions (middle) and Turbulence intensity (bottom) during February 20–28, 2005.	149
6.13	Top: Average wind speed profiles during the 22nd (left) and 23rd (right) as calculated by the standard MYJ model and compared with a modified roughness length (MYJzo) defined according to eq. (6.10), compared with average wind speed profiles at FINO1. Bottom left: Drag coefficients as a function of the aspect ratio. The solid black line is eq. (6.6); dashed black line is eq. (6.7); dashed gray line is eq. (6.8). Highlighted by circles and squares are points during the 22nd and 23rd, respectively. Bottom right: Drag coefficients as a function of wind speed. The solid black lines correspond with MYJ while the solid gray lines MYJzo.	150
6.14	A direct comparison between the 80 m T_i as calculated by MYJ (left) and g127b128 (right) during February 20-28, 2005.	151
6.15	November 9-16, 2005: Wind speeds at 80 m (top), wind (33 m) and wave directions (middle) and turbulence intensity (bottom).	152
6.16	Top: Wind speed profiles for two 12 hour periods on the 11th (left) and 14th (right) November 2005 comparing profiles at FINO1 with the standard MYJ model and with a modified roughness (MYJzo) using eq. (6.10). Bottom: Drag coefficients for the entire 9-16 November period where the two 12 hour periods are highlighted as circles (11th) and squares (14th) as a function of one-tenth the aspect ratio (left) and the 10 m wind speed (right). Bottom left: The dashed and solid curves are defined in the text. Bottom right: The black and light gray curves correspond with MYJ and MYJzo, respectively.	153

6.17 A direct comparison between the 80 m Ti as calculated by MYJ (left) and g127b128 (right) during November 9-16, 2005	154
---	-----

List of Tables

4.1	Calculation of the internal boundary layer height, h between 11:00 and 23:00 for the 4th, 6th, 7th and 8th according to eq. (4.6) using estimated geostrophic wind speeds shown in Fig. 4.4 and $x = 150$ km. Here, δ corresponds with the height of the low level jet (LLJ).	94
5.1	Turbulence statistics from some recent laboratory boundary layer experiments by Österlund (1999) and Carlier and Stanislas (2005) and a years worth of measurements at FINO1. The magnitude of $\overline{\gamma_1}$ is based on either eq. (5.15), (5.16) or (5.17) for $\overline{u'^2}$, $\overline{v'^2}$ and $\overline{w'^2}$, respectively.	118
5.2	Summary of different cases tested in the single column model below. The constants are defined in the text. Ri_c is the critical Richardson number as determined from the constants.	124

Chapter 1

Introduction

1.1 Introduction

Wind energy is proposed to partly replace finite fossil fuel resources whose consumption results in the emission of annually increasing amounts of greenhouse gases, depending on the level of economic activity (Friedlingstein et al., 2010). One estimate has worldwide coal production peaking in 2030 (Mohr and Evans, 2009), which if true, gives net energy importing regions such as the entire European Union apart from Denmark¹ approximately 20 years to find a replacement for this energy shortfall.

Wind energy is a renewable energy resource and thus it is proposed that offshore wind energy can provide at least one non-traditional, industrial scale energy source to meet future conventional energy production shortcomings where 150 GW of offshore wind energy is targeted by 2030 in Europe (EWEA, 2011). While wind energy itself does rely on fossil fuels at least during the construction phase, the use of other non-traditional fossil fuel emitting energy sources are also proposed as large scale energy shortfall replacements (e.g. tar/oil sands, Söderbergh et al., 2007). However, these come with the further disadvantages of an increase in greenhouse gas emissions again (e.g. Brandt and Farrell, 2007), and their own current technical problems and future production shortcomings (Mohr and Evans, 2010).

While wind speeds are generally higher and steadier offshore compared with that over land, there are additional technical and financial challenges associated with offshore wind energy compared with that onshore (Breton and Moe, 2009). One particular problem related to this work is the state of the sea in that particular wave and weather conditions offshore limits the times to which offshore sites can be accessed. For example, access via the sea to the FINO1 research platform (FINO: “Forschungsplattformen in der Nord- und Ostsee”) located roughly 45 km off Borkum Island in the German Bight is limited when significant wave heights are greater than 1.5 m (Kühnel and Neumann, 2010).

Work presented in this thesis will be centered on measurements recorded at the FINO1 platform, which is also located near the “alpha ventus” wind farm consisting of twelve 5 MW wind turbines. The site is unique in that it is located further out to sea than wind farms in other areas in order to protect the

¹http://epp.eurostat.ec.europa.eu/statistics_explained/index.php/Main_Page



Figure 1.1: Photograph of the FINO1 platform (source: bundesregierung.de).

sensitive coastal ecology in this area (www.alpha-ventus.de). This represents an opportunity to investigate offshore meteorological conditions not regularly investigated in the past and that are further relevant for wind energy applications. While the wind turbines have only been in place at alpha ventus since 2009, the FINO1 platform itself has been monitoring conditions since 2003 (Neumann et al., 2010), where some measurement periods during 2005 and 2006 will be considered in this work.

The FINO1 tower extends 100 m above the sea surface and sits on a platform, itself located about 20 m above the surface as illustrated in Fig. 1.1. While the conditions displayed in Fig. 1.1 appear calm, to illustrate the harsh conditions that can be encountered at this site, the structure just below the platform has in the past been damaged as a result of wave action during high wind events (Outzen et al., 2008). FINO1 is equipped with a broad range of meteorological and oceanography instruments, where the measurements used in this thesis have come out of the work of Türk (2008).

Equipment of particular relevance here are the wind speed measurements at 10 m vertical intervals between 30 and 100 m and turbulence measurements at 40, 60 and 80 m, while wave field information has been provided separately by the German maritime and hydrographic agency (BSH). A number of particularly high wind speed periods at FINO1 will be investigated in this thesis and compared with results reported in the literature and numerical simulations. The broader aim here is a deeper understanding of the behaviour of offshore meteorological parameters encountered at a site such as FINO1 relevant for wind energy purposes. It is intended that the work presented here will not just be useful towards further understanding the meteorological conditions at other offshore wind energy sites currently being developed in the North Sea even further from the coast than alpha ventus (www.offshore-wind.de), but also at other offshore sites around the world.

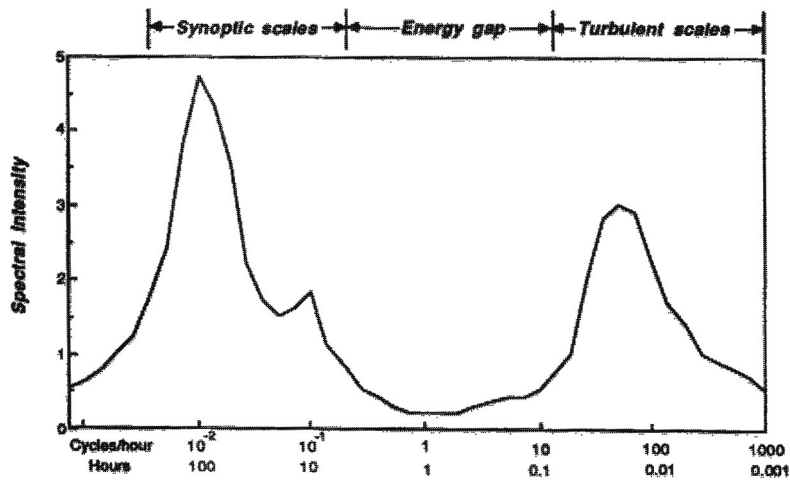


Figure 1.2: The figure 2.2 from Stull (1988) as adapted from Van der Hoven (1957) showing the relative contributions to horizontal wind speed variations (“spectral intensity”) from synoptic and turbulent scales of motion.



Figure 1.3: Photograph of wake clouds generated by the Horns Rev wind farm. (Christian Steiness, 2008, Vattenfall)

1.2 Problem Definition

While from fundamental analysis it can be found that the available wind power, P_o for a single wind turbine will be proportional to the third power of the wind speed, u by

$$P_o = \frac{1}{2}\rho Au^3, \quad (1.1)$$

this relationship will be complicated from a meteorological perspective by the effects of turbulence. Here, ρ is the air density and A is the turbine rotor cross-sectional area. Fig. 1.2, which is the figure 2.2 from Stull (1988) as adapted from Van der Hoven (1957), illustrates the time scales one can expect will influence

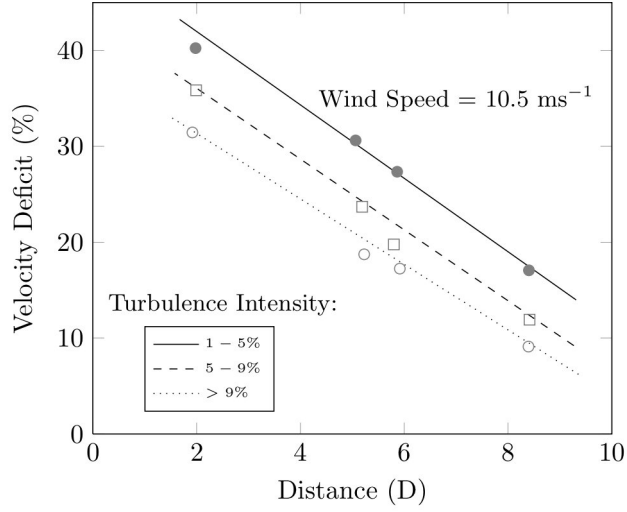


Figure 1.4: The effect of turbulence intensity on the reduction in wind speed (% deficit) behind a given wind turbine at a certain wind speed as a function of the wind turbine rotor diameter, D (source: adapted from the figure 2 of Elliott (1991)).

variation of the wind speed. It can be seen that the wind speed will vary mostly over scales of days ($O(100)$ hours) and minutes, attributable to synoptic scale events and to turbulence, respectively. From a wind energy perspective, the amount of turbulence is quantified via the turbulence intensity. For example, one can define a wind speed fluctuation, u' that deviates from the wind speed averaged over time T ,

$$U = \frac{1}{T} \int_0^T u dt, \quad (1.2)$$

by

$$u = U + u' \quad (1.3)$$

such that the average of all fluctuations during this period

$$\frac{1}{T} \int_0^T u' dt = 0. \quad (1.4)$$

From Fig. 1.2, the averaging time T is chosen to be approximately 10 minutes to capture the turbulent scales of motion while avoiding synoptic scales via the “energy gap” which is $O(1)$ hour. The mean wind speed U will then vary depending on the synoptic scale motion on time scales greater than 1 hour.

The turbulence intensity then first enters directly into the problem by taking the average of the wind speed raised to the third power to give (Devries, 1979)

$$\overline{u^3} = \frac{1}{T} \int_0^T (U + u')^3 = U^3 + 3U^2 \overline{u'} + 3U \overline{u'^2} + \overline{u'^3}, \quad (1.5)$$

where the second term on the right hand side is neglected, i.e.

$$\overline{u^3} = U^3 \left(1 + 3 \frac{\overline{u'^2}}{U^2} + \frac{\overline{u'^3}}{U^3} \right), \quad (1.6)$$

because of eq. (1.4). Assuming that the velocity probability distribution is symmetric, then

$$\overline{u^3} = U^3 (1 + 3\text{Ti}^2), \quad (1.7)$$

where the turbulence intensity is defined as

$$\text{Ti} = \frac{\sqrt{\overline{u'^2}}}{U}. \quad (1.8)$$

Hence, given a Ti of about 20%, then $\overline{u^3}$ can differ from U^3 by about 10%.

On the one hand, offshore turbulence intensities will often be much lower than 20% even in high wind speeds as will be shown in this thesis. On the other hand, offshore wind turbines will be located within a wind farm so that the actual Ti as seen by a turbine within a farm will likely be enhanced over the free stream Ti given by eq. (1.8) due to the wakes produced by other wind turbines. Wind turbine wakes are readily seen in the famous photograph taken by Christian Steiness of the Horns Rev wind farm in the Danish sector of the North Sea reproduced here in Fig. 1.3. The wakes are able to be seen here due to the advection of cold air over warm water, which due to the particular air-sea temperature difference, resulted in saturated air behind the turbines on account of the enhanced turbulent mixing (Emeis, 2010*a*). An example of the measured wind speed reduction within turbine wakes can be illustrated in Fig. 1.4 as reported by Elliott (1991) for an onshore wind farm. Fig. 1.4 shows the velocity deficit, that is the percentage difference in wind speed behind a wind turbine compared with the free stream wind speed, as a function of the distance behind the wind turbine rotor in the scale of the rotor diameter, D . It can be seen that the difference between the free stream and wake wind speeds decreases with increasing distance and with increasing turbulence intensity. The higher turbulence intensity will imply an enhanced mixing between the free and wake streams, and a quicker wind speed recovery behind the turbine.

While Fig. 1.4 shows measurements recorded onshore, the problem considered in this thesis concerns the calculation of the meteorological parameters, U and Ti for conditions offshore. For example, due to the high capital costs, offshore turbines will most likely be located within wind farms and will possibly be relatively closely spaced so that an accurate calculation of both U and Ti is necessary for wind power assessment. One example are the turbines within the Nysted offshore wind farm south of Lolland Island, Denmark where turbines are spaced within 10 rotor diameters of each other (Barthelmie et al., 2007). From a meteorological perspective, the offshore environment at FINO1 is complicated by the interaction with the coast (despite FINO1 being 60 km from the mainland), the generally lower surface roughness encountered offshore (although this is non-linearly dependent on the wind speed) and the lower turbulence intensities over water compared with over land (Lange, 2007).

The aim of the work to be presented here is to achieve a better calculation of the offshore parameters, U and Ti in hope that this will help forecasters better anticipate the expected wind energy power output from offshore wind farms. For example, the exact dependence of offshore surface roughness on atmospheric and sea parameters is a well known (Jones and Toba, 2001) and ongoing problem (Sullivan and McWilliams, 2010) which will be shown in this work to have consequences for the precise calculation of the offshore wind speed.

1.3 Methodology

Given the complexity of atmospheric flows, a full analytical description is beyond the capabilities of analysis since the governing equations are unsteady, non-linear partial differentials. To solve these equations, a numerical model is generally employed, but given the finite nature of computing resources, all scales of motion (at least from the perspective of wind energy) can still not possibly be resolved. Some of the relevant processes, especially turbulence, occur towards the earth's surface where the scales of motion take place within the finite bounds of the numerical differencing grid, but nonetheless influence the large scale solution so that neglecting their influence is not possible. In these situations one must retreat to statistics in conjunction with similarity solutions to describe these processes.

The effect of turbulence on the large scale solution for the wind speed can be seen via the conservation of momentum equation using index notation, which after a Reynolds decomposition (Stull, 1988) gives

$$\frac{\partial U_i}{\partial t} + U_j \frac{\partial U_j}{\partial x_j} = -\delta_{i3}g + f_c \epsilon_{ij3} U_j - \frac{1}{\rho} \frac{\partial P}{\partial x_i} + \nu \frac{\partial^2 U_i}{\partial x_j^2} - \frac{\partial \overline{u'_i u'_j}}{\partial x_j}. \quad (1.9)$$

Here, P is the average atmospheric pressure, g is gravity, f_c is the Coriolis parameter, ν is the kinematic viscosity, δ_{ij} is the Kronecker delta, ϵ is the alternating unit tensor.

Vastly simplifying eq. (1.9) is possible by assuming a steady, horizontally homogeneous flow parallel with the x_1 direction in the absence of a pressure gradient (Lumley and Panofsky, 1964). Assume then that we are sufficiently close to the surface such that Coriolis effects are small, but not too close so that viscosity begins to be influential so that eq. (1.9) reduces to

$$-\frac{\partial \overline{u'w'}}{\partial z} = 0. \quad (1.10)$$

After integrating eq. (1.10) and then multiplying by the air density, one obtains the surface stress

$$\tau = -\rho \overline{u'w'}, \quad (1.11)$$

from which results the most common boundary layer, turbulent velocity scale, the “friction velocity”

$$u_* = \sqrt{\frac{\tau}{\rho}}. \quad (1.12)$$

In practice, the average wind speed and surface stress are often not perfectly aligned so that the friction velocity is estimated by

$$u_* = \left(\overline{u'w'^2} + \overline{v'w'^2} \right)^{1/4}. \quad (1.13)$$

While eq. (1.9) did not yield any explicit solution, it did give us a scaling velocity, u_* which as we will see in the following chapters, exerts its influence on processes throughout. With the known scaling parameters, then similarity solutions can be found which with the help of measurements, results in explicit solutions that can consequently be used in parametrizations in more complex applications, e.g. numerical weather prediction. Perhaps the most famous of these

is the logarithmic velocity profile which describes the lowest level in numerical models and often the flow up to the hub height of wind turbines. In arriving at eq. (1.10), we assumed that the relevant length scale of interest is the height above the surface, z (in fact it explicitly appears in eq. (1.10)). Depending at what height we want to focus on above the surface, there are at least a couple of other possible length scales: as $z \rightarrow 0$, there is a “dissipative” length scale, $\frac{\nu}{u_*}$ and as $\overline{u'w'} \rightarrow 0$, we define an “outer” length scale, δ .

If in practice we assume after Barenblatt (1993) that the velocity gradient can possibly depend on all these length scales then

$$\frac{\partial U}{\partial z} = f(u_*, z, \nu, \delta), \quad (1.14)$$

where f is here and throughout, an arbitrary function. Here we have 5 variables in 2 dimensions (length, time) and hence by Buckingham’s Π theorem, 3 dimensionless groups result:

$$\Phi_m = f(z_+, \text{Re}_\delta), \quad (1.15)$$

where $\Phi_m = \frac{z}{u_*} \frac{\partial U}{\partial z}$ is the dimensionless wind shear, $z_+ = \frac{zu_*}{\nu}$ is the “wall coordinate” and Re_δ is the Reynolds number based on the outer length scale. In atmospheric flows, both Re_δ and z_+ are necessarily very large so that we can make the assumption that (Barenblatt, 1993) $f \rightarrow \kappa^{-1}$ as $\text{Re}_\delta \rightarrow \infty$ and $z_+ \rightarrow \infty$, where κ is von Karman’s constant.

Integrating eq. (1.15) then gives us the logarithmic velocity profile

$$\frac{U}{u_*} = \frac{1}{\kappa} \ln \left(\frac{zu_*}{\nu} \right) + C, \quad (1.16)$$

where von Karman’s constant and the constant C are then apparently universal, and thus a similarity solution has been found for all flows abiding by the assumptions made above. Eq. (1.16) can be further modified in atmospheric flows to account for a surface roughness much larger than the dissipative length scale. A roughness length scale, z_o is then used which also accounts for the decreasing C as the roughness increases:

$$\frac{U}{u_*} = \frac{1}{\kappa} \ln \left(\frac{z}{z_o} \right). \quad (1.17)$$

Eq. (1.17) is the foundation on which the theory of boundary layer turbulence is built and how it is represented in numerical models. It can be seen that similarity concepts are especially valuable in this field and will be used throughout this work beginning with treatment of the roughness length scale z_o in Chapter 2.

1.4 Scope

The following thesis is aimed at investigating to what effect the nature of offshore meteorology will affect the calculation of offshore meteorological parameters relevant for wind energy. The nature of the sea surface itself via its characteristic roughness length, z_o as defined through the logarithmic velocity profile will play a major role and this will be considered initially in Chapter 2 (Offshore surface roughness effects during high wind speeds at FINO1). There, the roughness

measured at three particular high wind speed periods at FINO1 during 2005 will be investigated and compared with some previous measurements reported in the literature, including during tropical cyclones. The dependence of the roughness on the wave field will then be analysed in Chapter 3 (Aspect ratio effects on offshore drag coefficients) where a first-order scaling of roughness effects based on the measured wave field at a buoy near FINO1 will be presented. While the scaling is able to successfully describe both measurements at FINO1 and those reported previously in the literature, departures from the expected scaling behaviour will lead to further investigations in Chapter 4.

The work in Chapter 4 (Air-Sea and land interaction effects at FINO1) presents an analysis of a particular flow during the spring of 2006 which resulted in a diurnal cycle in detected meteorological parameters by FINO1. Diurnal cycles are not as commonly detected offshore compared with onshore due to the resistance of the water surface to solar heating, but certain flow situations leading to interactions with the coast are to be expected at FINO1 as will be demonstrated here. With the nature of this flow, the interaction between the air and the sea can be uniquely investigated. For example, the scaling results of Chapter 3 can be used to investigate the roughness lengths during this period, where the wave field properties are also found to experience a periodic behaviour. This flow also allows investigation of the vertical structure of offshore turbulence over a good portion of the boundary layer, since the outer length scale, δ is found to be not much higher than the tower during most of this period. A comparison with numerical simulations shows clear differences between the turbulence anticipated by the model and FINO1 measurements, which results in underpredicted modelled wind speeds and leads to an investigation of the model in Chapter 5.

Chapter 5 (Mellor-Yamada-Janjić model modifications in WRF) investigates more closely one particular boundary layer parametrization scheme (the Mellor-Yamada-Janjić (MYJ) model) in the Weather Research and Forecasting (WRF) model. It will be shown that the misrepresentation of turbulence detected at FINO1 by this model as shown in Chapter 4 is a consequence of both theoretical (similarity theory) and practical limitations. With regards to practical limitations, an alternative way of specifying the model closure assumptions is proposed and demonstrated to give realistic results in the single column model within the WRF model. Tests in three-dimensional simulations are left to Chapter 6.

Chapter 6 (Applications for wind energy: Accounting for offshore roughness and turbulence intensity) will then bring the work initiated in Chapter 2 together to show potential benefits in the calculation of wind speed and turbulence intensity based on the preceding 4 chapters. However, it will be shown that there is still work to be done if an optimal anticipation of offshore wind power is to be attained. This is done by revisiting the high wind speed periods considered in Chapters 2 to 4, including the spring 2006 period. In all these periods an improved calculation of turbulence is demonstrated using changes to the MYJ model proposed in Chapter 5. Wind speeds also show some improvement, but there is clear room for further improvement where the exact reason for this will be identified. It will be demonstrated that wind speeds can also be improved with a precise consideration for the offshore surface roughness. This will however require a higher order analysis than that performed here in order for further progress in this area to be made. However, it is believed that

this thesis has laid out a pathway for further improvement in the calculation of offshore meteorological parameters from a wind energy perspective, as will be concluded in Chapter 7 (Conclusions).

Chapter 2

Offshore surface roughness effects during high wind speeds at FINO1

2.1 Introduction

This work will begin by analysing the nature of the surface roughness encountered offshore, which as one could imagine is appreciably different from that experienced over land. The surface roughness evolves with the speed of the air flow above and is usually parametrized using some variant of the classic Charnock (1955) parametrization to be defined below. Given the difficulties with modelling surface features over land surfaces (Raupach et al., 1991), it is believed that “over oceans, the drag laws are a bit easier to parameterize...” (Stull, 1988). However, there are also difficulties over water at, for example, very high wind speeds as experienced in tropical cyclones where a contradiction with Charnock’s parametrization is believed to exist (Powell et al., 2003). At very low wind speeds, the water surface can be much smoother than that over land which means the parametrization must be further adapted for such situations.

From the perspective of numerical weather prediction models, the importance of an accurate parametrization for wind energy purposes is crucial since the nature of the roughness determines the lower boundary of the theoretical logarithmic velocity profile. On a global scale, since the majority of the world’s surface is water, accurate offshore roughness parametrizations extend to other applications in meteorology and climatology.

The Charnock (1955) parametrization will be the starting point in this chapter for analysing the surface roughness at FINO1. Three relatively high wind speed periods which took place at FINO1 during 2005 will then initiate the investigation of the surface roughness at FINO1. The results of that study will then be compared with some results reported previously in the literature. From this analysis, an alternative drag law will be suggested which further explains the anticipated offshore surface roughness in tropical cyclone wind speeds better than Charnock (1955). These results will then lead to a more detailed treatment in the next chapter.

2.2 Surface roughness

The concept of surface roughness in general was mentioned in the previous chapter, but will here be considered specifically for the case of the sea surface. In everyday language, “roughness” is possibly something one more associates with solid surfaces, but it has meaning over water in the sense of a logarithmic velocity profile. In that sense it is often called “aerodynamic roughness” to distinguish it from actual roughness. Since the roughness of the water surface evolves with the state of the atmosphere above, the challenge over water surfaces is then to parametrize the aerodynamic roughness based on bulk air side properties. The most successful parametrization at this so far is due to Charnock (1955) whose work is widely used in numerical models. However, the Charnock (1955) parametrization does encounter difficulties at low wind speeds when the surface roughness is small (Smith, 1988), at very high wind speeds in tropical cyclones (Powell et al., 2003) and at intermediate wind speeds where there is uncertainty in the empirical constant (Fairall et al., 2003).

In the following section, offshore roughness will be introduced via classical concepts developed with respect to laboratory flows. This will lead to an introduction of the drag coefficient as used for offshore flows. The effects of stratification on the drag coefficient will then be considered. Out of these concepts will come Froude number scaling with which the marine drag coefficient is usually scaled. It will then be shown that Froude number scaling fails to collapse measurements from a number of different sources.

2.2.1 Offshore roughness

The starting point for analysis here is the logarithmic velocity profile introduced in the previous chapter

$$\frac{U}{u_*} = \frac{1}{\kappa} \ln \left(\frac{zu_*}{\nu} \right) + C, \quad (2.1)$$

valid in the absence of any appreciable surface roughness, where von Karman’s constant, κ and the integration constant, C are in theory universal. As the surface becomes rougher relative to the height of the inner length scale, $\frac{\nu}{u_*}$ there is a greater sink of momentum at the surface and the constant C in eq. (2.1) becomes a decreasing function of the size and spacing of the roughness elements. In this case, the logarithmic velocity profile is given by

$$\frac{U}{u_*} = \frac{1}{\kappa} \ln \left(\frac{z}{k_s} \right) + 8.5, \quad (2.2)$$

where k_s is the height of the roughness elements used in laboratory experiments performed by Nikuradse (1933), where pipes were artificially roughened with sand. Eq. (2.2) is valid for a so-called completely rough surface which is based on a roughness Reynolds number,

$$Re_k = \frac{u_* k_s}{\nu}, \quad (2.3)$$

and is said to occur for $Re_k \gtrsim 70$, while a smooth regime where eq. (2.1) is valid is entered for $Re_k \lesssim 5$. A transitional roughness regime occurs between these two extremes, where the behaviour of the surface roughness is much more ambiguous (Bradshaw, 2000).

Rewriting eq. (2.1) as a roughness length scale, z_o , i.e. the “aerodynamic roughness” gives

$$\frac{U}{u_*} = \frac{1}{\kappa} \ln \left(\frac{z}{z_o} \right), \quad (2.4)$$

which equating with eq. (2.2) gives a relationship between the equivalent sand grain roughness and z_o as

$$k_s \approx 30z_o. \quad (2.5)$$

From eq. (2.3), the fully rough regime is said to occur (Lange et al., 2004) for an aerodynamic roughness Reynolds number

$$Re_* = \frac{z_o u_*}{\nu} > 2.3. \quad (2.6)$$

The same relationship gives a smooth regime for $Re_* < 0.17$, valid when the height of the roughness elements are less than the viscous length scale, $\frac{\nu}{u_*}$.

Over water surfaces, Charnock (1955) famously proposed

$$z_o = \alpha \frac{u_*^2}{g}, \quad (2.7)$$

which results from dimensional considerations whereby the variables z_o , u_* and g can only form a single dimensionless group from Buckingham’s II theorem. The constant α is an empirical constant which does depend on the author (Donelan, 1990), but a commonly used value is 0.018 after the review of Wu (1980). With the relationship between k_s and z_o , Charnock’s parametrization predicts roughness elements O(1) cm which can be interpreted as the size of surface ripples that ride on top of the large scale, energy containing waves (Csanady, 2001). As opposed to eq. (2.7) however, a smooth flow is often assumed at low Reynolds numbers where (Smith, 1988)

$$z_o = \frac{\nu}{0.11u_*}. \quad (2.8)$$

The question of whether a flow over a water surface ever becomes fully rough in most practical offshore conditions was raised by Banner and Peirson (1998) based on their direct laboratory measurements of the tangential stress beneath the water. Their results suggest that the roughness Reynolds number given by (2.6) does not classify a rough flow regime, but rather the approximate magnitude at which the tangential stress is half that of the total stress as estimated from the logarithmic law. Extrapolating their results to the field, they conclude that offshore flow may not be fully rough below wind speeds of at least 15 ms^{-1} . Amorochio and Devries (1980) proposed something similar many years ago and conjectured that beyond about 20 ms^{-1} , the sea is saturated with breaking waves leading to form drag as the dominant drag generating mechanism. Their rough flow regime, as estimated from data available to them at the time including in tropical cyclones, is initiated at about $Re_* \sim 300$, a full two orders of magnitude larger than that traditionally assumed ($Re_* = 2.3$, Lange et al., 2004). They also proposed a “low roughness region” at low wind speeds for $Re_* < 1$ and a “transitional” regime bridging this with the rough flow regime.

From this we can see that Charnock’s parametrization, which as will be shown further below has difficulties at tropical cyclone wind speeds, i.e. at

speeds at least greater than 20 ms^{-1} , is thus modelling the transitional roughness regime. As Jiménez (2004) has demonstrated, the transitional roughness regime is even complicated in laboratory flows over different solid roughness elements (e.g. uniform packed spheres, triangular riblets), with no universal function being able to describe all possible geometries. For example, one particular recent investigation using a honed pipe at large Reynolds numbers (Shockling et al., 2006) showed a slightly different transitional behaviour compared with Nikuradse (1933)'s sand grains. If one can then imagine that there are different types of “sea-states” as with there being different types of roughness elements at a laboratory scale, this could go a long way to explaining the many different magnitudes of Charnock’s constant α reported (Donelan, 1990), and that it may even be a function of the wind speed (Fairall et al., 2003).

2.2.2 Drag coefficient

A skin friction coefficient can be defined in laboratory flows when the outer flow scale, U_∞ is well defined, i.e.

$$C_f = \frac{u_*^2}{U_\infty^2}, \quad (2.9)$$

and is Reynolds number dependent. One choice for an outer velocity scale in the atmospheric boundary layer is the geostrophic wind speed that will be introduced in Chapter 4, but then one must assume the pressure gradient is balanced by the Coriolis effect, as well as further experimental constants in addition to κ (Tennekes, 1973). Instead, a velocity scale within the logarithmic layer, U is used to form a “drag coefficient”, defined as

$$C_D = \frac{u_*^2}{U^2}. \quad (2.10)$$

Since U is within the atmospheric logarithmic layer, one avoids Reynolds number effects as seen in the previous chapter, but there is an extra stratification dependence as will be seen in the next subsection. Eq. (2.10) when combined with the logarithmic law, eq. (2.4), gives

$$C_D = \left[\frac{1}{\kappa} \ln \left(\frac{z}{z_o} \right) \right]^{-2}, \quad (2.11)$$

meaning that C_D is a function of both the height and the roughness length for a given friction velocity. With Charnock’s parametrization, C_D becomes

$$C_D = \left[\frac{1}{\kappa} \ln \left(\frac{gz}{\alpha u_*^2} \right) \right]^{-2}, \quad (2.12)$$

and anticipates an increasing C_D with wind speed at a constant height and is supported by measurements in the field at moderate wind speeds (Garratt, 1977). However, as will be shown below the exact functional dependence of C_D on wind speed is uncertain and likely depends on the nature of the water waves (Donelan, 1990). Moreover, recent experimental evidence suggests that the magnitude of the drag coefficient tends towards a constant value (Donelan et al., 2004; Black et al., 2007) and may even decrease at tropical cyclone wind speeds (Powell et al., 2003).

2.2.3 Stratification effects

Eq. (2.11) is only applicable in neutral stratification because the velocity scale in eq. (2.10) is a function of stratification and thus to “correct” for this effect, the classic Monin-Obukhov stability theory (Monin and Obukhov, 1954) is used. Let us assume that the stratified velocity gradient is only a function of the following parameters:

$$\frac{dU}{dz} = f(\overline{w'\theta'_v}, g, u_*, \theta_v, z), \quad (2.13)$$

where θ_v is the virtual potential temperature and $\overline{w'\theta'_v}$ is the vertical velocity-potential temperature covariance. In the original theory, Monin and Obukhov (1954) grouped $\frac{g}{\theta_v}$ into a single parameter, i.e. the buoyancy parameter, which comes from the conservation of energy equation. This consequently gives 5 variables as opposed to the 6 in eq. (2.13). However, for purposes of highlighting a contradiction below, let us assume the relevant variables according to (2.13). At any rate, both methods result in the equivalent, practical result.

Thus, given six variables in three dimensions, then from Buckingham’s Π theorem one obtains the dimensionless wind shear

$$\Pi_1 = \frac{dU}{dz} \frac{z}{u_*}, \quad (2.14)$$

a “flux ratio”

$$\Pi_2 = \frac{\overline{w'\theta'_v}}{u_* \theta_v} \quad (2.15)$$

and a Froude number

$$\Pi_3 = \frac{gz}{u_*^2}. \quad (2.16)$$

In neutral boundary layers, $\Pi_2 \rightarrow 0$, which would make the dimensionless wind shear a function of the Froude number, $\Pi_1 = f(\Pi_3)$ in the absence of stratification. However, any Froude number effects here are apparently not this explicit since, as it has been demonstrated above in neutral boundary layers, Π_1 reduces to a constant. In that case, one must write

$$\Pi_1 = cf(\Pi_2 \Pi_3), \quad (2.17)$$

where the constant $c = \kappa^{-1}$, so that $\Pi_2 \Pi_3 \rightarrow 0$ in the absence of stratification whereby $f(0) = 1$.

Eq. (2.17) then reduces to the classical result that

$$\Phi_m = f\left(\frac{z}{L}\right), \quad (2.18)$$

where $\Phi_m \equiv \Pi_1$, L is the Obukhov length scale

$$L = -\frac{u_*^3}{\kappa \frac{g}{\theta_v} \overline{w'\theta'_v}} \quad (2.19)$$

and $\frac{z}{L} \equiv \Pi_2 \Pi_3$ is the Monin-Obukhov stability parameter. The function f in eq. (2.18) takes different function forms depending on the sign of $\frac{z}{L}$, where

$$\Phi_m = \left(1 - 16 \frac{z}{L}\right)^{-1/4} \quad (2.20)$$

for unstable stratification ($\frac{z}{L} < 0$) and

$$\Phi_m = 1 + 5 \frac{z}{L}, \quad (2.21)$$

for stable stratification ($\frac{z}{L} > 0$), although the constants in these values can take different values depending on the author (Högström, 1996).

Rewriting eq. (2.18) so that

$$\frac{dU}{dz} = \frac{u_*}{\kappa z} \Phi_m, \quad (2.22)$$

then this can be integrated with respect to z (Paulson, 1970) i.e.

$$\int dU = \frac{u_*}{\kappa} \left[\int \frac{dz}{z} - \int \frac{1 - \Phi_m}{\zeta} d\zeta \right], \quad (2.23)$$

where $\zeta = \frac{z}{L}$, to yield a logarithmic law

$$U = \frac{u_*}{\kappa} \left[\ln \frac{z}{z_o} - \Psi_m \right] \quad (2.24)$$

that deviates from the theoretical one, eq. (2.4) by the function Ψ , where

$$\Psi = \int \frac{1 - \Phi_m}{\zeta} d\zeta. \quad (2.25)$$

Hence, from eqs. (2.21) and (2.20), then

$$\Psi = -5 \frac{z}{L} \quad (2.26)$$

for $\frac{z}{L} > 0$ and (Paulson, 1970)

$$\Psi = 2 \ln \left(\frac{1+X}{2} \right) + \ln \left(\frac{1+X^2}{2} \right) - 2 \tan^{-1}(X) + \frac{\pi}{2} \quad (2.27)$$

for $\frac{z}{L} < 0$ where

$$X = \left(1 - 16 \frac{z}{L} \right)^{1/4}. \quad (2.28)$$

From eq. (2.24) it can be seen that the wind speed increases in stable stratification, $\frac{z}{L} > 0$ and decreases in unstable, $\frac{z}{L} < 0$ relative to the theoretical logarithmic velocity profile.

Substituting eq. (2.24) into the drag coefficient, eq. (2.10) gives

$$C_D = \left[\frac{1}{\kappa} \left(\ln \frac{z}{z_o} - \Psi \right) \right]^{-2}. \quad (2.29)$$

From hereon, the theoretical logarithmic drag coefficient C_{Dn} will be distinguished from C_D according to eq. (2.29) by including a subscript “n”, i.e.

$$C_{Dn} = \left[\frac{1}{\kappa} \ln \frac{z}{z_o} \right]^{-2}, \quad (2.30)$$

and C_{Dn} is only a function of height and the aerodynamic roughness length.

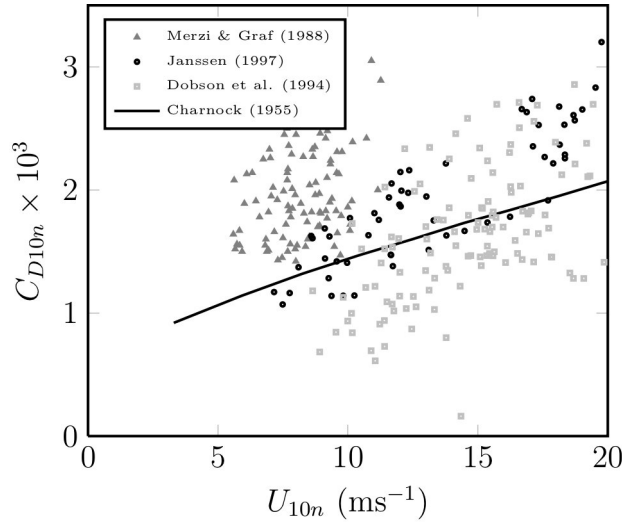


Figure 2.1: Sea (ocean) surface drag coefficients at 10 m as a function of the 10 m neutral wind speed as reported by Merzi and Graf (1988), Janssen (1997) and Dobson et al. (1994). Also included is Charnock's parametrization, eq. (2.12) for $\alpha = 0.018$.

2.2.4 Froude number effects

In offshore flows it is standard (e.g. Smith and Banke, 1975; Smith, 1980) to report drag coefficients at a height of 10 m so that

$$C_{D10n} = \left[\frac{1}{\kappa} \ln \frac{10}{z_o} \right]^{-2} \quad (2.31)$$

and correspondingly

$$U_{10n} = \frac{u_*}{\kappa} \ln \frac{10}{z_o}. \quad (2.32)$$

It is also then standard (e.g. Garratt, 1977; Donelan, 1990) to plot C_{D10n} as a function of the 10 m wind speed, i.e. $C_{D10n} = f(U_{10n})$. The classical result then finds that C_{D10n} is a linearly increasing function of the wind speed (e.g. Smith, 1980; Anderson, 1993; Yelland et al., 1998), i.e.

$$C_{D10n} (\times 10^3) = 0.079 U_{10n} + 0.40 \quad (2.33)$$

after Anderson (1993). This result is broadly evident in the drag coefficients as a function of wind speeds plotted in Fig. 2.1 which were reported over Lake Geneva by Merzi and Graf (1988), the North Sea by Janssen (1997) and the North Atlantic by Dobson et al. (1994). The linear dependence of C_{D10n} on U_{10n} is consistent with Charnock's drag law, eq. (2.12) which has also been plotted in Fig. 2.1. The measurements here however deviate from the exact function where a Charnock's constant, $\alpha = 0.018$ is used in eq. (2.12).

On the one hand, this approach is problematic since it is dimensionally inconsistent with a dimensionless number on one side of the equation and the velocity on the other. For that reason a plot of C_{D10n} against the wind speed

cannot be general so that other important parameters can easily cause a departure from any general fit to the measurements in a plot of $C_{10Dn} = f(U_{10n})$. On the other hand, mere dimensional inconsistency is a little too easy to criticise without good reason. As Donelan (1990) has stated in the past, there have not been too many other good options. Wu (1980) claims a plot of $C_{D10n} = f(U_{10n})$ is Froude number scaling, where the 10 m wind speed is taken as a proxy for $\frac{U_{10n}}{\sqrt{zg}}$, where g is the gravitational constant, and at a 10 m reference height, $z = 10$ m. Wu (1980) had some success collapsing laboratory measurements with those recorded in the field using Froude number scaling.

However, we can see from the group Π_2 above and eq. (2.17) that in the context of Monin-Obukhov similarity theory, Froude number effects are embedded into the Monin-Obukhov similarity parameter, ζ . Since $\zeta \rightarrow 0$ in neutral stratification, Froude number effects should not be relevant in $C_{D10n} = f(U_{10n})$ space. It can be seen in Fig. 2.1 that Froude number scaling does not appear to collapse the measurements displayed there, as recorded at a number of different locations. The likely explanation then is that C_{D10n} does not follow Froude number scaling, but rather depends on other parameters relevant to the sea surface itself. The measurements in Fig. 2.1 have been selected for the fact that they also include parameters describing the bulk wave parameters of the sea-surface. The next chapter will look at providing an alternative to Froude number scaling of these measurements based on those very bulk sea-state parameters. Before that is conducted, an alternative drag law to Charnock's will be proposed in the next section based on three particular periods at FINO1. While this drag law will not be as general as that proposed in the next chapter, it is in agreement with indirect estimates in tropical cyclones, and could be useful in applications not accounting explicitly for the wave field, as will be demonstrated later in Chapter 6.

2.3 FINO1

In the following section, the nature of the surface roughness during three particular periods of 2005 at FINO1 will be investigated from which an alternative drag law to that commonly used will be formulated. The FINO1 data itself will briefly be described where a more detailed description of the platform and measurements in general can be found in Türk (2008). The periods analysed here include a stable, high wind speed period during January 2005, an unstable period during February 2005 and an unstable period (although not quite exclusively) during November 2005. From these, a new empirical drag law which is valid at higher wind speeds is developed. For that reason, the higher wind speeds encountered during tropical cyclones will then be considered.

2.3.1 Data Description

The data used in this thesis originates from DEWI (German Wind Energy Institute) and has been processed by Matthias Türk whereby a full description of that work can be found in Türk (2008). A brief description of that processing and further processing will be given here. Turbulence measurements are conducted at 40, 60 and 80 m heights using Gill R3-50 sonic anemometers that sample at an effective frequency of 10 Hz. Measurements are rotated into the wind such

that mean lateral and vertical velocities are zero after which, after removing a linear trend, 10 minute averages of standard deviations and covariances are calculated. One hour averages have then been calculated from the 10 minute means after rejecting measurements believed to be within the shadow of the tower (100 to 160° & 280 to 350°), wind direction fluctuations at 80 m greater than 10 degrees on a 10 minute timescale (i.e. unsteadiness) and rain detected at 90 m but not at 20 m (i.e. “light rain” is still considered). A comparison between measurements with and without a rain signal at 20 m will be shown below to be little different.

2.3.2 January 2005

Very high wind speeds were detected at the FINO1 platform during 4–10, January 2005 which featured the named storm “Erwin” on the 8th. In this period, hub height wind speeds up to 30 ms^{-1} were measured as is displayed in Fig. 2.2 (top), as well as wave heights $O(10 \text{ m})$ (Emeis and Türk, 2009). Also shown in Fig. 2.2 are the 90 m wind direction (middle) and 90 and 33 m relative humidities (bottom). The wind came predominantly from the south-west where depending on the precise wind direction, the fetch (i.e. the distance to the nearest coast) can reach roughly 500 km. This makes such a flow of a typically marine nature as evident by the magnitude of relative humidities which are consistently above 80% and sometimes tending towards 100% throughout the tower layer. The small difference in relative humidities between 90 and 33 m is an indicator of the strong vertical mixing that occurred during this period.

The very high wind speeds here means that the tower measurements are within or close to the surface layer which is typically regarded as the lower 10% of the boundary layer (Panofsky and Dutton, 1984). The surface layer is distinguished from the rest of the boundary layer by nearly constant magnitudes of Reynolds stresses within this level. In order to be able to gauge the departure of measurements at 40 m from true surface values, friction velocities as calculated by the 80 and 40 m sonic are displayed in Fig. 2.3 (top). It is evident that the 40 m u_* is consistently higher than the 80 m measurement which would suggest that the 40 m measurement is underestimating the true u_* . An alternative estimate for u_* is to look at the standard deviation of the vertical velocity which is closely related to u_* by (e.g. Panofsky and Dutton, 1984)

$$\frac{\sigma_w}{u_*} = \text{constant}, \quad (2.34)$$

where this constant is a function of stability. Fig. 2.7 shows a time series of σ_w at 40 and 80 m where a good agreement between the two is seen for the entire time period, suggesting σ_w at 40 is possibly close to the surface value.

Friction velocities (left) and drag coefficients (right) as inferred from u_* at 40 m are displayed in Fig. 2.4 (top) as a function of wind speed. For comparison, the open ocean measurements reported by Dobson et al. (1994) are included in Fig. 2.4 (bottom). In all Fig. 2.4, the solid line is Charnock’s parametrization for $\alpha = 0.018$ and the dashed line is a regression curve defined by

$$u_* = a_1 U_{10n} + a_2, \quad (2.35)$$

where the regression constants, $a_{1,2} = (0.057, -0.26)$ for $U_{10n} > 10 \text{ ms}^{-1}$. Eq. (2.35) can then be substituted back into $C_{D10n} = \frac{u_*^2}{U_{10n}^2}$ to give a new drag law

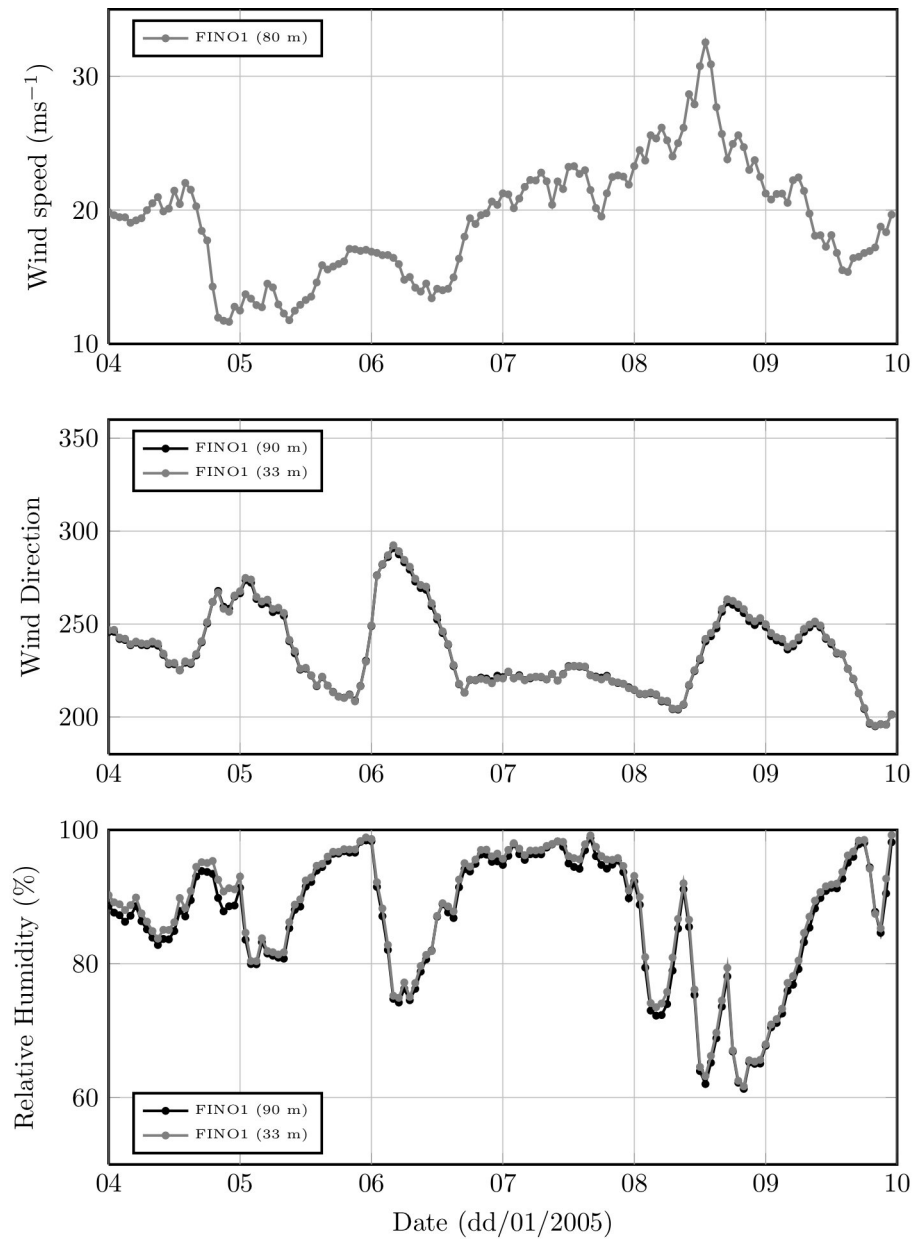


Figure 2.2: Wind speeds at 80 m (top), wind direction at 90 m and 33 m (middle) and relative humidities at 90 and 33 m (bottom) as recorded at FINO1 during January 4–10, 2005.

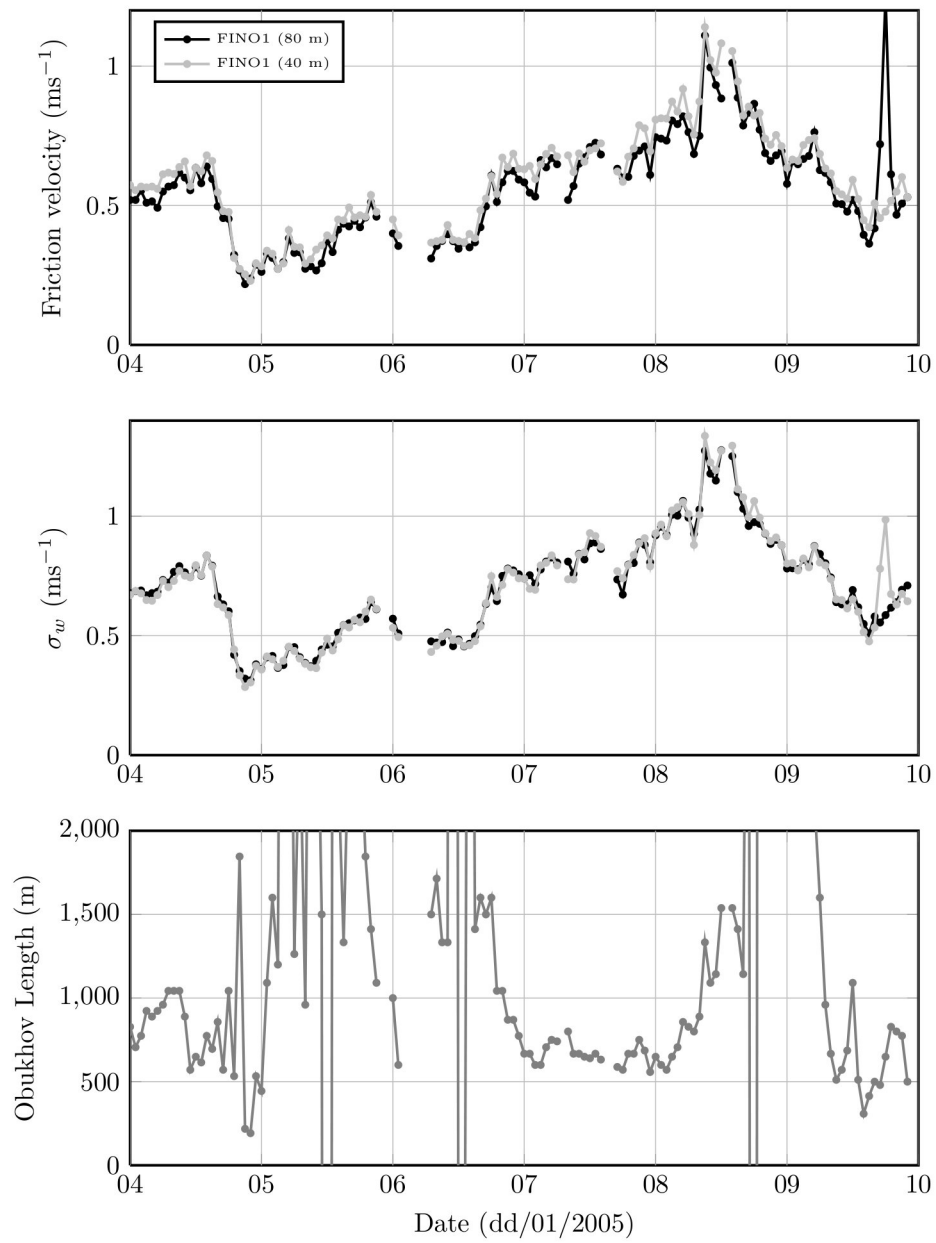


Figure 2.3: Friction velocities (top) and vertical standard deviations (middle) at 80 and 40 m, and Obukhov lengths as estimated from the 40 m sonic (bottom) as recorded at FINO1 during January, 4–10.

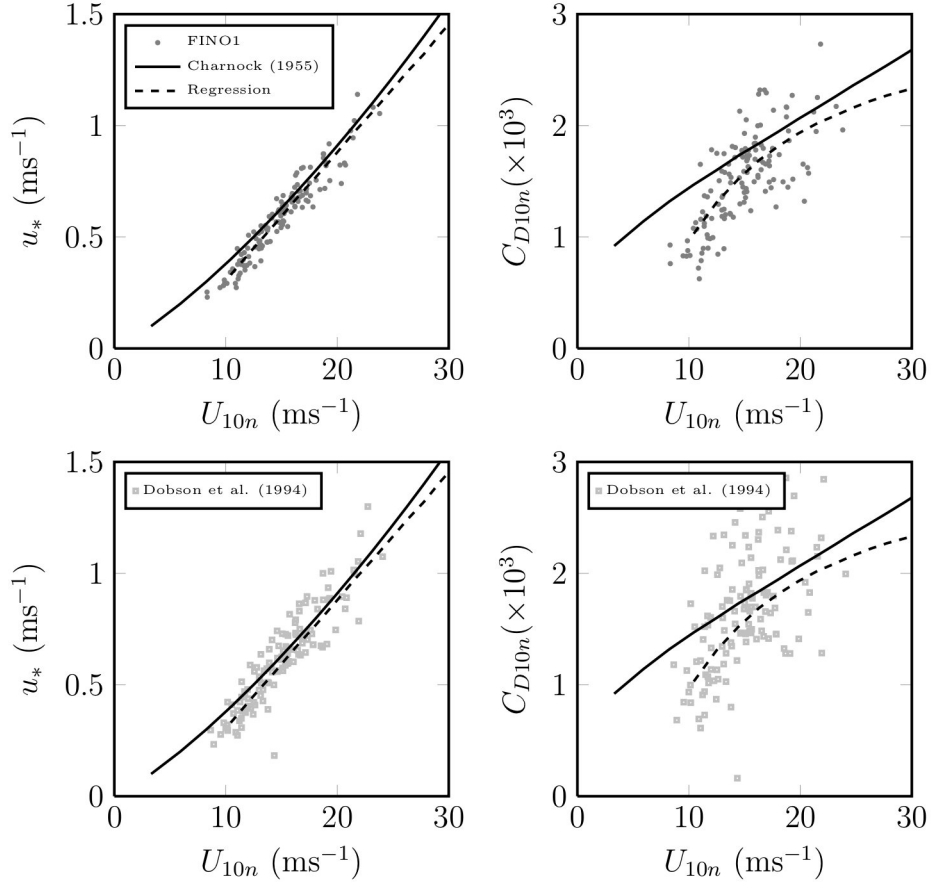


Figure 2.4: Top: Friction velocities (left) and drag coefficients (right) as a function of wind speed using u_* estimated from the 40 m sonic during January 4–10, 2005. Bottom: Measurements of drag coefficients (left) and friction velocities (right) as reported by Dobson et al. (1994). The solid line is Charnock's law for $\alpha = 0.018$ and the dashed line is a regression in $u_* = f(U_{10n})$ space based on the FINO1 measurements (i.e., top left).

in Froude number space, i.e.

$$C_{D10n} = \frac{(a_1 U_{10n} + a_2)^2}{U_{10n}^2}, \quad (2.36)$$

where this curve is also displayed in Fig. 2.4 for $a_{1,2} = (0.057, -0.26)$.

Estimates of u_* are in fairly good agreement with Charnock's parametrization for $U_{10n} > 15 \text{ ms}^{-1}$. At lower wind speeds, eq. (2.35) is likely a better description of the data. The behaviour of C_{D10n} at lower wind speeds, i.e. below Charnock's parametrization, is also consistent with the measurements reported by Dobson et al. (1994), reproduced here in Fig. 2.4 (bottom). However, that the estimate of u_* at 40 m is likely underestimating the true value by a small amount can be seen in average wind profiles during the 5th and 7th displayed in Fig. 2.5. The Obukhov lengths for this period at 40 m as shown above in Fig.

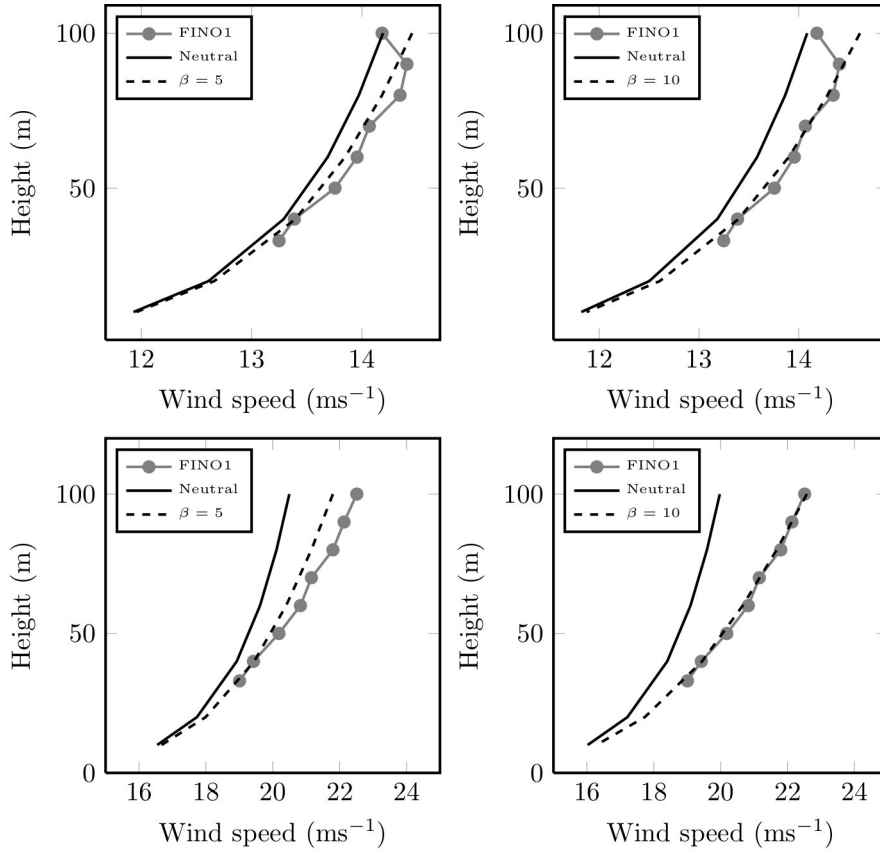


Figure 2.5: Average wind profiles during the 5th (top) and 7th (bottom) of January 2005 compared with equivalent neutral wind profiles assuming $\beta = 5$ (left) and $\beta = 10$ (right) in eq. (2.39).

2.3 (bottom) are generally well over 500 m illustrating the near neutral stratification of this period. However, wind speed profiles still show a clear deviation from a purely neutral velocity profile within the tower layer.

The equivalent neutral wind speed profile has been calculated based on the 40 m sonic and cup anemometer. From the Monin-Obukhov wind profile, eq. (2.24) the neutral 40 m wind speed is calculated using

$$U_{40n} = U_{40} + \frac{u_*}{\kappa} \Psi \left(\frac{40}{L} \right). \quad (2.37)$$

The roughness length can then be found via the theoretical logarithm

$$z_o = z \exp \left(\frac{-kU_{40n}}{u_*} \right), \quad (2.38)$$

so that the neutral profile can then be calculated throughout the tower layer and these are the solid profiles throughout Fig. 2.5. The true wind profile throughout the layer at heights other than 40 m are then calculated based on the Monin-Obukhov wind profile and these are the dashed profiles in Fig. 2.5. Fig. 2.5 then

shows average calculated wind profiles during assuming $\beta = 5$ (left) and $\beta = 10$ (right) in

$$\Psi = -\beta \frac{z}{L} \quad (2.39)$$

in stable stratification. It can be seen here that the better agreement using $\beta = 10$ as opposed to the more standard $\beta = 5$ (Högström, 1996) is likely a consequence of an underestimated 40 m friction velocity.

2.3.3 February 2005

In contrast to the January period above, February 20–28, 2005 brought colder north-easterly air to the platform resulting in an unstably stratified flow. Fig. 2.6 shows wind speeds (top), wind direction at 90 and 33 m (middle) and relative humidity at 90 and 33 m (bottom). High wind speeds during this period were also detected reaching about 20 ms^{-1} at 80 m during the 23rd. The excellent vertical mixing during the 23rd resulted in near saturated air as seen in the relative humidity. The rain gauge at 20 m indicated intermittent rain throughout this period and during most of the 23rd. As mentioned in section 2.3.1 above, data are rejected only if rain was detected at 90 m, which allows us to consider at least some results during the very high wind speed period of the 23rd. There was a rapid change in the wind direction beginning on the 26th corresponding with the passage of a cold front. During the 24th, the wind weakened and turned to the east with reduced vertical mixing and the possible advection of drier continental air.

A time series of friction velocities, vertical standard deviations of velocity and Obukhov lengths are displayed in Fig. 2.7. In contrast to the period above in stable stratification, it can be seen that there is good agreement between the 80 and 40 m friction velocities, even in weaker winds on the 25th. Hence, the 40 m friction velocity during this period could be quite close to the true surface value. The vertical velocity standard deviations show a clear separation between the 40 and 80 m values, increasing with height as could be expected in a convective boundary layer, and hence σ_w (40 m) is likely overestimating the surface value. Obukhov lengths illustrate unstable stratification throughout this period. Consequently, average wind profiles as displayed for the 23rd and 25th in Fig. 2.8 show less wind shear than the theoretical logarithms illustrated by the solid black curves. The dashed curves as calculated from the Monin-Obukhov similarity formulae introduced above based on the 40 m friction velocity and wind speeds agree with the wind levels higher up. The agreement of wind profiles calculated using Monin-Obukhov theory with standard constants using the 40 m measurements in this case contrasts with the January case above where the constant, β had to be adjusted to fit the measured profiles.

According then to the same logic that suggested 40 m measurements were slightly underestimated during January, the 40 m measurement here during February should be approximately representative of the surface values. This is important because drag coefficients in Fig. 2.9 (top right) deviate significantly from Charnock's parametrization for $\alpha = 0.018$ (solid black line). A linear regression in $u_* = f(U_{10n})$ space has also been calculated for this period giving $a_{1,2} = (0.042, -0.01)$ and this curve, defined by eq. (2.36) above clearly shows a levelling off well below 20 ms^{-1} . Neglected from the regression are measurements less than 5 ms^{-1} which may well be in a smooth flow regime. A smooth

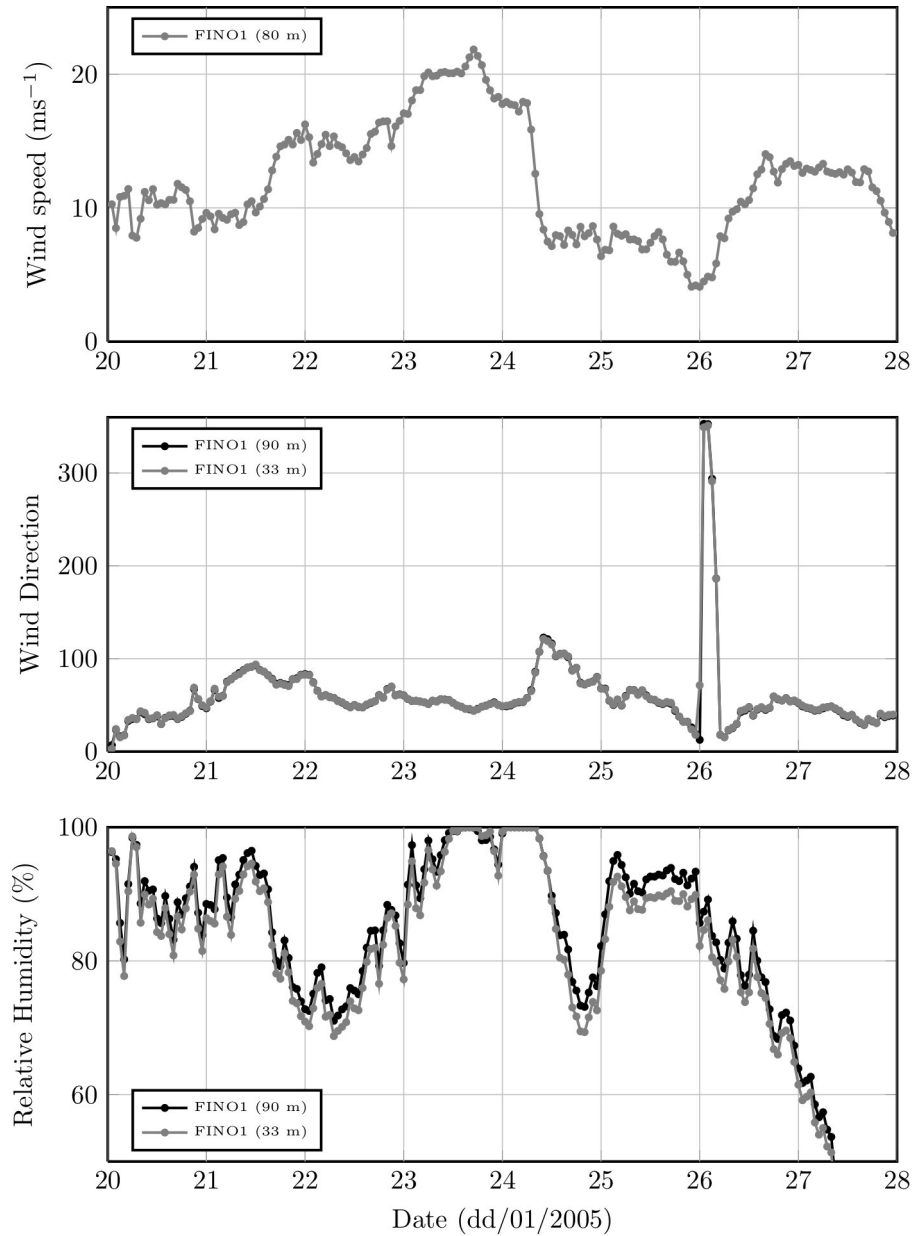


Figure 2.6: Wind speeds at 80 m (top), wind direction at 90 m (middle) and relative humidities at 90 and 33 m (bottom) at FINO1 during February, 20–28, 2005.

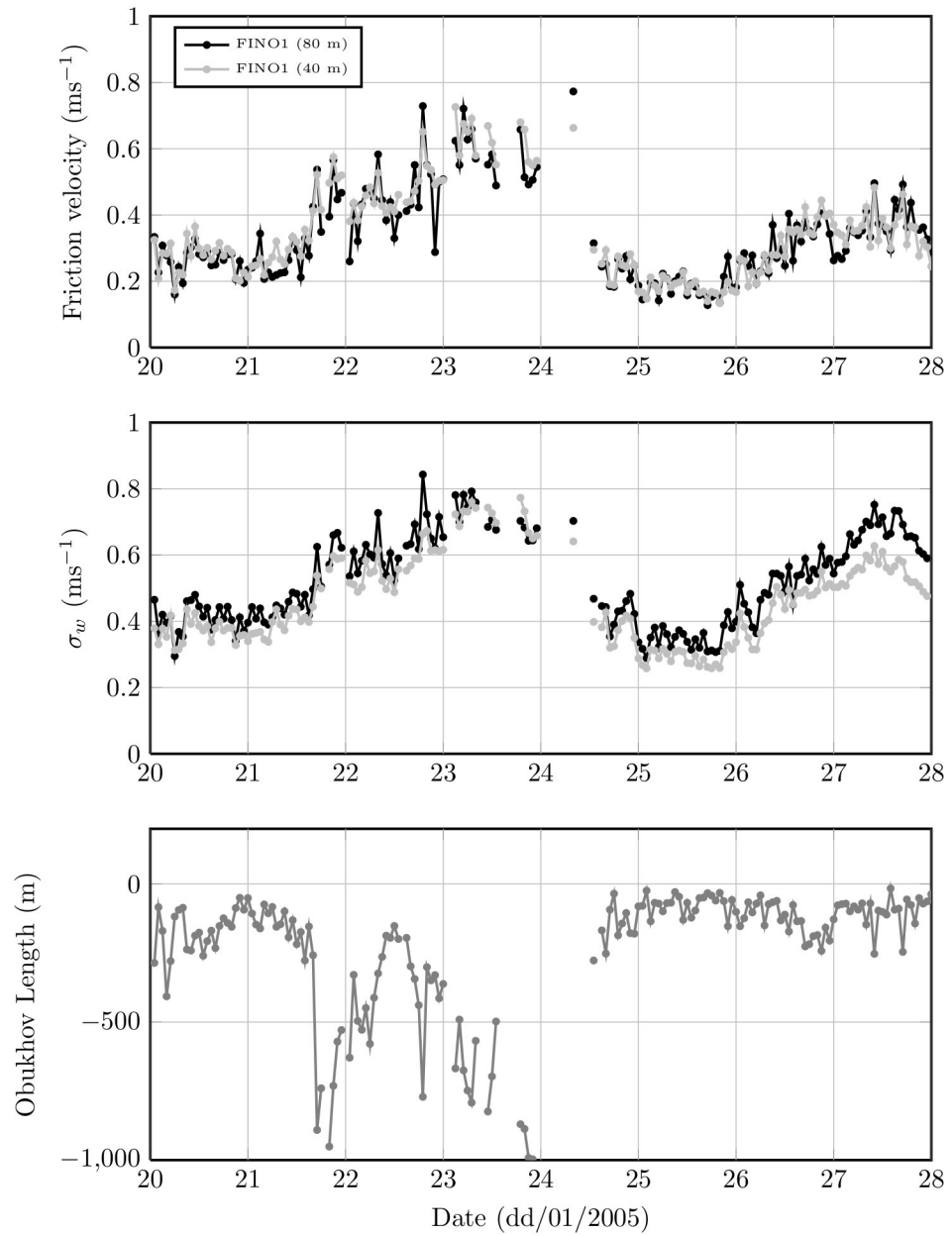


Figure 2.7: Friction velocities (top) and vertical standard deviations (middle) at 80 and 40 m, and Obukhov lengths as estimated from the 40 m sonic (bottom) as recorded at FINO1 during February, 20–28, 2005.

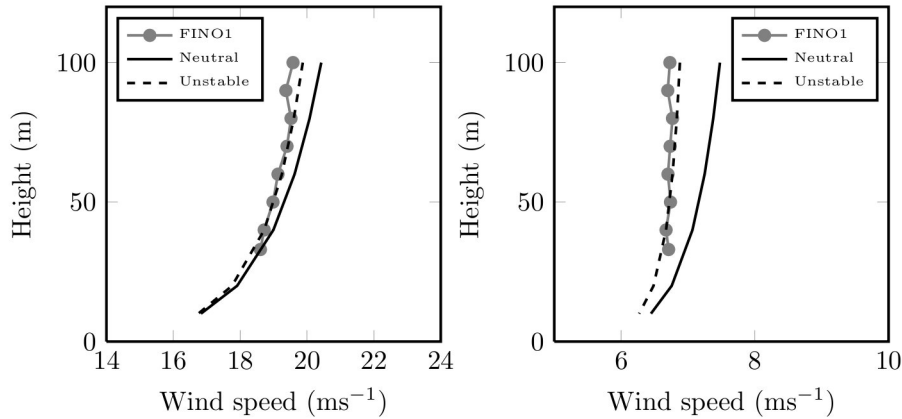


Figure 2.8: Average wind speed profiles during the 23rd (left) and 25th (right) of February 2005 compared with equivalent neutral wind profiles (solid black curve) and the unstable profiles from Monin-Obukhov similarity theory based on the 40 m sonic and cup anemometers.

flow regime results in an increasing C_{D10n} for decreasing wind speeds.

One reason for the significantly lower C_{D10n} with respect to Charnock and the strong linear dependence in $u_* = f(U_{10n})$ space may be a consequence of rain affected sonics, particularly during the 23rd which according to the 20 m rain gauge (but not at 90 m), rained the whole day. However, plotting $u_* = f(U_{10n})$ without any rain detected at 20 m (Fig. 2.9, bottom left) and with (Fig. 2.9, bottom right) does not yield a clear separation in the measurements. It could be possible that at these wind speeds, any water has little chance to accumulate on the sonic structure. If one believes the drag coefficients here, the rain itself could either be affecting the turbulence within the air, or the nature of the water surface below (Jones and Toba, 2001). The high wind speeds here and during the January period above could be generating sea spray, whereby in addition to the rain, the air becomes a multiphase flow. In fact, the effect of sea spray is expected to be important for storm development at higher wind speeds (Andreas and Emanuel, 2001). It is well known from laboratory scale experiments that the addition of particles to the air will affect the underlying turbulence (Kenning and Crowe, 1997).

A different train of thought from these issues will be followed here, where the significance of the wave field will be considered in the next chapter. To briefly anticipate results there, Fig. 2.9 (bottom) shows the measurements in the Baltic Sea reported by Johnson et al. (1998) which, apart from some low wind speed data, appear to agree well with Charnock's parametrization once more shown as the solid curve. In Froude number space, Fig. 2.9 (bottom right) shows the Johnson et al. (1998) measurements clearly sitting above the February 2005 regression curve based on eq. (2.36) above, and hence a lack of Froude number similarity. It will be shown in the next chapter however, that the February 2005 results demonstrate a similar scaling with at least some of the Johnson et al. (1998) results when considering the wave field.

Contrasting this period with the January case above (which agreed with

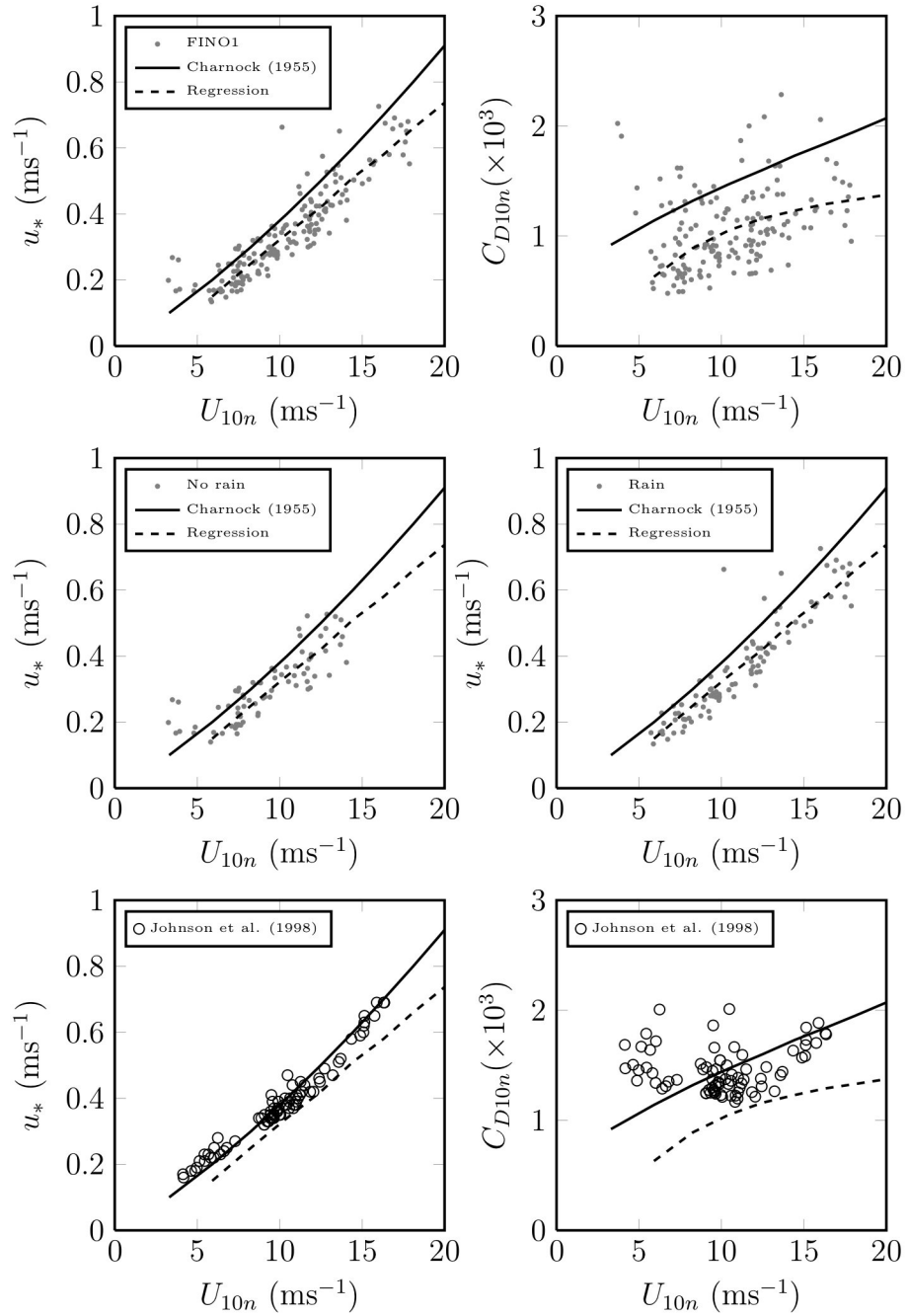


Figure 2.9: Top: Friction velocities (left) and drag coefficients (right) as a function of wind speed as measured at FINO1 between February 20-28, 2005. Middle: Measurements during this same period with no rain detected at the 20 m measurement (left) and with rain detected at the 20 m measurement (right). Bottom: For comparison are measurements of u_* and C_{D10n} as a function of wind speed in the Baltic as reported by Johnson et al. (1998). The solid line is Charnock's law for $\alpha = 0.018$, the dashed is a regression for $a_{1,2} = (0.042, -0.01)$ using all measurements.

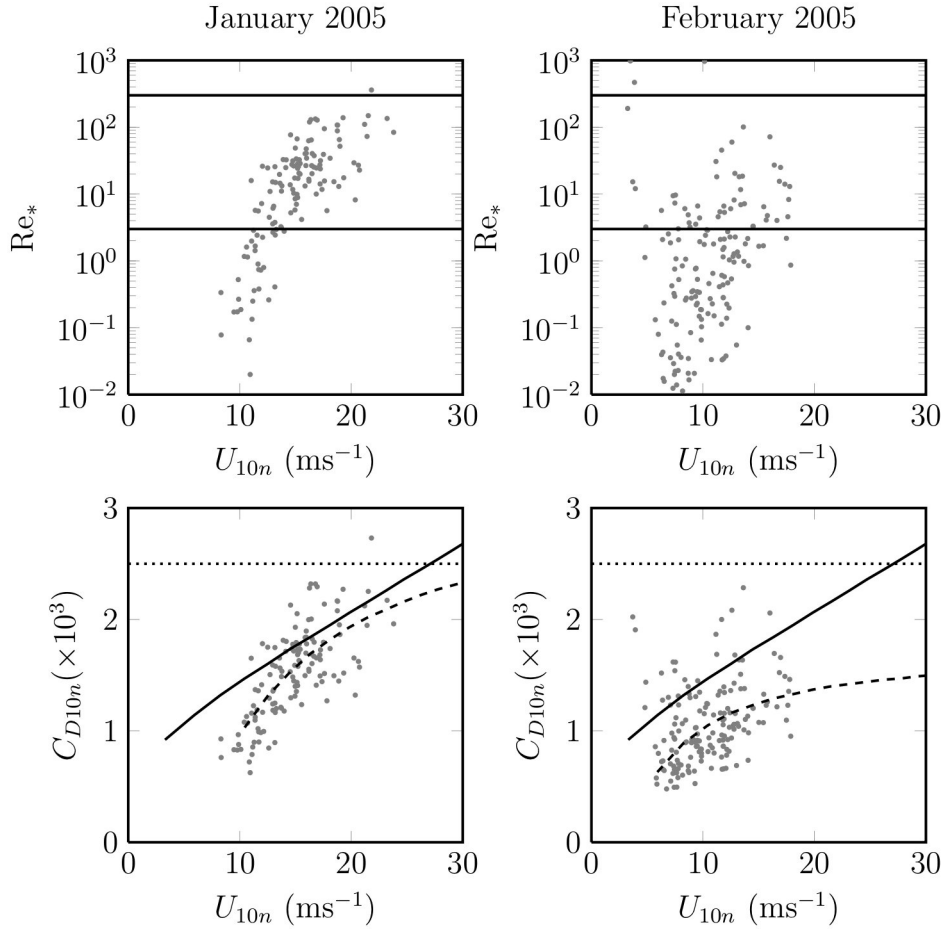


Figure 2.10: Roughness Reynolds number (top) and C_{D10n} (bottom) as a function of wind speed during January 2005 (left) and February 2005 (right). The two solid lines (top) are for $Re_* = 300$ and 3. The solid line (bottom) is Charnock's parametrization for $\alpha = 0.018$. The dashed curves are eq. (2.36) for $a_{1,2} = (0.057, -0.26)$ (left) and $(0.042, -0.01)$ (right). The dotted line is eq. (2.40) after Amorcho and Devries (1980).

Charnock's parametrization at higher wind speeds), it can be seen that Froude number scaling fails to collapse the measurements here at a single site, in addition to what has already been displayed from the collection measurements from the literature shown above in Fig. 2.1. Fig. 2.10 shows roughness Reynolds numbers for both January (left) and February (right) as a function of wind speed. The horizontal solid lines in this figure correspond with different supposed rough flow regimes, $Re_* = 300$ and $Re_* = 3$ as discussed above. Taking $Re_* > 300$ as the rough flow limit means that essentially all measurements during these two periods are not fully rough, but rather in a transitional regime. Hence, given the complexity of laboratory flows over well defined solid roughness elements in the transitional regime (Jiménez, 2004), it is then not surprising that determining

the equivalent drag laws over a dynamic water surface has in the past proved extremely difficult (Jones and Toba, 2001).

If one could further interpret “rough flow” as meaning a constant drag coefficient and thus z_o independent from u_* such as that found over much rougher land surfaces, neither of these two cases give drag coefficients (also shown in Fig. 2.10) that are constant. Although, both tend to level-off when approaching $Re_* = 300$ and 3 for the January and February, 2005 periods, respectively, suggesting they are both approaching their own rough flow regimes. The dotted horizontal line in these figures is the proposed drag law in the rough flow regime ($Re_* > 300$) proposed by Amorocho and Devries (1980),

$$C_{D10n} = 2.5 \times 10^{-3}. \quad (2.40)$$

Anticipating results in the next chapter, these two periods following different wave field scaling regimes and hence, this may result practically in different transitional roughness regimes.

2.3.4 November 2005

The case above during January gave predominantly stable stratification, while February 2005 resulted in unstable stratification. During November 2005, unstable stratification resulted for most of the period between 9–15 except during the 11th, with relatively high wind speeds as evident from Fig. 2.11 (top). The wind direction is generally south-westerly and sometimes north-westerly as seen in Fig. 2.11 (middle). Relative humidities approach 100% during the 11th and also brought rain, but are generally over 60% (Fig. 2.11, bottom). The spike in the wind direction during the 13th is likely a result of the tower disturbing the flow at this point, where turbulence values have been removed during these periods as seen in Fig. 2.12. In order to estimate the departure of 40 m measurements from the surface values, time series of friction velocities and vertical standard deviations are shown in Fig. 2.12 (top and middle) at 40 and 80 m. To indicate the sign of stability, Obukhov lengths as calculated from the 40 m sonic anemometer are displayed in Fig. 2.12 (bottom), where the stable period during the 11th is evident. As we have seen above with respect to the stable January period, σ_w does not vary with height to the extent that u_* does. One can see this here during the latter part of the 10th and during the 11th where this is good agreement with σ_w (40 m) and σ_w (80 m). During the other (unstable) times, one can see an increase with height of σ_w , and a decrease with height of u_* .

Fig. 2.13 shows friction velocities (left) and drag coefficients (right) as a function of wind speed during this period (top) and compared with measurements reported by Anderson (1993) in the open ocean (bottom). Measurements during this period generally sit below Charnock’s parametrization for $\alpha = 0.018$, which can also be seen in those reported by Anderson (1993) where $\alpha = 0.01$ could fit those results better. Two particular time periods have been highlighted in Fig. 2.13(top) as gray circles and squares corresponding with the 11th (13:00 - 24:00) and the 14th (13:00 - 24:00), respectively. There was rain detected at 20 m during the 11th, but these data follow a similar trend to those without rain. It is evident that measurements during the 11th correspond well with Charnock’s parametrization for $\alpha = 0.018$ (solid curve), while measurements during the

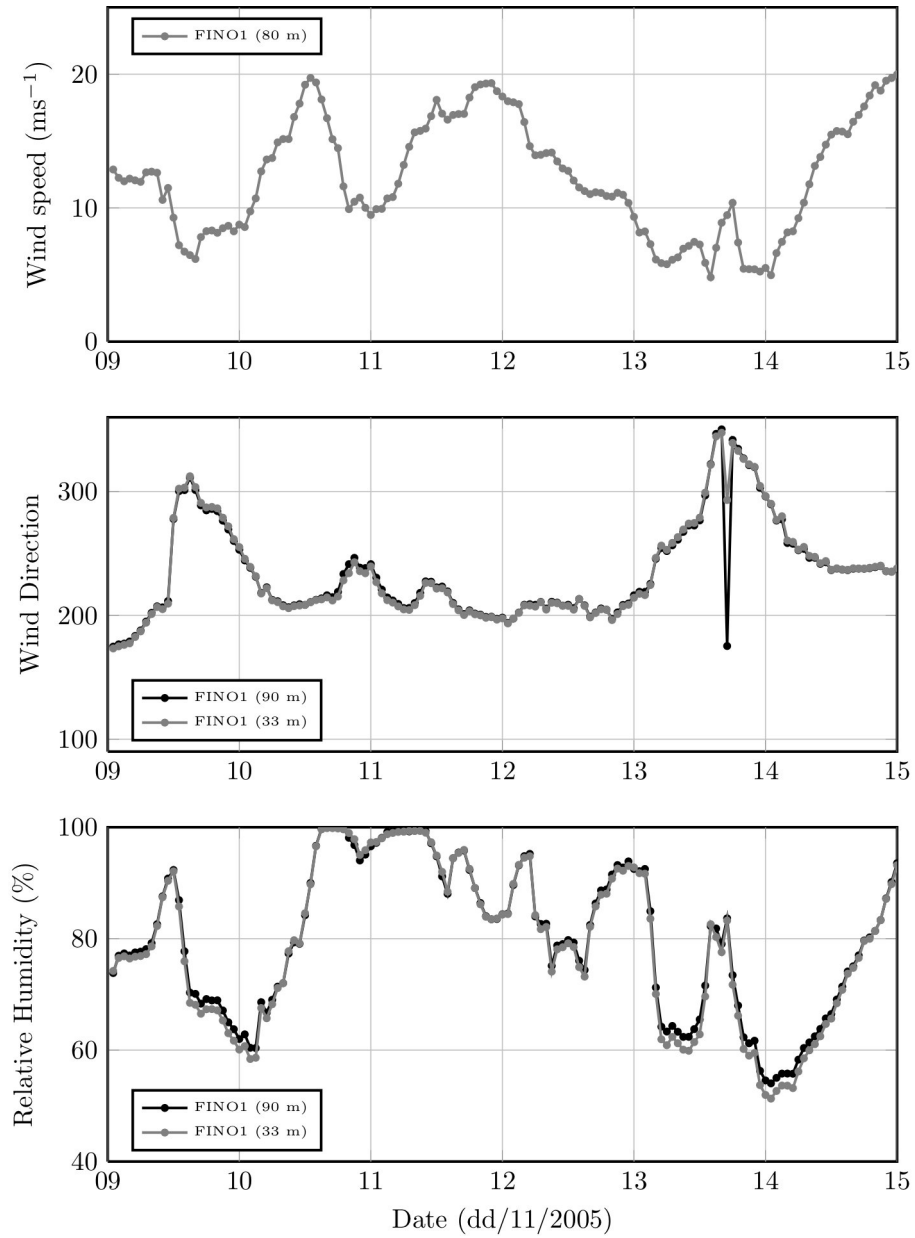


Figure 2.11: Wind speeds at 80 m (top), wind direction at 90 m (middle) and relative humidity at 90 and 33 m (bottom) at FINO1 during November, 9–15 2005.

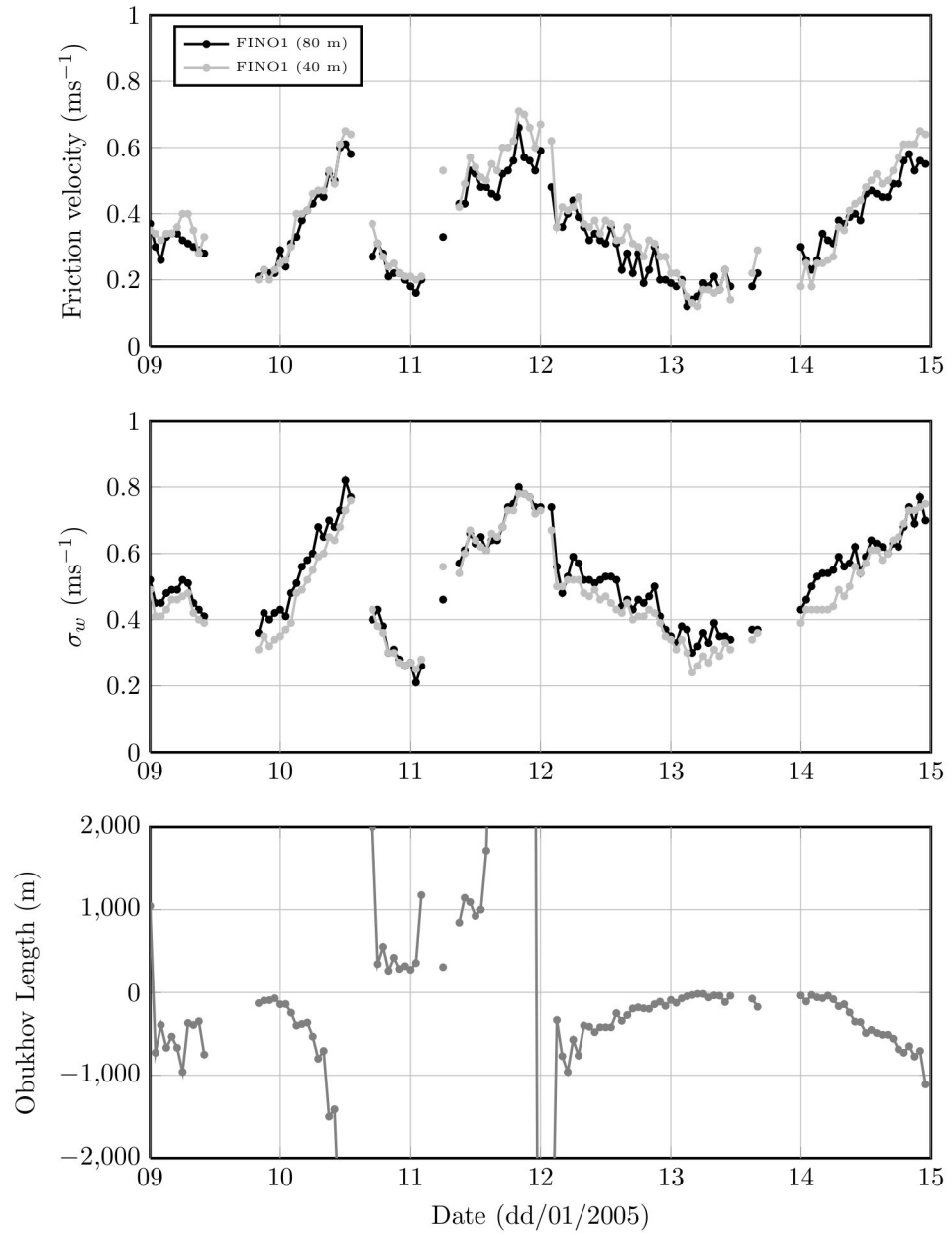


Figure 2.12: Friction velocities (top) and vertical velocity standard deviations (middle) at 80 and 40 m and Obukhov lengths from the 40 m sonic (bottom).

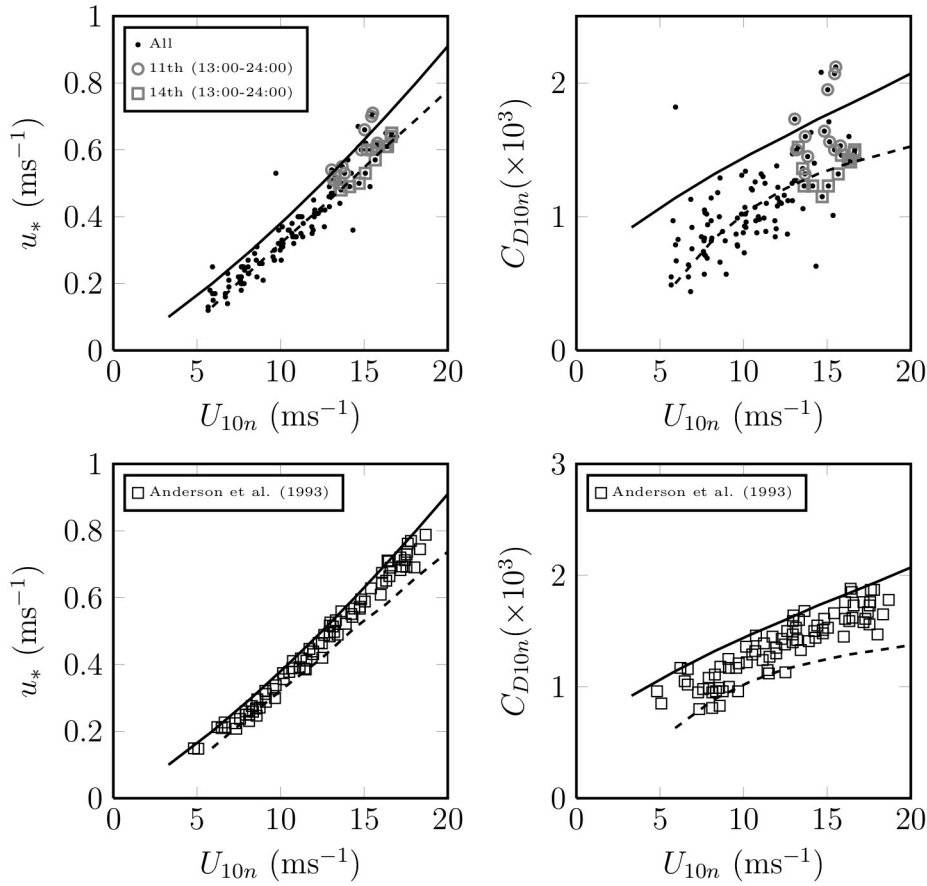


Figure 2.13: Friction velocities (left) and drag coefficients (right) as a function of wind speed as measured at FINO1 between November 9–15, 2005 (top) and measurements reported by Anderson (1993) (bottom). The solid line is Charnock's law for $\alpha = 0.018$. The dashed curve is the linear regressions in $u_* = f(U_{10n})$ space for measurements in the top left figure.

14th are in better agreement with the linear function in $u_* = f(U_{10n})$ space using the constants $a_{1,2} = (0.048, -0.015)$ (dashed curve). Average wind speed profiles for these two twelve hour periods are also displayed in Fig. 2.14. The stratification during these two periods show that, relative to the theoretical logarithmic wind profile, wind speeds are increased and decreased during the 11th and 14th, respectively. The profiles here have once more been calculated based on the 40 m sonic and cup anemometers as with the other two periods and a $\beta = 10$ in eq. (2.39) was again used in stable stratification here (note that Anderson (1993) used $\beta = 7$). No adjustment to the constants in Monin-Obukhov formulae were required in unstable stratification.

From just these measurement periods at FINO1 displayed here, it can be seen that drag coefficients during stable stratification agree with Charnock's law, whereas during unstable stratification, a linear regression in $u_* = f(U_{10n})$ space is used. Similarly, the stable January 2005 period gave agreement with

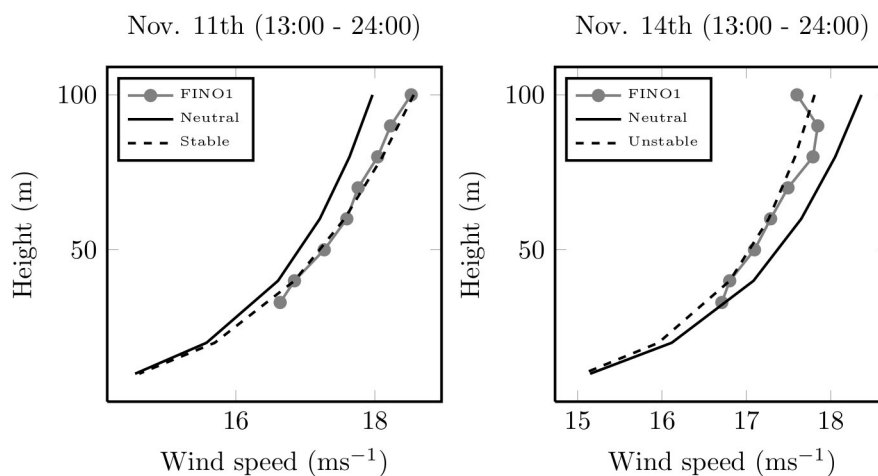


Figure 2.14: Average wind speed profiles during the 11th (13:00 – 24:00) (left) and 14th (13:00 – 24:00) (right) of November 2005 compared with equivalent neutral wind profiles (solid black curve) and the stable (left, $\beta = 10$) and unstable (right) profiles from Monin-Obukhov similarity theory based on the 40 m sonic and cup anemometers.

Charnock, whereas the unstable February 2005 period brought significant disagreement. As C_{D10n} is related singularly with z_o via the logarithmic law, a stability dependence of z_o would be in violation of Monin-Obukhov similarity theory (although some latent dependence should not be ruled out in the author’s opinion). Instead, we shall look in the next chapter for an alternative explanation for the different dependency of C_{D10n} on the Froude number detected at FINO1, which will include a consideration for the wave field.

2.4 Tropical cyclone wind speeds

Fig. 2.13 showed that the greatest difference between the different periods here occurs at higher wind speeds and that the alternative drag law proposed here, eq. (2.36) deviates most substantially from Charnock at high wind speeds. The alternative drag law would also be more consistent with other estimates at higher wind speeds. For example, theory into the development of tropical cyclones suggests that the maximum obtainable wind speed is sensitive to the ratio of the heat or humidity exchange coefficient to the drag coefficient, and that the maximum wind speed is an increasing function of this ratio (Emanuel, 1995). This theory however is in contradiction with other drag laws that make C_{D10n} a linear function of U_{10n} , increasing indefinitely with the wind speed (Smith et al., 1992, 1996). There are some measurements that have recently become available taken from aircraft in hurricanes (French et al., 2007) and North Atlantic storms (Petersen and Renfrew, 2009) that suggest that C_{D10n} does follow an expected behaviour suggested by (Emanuel, 1995). This adds to the indirect evident whether it is radiosondes dropped into hurricanes (Powell et al., 2003),

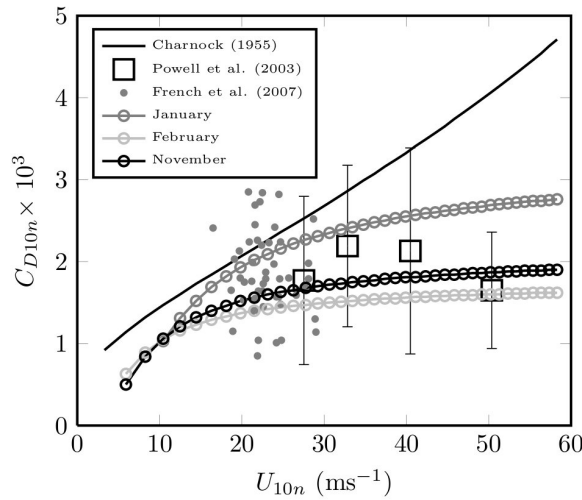


Figure 2.15: The drag coefficient as a function of the 10 m wind speed according to Charnock (1955)’s parametrization for $\alpha = 0.018$ (solid line). The squares with error bars are the estimates of Powell et al. (2003) using radiosonde profiles in tropical cyclones. Gray dots are direct aircraft measurements reported by French et al. (2007). The curves corresponding with the January, February and November, 2005 measurements defined according to eq. (2.36) for the linear regression constants specified in the text.

laboratory measurements (Donelan et al., 2004) or modelling studies (Moon et al., 2007) that also suggest C_{D10n} levels off at higher wind speeds and may even decrease.

For example, the estimates of (Powell et al., 2003) and measurements of French et al. (2007) are displayed in Fig. 2.15 in comparison with Charnock (1955)’s parametrization for $\alpha = 0.018$ and the curves resulting from substituting linear regressions into eq. (2.36) for the measurements during January, February and November, 2005 at FINO1. Here it can be seen that the alternative drag law based on eq. (2.36) would be more consistent with the estimates of (Powell et al., 2003) compared with Charnock (1955)’s parametrization. The scatter in the measurements and estimates of French et al. (2007) and Powell et al. (2003) may constitute experimental uncertainty, while the results at FINO1 suggest that there could also be a physical explanation for this uncertainty in that Froude number scaling does not collapse measurements.

2.5 Conclusion

Offshore surface roughness has been introduced from the perspective of traditional laboratory concepts such as “smooth” and “rough” flow regimes. Modelling offshore roughness depends critically on the parametrization proposed by Charnock (1955), but this approach as evident in the literature and using measurements at FINO1, encounters problems at all wind speeds. This is particularly evident at tropical cyclone wind speeds where there is considerable evidence for

a rolling-off in the drag coefficient with wind speed as opposed to the linear relationship which follows from Charnock's parametrization. An alternative drag law has been proposed in this chapter that accounts for this rolling-off effect. The physical meaning behind this, and the failure of Charnock's parametrization to account for all potential flow cases, is that below approximately 20 ms^{-1} when the rolling-off is first detected, the water surface is likely in a transitionally rough regime. This transitionally rough regime is just as difficult to account for in well defined laboratory flows over well defined solid roughness elements.

Chapter 3

Aspect ratio effects on offshore drag coefficients

3.1 Introduction

In the previous chapter, the nature of the wavy water surface itself was ignored in favour of focusing on purely air-side measurements. However, as elucidated many decades ago in Hidy and Plate (1966), a turbulent flow over water generates a surface current and waves which in turn modify the state of the turbulent air above. Hence, considering only the air flow above the water is only half of the story. For the purposes of simplicity however, standard numerical weather prediction models do neglect the evolution of the water waves and instead include much simpler parametrizations based on the concepts of smooth and rough flow regimes and Charnock's roughness length parametrization (Charnock, 1955) as introduced in the previous chapter (e.g. Janjić, 1990). However in the previous chapter, it was shown that in contrast to the functional form implied by the Charnock (1955) parametrization, it is possible that the friction velocity becomes linearly dependent on the wind speed at higher wind speeds. By forming an alternative drag law using this linear functional dependence, a roll-off in the magnitude of the drag coefficient at tropical cyclone wind speeds will result and would be consistent with estimates within tropical cyclones (Powell et al., 2003).

Of more practical concern for wind energy purposes at more realistic North Sea wind speeds are the significantly lower drag coefficients detected during the February 2005 period compared with January 2005, the latter being in better agreement with Charnock's parametrization for $\alpha = 0.018$. The previous chapter simply attributed this to the complexity of the transitional roughness regime as expected in offshore flows at wind speeds less 20 ms^{-1} (Amorocho and Devries, 1980). Instead in the following chapter, a first-order explanation for the different drag coefficients detected during these two periods will be investigated, but based on the sea. In addition to considering FINO1 measurements, reported drag coefficients in addition to wave field measurements as sourced from the open literature in coastal environments (e.g. Janssen, 1997), lakes (Merzi and Graf, 1988), the open ocean (Dobson et al., 1994) and the Baltic Sea (Johnson et al., 1998) will be considered. As demonstrated at FINO1 in the previous chapter when looking purely at air-side measurements, a varying behaviour of the drag

coefficient at a single site is also possible and it is proposed here that this is due to the varying nature of the sea surface. There have been many attempts to find a general definition of the drag coefficient based on the state of the sea (Jones and Toba, 2001) but there does not yet appear to be a general explanation that can explain the wide variety of conditions experienced in the field (Sullivan and McWilliams, 2010). For example, there have been attempts to make Charnock’s “constant” itself a function of sea parameters (Smith et al., 1992; Taylor and Yelland, 2001), but perhaps as a measure of their success, the most commonly used parametrization for offshore surface fluxes does not necessarily account for the effect of waves explicitly (Fairall et al., 2003), although there are options based on concepts such as the wave age and wave steepness (see below).

In the following chapter, a first-order explanation for the behaviour of the marine drag coefficient as a function of the wave field as has been measured in range of conditions will be described. This explanation includes a general parametrization that both captures the levelling-off of the drag coefficient as found in the previous chapter, but also the non-constant magnitude of Charnock’s constant. The parametrization will be based on measurements previously reported in the literature, that measured at FINO1 and further tested using buoy measurements at tropical cyclone wind speeds (i.e. during Rita, 2005). The structure of the following chapter is as follows: The physical laws governing the important wave parameters will be first discussed and then extended for purposes here. This extension then leads to a new parametrization of the drag coefficient in terms of the sea state. Anticipating results below, this problem will be reduced to a consideration for aspect ratio effects. The aspect ratio is only a first-order effect and hence some suggestions are then offered for proceeding with the work presented here for the purposes of a higher-order analysis.

3.2 Scaling Analysis

3.2.1 Introduction

In this section, Toba’s $\frac{3}{2}$ power law (Toba, 1972) is first revisited, and then extended to anticipate drag coefficients based on the state of the sea. This results in the drag coefficient being viewed as a function of the aspect ratio, which is the inverse wave steepness. In this respect, the problem of determining the drag over a water surface is reduced to a question of geometric similarity; waves of a similar characteristic shape have similar drag coefficients. This point of view deviates from a significant fraction of the work conducted up until now which has focused on the primacy of the wave age as the relevant first-order scaling parameter. The wave age is defined as a ratio of the dominant wave phase speed c_p (i.e. the “peak” in the wave spectrum) to the friction velocity. For example, a collection of proposed relationships can be found in the table 2.1 within Jones and Toba (2001) with a common approach (e.g. Johnson et al., 1998) writing Charnock’s constant α in

$$z_o = \alpha \frac{u_*^2}{g} \quad (3.1)$$

as

$$\alpha = f\left(\frac{u_*}{c_p}\right), \quad (3.2)$$

with f usually taking the functional form of a power law function. For example, Smith et al. (1992) write

$$\alpha = 0.48 \frac{u_*}{c_p} \quad (3.3)$$

based on measurements recorded during the HEXOS¹ campaign in the North Sea. A selection of these HEXOS results as published by Janssen (1997) will be considered further below. Janssen (1997)'s own evaluation of the data was inconclusive with regards to a genuine correlation between C_{D10n} and the wave age.

The belief in the primacy of the wave age is based on the concept of a relative velocity between the air flow and phase speed (Donelan, 1990), the consequence of which is that the wind cannot transfer momentum to faster moving waves. Thus it follows from eqs. (3.3) and (3.1) that the aerodynamic roughness length is said to decrease with increasing $\frac{c_p}{u_*}$ (e.g. Drennan et al., 1999). However, the use of the wave age as a parameter itself is controversial and has led to difficulties in separating real physical correlations from apparent ones based on the inherent uncertainty in the measurement of u_* (Janssen, 1997; Mahrt et al., 2003; Lange et al., 2004). That is, a plot of $C_{D10n} = f\left(\frac{u_*}{c_p}\right)$ contains u_* in both dimensionless groups. An early exception to the wave age approach is the work of Hsu (1974) which attempted to extend Charnock's parametrization for z_o to include the effects of the wave steepness which is defined as the ratio of the characteristic wave height to the characteristic wave length. However, a recent comparison between a wave age scaling for z_o and a wave steepness using eight different data sets from a range of locations did not yield a clear conclusion in favour of either wave age or wave steepness approach (Drennan et al., 2005).

The following analysis is aimed at a "first-order" scaling of the drag coefficient assuming geometric similarity, but some higher order effects will also be considered. Here, "first-order" implies that the majority of measurements be placed onto a single graph based in terms of two dimensionless parameters. A "higher-order" analysis then necessitates further dimensionless groups for a more refined description. For example, there are further complications to the ideas to be presented below that would require more dimensionless groups, including directional issues such as the effect of swell travelling at an angle to the flow (Geernaert et al., 1993; Donelan et al., 1997; Larsen et al., 2003), unsteadiness (Rieder, 1997) and upwards momentum transfer from the sea to the air at low wind speeds (Grachev and Fairall, 2001). Here, "swell" is a descriptive term given to long, fast moving waves that have been generated non-locally and can be contrasted with locally generated waves called "wind-waves". A specific definition for swell has been presented as $\frac{c_p}{u_*} > 35$ (Jones and Toba, 2001). Some higher order issues will be explored in the next chapter. Hence, attempting to view the problem merely through a stationary geometric similarity perspective may not suffice.

The results of the scaling analysis to be initiated in the next section will be compared with measurements reported in the literature, online and at FINO1 and it will be shown that they all demonstrate a broadly similar geometric behaviour, but with an important distinction to be further elucidated in the later sections that will require a higher order analysis in the future. It will be shown

¹Humidity Exchange Over Sea

that measurements considered here demonstrate a similar dependence on the aspect ratio which is the inverse wave steepness. The aspect ratio scaling will then be applied to buoy measurements recorded during hurricane Rita which swept through the Mexican gulf in 2005 to estimate drag coefficients at wind speeds up to 40 ms^{-1} . Aspect ratio scaling anticipates both the expected levelling off of the drag coefficient in deep water, but predicts a rapid increase in drag coefficients in shallower water.

3.2.2 Toba's $\frac{3}{2}$ power law

Waves driven locally by the wind (wind waves) have been traditionally described by Toba's $\frac{3}{2}$ power law (Toba, 1972). The law follows from the following functional relationship whereby

$$f(H_s, T_p, g, u_*) = 0, \quad (3.4)$$

where H_s is the significant wave height, T_p is the wave period, g is the gravitational constant and u_* is the friction velocity. The significant wave height is a traditional height scale for waves in oceanography and is the height loosely corresponding with the average height of the highest one-third of all waves (Kotsch, 1977). Statistically, $H_s = 4\sqrt{\sigma^2}$, where σ^2 is the variance of the surface elevation. For wind-waves there is a distinct frequency peak f_p in the σ frequency spectrum, whereby $T_p = f_p^{-1}$. The relationship between T_p and the peak wave length, λ_p can be found via the linear dispersion relation (Det Norske Veritas, 2010) where

$$T = \left[\frac{g}{2\pi\lambda} \tanh\left(\frac{2\pi d}{\lambda}\right) \right]^{-1/2}, \quad (3.5)$$

where d is the water depth. Classifying the wave field via a single peak assumes that surface elevation spectra follow some self-similar behaviour in a manner that velocity profiles are able to be scaled, and hence classified via u_* . There is much experimental evidence for the self similar nature of wind-waves (e.g. Csanady, 2001). However, for wind-waves in the presence of swell, more than one spectral peak can be present thus complicating the determination of conventional scaling parameters (Dobson et al., 1994).

In the framework of Toba (1972), eq. (3.4), u_* is an independent variable; that is, it is assumed that there is a one-way coupling between the air and the sea. Given eq. (3.4) then

$$\frac{gH_s}{u_*^2} = f\left(\frac{gT_p}{u_*}\right) \quad (3.6)$$

follows wherefrom Toba (1972) argued that

$$\frac{gH_s}{u_*^2} = B \left(\frac{gT_p}{u_*}\right)^{3/2}, \quad (3.7)$$

where B is an empirical constant, equal to approximately 0.06. As an example, plotted in Fig. 3.1 are measurements from the FINO1 platform during January 4-10, 2005 and during February 20-28, 2005 (see the previous chapter) where there is agreement with eq. (3.7) for both periods. However, as alluded to above with reference to the wave age in eq. (3.2), the problem of an artificial correlation

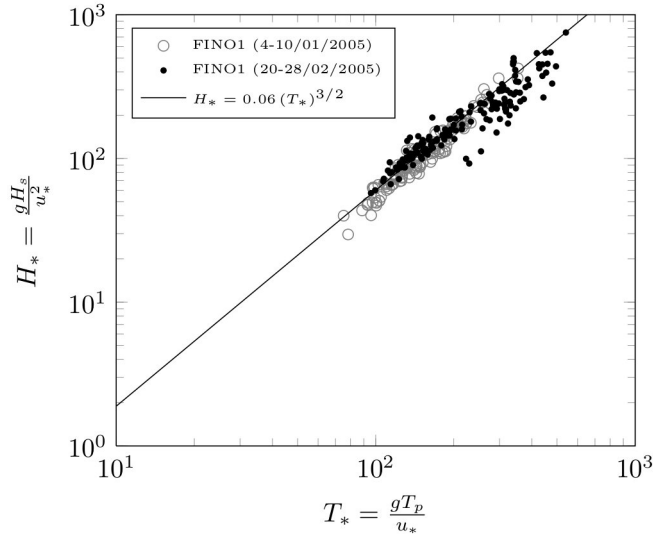


Figure 3.1: Illustration of Toba's $\frac{3}{2}$ law showing the measurements at FINO1 during January 4–10, 2005 and February 20–28, 2005 and the line defined by eq. (3.7) for $B = 0.06$.

is also present in Fig. 3.1 due to the presence of errors in u_* being present in both dimensionless groups in eq. (3.7). Below, it will be demonstrated that there is a more subtle scaling than that suggested by eq. (3.7) which leads to a distinctly different scaling between the January and February periods.

3.2.3 Extension of Toba's $\frac{3}{2}$ power law

Toba (1972) assumes that the wind speed, U does not enter into eq. (3.4) because U is uniquely determined by the relationship between u_* and U as dictated by the neutral drag coefficient C_{D10n} , where

$$u_* = \sqrt{C_{D10n} U_{10n}}, \quad (3.8)$$

and they are inter-convertible in this way. Hence, if u_* and U_{10n} are uniquely determined by C_{D10n} , either u_* or U_{10n} (but not both) can appear in eq. (3.4) above. However, there is plenty of evidence in the literature that suggests the drag coefficient is not uniquely determined by the wind field, but is also a function of the state of the sea (Donelan, 1982, 1990; Donelan et al., 1997). If one accepts the hypothesis that the relationship between u_* and U_{10n} may in fact depend on the sea state parameters H_s and T_p , then eq. (3.4) must be written as

$$f(H_s, T_p, U_{10n}, u_*, g) = 0. \quad (3.9)$$

Note that some authors (e.g. Toba et al., 1990; Johnson et al., 1998) have used Toba's $\frac{3}{2}$ power law to derive a relationship between the drag coefficient and the sea-state which is a contradiction since by eq. (3.4), which follows from (3.8), the law assumes a drag coefficient independent from the sea-state from the outset.

From Buckingham's Π theory, eq. (3.9) results in three dimensionless groups,

$$\Pi_1 = \frac{gH_s}{u_*^2}, \quad (3.10)$$

$$\Pi_2 = \frac{gT_p}{u_*} \quad (3.11)$$

and

$$\Pi_3 = \frac{U_{10n}}{u_*}. \quad (3.12)$$

Writing these three groups in the following form

$$\frac{1}{\Pi_3} = c \frac{\Pi_1}{\Pi_2^2}, \quad (3.13)$$

then assuming the constant $c = 2\pi a$ (a being a constant) and the deep water wave-length (via eq. (3.5))

$$\lambda_p = \frac{gT_p^2}{2\pi}, \quad (3.14)$$

gives

$$u_* = aU_{10n} \frac{H_s}{\lambda_p}. \quad (3.15)$$

Eq. (3.15) gives a relationship for the drag coefficient as

$$C_{D10n} = a \left(\frac{H_s}{\lambda_p} \right)^2. \quad (3.16)$$

The roughness length can then follow from the logarithmic law, i.e.

$$z_o = 10 \exp \left(\frac{-\kappa}{\sqrt{C_{D10n}}} \right). \quad (3.17)$$

3.2.4 The aspect ratio

Eq. (3.16) implies that C_{D10n} is completely functionally dependent on (and proportional to) the squared wave steepness. This reminds one of the behaviour of the aspect ratio over an idealised ellipse in a laboratory, where ℓ and D are the characteristic ellipse length and height, respectively. The relationship between the drag force over an ellipse in a laboratory flow, e.g.

$$C_D = \frac{D_F}{\frac{1}{2}\rho U_\infty^2 b\ell}, \quad (3.18)$$

where b is the ellipse span, U_∞ is the free stream velocity and D_F is the drag force, is illustrated in Fig. 3.2 (left) where the figure 9.19 from Munson et al. (2002) is displayed. At low aspect ratios, the ellipse acts as a bluff body with the occurrence of flow separation leading to a rapid increase in C_D with decreasing $\frac{\ell}{D}$. In such a case, form drag which is related to the bulk shape of the object as opposed to skin friction drag which is related to the nature of the surface is more significant. At high aspect ratios, the ellipse tends to the shape of a flat plate leading to the minimal deflection of streamlines and hence form drag negligible,

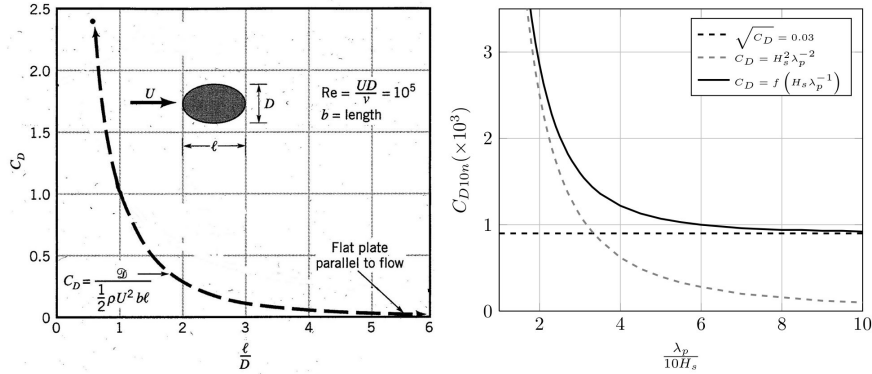


Figure 3.2: Left: The figure 9.19 from Munson et al. (2002) with some aspects removed showing the relationship between the drag coefficient and aspect ratio for an ellipse of length ℓ and height D . Right: The relationship between the offshore drag coefficient derived from eq. (3.16) (gray dashed line), a constant drag coefficient assuming $C_{D10n}^{1/2} = 0.03$ (dashed black line) and a correlation equation between these two (solid black line).

leading to a relatively low and approaching constant C_D with increasing $\frac{\ell}{D}$ (Munson et al., 2002).

Fig. 3.2 (right) shows the drag coefficient ($\times 10^3$) over water waves according to eq. (3.16) assuming $a = 1$ plotted as the gray dashed line as a function of one-tenth the aspect ratio. One-tenth the aspect ratio, $\frac{\lambda_p}{10H_s}$ or ten times the inverse wave steepness is displayed in anticipation of the measurements that fit on this chart as will be shown below. In analogy with the behaviour of the drag coefficient over an ellipse, eq. (3.16) anticipates $C_{D10n} \rightarrow \infty$ as $\frac{\lambda_p}{10H_s} \rightarrow 0$ and $C_{D10n} \rightarrow 0$ as $\frac{\lambda_p}{10H_s} \rightarrow \infty$.

One is reminded of the idea presented in Amorocho and Devries (1980) and discussed in the previous chapter that, at very high wind speeds or at low aspect ratios, form drag on account of flow separation over breaking waves dominates the flow entirely. At the other scale, we do not expect $C_{D10n} \rightarrow 0$ but rather to enter a smooth flow regime as explained in the previous chapter. Consequently, as an approximation at high aspect ratios, one could specify as suggested by Amorocho and Devries (1980),

$$C_{D10n}^{1/2} = 0.03 \quad (3.19)$$

and this is the horizontal dashed black line in Fig. 3.2. Eq. (3.19) however neglects the effects of upward momentum transfer expected at very low wind speeds due to swell (Grachev and Fairall, 2001) or any other likely effects of swell such as an angular dependency between the wind and swell (e.g. Grachev et al., 2003).

It will then be assumed that eq. (3.19) and eq. (3.16) denote two contrasting asymptotic scaling regimes, a constant and a pure wave steepness scaling. For that reason, a correlating function that bridges these two regimes is required, where one can think of this as attempting to model the complex transitional roughness regime introduced in the previous chapter. This correlation function

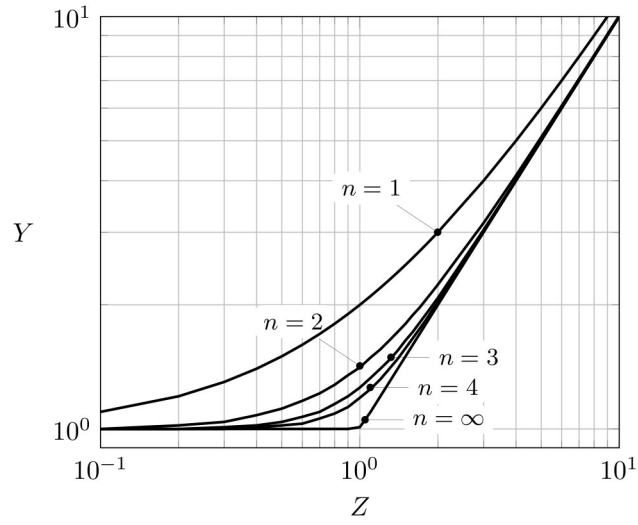


Figure 3.3: Eq. (3.22) on logarithmic axes for various exponents n (adapted from the figure 1 of Churchill and Usagi (1972)).

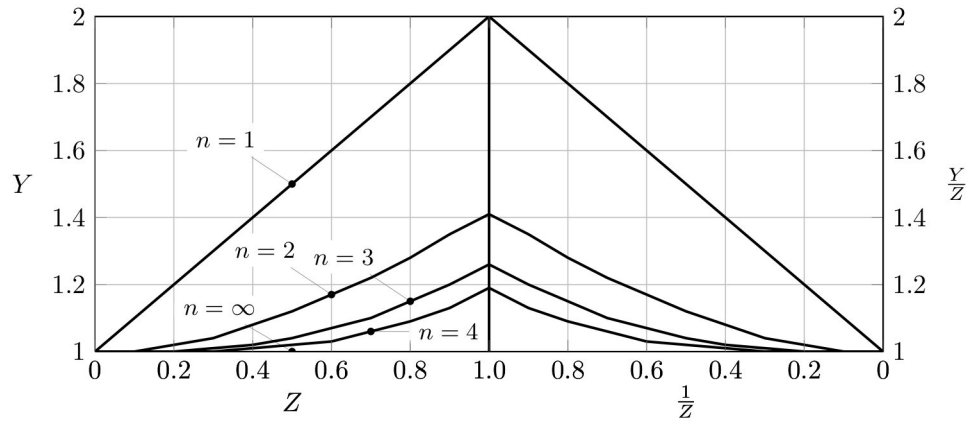


Figure 3.4: A working plot for correlation based using eqs. (3.22) and (3.23) (adapted from the figure 2 of Churchill and Usagi (1972)).

is shown as the solid line in Fig. 3.2 (right) and is defined according to

$$\left(C_{D10n}^{1/2}\right)^n = 0.03^n + \left(\frac{H_s}{\lambda_p}\right)^n, \quad (3.20)$$

where n is an exponent equal to 3 as found from the measurements below. The description of this function and the determination of the exponent n will be carried out in the next section.

3.2.5 General correlating expression

A general correlation connecting the two asymptotic regimes presented above in Fig. 3.2 defined according to the constant drag coefficient, eq. (3.19) and the squared wave steepness, eq. (3.16) will be described in this section. These asymptotes are assumed to be valid in the limit of $\frac{\lambda_p}{H_s} \rightarrow \infty$ and $\frac{\lambda_p}{H_s} \rightarrow 0$, respectively. For that reason, the Churchill-Usagi method (Churchill and Usagi, 1972) can then be used to find a correlating expression between these asymptotes based on the following functional form:

$$y^n(x) = y_\infty^n(x) + y_o^n(x), \quad (3.21)$$

where y and x are arbitrary dependent and independent parameters, respectively and n is the single empirical exponent. Here, y_∞ is the relationship between y and x as $x \rightarrow \infty$, while y_o is the relationship between y and x for $x \rightarrow 0$. Eq. (3.21) is useful for finding an empirical relationship between asymptotic functional forms where theory is lacking in the intermediate region. For example, eq. (3.21) can be applied to the drag coefficient over a sphere (i.e. eq. (3.18) for $\ell = D$), which theoretically reduces to $C_D = 24/Re$ (Re is the Reynolds number) as $Re \rightarrow 0$, but is roughly constant at much higher Reynolds numbers (although a turbulent boundary layer will require another function at even higher Reynolds numbers) (Munson et al., 2002).

By defining $Y = \frac{y}{y_o}$ and $Z = \frac{y_\infty}{y_o}$, eq. (3.21) can be rearranged to give

$$Y^n = 1 + Z^n \quad (3.22)$$

and

$$\left(\frac{Y}{Z}\right)^n = 1 + \frac{1}{Z^n}. \quad (3.23)$$

Eq. (3.22) has been plotted in Fig. 3.3 in logarithmic coordinates on both axes for $n = 1$ to 4 and ∞ . It can be seen that the selection of n is most sensitive to changes in Y at $Z = 1$. This region of Fig. 3.3 can be emphasised by inspecting a linear plot of Y versus Z (eq. (3.22)) for $0 \geq Z \geq 1$ and $\frac{Y}{Z}$ versus $\frac{1}{Z}$ (eq. (3.23)) for $0 \geq \frac{1}{Z} \geq 1$. An example of this type of plot is shown in Fig. 3.4 for $n = 1$ to 4 and ∞ , where the left hand side shows Y versus Z and the right hand side shows $\frac{Y}{Z}$ versus $\frac{1}{Z}$. Figs. 3.3 and 3.4 are showing the same information but Fig. 3.4 is used to determine n , as well as the quality of the correlation of the measurements with eq. (3.22). The idea here is that you want to minimise the error in the selection of n at the point of its most sensitive variation, i.e. at $Z = 1$.

Using the asymptotes defined according to the constant drag coefficient, eq. (3.19) and pure wave steepness scaling, eq. (3.16), a functional form for C_{D10n} according to eq. (3.21) can then be constructed whereby the correlation

$$\left(C_{D10n}^{1/2}\right)^n = 0.03^n + \left(\frac{H_s}{\lambda_p}\right)^n, \quad (3.24)$$

and hence $y = C_{D10n}^{1/2}$, $Y = \frac{C_{D10n}^{1/2}}{\frac{H_s}{\lambda_p}}$ and $Z = \frac{0.03}{\frac{H_s}{\lambda_p}}$. The validity of eq. (3.24) and the magnitude of the exponent n must then be found from charts like Fig. 3.3 using field measurements to be performed in the next section. As seen from Fig.

3.4, an exponent of $n = \infty$ corresponds with the horizontal line defined by Y and $\frac{Y}{Z} = 1$ which by the definitions of Y and Z means from eq. (3.16)

$$C_{D10n} = \left(\frac{H_s}{\lambda_p} \right)^2 \quad (3.25)$$

for $Z = \frac{0.03}{\frac{H_s}{\lambda_p}} \leq 1$ and

$$C_{D10n}^{1/2} = 0.03 \quad (3.26)$$

for $Z = \frac{0.03}{\frac{H_s}{\lambda_p}} \geq 1$.

3.3 Data analysis

In this section, the functional form of the correlation eq. (3.24) will be tested and the exponent n will be determined at FINO1 with some further information being found using measurements reported in the literature or online. At the end of this section, eq. (3.24) will be tested on buoy measurements measured during hurricane Rita (2005).

3.3.1 FINO1

The air-side FINO1 measurements during January, February and November 2005 have been introduced in the previous chapter and are again considered here as a function of the sea-state. Significant wave heights and peak wave periods as calculated from a Waverider buoy approximately 200 m from FINO1 have been provided by the German maritime and hydrographic agency (BSH). The wave periods have then been transformed to wave lengths using the linear dispersion relation, eq. (3.5) assuming a water depth of $d = 30$ m. Shown in Fig. 3.5 are the time periods for January (top), February (middle) and November (bottom) in the framework of the Churchill-Usagi method where the left hand column shows Y against Z and the right hand column shows $\frac{Y}{Z}$ versus $\frac{1}{Z}$.

The January measurements in Fig. 3.5 are, with respect to the February and November periods, in most agreement with the correlation eq. (3.24) where an exponent of $n = 3$ could be a good approximation. The February period demonstrates a completely different behaviour where the scatter there is more in agreement with $n = \infty$. The apparently different scaling between the January and February periods can be seen more clearly in Fig. 3.6 where drag coefficients as a function of one-tenth the aspect ratio are displayed. Fig. 3.6 (top) shows bin averages during the January (gray circles) and February (black triangles) periods and Fig. 3.6 (bottom) shows hourly averages illustrating the scatter from which the bin averages were found. The bin averages demonstrate that the January period fits well with the correlation

$$C_{D10n} = \left(0.03^3 + \left(\frac{H_s}{\lambda_p} \right)^3 \right)^{2/3}, \quad (3.27)$$

while the February period corresponds with pure asymptotic scaling

$$C_{D10n} = \left(\frac{H_s}{\lambda_p} \right)^2 \quad (3.28)$$

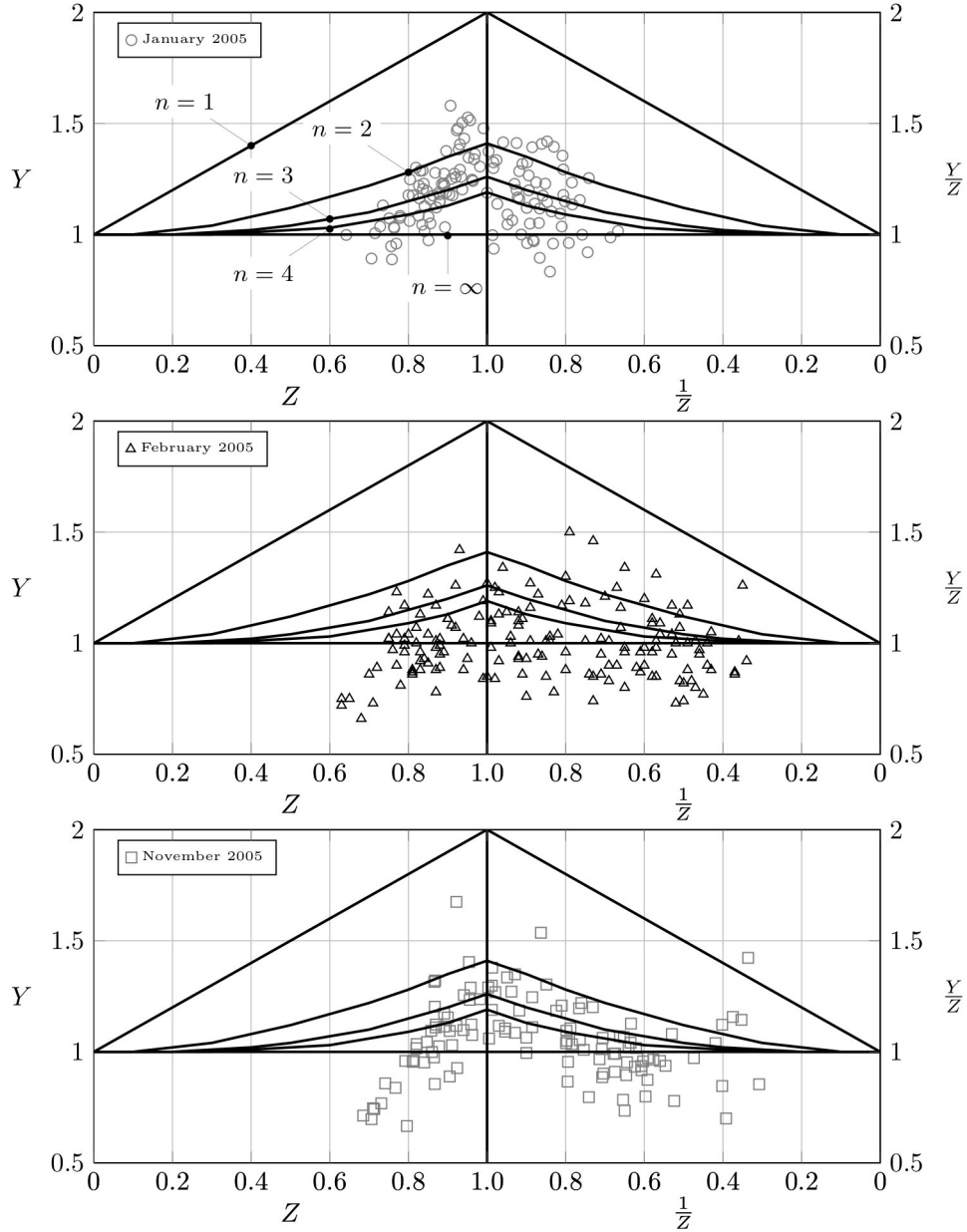


Figure 3.5: Y versus Z (left hand side) and $\frac{Y}{Z}$ versus $\frac{1}{Z}$ (right hand side) as calculated at FINO1 for the periods during January (top), February (middle) and November (bottom) 2005 as calculated for various n (1, 2, 3, 4 and ∞) based on eqs. (3.22) and (3.23). Here, $Y = \frac{C_{D10n}^{1/2}}{\frac{H_s}{\lambda_p}}$ and $Z = \frac{0.03}{\frac{H_s}{\lambda_p}}$.

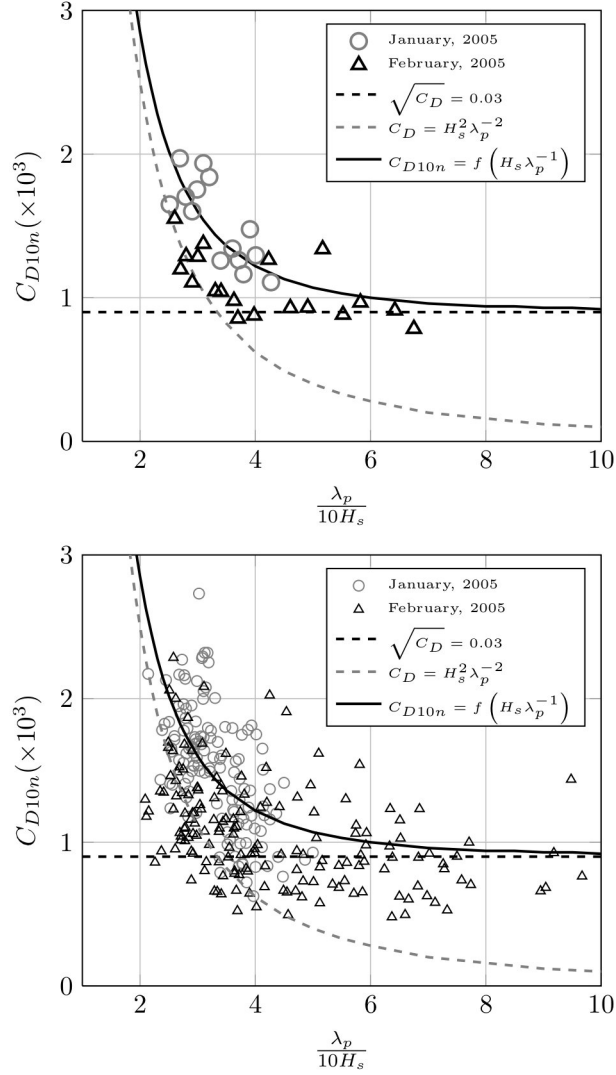


Figure 3.6: Drag coefficients as a function of one-tenth aspect ratios during January and February 2005. The solid black, dashed gray and dashed gray lines are the correlation equation, eq. (3.27) the wave steepness asymptote (3.16) and the constant drag coefficient asymptote (3.19). The top figure shows bin averages and the bottom figure shows one hour means.

for $\frac{H_s}{\lambda_p} \geq 0.03$ and

$$C_{D10n}^{1/2} = 0.03 \quad (3.29)$$

for $\frac{H_s}{\lambda_p} \leq 0.03$. Such a subtlety was not readily evident using Toba's 3/2 power law in Fig. 3.1 above. This contrasting scaling behaviour is also evident in the measurements previously reported in the literature as will be demonstrated below.

Time series of drag coefficients as estimated from the sonic and cup anemome-

ters (black lines) compared with that estimated from the buoy (gray) are displayed in Fig. 3.7. From the aspect ratio plot in Fig. 3.6, the January and November time series are compared with the smooth correlation eq. (3.27) while the February time series is compared with the asymptotic scaling, eqs. (3.28) and (3.29). One can think of pure wave steepness scaling as a rough flow regime, where in the previous chapter, the February period reached a constant C_{D10n} and hence rough flow regime for $Re_* \sim 3$. The smooth correlation represents a more gradual transition between the smooth and rough regimes whereby the January period showed that a constant C_{D10n} is only found at much higher $Re_* \sim 300$.

The January case too however does not exhibit exclusive scaling with eq. (3.27). For example, consider the period centered on the 5th in Fig. 3.7 (top) where the buoy measurements based on the smooth correlation equation overestimate C_{D10n} as found from the sonic and cup anemometers. Fig. 3.8 focuses on this period where evidence of both types of scaling can be witnessed. Fig. 3.8 (top) shows C_{D10n} versus the aspect ratio but plotted as a phase diagram in time where the points connect the period during the 4th and the 5th of January, 2005. Most of the points are clustered nearer a scaling with eq. (3.27) during the beginning and end of this sub-period. Within this time-frame is a changing of the wind direction to match that of the waves as seen in Fig. 3.8 (bottom) and this period has been highlighted by black bullets in both the phase diagram and the wind direction. Within the phase diagram, the black points illustrate the transition between asymptotic scaling at high aspect ratios (i.e. with $C_{D10n}^{1/2} = 0.03$) and then with wave steepness scaling at low aspect ratios. Towards the end of the sub-period, scaling with eq. (3.27) appears to be recovered. The relative wind and wave directions is a higher order consideration beyond the current scope, but will be looked at again in the next chapter during a period at FINO1 when this behaviour is easier to recognise.

3.3.2 Literature

In order to demonstrate that the results at FINO1 above are not quite unique, this section will present some measurements reported in the literature. The selection is limited to measurements of the friction velocity and wind speed in the presence of wave property measurements. Although the selection is not extensive, these measurements suggest a broadly consistent behaviour with that displayed above at FINO1.

Fig. 3.9 shows plots of Y against Z (left hand side) and $\frac{Y}{Z}$ and $\frac{1}{Z}$ (right hand side) for measurements as reported by Janssen (1997) in the North Sea, the open ocean exposed SCOPE² measurements (Grachev and Fairall, 2001) off the southern Californian coast (top), Dobson et al. (1994) in the North Atlantic (middle), Johnson et al. (1998) in the Baltic Sea and Merzi and Graf (1988) over Lake Geneva (bottom). The wave steepness has been calculated from the wave lengths and significant wave heights as tabulated by Merzi and Graf (1988), from the significant wave heights and phase velocities (using the linear dispersion relation) as tabulated by Dobson et al. (1994) and Janssen (1997) and via significant wave heights, phase velocities and wave periods ($\lambda_p = c_p T_p$) as tabulated by Johnson et al. (1998). Significant wave heights and phase velocities

²San Clemente Ocean Probing Experiment

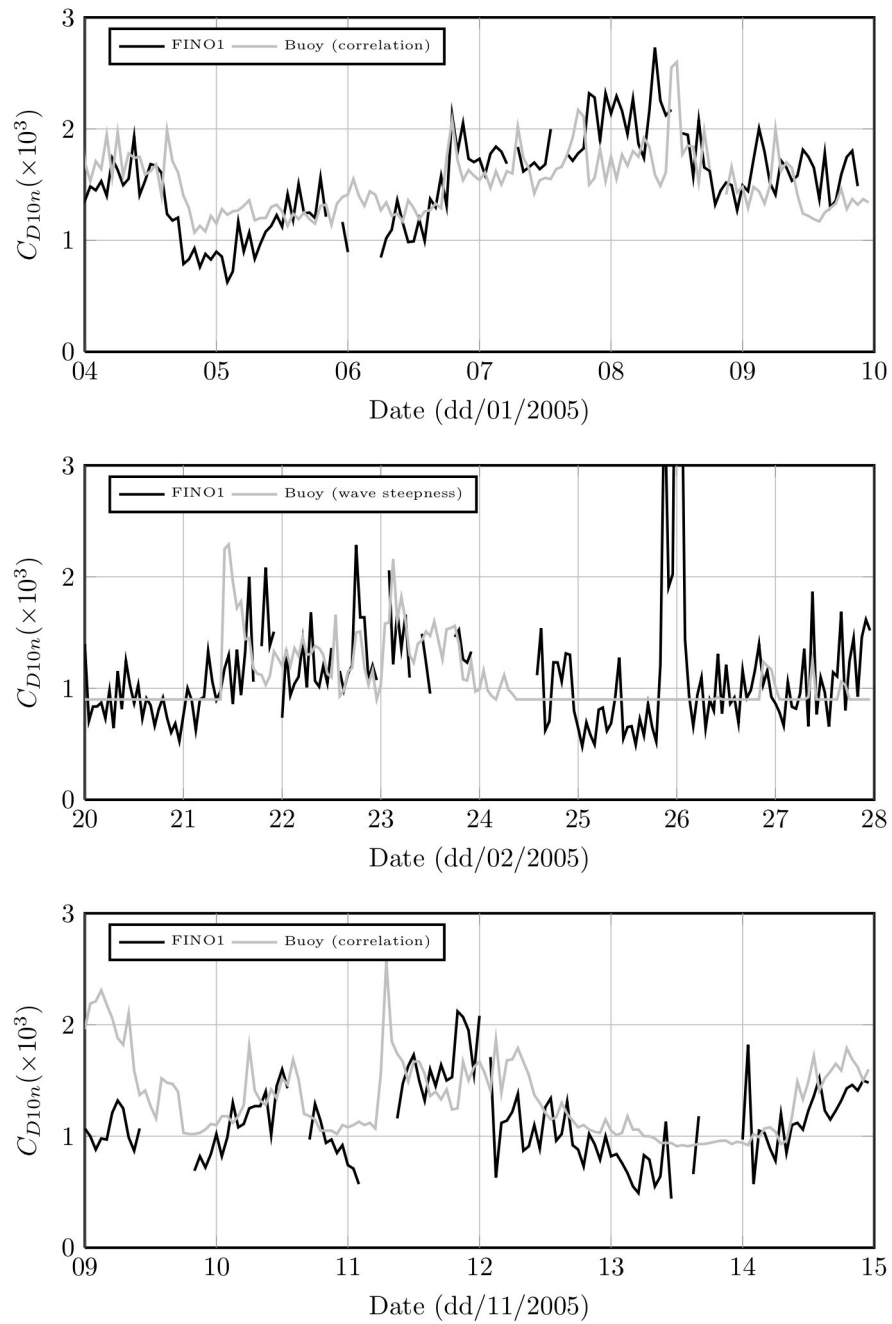


Figure 3.7: January 2005 (top), February 2005 (middle) and November 2005 (bottom): Drag coefficients as measured from the FINO1 tower compared with C_{D10m} inferred from buoy measurements according to the correlation eq. (3.27) (top), the asymptotic relations, eq. (3.28) and (3.29) (middle), and the correlation equation again (bottom).

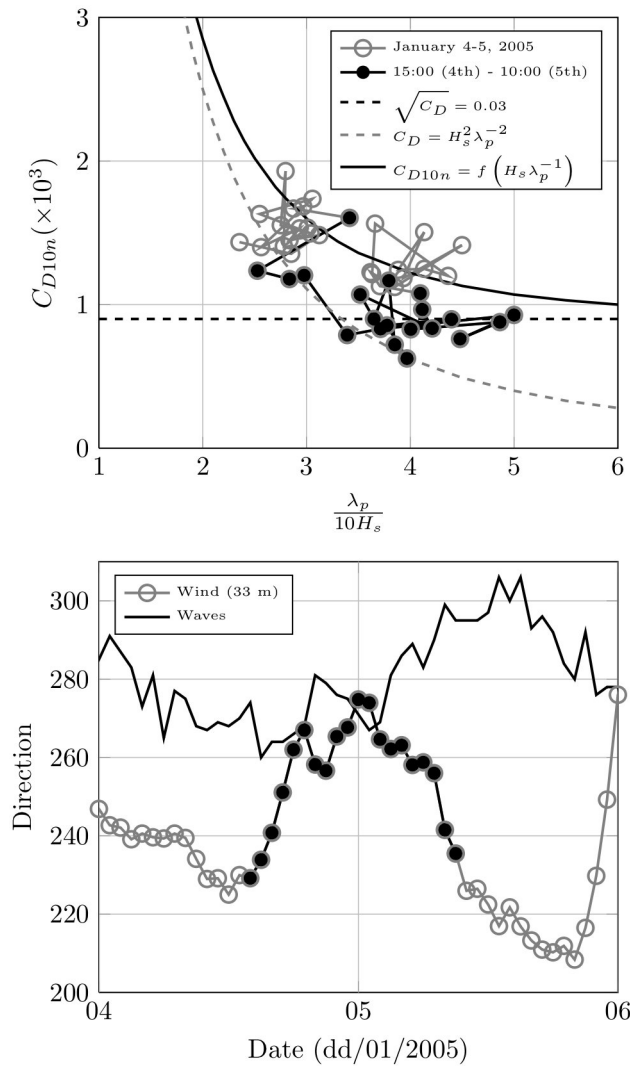


Figure 3.8: Top: Phase diagram of C_{D10n} against $\frac{\lambda_p}{10H_s}$ from January 4–5th, 2005. A period within this period is indicated by black bullets for the 4th (14:00) to the 5th (5:00) illustrating the scaling with eq. (3.16) during this time. Bottom: Wind (33 m) and wave directions during the same period, also showing the black bullets corresponding with those in the phase diagram.

are also available online with the SCOPE³ data. The SCOPE measurements were further corrected for stratification using the Monin-Obukhov similarity formulae presented in the previous chapter.

Fig. 3.9 (top) demonstrates that the measurements reported by Janssen (1997) and the SCOPE results give $n = 3$. The scatter at very high aspect ratios (towards the right hand side of Fig. 3.9) could be due to a number of reasons such as unsteadiness and swell. Scatter towards the edges compared

³<ftp://ftp.etl.noaa.gov/users/cfairall/fluxdata/scope/SCOPE2.TXT>

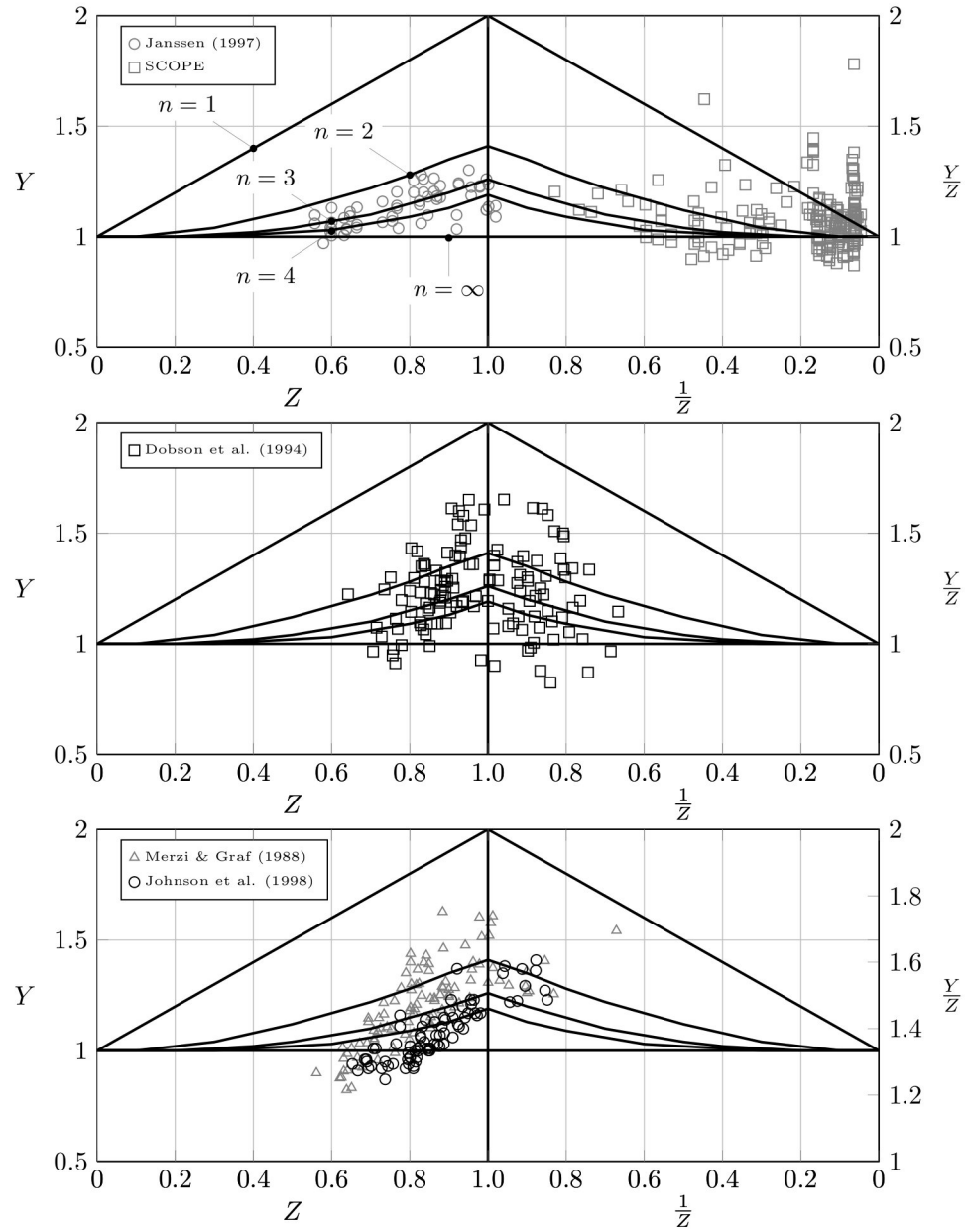


Figure 3.9: Y versus Z (left hand plots) and Y/Z versus $1/Z$ (right hand plots) for $n = 1, 2, 3$ and 4 according to eqs. (3.22) and (3.23) where $Y = C_{D10n}^{1/2} / \frac{H_s}{\lambda_p}$ and $Z = 0.03 / \frac{H_s}{\lambda_p}$. Top: Measurements reported by Janssen (1997) in the North Sea and SCOPE measurements exposed to the open Pacific Ocean. Middle: Measurements reported by Dobson et al. (1994) in the North Atlantic. Bottom: Measurements reported by Merzi and Graf (1988) and Johnson et al. (1998) over Lake Geneva and in the Baltic Sea, respectively.

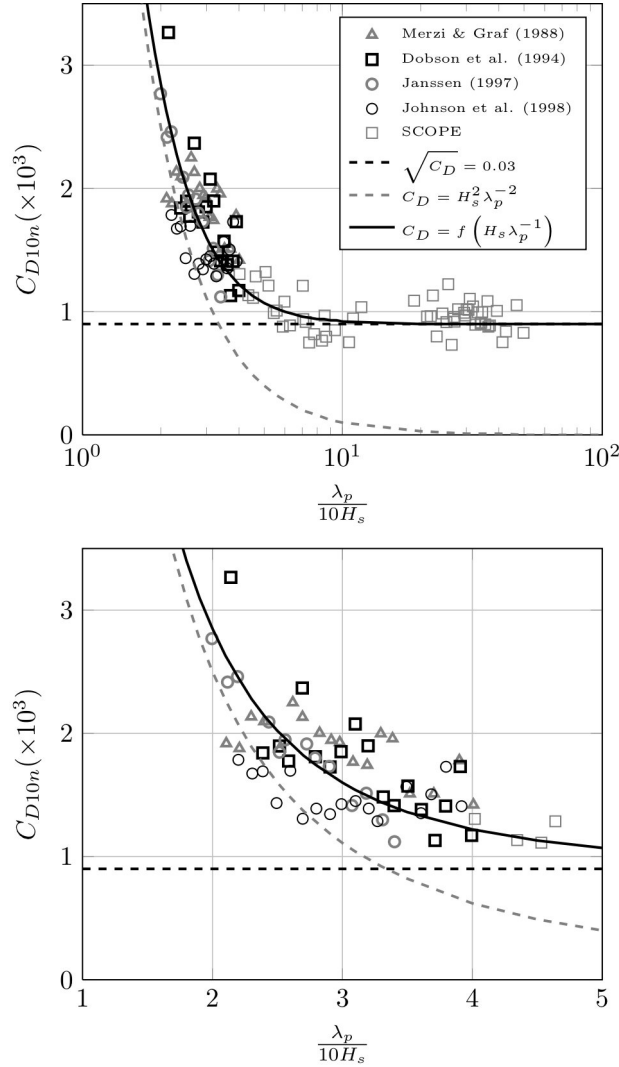


Figure 3.10: Top: Bin averaged (note the logarithmic x-axis scale) drag coefficients calculated from tabulated data provided by Merzi and Graf (1988), Dobson et al. (1994), Janssen (1997) and Johnson et al. (1998) and the online SCOPE (Grachev and Fairall, 2001) measurements, plotted as a function of one-tenth of the aspect ratio, $\frac{\lambda_p}{10H_s}$. Also included are functions corresponding to eq. (3.8) for $C_{D10n}^{1/2} = 0.03$ (gray dashed line), eq. (3.16) (black dashed line) and eq. (3.27) (solid black line) which is an interpolating function between the two asymptotes. Bottom: Same as the top figure but focused on the low aspect ratio region and the scale of both axes are linear.

with at $Z = 1$ in Fig. 3.9 has less of an effect on the overall calculation of n . There is considerably more scatter in the measurements of Dobson et al. (1994) which are located more towards $Z = 1$ (Fig. 3.9 (middle)), but on average $n = 3$ is still likely the best choice. The measurements of Merzi and Graf (1988) and Johnson et al. (1998) show a further ambiguity in the selection of n . Towards $Z = 1$, those measurements suggest $n \approx 2.5$, however there is a rapid fall of Y with decreasing Z which is inconsistent with the functional form of the correlation equation. For $Z < 0.8$, both the Merzi and Graf (1988) and Johnson et al. (1998) seem to follow $n \approx \infty$, implying a non-smooth transition between the correlation equation and the asymptotic wave steepness regime.

This is evident in Fig. 3.10, where bin averaged drag coefficients as a function of one-tenth aspect ratios are displayed. Fig. 3.10 (top) shows a logarithmic x-axis between 1 and 100 while Fig. 3.10 (bottom) is a linear x-axis focusing on the low aspect ratio, shoulder region in the top figure. While the measurements are in broad agreement with the trend given by the correlation equation, it is evident that the measurements of Johnson et al. (1998) in particular do not follow a smooth transition towards the wave steepness scaling. Fig. 3.10 (bottom) show that the Johnson et al. (1998) data “jump” from the correlation equation to the squared wave steepness eq. (3.28) and subsequently follow that curve for decreasing aspect ratios. Thus, the scaling of the Johnson et al. (1998) measurements and the February 2005 case at FINO1 are somewhat similar, although the February 2005 period displays a smoother transition to asymptotic wave steepness scaling beyond the smooth regime. The measurements of Merzi and Graf (1988) follow the trend of the correlation equation (albeit above the equation itself corresponding approximately with $n = 2.5$) for decreasing aspect ratios, and then decay towards eq. (3.28) for even lower aspect ratios. The best performing in terms of the correlation equation are the HEXOS measurements of Janssen (1997) which were purposely made to be free from the effects of swell, whereas the other measurements were either recorded in open ocean conditions (Dobson et al., 1994), or were possibly complicated by a limited fetch (Merzi and Graf, 1988; Johnson et al., 1998). A higher-order analysis paying attention to spectral information may be required to sort these issues out.

3.3.3 Tropical Cyclones

To see whether the correlation equation can also give the expected functional form of C_{D10n} in tropical wind speeds, hurricane Rita (September 2005) which passed through the Mexican Gulf during 2005 will be considered here. The measurements of the significant wave height, dominant wave period and the wind speed (which is assumed to be approximately neutral and transformed to a height of 10 m using the logarithmic law) here comes from the NOAA buoy center⁴. Excellent data was recorded from Hurricane Rita as the core passed very close (about 4 km) to the buoy 42001⁵ located in the Mexican gulf with measured wind speeds up to 40 ms^{-1} . Fig. 3.11 (top) shows drag coefficients as a function of the wind speed and (bottom) friction velocities as a function of the wind speed. Fig. 3.11 (right column) also shows the buoy 42035⁶ which is located at a water depth of 13.7 m compared with 42001 which is in much deeper water

⁴<http://www.ndbc.noaa.gov/hurricanes/2005/rita/>

⁵http://www.ndbc.noaa.gov/station_page.php?station=42001

⁶http://www.ndbc.noaa.gov/station_page.php?station=42035

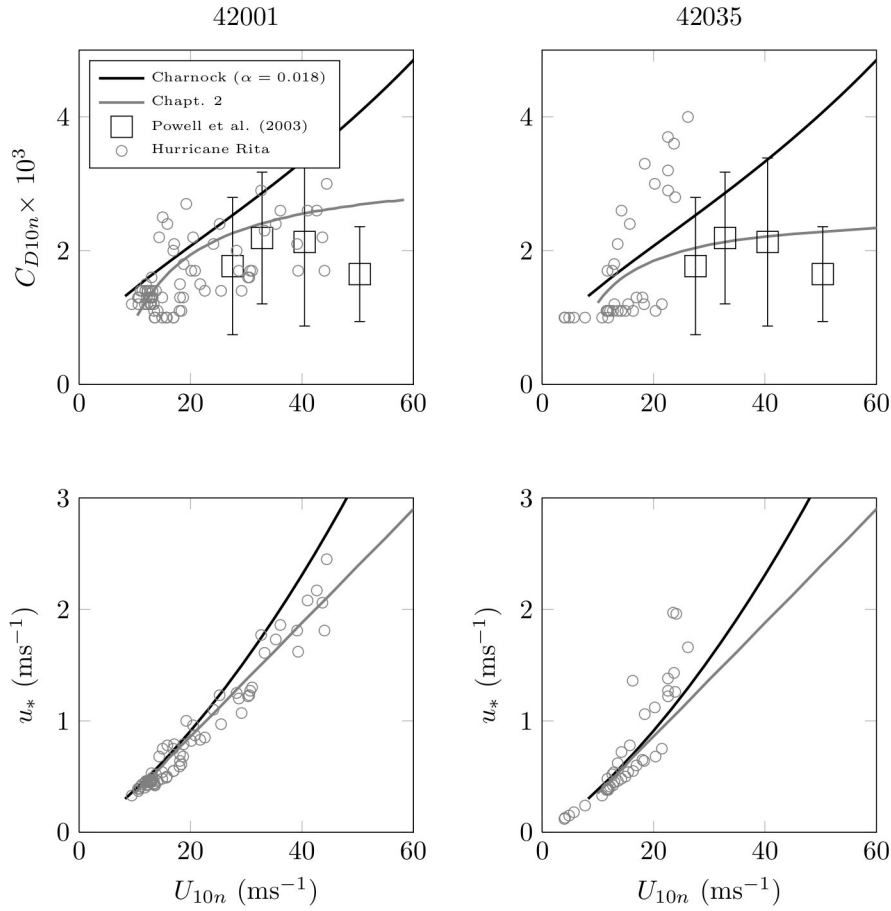


Figure 3.11: Top: Estimates of C_{D10n} as a function of wind speed calculated using eq. (3.27) using measurements from buoys located in the Mexican gulf (stations 42001 (left) and 42035 (right)). For comparison are the estimates in tropical cyclones from Powell et al. (2003), Charnock's parametrization for $\alpha = 0.018$ and eq. (3.30) for $(a_{1,2} = (0.057, -0.26))$ (January, 2005 at FINO1). Bottom: The corresponding plots of friction velocities as a function of wind speed. Buoys 42001 and 42035 correspond with the periods 21–24 September and 23–25 September 2005, respectively.

at 3365 m. The periods on display in Fig. 3.11 are 21–24 September, 2005 (left) and 23–25 September, 2005 (right). Wave periods at buoy 42035 are converted to wave lengths using the linear dispersion relation.

The estimates of C_{D10n} using the wave periods and significant wave heights inserted into the correlation equation are displayed in Fig. 3.11 in comparison with the estimates of Powell et al. (2003), Charnock (1955)'s parametrization assuming $\alpha = 0.018$ and the drag law from the previous chapter

$$C_{D10n} = \frac{(a_1 U_{10n} + a_2)^2}{U_{10n}^2}, \quad (3.30)$$

where during January 2005 at FINO1, $a_{1,2} = (0.057, -0.26)$. At very low aspect ratios, the correlation equation tends towards the wave steepness asymptote. The lowest aspect ratio detected during Rita by 42001 was approximately 1.9, which is interestingly still within the range of Fig. 3.10 (bottom) and hence gives C_{D10n} not much higher than that measured at conventional wind speeds. Thus, it can be seen that the correlation equation gives the expected levelling off of C_{D10n} in Fig. 3.11 (left) consistent with the estimates of Powell et al. (2003), which is furthermore in agreement with eq. (3.30). The wind speeds here were unfortunately not high enough to assess the apparent reduction in C_{D10n} for the even higher wind speeds as suggested by Powell et al. (2003).

It is further evident in Fig. 3.11 (left) from the estimates of the correlation equation that Charnock's parametrization assuming $\alpha = 0.018$ will overestimate C_{D10n} during Rita at 42001. On the other hand, Charnock will underestimate C_{D10n} at the station 42035 at about a 13.7 m water depth closer to the Texan coast as displayed in Fig. 3.11 (right). The storm did not pass as close to 42035 compared with 42001 and hence the wind speeds are weaker. Nonetheless, the trend displayed in Fig. 3.11 (right) does not suggest a roll-off of C_{D10n} with increasing wind speed but indicate a steadily increase of C_{D10n} , consistent with the functional form suggested by Charnock (1955), albeit with a much larger α than usually assumed. Whereas buoy 42001 was at a 3365 m water depth and hence in genuinely deep water, buoy 42035 is at a water depth that is able to support steeper waves for a given wind speed.

For practical purposes in the absence of wave field information, a function such as eq. (3.30) could be appropriate in deeper water, while in shallower water, Charnock (1955)'s parametrization with $\alpha > 0.018$ would be required. It may be unwise to use eq. (3.30) in shallower water since as Donelan (1982) points out, experience says that higher drag coefficients are required for storm surge modelling. Eq. (3.27) should be more useful in general since it based on aspect ratio scaling as opposed to Froude number scaling, i.e. $C_{D10n} = f(U_{10n})$.

3.4 Conclusions

A first-order scaling of the neutral drag coefficient has been proposed that can account for certain variations in the behaviour of C_{D10n} that may occur depending on the nature of the wave field. It is proposed that C_{D10n} scales with the squared wave steepness, $\frac{H_s^2}{\lambda_p^2}$ at low aspect ratios and tends towards a constant at high aspect ratios. Here, the aspect ratio is the inverse wave steepness. The scaling of C_{D10n} at low aspect ratios is found by extending Toba's 3/2 law to account for a drag coefficient dependent on the sea-state as is generally encountered in practice. A general relationship can then be found using the Usagi-Churchill method that bridges the two scalings at intermediate aspect ratios if necessary.

With respect to the measurements encountered in the field as reported in the literature and at FINO1, it is found that measurements can either follow a scaling based purely on $\frac{H_s^2}{\lambda_p^2}$ at low aspect ratios (e.g. during February 2005 at FINO1) or follow the correlating function matching the two asymptotic scaling regimes (e.g. during January 2005). The two scaling regimes suggested here reflects a different transition between the smooth and rough flow regime concepts

introduced in the previous chapter. A pure wave steepness scaling is an immediate transition to rough flow beyond the smooth regime (approximated here as a constant C_{D10n}) whereas the correlation equation reflects a more gradual transition. Recalling the discussion the previous chapter, the transition regime is difficult even over solid, well defined surfaces and will thus require a higher order analysis offshore than that attempted here to further sort these effects out. This issue will be investigated in the next chapter.

For very low aspect ratios such as that encountered in tropical cyclones, the interpolated function tends to the squared wave steepness scaling and thus should be applicable. The levelling off of the marine drag coefficient as previously estimated in tropical cyclones by Powell et al. (2003) is detected based on buoy measurements using this scaling in deep water during hurricane Rita (2005). In more shallow water, the scaling here anticipates no levelling off but a rapid increase in the drag coefficient which is possibly more consistent with storm surge modelling efforts.

Chapter 4

Air-Sea and land interaction effects at FINO1

4.1 Introduction

In the previous two chapters, the nature of the sea surface and its influence on the aerodynamic roughness length was the principle focus of investigation. This issue was investigated with the help of three particular high wind speed periods as detected by the FINO1 platform. Those cases displayed a “typical” marine behaviour in the sense that there was an absence of any clear diurnal cycle in the wind fields, in contrast to what can be expected over land (Stull, 1988). The lack of an offshore diurnal cycle is attributable to the unresponsive nature of the water surface to solar forcing (i.e. its large heat capacity). It is possible however, given a sufficiently large temperature gradient between the land and the sea and a suitable wind direction from land to sea, for a diurnal cycle to be detected offshore (Barthelmie et al., 1996). Such a case will be the topic of investigation in the following chapter, where a clear diurnal cycle was detected in both wind, temperature, turbulence and even the wave and sea fields during a 7 day period of May 2006.

The theme of offshore surface roughness will be further considered during this period, where the somewhat unique nature of the case allows at least one particular aspect alluded to in the previous two chapters to be investigated, i.e. the unsteadiness of the wind-wave interaction. However, given the nature of the case, some further interesting properties with regard to the turbulence above the surface are detected. Since this has practical relevance with regards to the ability of turbulence parametrization schemes within numerical models to deal with boundary layer turbulence in general, the next chapter will divert from the topic of offshore roughness in pursuit of this issue. Both the roughness and turbulence parametrization themes will again be considered together in Chapter 6.

During the spring and summer months, the temperature contrast between land and sea in relatively closed seas such as the North Sea, can reach $O(10^\circ\text{C})$ as will be demonstrated below at FINO1. For example, Smedman et al. (1997) reported a temperature difference of 20°C in the Baltic Sea. Such a land-sea temperature contrast can lead to an offshore temperature inversion (i.e. an ele-

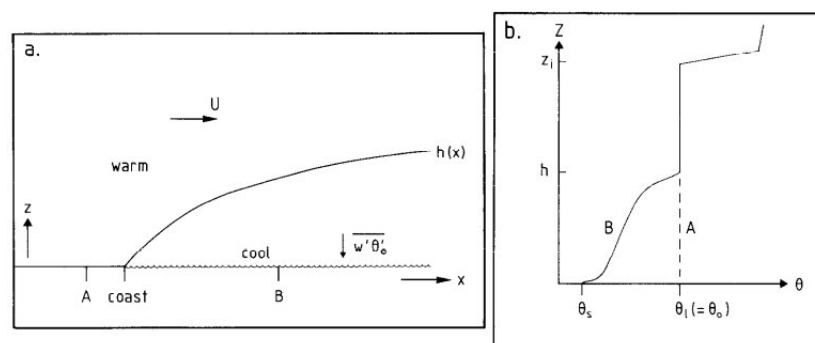


Figure 4.1: The figures 1a and 1b from Garratt (1987) showing the growth of an internal boundary layer as warm continental air flows over a cold sea (a) and the corresponding vertical profiles of potential temperature over land (θ_l) and over sea (θ_s) (b).

vated and rapid increase) that caps the height of a very stable internal boundary layer (Csanady, 1974). In general, internal boundary layers form when there is an abrupt change in the characteristics of the surface, such as the roughness from land to sea. The effects of an abrupt change in surface roughness are felt at much shorter fetches compared with the effects of stratification (Barthelmie and Palutikof, 1996) and hence this is unlikely to be especially felt at FINO1.

On the other hand, stably stratified internal boundary layers can persist for $O(100 - 1000 \text{ km})$ offshore with height-fetch ratios of $O(1/2000)$ (Garratt, 1990) until the air eventually becomes well mixed and assumes the structure of a typical marine boundary layer (Garratt and Ryan, 1989). This situation has been illustrated nicely in the figures 1a and 1b of Garratt (1987), reproduced here in Fig. 4.1, showing the growth of an internal boundary layer as warm continental air flows over a colder sea (a). The potential temperature profiles are correspondingly displayed over land and sea (b), where over sea a low level temperature inversion at height, h is detected below the boundary layer height, z_i which formed over land. A well mixed boundary layer over land is assumed where the potential temperature near the surface, θ_l , approximates that at the boundary layer height, and above h over sea.

In the following chapter, a stably stratified internal boundary layer as detected at the FINO1 platform during May 2006 will be introduced, analysed and then compared with numerical modelling results. The results from previous analyses of stable internal boundary layers will first be introduced for the purposes of describing this particular period. There are a number of theories starting from both first principles and dimensional analysis that will prove useful in interpreting the measurements at FINO1. Numerical modelling, at least from the perspective of the Weather Research and Forecasting model, will then be introduced with a particular emphasis on the Mellor-Yamada-Janjić planetary boundary layer parametrization. The May 2006 stable internal offshore boundary layer as detected at FINO1 will then be described from the perspective of the mean fields, followed by analysis of the turbulence. A comparison between the wind speed, turbulence and drag coefficients as estimated from the

wave field will conclude the chapter, leading to a deeper investigation of the Mellor-Yamada-Janjić parametrization in the next chapter.

4.2 Results from previous analyses

Previous analyses of stable internal boundary layers have developed some formulae that will prove useful further below at FINO1 and will thus be introduced here. According to Mulhearn (1981), the stable internal boundary layer height, h

$$h = f(\rho, U, x, \Delta\rho, g) \quad (4.1)$$

where ρ is the average air density, $\Delta\rho$ is the density difference between air at the sea surface and that over land, x is the fetch and U is a velocity scale which according to Mulhearn (1981) is the wind speed above the boundary layer but below the temperature inversion. Eq. (4.1) can then be written as a consequence of Buckingham's Π theorem as

$$\Pi_1 = c\Pi_2^n\Pi_3 \quad (4.2)$$

where c is a constant, n an exponent,

$$\Pi_1 = \frac{h}{x}, \quad (4.3)$$

$$\Pi_2 = \frac{\Delta\theta}{\theta} \quad (4.4)$$

(here densities are converted to potential temperatures) and a Froude number:

$$\Pi_3 = \frac{U}{\sqrt{xg}}. \quad (4.5)$$

Mulhearn (1981) found c and n to be equal to 0.0146 and -0.47, respectively, based on some previously reported measurements over Massachusetts Bay, USA (e.g. Craig, 1949). Further support to eq. (4.1) was given by the analysis of Garratt (1987) who was able to derive from first principles (i.e. the steady, two-dimensional conservation of heat equation neglecting moisture and radiation)

$$h = cU\sqrt{x} \left(\frac{g\Delta\theta}{\theta} \right)^{-0.5}, \quad (4.6)$$

with the constant $c = 0.014$ determined from numerical simulations in agreement with Mulhearn (1981)'s value. In the theory of Garratt (1987) however, c in eq. (4.2) is a function of many other things including the shape of the vertical θ profile, which implies the formulation of eq. (4.1) is incomplete, and requires further variables. In practice, this constant can take a range of values between 0.015 and 0.035 according to Garratt and Ryan (1989).

Another way of estimating h if u_* is known (which unfortunately as will be shown below, it is not at FINO1 during this period) could be the single dimensionless group (Csanady, 1974)

$$\frac{bh}{u_*^2} = A, \quad (4.7)$$

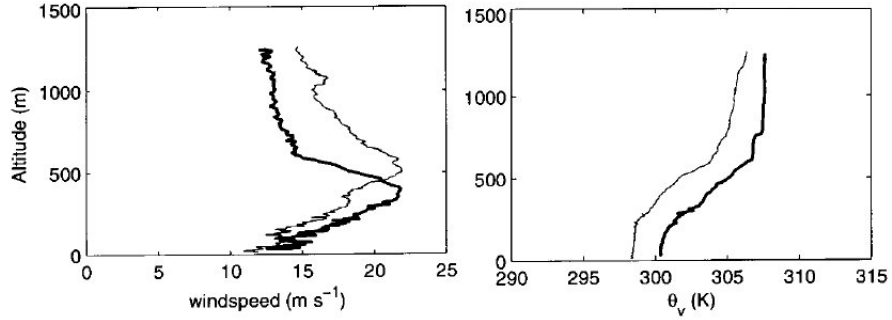


Figure 4.2: Adapted from the figure 2 from Brooks and Rogers (2000) showing wind speed and virtual potential temperature profiles recorded by aircraft at two different locations over the Persian Gulf during the passage of a stable internal boundary layer.

where b is $g \frac{\Delta\rho}{\rho}$ and A is a constant. Csanady (1974) then derives relationships (using the steady equations of motion in the outer layer) giving the angle between the boundary layer averaged horizontal wind \bar{U} and the geostrophic wind as a function of b whereby

$$\bar{U} = V_g \cos \theta_* \quad (4.8)$$

and

$$\frac{b}{Af_c} = V_g \sin \theta_*, \quad (4.9)$$

where a geostrophic balance

$$V_g = \frac{1}{\rho f_c} \frac{dP}{dx}, \quad (4.10)$$

steadiness and horizontal homogeneity are assumed. Here, θ_* is the angle between u_* and V_g , P is the pressure, f_c is the Coriolis parameter. As will be seen below, these relationships show that with increasing temperature difference between the sea surface and land surface (i.e. $\Delta\rho$), the angle between \bar{U} and V_g increases while the magnitude of \bar{U} decreases.

However, from a wind energy perspective, the velocity profile itself and not just the layer averaged wind speed \bar{U} is of interest. For example, low level jets (LLJ) have been detected previously in stable offshore internal boundary layers in the Baltic sea (Smedman et al., 1995), but this has possibly received less attention in the North Sea where temperature differences between the land and water are less dramatic. An example of a measured wind speed profile within a stable internal boundary layer as recorded by Brooks and Rogers (2000) with an aircraft over the Persian Gulf is shown in Fig. 4.2, which is their adapted figure 2. Fig. 4.2 (left) shows the occurrence of a low level wind speed maximum (i.e. a “low level jet”) detected at roughly h , corresponding with the height of the neutral layer above the stable temperature inversion as seen in Fig. 4.2 (right). Similarly, LLJs were also detected during May 2006 at the FINO1 platform to be demonstrated below at apparently roughly h as well. LLJs are of further practical interest since their occurrence within the blade span of wind energy converters will result in greatly enhanced bending moments.

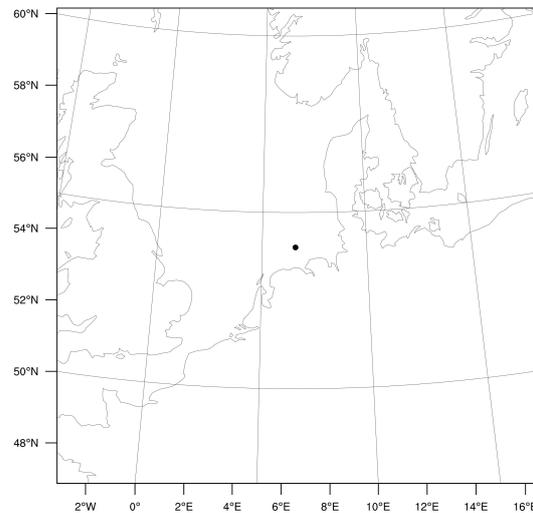


Figure 4.3: The 151 x 151 (10 km resolution) domain centered on FINO1.

To summarise these results, eqs. (4.6), (4.8), (4.9) and Fig. 4.2 show that with an increasing temperature difference between the land and the sea, one can expect a decreasing internal boundary layer height, h , increasing angle between the boundary layer averaged wind and geostrophic wind with the possible occurrence of low level jets. The information in this section will help interpret FINO1 measurements below, and the results of the numerical model to be introduced next.

4.3 General description of WRF and the Mellor-Yamada-Janjić Model

Numerical modelling to be presented in the following section will be conducted using the community based Weather Research and Forecasting (Advanced Research WRF, version 3.1) model (Skamarock et al., 2008). The model solves the full equations of motion (e.g. the conservation of momentum introduced in Chapter 1) on a horizontally and vertically staggered grid. A basic single domain, 151×151 , 10 km horizontal resolution is deployed here with 51 vertical levels, centered on the FINO1 platform (see Fig. 4.3). The model is initialised using the NCEP final operational global analysis (at about a 100 km resolution) as readily available online¹, as well as NCEP real-time, global, sea surface temperature analysis (at about a 10 km resolution) also available online².

In general, processes not explicitly resolved by the numerical grid need to be parametrized. Of particular interest for wind energy applications are the surface layer and planetary boundary layer parametrizations. However, all physical parametrizations will interact to some degree where for example, incoming solar radiation helps determine the heat flux at the ground which helps the surface

¹<http://dss.ucar.edu/datasets/ds083.2/>

²<ftp://polar.ncep.noaa.gov/pub/history/sst/>

4.3. General description of WRF and the Mellor-Yamada-Janjić Mode88

layer scheme calculate the boundary conditions for the boundary layer parameterisation which determines the moisture throughout the boundary layer which the microphysics parameterisation uses to anticipate cloud formation thus affecting the amount of incoming solar radiation to the surface (Warner, 2011).

The Mellor-Yamada-Janjić (MYJ) planetary boundary layer scheme is used here, which also comes with its own surface layer parametrization (Janjić, 1994, 2002). As described in Chapter 1, the appearance of covariances in the equations of motion after Reynolds averaging complicates simple treatment. For this purpose, a boundary layer parametrization is employed, where the concept of an eddy viscosity, K_m is used to relate stresses to local gradients via

$$\overline{u'w'} = -K_m \frac{\partial U}{\partial z}, \quad (4.11)$$

which shifts the problem to one of determining K_m . For that purpose, a parametrization of the prognostic turbulent kinetic energy (TKE, $\frac{1}{2}q^2$) equation is used where (Stull, 1988)

$$\frac{\partial \frac{1}{2}q^2}{\partial t} = \frac{g}{\Theta_v} \overline{w'\theta'} - \overline{u'w'} \frac{\partial U}{\partial z} - \frac{\partial}{\partial z} \left(\frac{1}{\rho} \overline{p'w'} + \frac{1}{2} \overline{q^2 w'} \right) - \epsilon. \quad (4.12)$$

Here, the right hand side terms represent, respectively, the production of TKE due to buoyancy and wind shear, the diffusion of TKE far from the surface and, the dissipation of TKE, ϵ . The eddy viscosity (and heat exchange coefficient) can then be calculated diagnostically with the help of a characteristic turbulent length scale ℓ broadly via (Stensrud, 2007)

$$K_m = \ell \sqrt{\text{TKE}}. \quad (4.13)$$

The length scale can then be made to be dependent on height, stability, buoyancy and dissipation scales depending on the model (Holt and Raman, 1988). The boundary layer parametrization operates one-dimensionally and employs a vertical staggering whereby the TKE and K_m are located at the layer interfaces, while the mean parameters are located within the layers (Janjić, 2002).

Since $-\overline{u'w'} \equiv u_*^2$ at the surface, the surface layer scheme employs the Charnock (1955) parametrization offshore using $\alpha = 0.018$ in conjunction with Monin-Obukhov similarity theory (Monin and Obukhov, 1954) as introduced in Chapter 2. A smooth flow regime is employed at low wind speeds where $z_o = \frac{0.11\nu}{u_*}$ (Janjić, 1994), which practically corresponds roughly with wind speeds below about 7 ms^{-1} . The surface layer then provides the lower boundary condition for the planetary boundary layer scheme where there the TKE is calculated according to

$$\text{TKE} = \frac{1}{2} B_1^{2/3} u_*^2, \quad (4.14)$$

where B_1 is a model constant set to 11.9 by Janjić (2002). With regards to other physics options in WRF, the Dudhia and rapid radiative transfer model (RRTM) shortwave and longwave radiative schemes, WRF single moment 3 microphysics, the Noah land-surface model and the Betts-Miller-Janjić cumulus parameterisation are used (Skamarock et al., 2008).

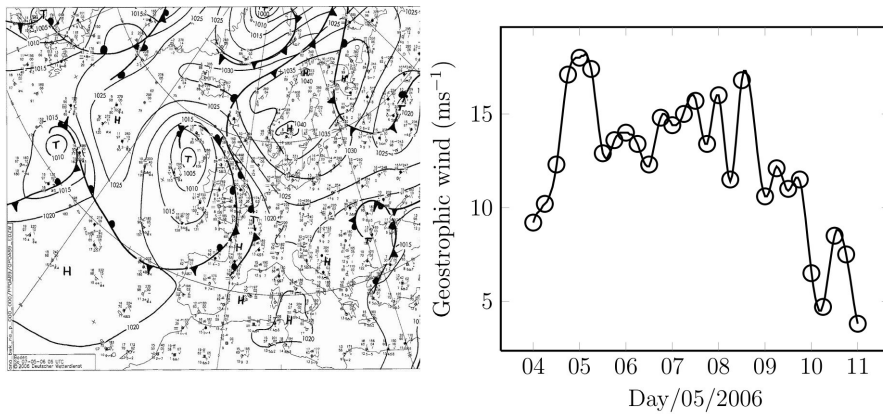


Figure 4.4: DWD surface pressure map (as archived by Wetter3.de) on indicative of the period 04/05/06 - 11/05/06 (here 07/05/06 6 UTC) showing a high over Scandinavia and low just east of Ireland (left). The estimated geostrophic wind at FINO1 for the entire period (right).

4.4 Results

In this section, analyses and simulations will be presented for a stable period where warm and dry air was advected from land out to the FINO1 platform in the North Sea during May 4–11, 2006. Mean observations during this period will be presented first, followed by turbulence measurements. For the purposes of comparison with the numerical model, the turbulence measurements will then be attempted to be scaled using estimates of the friction velocity, u_* and the outer length scale based on estimates of the inversion height, h based on eq. (4.6). Outputs from the WRF-MYJ model will demonstrate that the modelled wind speed underpredicts the hub height wind speed (i.e. at 80 m) and that the anticipated vertical structure of TKE by the MYJ parametrizations contradicts measurements. The surface layer scheme, while it appears to broadly anticipate roughness lengths correctly based on the correlation developed in the previous chapter, does not capture the full complexity as will be demonstrated below.

4.4.1 Mean fields

The clearest cases of stable stratification over the North Sea will occur during periods when warm air originating over land is advected out over sea when the water is at its coldest during the year: spring and early summer. At FINO1, this can occur with southerly and easterly flows such as that which occurred between May 4–11, 2006 where a relatively constant easterly wind brought warmer air during the day over the still relatively colder North Sea. The surface pressure map displayed in Fig. 4.4 (left) for 07/05/06 illustrates a high pressure centered over Scandinavia and a low pressure system just west of Ireland. Both of these features which remained approximately stationary for about a week, resulted in the pumping of warmer and dryer continental air over the cooler North Sea. The resultant geostrophic wind has been estimated from a series of pressure maps like that displayed in Fig. 4.4 (left) using with the result displayed in Fig. 4.4

(right). Relative steady synoptic scale conditions are evident during the first 6 days with the geostrophic wind falling by approximately 50% during the 10th.

For most periods during the year, there is a lack of a diurnal cycle offshore, especially at FINO1 as shown in the previous chapter. However, in this case there is a particularly distinct diurnal cycle evident in time series of the wind speed and relative humidity as shown in Fig. 4.5, but also in the wind direction. The vertical grid in Fig. 4.5 indicates 0:00 (UTC) each day with local European summer time 2 hours ahead. Fig. 4.5 suggests that the angle between the geostrophic wind and U_{80} increases during the day, and hence with increasing land-sea temperature difference, consistent with the analysis of Csanady (1974), i.e. eqs. (4.8) and (4.9). It can be seen that a wind speed maximum at 80 m occurs during the afternoon, corresponding with the greatest temperature difference between that over land and the sea surface. However, whether the average wind speed within the internal boundary layer \bar{U} decreases is another issue. The relative humidity also falls significantly during the day, indicating the passage of drier continental air compared with that at night. The air is generally drier than expected throughout the period where at 90 m, the relative humidity consistently drops to 40%. The difference in relative humidity between the different heights is a clear indication of poor vertical mixing during this period. The aircraft measurements of Brooks and Rogers (2000) also displayed poor humidity exchange in such a boundary layer in the Persian gulf, where mixing ratios fell to negligible magnitudes above the inversion layer.

Shown in Fig. 4.5 (top) are attempts by the WRF model to calculate the 80 m wind speed (solid black line) where a consistent underprediction of the measured wind speed throughout the daily cycle is detected. Here the wind speed is the horizontal wind speed,

$$U_h = \sqrt{U^2 + V^2}, \quad (4.15)$$

where U and V are east-west and north-south wind components, respectively. Such a model performance would be clearly unsatisfactory from the perspective of any potential wind energy forecasts. A simple explanation could be that there is a lack of model resolution, with it being only 10 km in magnitude. As pointed out by Garratt (1987), internal boundary layers such as these grow slowly and hence a relatively larger grid size should be capable of handling such flows. The wind is easterly and hence approximately 150 km west of the coast giving roughly 15 grid points for the model to respond to the changing boundary conditions. As will be shown further below, a higher vertical resolution closer to the surface does not improve the situation.

Fig. 4.6 (top) shows the time series of temperatures at 100 and 33 m, as well as at the sea surface, where the difference between the sea and the 100 m measurement reaches 15°C during the 4th, but decreases to about 10°C during the 10th. In general, the high heat capacity of water means that the sea surface temperature (SST) responds weakly to the air temperature. Here however, Fig. 4.6 shows a SST increasing by approximately 2°C during this period. During the 4th and also the 10th, it appears that the SST is even weakly responsive to the air temperature diurnal cycle.

The difference between the 100 and 33 m measurements is small during the evening implying the disappearance of the temperature inversion within the FINO1 tower layer during these periods. Also shown in Fig. 4.6 is the model

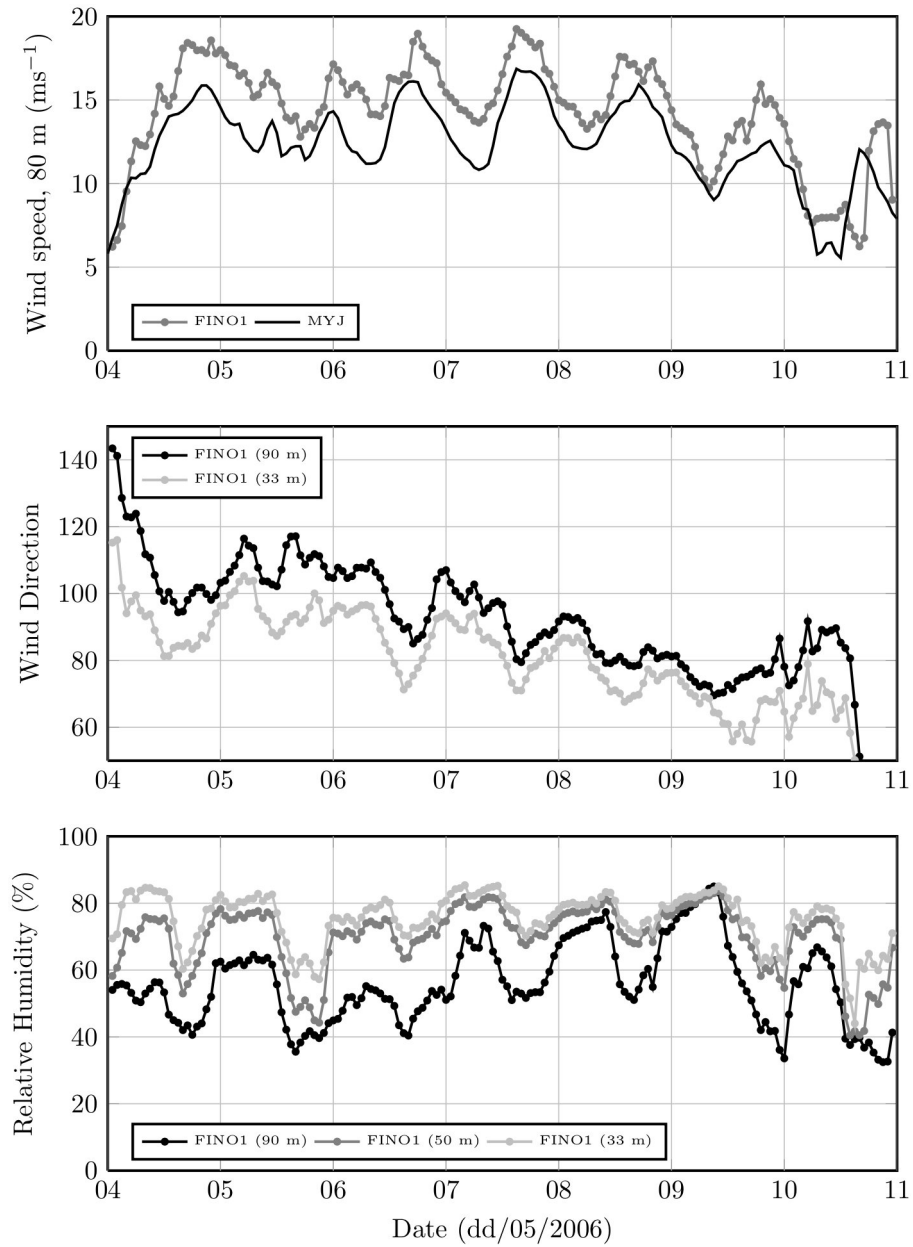


Figure 4.5: Wind speed according to the 80 m cup anemometer compared with the 80 m wind speed according to the WRF model (top). Wind direction at 90 and 33 m as measured by wind vanes at FINO1 (middle). Relative humidity as measured at 90, 50 and 33 m by hygrometers at FINO1 (bottom).

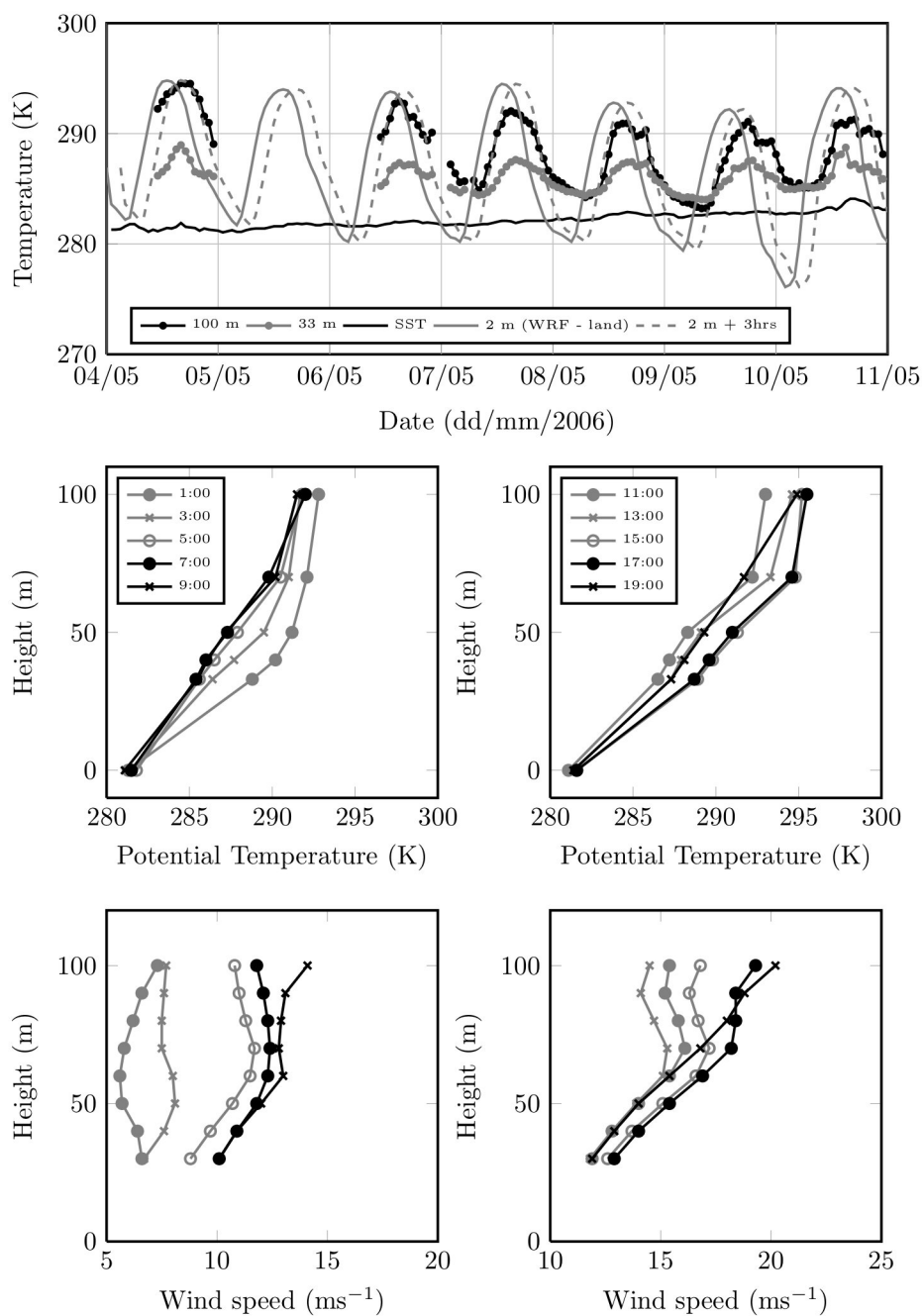


Figure 4.6: Time series of temperature at 100 m, 33 m and the sea surface (SST) at FINO1 in comparison with the modelled 2 m temperature over land directly east of FINO1 (top). The dashed line shows the modelled temperature shifted three hours forward. Potential temperature (middle) and wind speed profiles (bottom) during the 4th as shown every second hour (UTC).

calculated 2 m temperature over land directly east of the FINO1 tower which is higher than the 100 m measurement during the day, falling approximately to that of the sea surface and less at night. The diurnal temperature cycle over land is evident at FINO1, but lagging in phase by about three hours as the continental air travels to FINO1. This can be seen from the dashed line showing the 2 m land temperature shifted three hours later and corresponding with the 100 m temperature at FINO1. From the phase difference between the FINO1 and land temperatures (~ 3 hours) and the distance between FINO1 and the coast (~ 150 km), a velocity scale can be formed giving about 14 ms^{-1} for this particular period, which is in some agreement with the calculated geostrophic winds in Fig. 4.3.

During the earlier part of the 4th, the internal boundary layer height corresponding with the temperature inversion, h may have been within the tower layer as is suggested from potential temperature profiles in Fig. 4.6 (middle), where profiles are displayed during the 4th beginning at 1:00 (UTC) and shown for every subsequent second hour until 19:00. The potential temperature is calculated as (Stull, 1988)

$$\theta \approx T + \frac{g}{C_p} z, \quad (4.16)$$

where T is the temperature, z is the height, g is the gravitational constant and C_p is specific heat for air. There are certain periods whereby the shadow of the tower was influencing the measurements and these are indicated by the missing temperatures in Fig. 4.6 (top), i.e. the early hours of the 4th, during the 5th and into the 6th. This is possibly evident in the wind speed profiles as displayed in Fig. 4.6 (bottom) in the early hours of the 4th. At 1:00, the potential temperature shows a profile with a negative curvature (upwards concave) in contrast to later in the day where curvature becomes, apparently, concave downwards. Garratt and Ryan (1989) have previously identified a positive curvature as a feature of the offshore IBL, which, in contrast to a negative curvature, occurs when turbulent cooling is more important than radiative cooling (Andre and Mahrt, 1982). Towards the start of the day, the temperature at FINO1 decreases until 9:00, at which point the temperature begins to increase as continental air arrives. It can be seen that there is low level temperature inversion above 30 m during the day, where a near neutral layer is possibly recovered between the 70 and 100 m measurements from 11:00 onwards, suggestive of the height of the temperature inversion. The vertical structure of potential temperature detected here corresponds with the illustration of Garratt (1987) shown above (Fig. 4.1), where h here at 11:00 corresponds with the onset of a neutral layer at approximately 70 m. The appearance of a low level jet and its corresponding wind speed maximum within the FINO1 tower is dependent on the position of the inversion where it can be seen that at 19:00, the jet disappears from the view of the tower, corresponding with the disappearance of the neutral layer between 70 and 100 m at that time.

Since determining h from the measurements of θ is not always possible at FINO1 (h decreases with $\Delta\theta$ via eq. (4.6)), eq. (4.6) can possibly be used as an alternative to estimating the height of the inversion. This can be done by assuming U is the velocity scale inferred from the phase difference between the modelled and measured temperatures (14 ms^{-1}), a fetch of 150 km, $\Delta\theta$ as the potential temperature difference between the sea surface temperature as measured at FINO1 and the 2 m onshore temperature as estimated from the

Table 4.1: Calculation of the internal boundary layer height, h between 11:00 and 23:00 for the 4th, 6th, 7th and 8th according to eq. (4.6) using estimated geostrophic wind speeds shown in Fig. 4.4 and $x = 150$ km. Here, δ corresponds with the height of the low level jet (LLJ).

UTC (4th)	h (m)	δ (m)	UTC (6th)	h (m)	δ (m)
11:00	107	70	11:00	112	70
12:00	95	70	12:00	100	80
13:00	87	70	13:00	92	70
14:00	82	60	14:00	89	70
15:00	81	70	15:00	86	-
16:00	82	70	16:00	85	-
17:00	81	80	17:00	86	-
18:00	82	-	18:00	88	-
UTC (7th)	h (m)	δ (m)	UTC (8th)	h (m)	δ (m)
11:00	117	-	11:00	127	-
12:00	102	80	12:00	111	-
13:00	93	80	13:00	101	-
14:00	88	80	14:00	96	-
15:00	84	-	15:00	94	-
16:00	83	-	16:00	93	-
17:00	83	-	17:00	93	-
18:00	85	-	18:00	95	-
UTC (9th)	h (m)	δ (m)	UTC (10th)	h (m)	δ (m)
11:00	156	-	11:00	118	80
12:00	127	-	12:00	107	-
13:00	112	-	13:00	98	-
14:00	103	-	14:00	94	-
15:00	98	80	15:00	93	-
16:00	96	-	16:00	93	40
17:00	96	-	17:00	93	40
18:00	98	-	18:00	94	70

model directly east of FINO1 (see Fig. 4.6) and θ being the average of these two temperatures. However, h from eq. (4.6) is also subjective on account of the precise value of the constant c , where here $c = 0.01$ has been used which is roughly that found by Mulhearn (1981) and Garratt (1987) ($c = 0.014$). In Table 4.1, h as calculated according to eq. (4.6) has been tabulated along with the low level jet height, δ as estimated visually as done in Fig. 4.6. In practice, δ may be slightly less than h (Smedman, 1988), consistent with the offshore stable internal boundary layer measurements of Brooks and Rogers (2000) which have been reproduced in Fig. 4.2 above. Smedman (1988) measured both δ and h over land where it is apparent they are most similar during steady periods.

For the few measurements of δ available, one can see an approximate correlation between h and δ . For example, wind speed profiles during the 4th are depicted in Fig. 4.6 (bottom) and show a low level jet throughout the day whose height rises from about 50 m above the surface at 3:00 to 70 m at 17:00, but

appears to rise above the tower at 19:00, in correlation with the behaviour of h . One can see the peak in the wind speed profile at approximately 70 m at 13:00 and hence this value appears in Tab. 4.1. The 1:00 measurement is possibly unreliable because of tower flow distortion at this time (wind direction: 100 – 160°) (see Fig. 4.5). The 100 m wind speed measurement sometimes deviates from the other heights on account of lightning rods placed at regular intervals at this particular measurement level, thus it is difficult to detect wind speed maxima higher than 80 m. During the 6th for example, h is at its highest for the times considered here and hence no LLJ was detected. On the 10th, the lowest h occurred, likely due to the lower wind speeds (see the geostrophic winds in Fig. 4.4) with the correspondingly lowest low level jets. During the middle of the day however, the low level jets disappeared for reasons to be described further below.

4.4.2 Turbulent fields

In this section, the turbulence fields will be analysed since this will offer further insight into the mean fields presented above, including the model results to be discussed further below. Fig. 4.7 for example shows a time series of heat fluxes (top), turbulence intensity (middle) and “local” friction velocities (bottom) at 40, 60 and 80 m at FINO1. Heat fluxes are estimated by multiplying sonic measured vertical velocity-temperature covariances $\overline{w'\theta'}$ by ρC_p , where C_p is the specific heat for dry air. The friction velocities are seen to clearly decrease with increasing height and hence they are only “local” values whereby

$$u_L = \left(\overline{u'w'^2} + \overline{v'w'^2} \right)^{1/4}, \quad (4.17)$$

where the friction velocity u_* is defined by

$$u_* = \lim_{z \rightarrow 0} u_L. \quad (4.18)$$

Turbulence intensities are defined as

$$\text{Ti} = \frac{\sqrt{\overline{u'^2}}}{U_h}, \quad (4.19)$$

where $\overline{u'^2}$ is the streamwise fluctuating velocity and U_h is the mean horizontal wind speed.

That a low level temperature inversion could persist so low for so long can be seen from heat fluxes which at times display negligible magnitudes. These times are during the day and generally at 80 m. In Fig. 4.7, periods where tower effects distorting the flow are believed to be significant (for wind directions between 100 and 160°) have been removed. It was estimated above that the height of the temperature inversion is often at about 80 m and this is possibly evident in heat fluxes, particularly at 80 m. Here, the sonic at 80 m gives heat fluxes consistently lower than at the other heights, and often at an opposite diurnal phase. This is evident during the 7th where even a slight upward heat flux is detected, possibly on account of the persistent upward humidity flux into the dryer 80 m air. An upward humidity flux overwhelming the downward heat flux resulting in a slightly convective boundary layer has been suggested and even

measured before in such a boundary layer (Mulhearn, 1981; Brooks and Rogers, 2000). Turbulence intensities are generally less than 5% at all heights and better correlated at all heights compared with heat fluxes. Over land, one could expect Ti to be up to an order of magnitude larger than that detected here, despite the closeness of the surface and a significant wind shear as shown above in Fig. 4.6.

In order to assess the particular turbulence regime of this boundary layer, an attempt will be made to scale streamwise variances ($\overline{u'^2}_+ = \frac{\overline{u'^2}}{u_*^2}$) according to outer scaling, i.e. (e.g. Caughey et al., 1979)

$$\overline{u'^2}_+ = f\left(\frac{z}{z_i}\right), \quad (4.20)$$

without a measurement of either u_* or the outer length scale, z_i . This approach can be contrasted with local scaling, i.e. as conducted by Brooks and Rogers (2000) in their internal boundary layer. The argument in favour of local scaling in stable stratification is that vertical motions are sufficiently damped as z increases such that the interaction of turbulent motions with the surface becomes negligible, and thus some other length scale is more relevant (Mahrt and Vickers, 2003).

Without a direct estimate for u_* , one could assume a vertical profile of the local friction velocities u_L where after Nieuwstadt (1984), u_* is estimated from

$$\frac{u_L^2}{u_*^2} = \left(1 - \frac{z}{\delta}\right)^{3/2}. \quad (4.21)$$

The outer length scale, δ in eq. (4.21) as estimated from eq. (4.6) and tabulated in Table 4.1 will be used in place of z_i in eq. (4.20). For the purposes of comparison with results reported in the literature, the turbulent kinetic energy (TKE), defined as

$$\text{TKE} = \frac{1}{2} \left(\overline{u'^2} + \overline{v'^2} + \overline{w'^2} \right), \quad (4.22)$$

will be considered comparable with the streamwise variance, $\overline{u'^2}$. This is about 5–10% accurate in stable stratification according to the estimates of Banta et al. (2006), and is also consistent with the measurements at FINO1 here (Fig. 4.8). For example, Banta et al. (2006) assume $\sigma_{u+} \approx 2.44$, $\sigma_{v+} \approx 1.92$ and $\sigma_{w+} \approx 1.33$ and so it follows that $\sigma_v = 0.79\sigma_u$ and $\sigma_w = 0.54\sigma_u$. Hence, from eq. (4.22),

$$\text{TKE} = \frac{1}{2} \left(\overline{u'^2} + 0.79^2 \overline{u'^2} + 0.54^2 \overline{u'^2} \right) = 0.96 \overline{u'^2}. \quad (4.23)$$

This is further useful practically since $\overline{u'^2}$ is more often used in wind energy than the TKE, whereas the TKE is calculated by the numerical model.

With these assumptions, Fig. 4.9 shows measurements of TKE plotted according to

$$\frac{\overline{u'^2}}{u_*^2} = f\left(\frac{z}{z_i}\right), \quad (4.24)$$

where $\overline{u'^2} \equiv \text{TKE}$, $z_i = \delta$. The solid line from Caughey et al. (1979) is also shown in Fig. 4.9 for reference and is based on measurements in stable stratification over homogeneous terrain over land. The turbulence measurements during the 5th are likely to be unreliable due to tower flow distortion on account of the

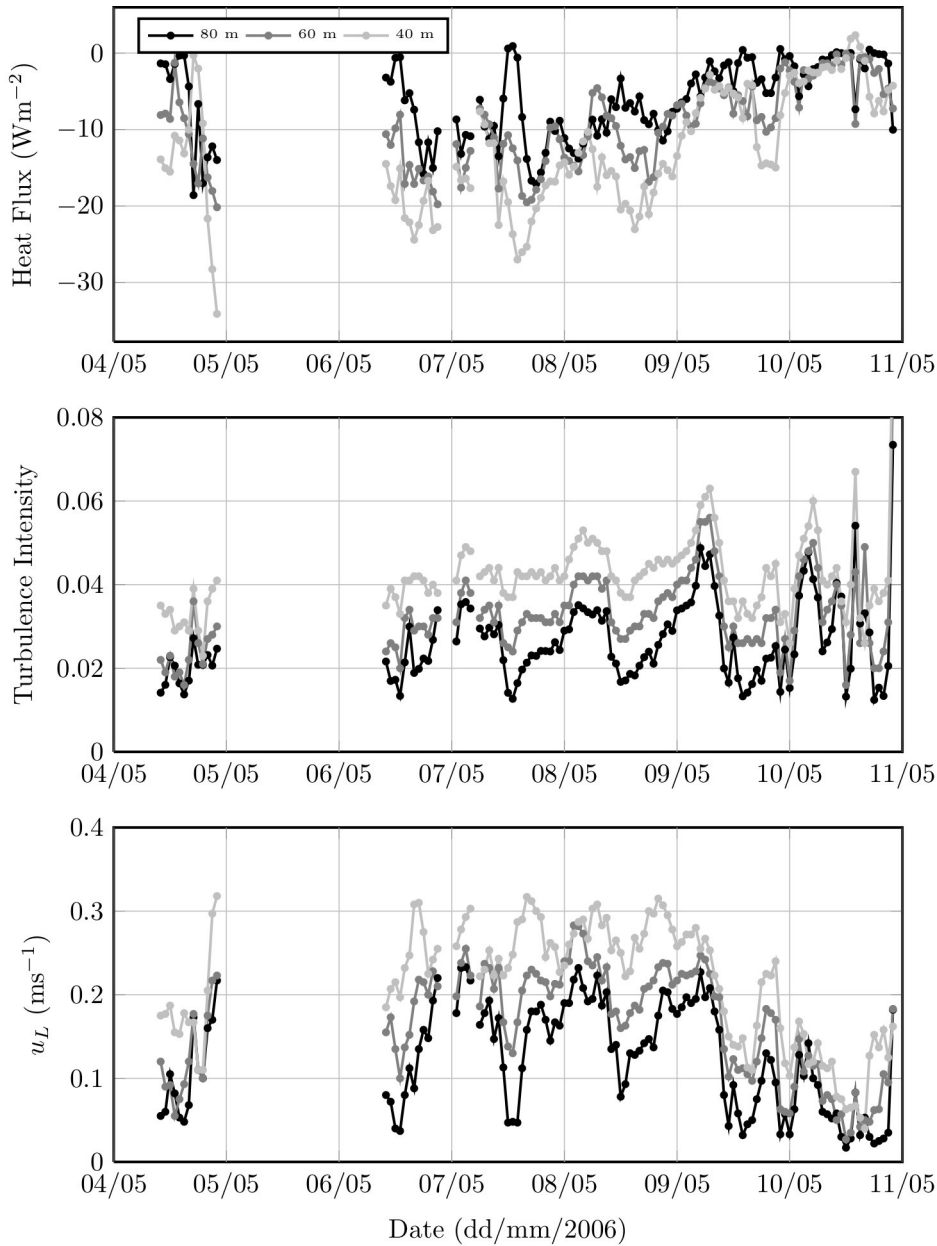


Figure 4.7: Heat fluxes (top), turbulence intensities (middle) (eq. (4.19)) and local friction velocities (bottom) (eq. (4.17)) at 80, 60 and 40 m at FINO1.

wind direction and are thus not considered here. The time periods shown in Fig. 4.9 have also been limited to that where there is believed to be an internal boundary layer (and hence eq. (4.6) is able to be applied). In other words, no attempt is made to scale those cases for where the land temperature, θ_ℓ is less than the SST, θ_s which can occur during the night.

It can be seen in Fig. 4.9 that a satisfactory scaling may have been achieved

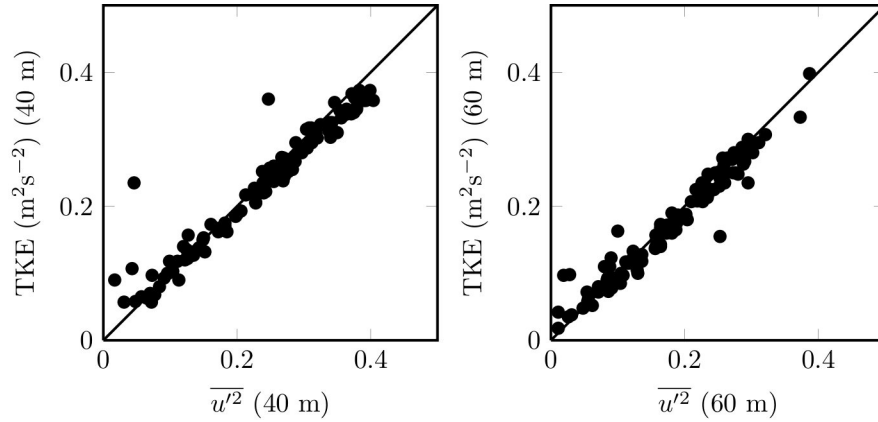


Figure 4.8: Comparison between the TKE and streamwise variances as measured at 40 (left) and 60 m (right) during the period May 4-11, 2006.

here via the assumptions made through eqs. (4.21) and (4.6), although the nature of the assumed function form for eq. (4.21) may make results appear better than they are in reality. The point of this is that if the scaling in Fig. 4.9 is genuine, the vertical structure of turbulence within this stable internal boundary layer may take a similar functional dependence as that found over homogeneous, flat terrain over land. The analysis here would be more rigorous were independent measurements of u_* and z_i available, however, one can see whether there is still some degree of physical truth in Fig. 4.9 by investigating what occurs when the scaling rapidly deteriorates as appears to be the case during the 10th. During this day, the geostrophic wind was lower compared with the rest of the period (see Fig. 4.4), and the measurements at FINO1 may well have even been above the inversion height. This is possibly already evident from Table 4.1 above, where the estimated h was about twice that of the LLJ height. As has been seen in Fig. 4.7 above, the 10th gave very low magnitudes of turbulence where heat fluxes were nearly negligible and u_L was roughly 0.05 ms^{-1} .

To help explain the scatter in Fig. 4.9 (bottom left), TKE_+ from just the 40 m measurement is displayed in Fig. 4.10, where the measurement points are connected as a time series. For example, the times 9:00 and 15:00 have been indicated explicitly in Fig. 4.10. Also shown is TKE_+ as a function of the local Monin-Obukhov similarity parameter, $\frac{z}{L_L}$, where the local Obukhov length is defined as

$$L_L = \frac{-u_L^3}{\kappa \frac{g}{\theta} w' \theta'}. \quad (4.25)$$

It is evident from Fig. 4.10 that the departure from stably stratified, outer layer scaling centered on 15:00 is simply because the layer becomes unstably stratified as evident by the negative $\frac{z}{L_L}$ during this period. A closer look at wind speed profiles illustrates relatively linear wind speeds with height, indicative of very stable stratification, until about 11:00. From that point forward, a constant wind speed with height develops at 14:00 indicative of a convective layer, despite the temperature of air being about 10°C higher than the SST. After this, a

LLJ jet at 40 m develops but increases in height after 17:00. It can be seen from Fig. 4.10 that the scaling departs from the curve of Caughey et al. (1979) in convective conditions, but returns once stable stratification resumes. The convective conditions here are likely on account of the upwards humidity flux working against the downwards heat flux. Independent measurements of the humidity and heat fluxes would be required to separate these effects.

While it is not expected that the MYJ model is able to anticipate correctly such a complex flow during the 10th, at least without a significantly increased vertical resolution, the other days presented in Fig. 4.9 should in principle be well modelled since they appear to agree well with conventional outer layer scaling. However, as will be demonstrated in the next section, the model fails to emulate the behaviour found in Fig. 4.9.

4.4.3 Model results

In this section, outputs from the MYJ model will be compared with FINO1 measurements. Above in Fig. 4.5, it has been shown that the MYJ has under-predicted the hub height wind speed at FINO1 throughout this period. There are two issues here: whether the surface layer scheme has performed accurately (treated first) and then whether the boundary layer parametrization scheme is realistic.

In the previous chapter, it was shown that, to a first order, the magnitude of C_{D10n} could be estimated purely from the wave field using the correlation

$$C_{D10n} = \left(0.03^3 + \left(\frac{H_s}{\lambda_p} \right)^3 \right)^{2/3}, \quad (4.26)$$

where H_s is the significant wave height and λ_p is the peak wave length. The drag coefficient as calculated from buoy measurements at FINO1 is shown in Fig. 4.11 (top) along with C_{D10n} calculated from the modelled MYJ friction velocity, Obukhov length and 10 m wind speed (see Chapter 2 for these formulae). If the real drag coefficients scale with eq. (4.26) and not merely the pure wave steepness asymptote (see Chapter 3), the MYJ surface layer scheme is broadly accurate (remember that C_{D10n} is equivalent to discussing z_o) with the estimates using the buoy data. On the other hand, if drag coefficients during this period scale merely with $\frac{H_s^2}{\lambda_p^2}$, then the surface layer scheme may be overestimating roughness lengths, which could then partly explain the underestimated wind speeds in Fig. 4.5 above.

In either case, the MYJ model has not at all detected the approximate half day oscillation in the wave field via eq. (4.26) seen in Fig. 4.11 (top). This behaviour is physical since the oscillation is evident in the 40 m local friction velocities reproduced in Fig. 4.11 (middle). In the previous chapter, we have seen the effects on C_{D10n} that can arise as the wind travels at different angles to the waves as evident during the January 2005 period. The consequence of this is that the wind “sees” a different roughness structure depending on the angle of attack of the wind. It could be that the fine scale roughness is of a two-dimensional nature while the wind can flow over the waves at an uncertain angle.

For example, consider the wind and wave direction in Fig. 4.11 (bottom). As discussed above, the wind direction oscillates diurnally, where the average

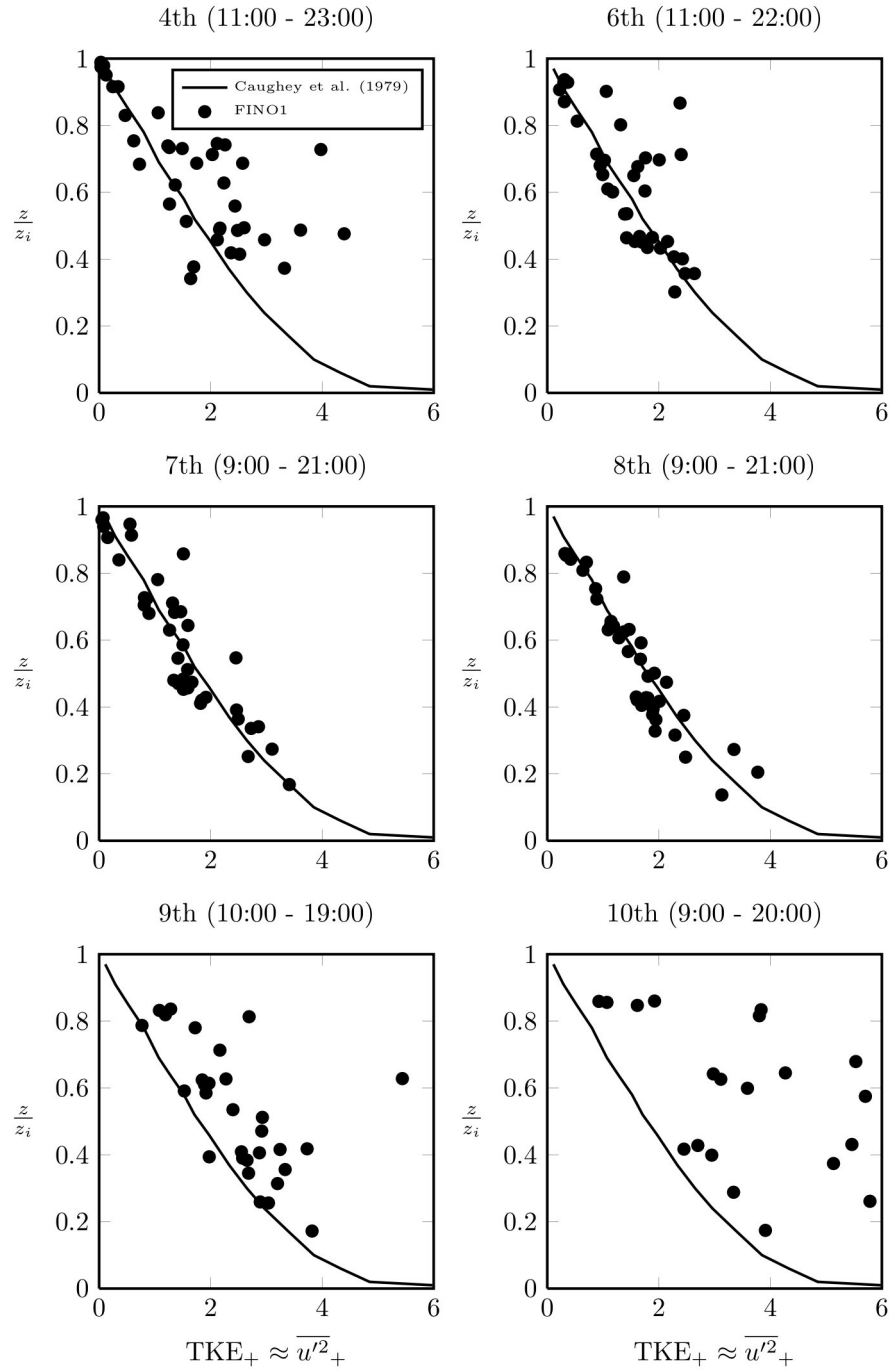


Figure 4.9: TKE₊ at FINO1 assuming $\text{TKE} \approx \overline{u'^2}$ and u_* from u_L interpolated to the surface using eq. (4.21). The scaling is compared with that performed by Caughey et al. (1979) (it is their solid curve from their figure 5 (top left)).

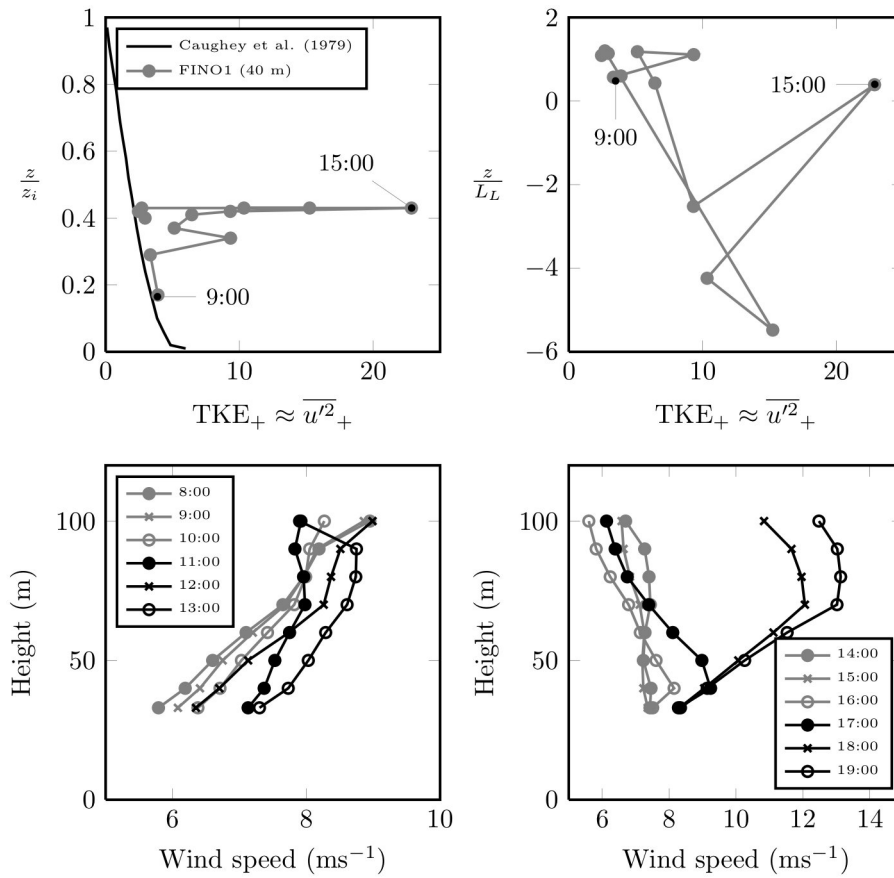


Figure 4.10: Scaled TKE during the 10th from 6:00 – 20:00 similar to that performed in Fig. 4.9, but concentrating on the 40 m measurement (top left). Also shown that are the times 12:00 and 18:00 indicating the departure from outer scaling. TKE_+ as a function of the local Monin-Obukhov stability parameter indicating illustrating instability between 12:00 and 18:00 (top right). Wind speed profiles from 8:00 – 13:00 (bottom left) and from 14:00 – 19:00 (bottom right).

wind angle throughout a stable internal boundary layer departs further from the geostrophic wind with increasing land-sea temperature gradient (i.e. the wind orientates itself at angles further to the left of the geostrophic wind during the day). Because of the nature of this period, what can now readily be seen in Fig. 4.11 (bottom) is exactly what occurred during the 5th of January 2005 as presented in the previous chapter. That is, the drag coefficient is highly correlated with the relative, unsteady movement of the wind and wave field. This is perhaps easier to see if we plot a time series of a 5 hour moving average of the difference in the rate of change of the wind direction and the rate of change in the wave direction, i.e. $\frac{d(\theta_{wind} - \theta_{wave})}{dt}$ in Fig. 4.12 and compare it with a time series of a 5 hour moving average of 50 times the rate of change of the drag coefficient as estimated from buoys using eq. (4.26). Furthermore, to manually match the phase of the difference between the wind and the wave

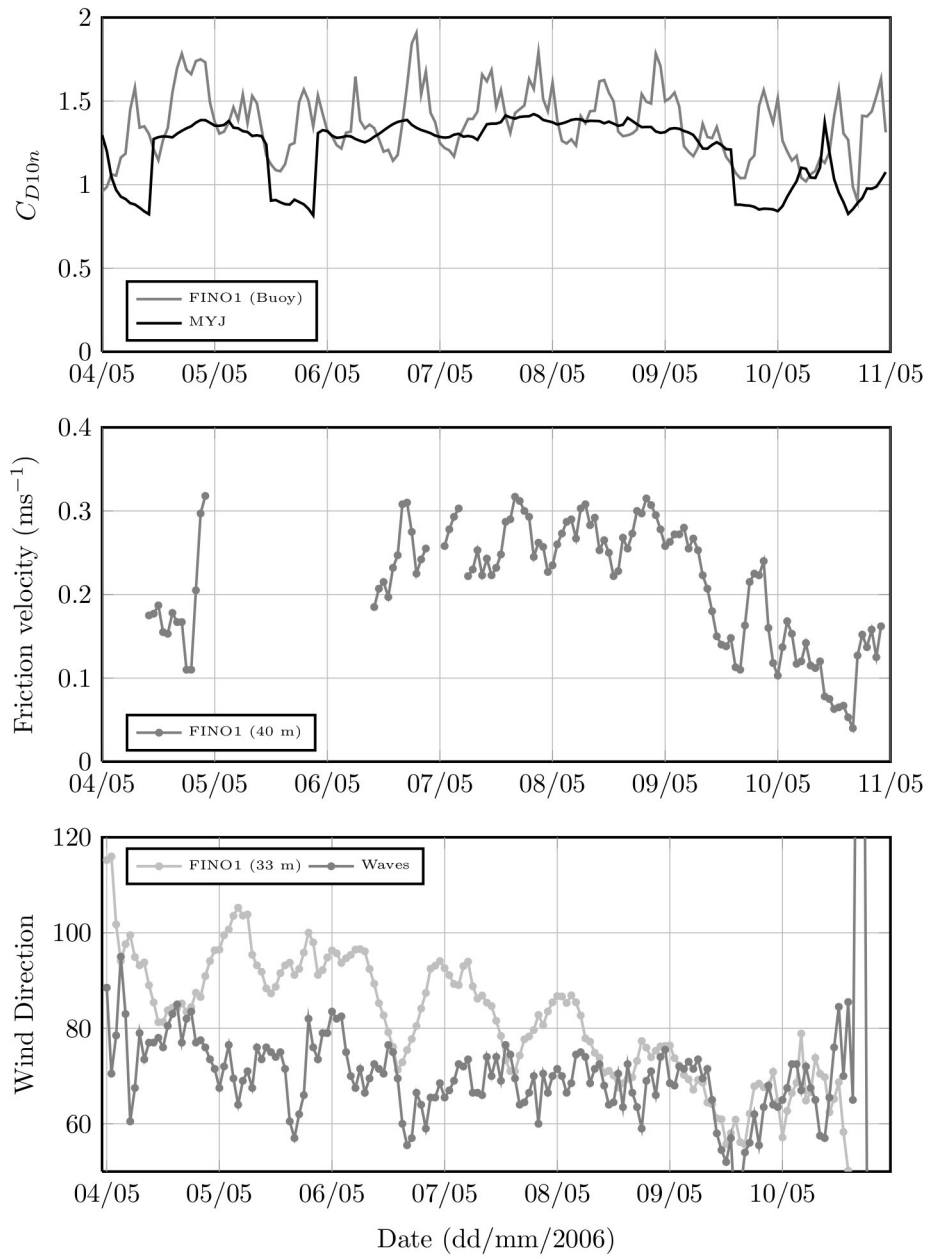


Figure 4.11: Drag coefficients as estimated from buoy measurements using eq. (4.26) compared with the MYJ model (top). Local friction velocities at 40 m (middle). Wind (33 m) and wave directions (bottom).

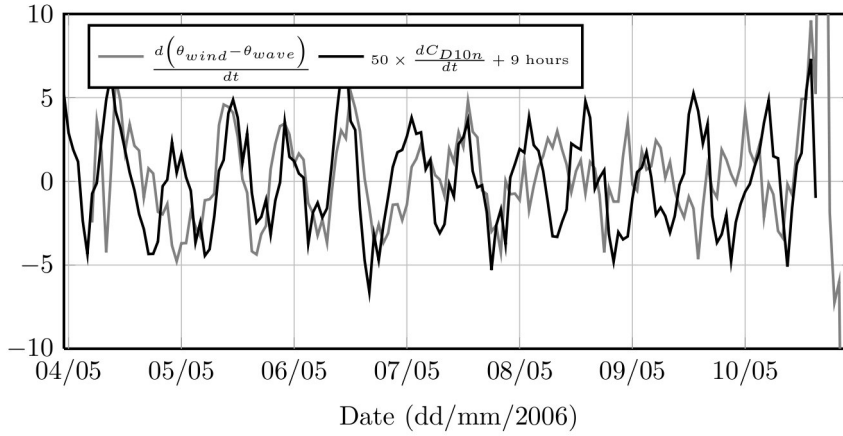


Figure 4.12: Time series of the difference between the rate of change of wind and wave direction (5 hour moving average) compared with 50 times the rate of change of the drag coefficient estimated from buoy measurements plus 9 hours in time (also a 5 hour moving average).

angle, $\frac{dC_{D10m}}{dt}$ is used 9 hours ahead of time. Fig. 4.12 shows a good correlation during the 5th, 6th and 7th, but $\frac{d(\theta_{wind}-\theta_{wave})}{dt}$ and $\frac{dC_{D10m}}{dt}$ appear to be about 12 hours out of phase during the 8th and the 9th, when by Fig. 4.11 (bottom), the wind and waves realign. As one can imagine, the model as it is based merely on the Charnock (1955) roughness parametrization for $\alpha = 0.018$ (and hence will only vary with the wind speed) is unlikely to capture this phenomena.

More immediate progress could be made if we consider the TKE as output from the MYJ model in comparison with the FINO1 measurements in the context of the outer layer scaling displayed above in Fig. 4.13. The MYJ model calculates the TKE using a parameterisation for the TKE equation presented above where in Fig. 4.13, the TKE has been normalised by the model calculated friction velocity to give TKE_+ . The model heights are normalised by the same inversion height, h used in Fig. 4.13, as has been calculated above for the FINO1 measurements in Fig. 4.9. If the modelled boundary layer height corresponds with h , Fig. 4.13 will show the normalised TKE tending to 0 as with the measurements, but not exactly since above the modelled boundary layer, the MYJ-TKE is set to $0.1 \text{ m}^2\text{s}^{-2}$. The actual modelled PBL height is roughly 200 m during this period and thus is often higher than that anticipated here (see Table 4.1).

Once more, at the model surface, the TKE is defined according to $TKE = \frac{1}{2} B_1^{2/3} u_*^2$, where B_1 is a model constant set to 11.9 by Janjić (2002). One can see this in Fig. 4.13 where the $TKE_+ \rightarrow \frac{1}{2} B_1^{2/3} = 2.6$ as $\frac{z}{z_i} \rightarrow 0$. It is then apparent from Fig. 4.13, if the results there can be generalised for stable boundary layers, that the TKE will in general be significantly underpredicted close to the surface assuming u_* has been calculated correctly. It is likely then that the constant in eq. (4.14), B_1 , is set too low in the model. However, there is a more fundamental problem with the model in general that will be discussed in the next chapter. In addition to incorrect boundary conditions, the rate of decay of TKE with height

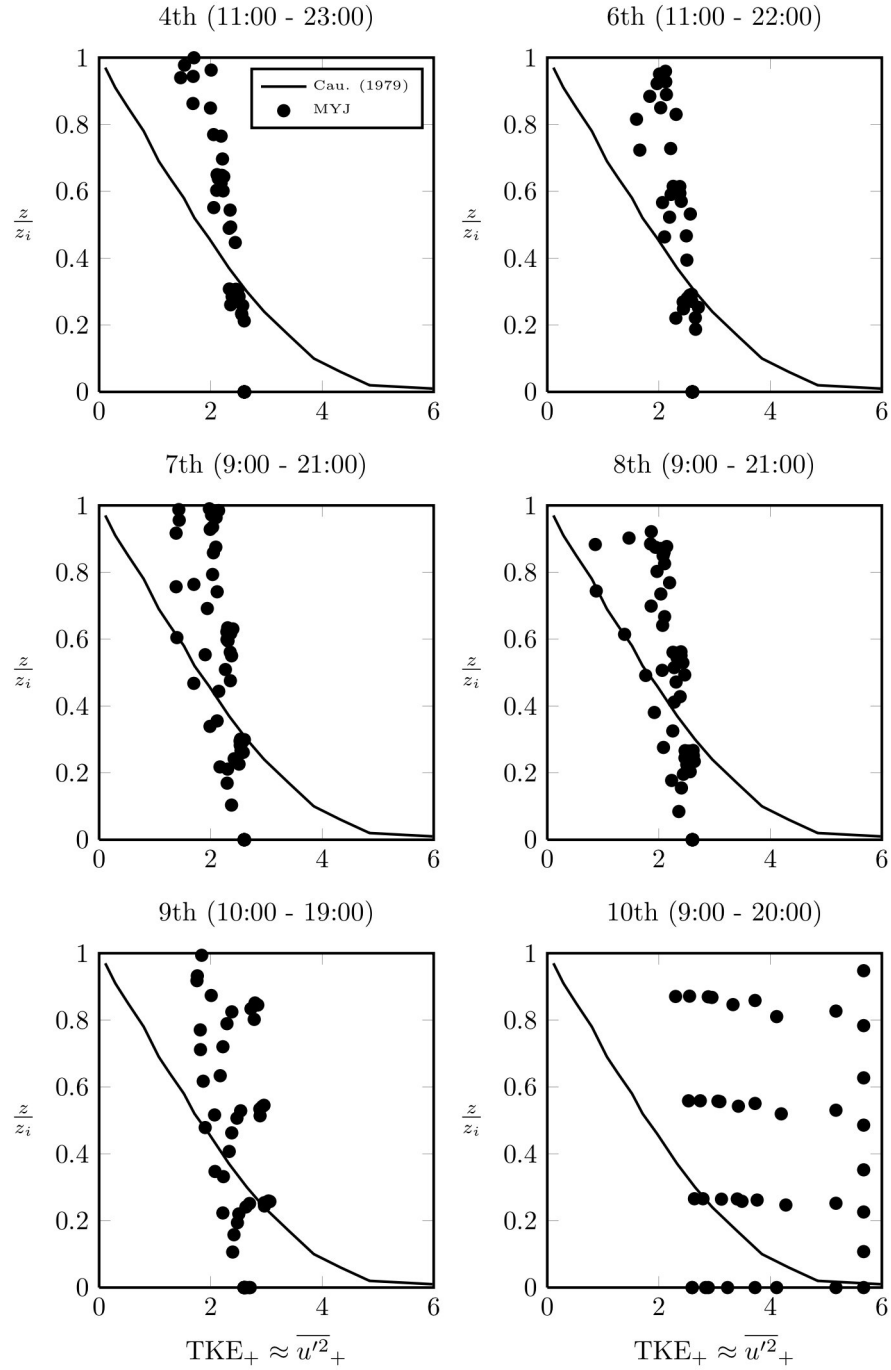


Figure 4.13: Scaled TKE (TKE_+) as calculated by the MYJ model assuming $TKE \approx \overline{u'^2}$. The periods here correspond with those in Fig. 4.9 above.

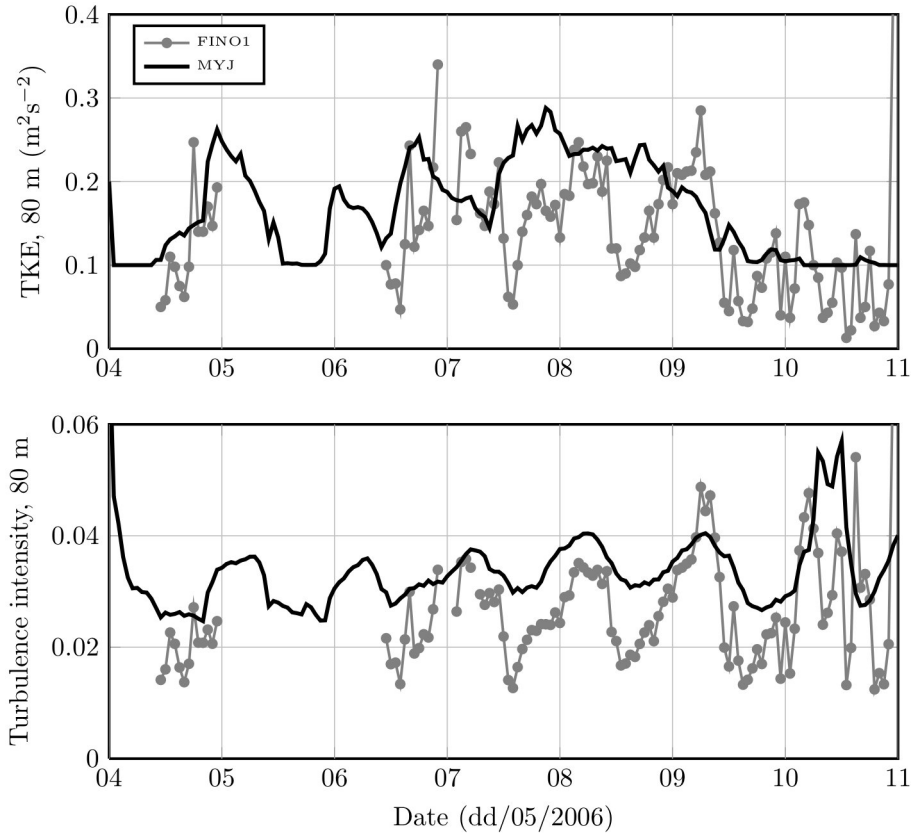


Figure 4.14: Absolute TKE and turbulence intensity as measured at FINO1 and calculated by the MYJ model.

by the MYJ model is also underpredicted. While the TKE is underpredicted close to the surface, the model overshoots the TKE towards the middle of the boundary layer and hence will overpredict the magnitude of the TKE as $z \rightarrow z_i$. Since the majority of the measurements at FINO1 during this period are towards the top of the boundary layer, the result is an overprediction of TKE as evident in the time series displayed in Fig. 4.14 (top).

Remembering though that the wind speed was underestimated by the model (see previously in Fig. 4.5) and hence so too the friction velocity, then from eq. (4.14), the TKE is fortuitously closer to the measurements (but nonetheless too high in general). The turbulence intensity on the other hand, in addition to being a practically relevant parameter in the assessment of the expected wind turbine power output, can be used somewhat to normalise this effect out and is defined here as

$$Ti = \frac{\sqrt{\text{TKE}}}{U_{80}}. \quad (4.27)$$

Here, U_{80} is the 80 m horizontal wind speed. In this way, Fig. 4.14 (bottom) displays a consistent overprediction of the turbulence intensity by the MYJ model in comparison with the measurements.

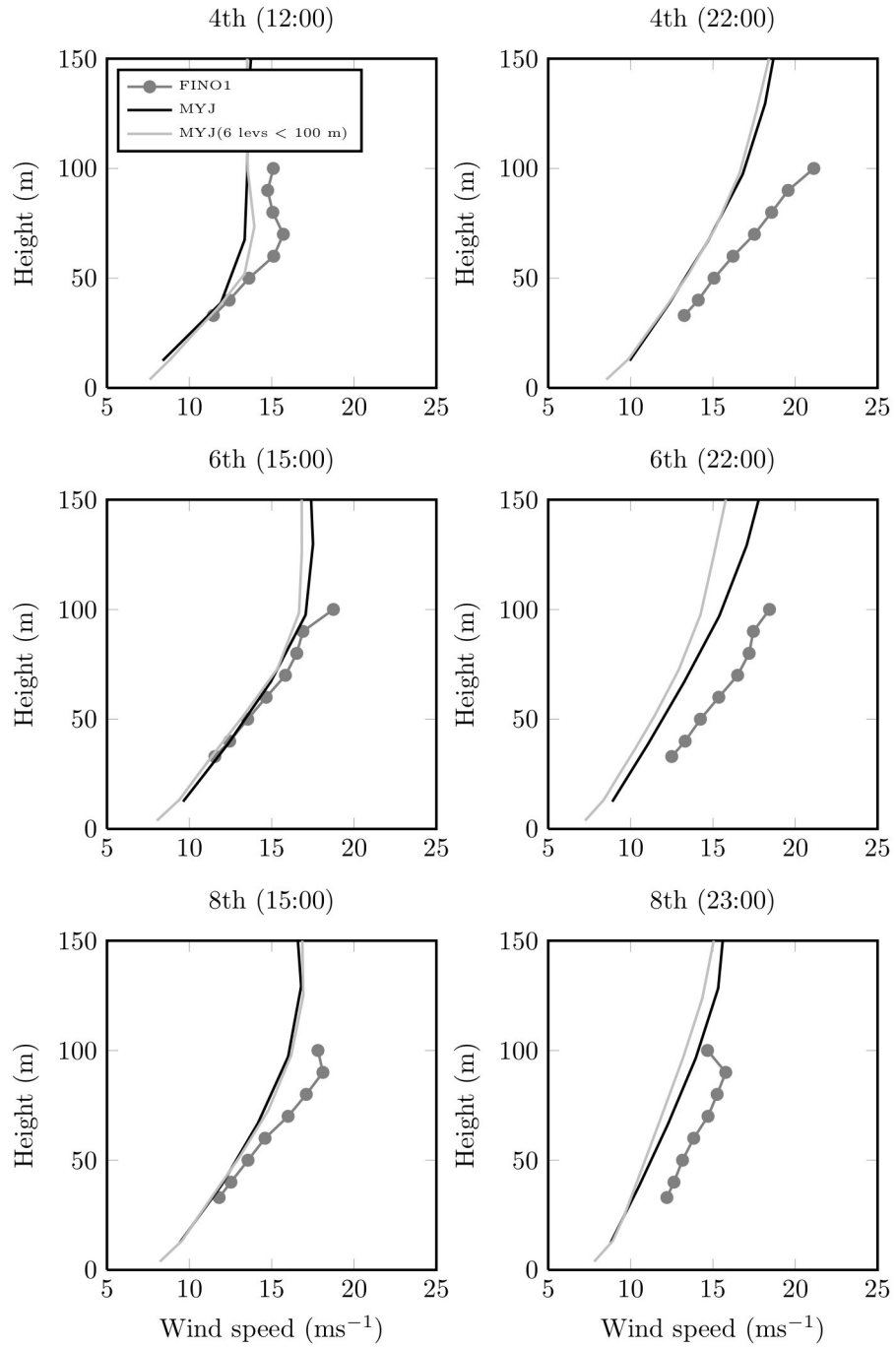


Figure 4.15: Velocity profiles at FINO1 during the 4th (top), 6th (middle) and 8th (bottom) at various times in comparison with the MYJ model and when using an extra 6 levels less than 100 m.

Since the decay of TKE with height is underpredicted by the model, the wind shear is correspondingly underpredicted as demonstrated by comparing wind profiles during the 4th, 6th and 8th at 15:00 and 23:00 in Fig. 4.15. There, the MYJ model, in addition to a version using a few more vertical levels below 100 m, show a similar underestimated wind shear, except for perhaps on the 6th at 15:00. The wind shear and the vertical structure of TKE are connected via the TKE equation as presented above in eq. (4.12), whose interaction also depends on buoyancy, dissipation and pressure transport which have all been parametrised within the model. While these parameterisations may not suffice here and there are more complex models available (e.g. Nakanishi, 2001) than that employed by the MYJ model, it appears that a significant improvement in the calculation of wind speeds and turbulence intensity is possible by merely changing the model boundary conditions as defined by eq. (4.14). This will be the topic of investigation in the next chapter.

4.5 Conclusions

A period during spring with relatively steady and strong easterly winds brought dry and warm air to FINO1. The cold water in the North Sea, some 10°C cooler than the air above resulted in a low level temperature inversion preventing the vertical exchange of mass and momentum between the air close to the surface and that above the inversion. The height of the inversion was O(100 m) throughout this period, where the FINO1 tower sat just below it. FINO1 was however sometimes high enough to detect low level wind speed maxima (a low level jet) when the inversion was low enough. A low level jet has been measured previously in a comparable offshore flow by Brooks and Rogers (2000) using a research aircraft in the Persian Gulf, where a similar relationship between the LLJ and inversion height was evident.

There was some success in scaling the streamwise variances using outer layer scaling despite the absence of either the characteristic velocity scale (u_*) or the outer length scale (z_i). Both of these had to be estimated using indirect means, i.e. eqs. (4.6) and (4.21), respectively. In comparison with the FINO1 measurements, the WRF model showed a consistently underpredicted hub height wind speed throughout the period, independent from the temperature difference between the land and sea. Very broadly, the roughness lengths could be relatively well predicted by the model, but this conclusion rests on the particular wave aspect ratio scaling regime during this period (see the previous chapter). The complexity of accurately determining offshore roughness lengths has been clearly demonstrated here where estimates of the drag coefficient using the correlation of the previous chapter show that C_{D10n} will to a higher order depend on the rate of change of the angle between of the wind and the waves. Now that there are a number of dedicated offshore towers for wind energy research, periods such as these detected at FINO1 could prove highly useful in the future for fundamental air-sea interaction research. Although it is noted that the alpha ventus wind farm installed to the east of FINO1 in 2009, would now disturb a similar flow.

The Mellor-Yamada-Janjić (MYJ) boundary layer parameterisation was employed within the WRF model which uses a single prognostic equation for the turbulent kinetic energy (TKE) in order to anticipate exchange coefficients, and

consequently to parametrise the subgrid turbulent fluxes. The TKE as calculated by the MYJ model, when scaled using the same scaling employed on the FINO1 measurements, indicated that the magnitude of turbulence would be underpredicted close to the surface and overpredicted towards the top of the boundary layer by the model. This resulted in a consistent overprediction of the hub height turbulence intensity, since the hub height in this flow is positioned towards the height of the boundary layer.

If one can generalise these results to other cases, it is suggested that the MYJ model will underestimate the TKE close to the surface and overestimate it towards the top of the boundary layer in stable stratification. This could well be that the boundary conditions (i.e. the closure constants) of the MYJ simply need to be adjusted. This will be a topic of the next chapter, where an improved profile of TKE will be sought, resulting in improved wind speed profiles to be demonstrated in Chapter 6.

Chapter 5

Mellor-Yamada-Janjić model modifications in WRF

5.1 Introduction

In the previous chapter it was found that the vertical structure of the turbulent kinetic energy (TKE) as anticipated by the Mellor-Yamada-Janjić (MYJ) scheme in the Weather Research and Forecasting (WRF) model appeared inconsistent with the expected behaviour of a conventionally stable boundary layer. This was found by applying outer layer scaling,

$$\overline{u'^2}_+ = f\left(\frac{z}{z_i}\right), \quad (5.1)$$

to measurements at FINO1, where the height of the internal boundary layer was used for outer length scale z_i . Outer layer scaling which is valid further from the surface can be contrasted with inner layer scaling which assumes,

$$\overline{u'^2}_+ = f\left(\frac{zu_*}{\nu}\right), \quad (5.2)$$

where here z is normalised by the inner length scale $\frac{\nu}{u_*}$ (and will be labelled as z_+ below). However, inner layer scaling for $\overline{u'^2}_+$ has in the past been questioned (e.g. Fernholz and Finley, 1996) and recently demonstrated to be in contradiction to the measurements (DeGraaff and Eaton, 2000; Hutchins et al., 2009).

The closure constants for Mellor-Yamada models (defined below) as set out by Mellor and Yamada (1982) have however been based on inner layer scaling. Nonetheless, Mellor and Yamada (1982) noted that their model is relatively more simple than others appearing in the literature and in addition to this, its success could possibly also be attributed to the ease with which the closure constants are found, albeit from neutral laboratory measurements of quantities based on eq. (5.2). The analysis of Wichmann and Schaller (1986) finds that for all models employing the same closure assumptions as Mellor and Yamada (1982), i.e. for turbulence and temperature dissipation from Kolmogorov (1942) and pressure-strain and temperature covariances from Rotta (1951), the closure constants

reduce to comparable values. More complex parametrizations for pressure-strain and pressure-temperature covariances exist such as that by Andr en (1990) and Nakanishi (2001) but this requires the specification of further closure constants, where Nakanishi (2001) employs a large eddy simulation for that purpose. The limited number of closure constants (and thus assumptions) was one of the key reasons Mellor and Yamada (1982) kept their model relatively simple in the first place.

It could be asked why should one look at this now since the Mellor-Yamada model is a well established approach and more advanced models are available than that proposed by Mellor and Yamada (1982) (e.g. from Nakanishi and Niino, 2004, 2006). One answer to that is that more advanced models such as those by Nakanishi (2001) also rely on the same inner scaling as that of Mellor and Yamada (1982). Furthermore, although the paper is five years old at the time of writing, by inspecting the models, including both operational and research, that took part in the intercomparison described in Cuxart et al. (2006), it is apparent that roughly half, and most of the operational models, use a “first-order closure” which is even simpler than the 1.5 order closure of Mellor and Yamada (1982). The other half use a diagnostic equation for the TKE as with the Mellor-Yamada model and a few (all research) use a prognostic equation for dissipation as is common in engineering applications. The likely reason for this is that, as Cuxart et al. (2006) point out, and as has been stated previously with respect to the work of Warner (2011), boundary layer parametrizations need also to be able to interact with other parametrizations and hence more complex models that rely on more parametrizations will likely complicate this interaction.

The aim here thus is to gain some improvement in both mean and turbulent fields without the added cost of too much extra complexity. While the broader aim here is to improve the calculation of offshore wind profiles and turbulence intensity, the hope is that the results here will also be useful for other more general meteorological applications, including climatology where a minimal computational burden is perhaps more critical.

In the following chapter, a simple method of improving the calculation of TKE in the MYJ-WRF model will be demonstrated. The equations governing the basis of the MYJ model, including the closure assumptions, will be first introduced and then a strategy for modifying these assumptions will be employed. The modified model will then be tested in the single column model within WRF to ensure the modifications here give a realistic behaviour before being tested in the next chapter on some real simulations, including the May 2006 case presented in the previous chapter.

5.2 Description of the MYJ model

The Mellor-Yamada-Janji c model is the current incarnation of the Mellor-Yamada model in WRF as introduced and elaborated in Mellor (1973), Mellor and Yamada (1974), Yamada and Mellor (1975) and Mellor and Yamada (1982). Following Mellor and Yamada, Janji c (1990), Janji c (1994) and Janji c (2002) has since worked to incorporate the model in mesoscale models, thus requiring closer attention to, in particular, numerical instabilities that arose with the traditional version.

In the context of turbulent closure schemes, the MYJ model is classified as a 1.5 order meaning that only some of the terms in the Reynolds stress matrix,

$$\begin{pmatrix} \overline{u'^2} & \overline{u'v'} & \overline{u'w'} \\ \overline{v'u'} & \overline{v'^2} & \overline{v'w'} \\ \overline{w'u'} & \overline{w'v'} & \overline{w'^2} \end{pmatrix}, \quad (5.3)$$

are parametrized in the sense that a diagnostic, as opposed to a prognostic, equation is formed. A further four terms are also required for covariances and the variance of temperature. In a first order model (Stull, 1988), all terms in (5.3) are parametrized and one is left merely with prognostic equations for the wind speed, i.e.

$$\frac{\partial U}{\partial t} = f_c (V - V_g) - \frac{\partial \overline{u'w'}}{\partial z}, \quad (5.4)$$

$$\frac{\partial V}{\partial t} = -f_c (U - U_g) - \frac{\partial \overline{v'w'}}{\partial z}, \quad (5.5)$$

and virtual potential temperature (and water vapour)

$$\frac{\partial \Theta_v}{\partial t} = -\frac{\partial \overline{w'\theta'_v}}{\partial z}. \quad (5.6)$$

Here, U and V are east-west and north-south wind speeds, U_g and V_g are east-west and north-south geostrophic wind speeds, f_c is the coriolis parameter, θ_v is the virtual potential temperature, u' , v' and w' are velocity fluctuations, t is time and z is the vertical coordinate. In a second order model, all terms in eq. (5.3) are prognostic and as one can imagine, the computational burden of such a model is relatively larger.

A second order model corresponds to a “level 4” model in the hierarchy of Mellor and Yamada (1974) containing the full 10 equations for the terms in (5.3), including the temperature variance, but was found to give similar results with the “level 3” model. The level 3 model contains only terms for the trace of (5.3) (twice the TKE) and the temperature variance, and thus represents a significant numerical improvement, while not losing too much in the way of physics (Yamada and Mellor, 1975). A further sacrifice to Mellor and Yamada (1974)’s analysis was to reject the temperature variance equation (now a level 2.5 model), since with the addition of extra scalars such as water vapour leading to further equations such as temperature-vapour covariances, the number of extra equations “gets out of hand” (Mellor and Yamada, 1982). For example, the approach of Andre et al. (1978) leads to 33 prognostic equations after accounting for triple covariances.

The level 2.5 Mellor-Yamada model, which is now a bare minimum to be classified as 1.5 order closure, has a sole prognostic equation for TKE, where (Mellor and Yamada, 1982)

$$\frac{D}{Dt} \left(\frac{q^2}{2} \right) - \frac{\partial}{\partial z} \left[\ell q S_q \frac{\partial}{\partial z} \left(\frac{q^2}{2} \right) \right] = -\overline{u'w'} \frac{\partial U}{\partial z} - \overline{v'w'} \frac{\partial V}{\partial z} + \frac{g}{\theta} \overline{w'\theta'} - \epsilon. \quad (5.7)$$

Here, S_q is a constant, $\frac{q^2}{2}$ is the TKE and the turbulence dissipation is parametrized as

$$\epsilon = \frac{q^3}{\ell B_1}, \quad (5.8)$$

where B_1 is a closure constant and ℓ is the ‘‘master length scale’’ appearing in all diagnostic parametrizations. The diagnostic equation for the temperature variance is

$$\overline{\theta'^2} = -\frac{B_2 \ell}{q} \overline{w' \theta'} \frac{\partial \theta}{\partial z} \quad (5.9)$$

with B_2 a further constant, where the other closure constants A_1, A_2, C_1 appear in diagnostic terms in (5.3) and velocity-temperature covariances (9 terms), e.g. (Mellor and Yamada, 1982)

$$\overline{u'^2} = \frac{q^3}{3} + \frac{A_1 \ell}{q} \left[-4 \overline{w' u'} \frac{\partial U}{\partial z} + 2 \overline{w' v'} \frac{\partial V}{\partial z} - 2 \frac{g}{\theta} \overline{w' \theta'} \right], \quad (5.10)$$

$$\overline{v'^2} = \frac{q^3}{3} + \frac{A_1 \ell}{q} \left[2 \overline{w' u'} \frac{\partial U}{\partial z} - 4 \overline{w' v'} \frac{\partial V}{\partial z} - 2 \frac{g}{\theta} \overline{w' \theta'} \right], \quad (5.11)$$

$$\overline{w'^2} = \frac{q^3}{3} + \frac{A_1 \ell}{q} \left[2 \overline{w' u'} \frac{\partial U}{\partial z} + 2 \overline{w' v'} \frac{\partial V}{\partial z} + 4 \frac{g}{\theta} \overline{w' \theta'} \right], \quad (5.12)$$

$$\overline{u' w'} = \frac{A_1 \ell}{q} \left[-\left(\overline{w'^2} - C_1 q^2 \right) \frac{\partial U}{\partial z} + \frac{g}{\theta} \overline{w' \theta'} \right] \quad (5.13)$$

and

$$\overline{w' \theta'} = \frac{3 \ell A_2}{q} \left[-\overline{w'^2} \frac{\partial \theta}{\partial z} + \frac{g}{\theta} \overline{\theta'^2} \right]. \quad (5.14)$$

Here, ℓ is the master length scale defined below. Further equations for $\overline{v' w'}$, $\overline{u' v'}$, $\overline{u' \theta'}$, $\overline{v' \theta'}$ are not repeated here.

The closure constants A_1, A_2, B_1, B_2, C_1 are not independent from each other, but rather, after simplifying eqs. (5.10), (5.11) and (5.12) by assuming neutrality and $\frac{\partial V}{\partial z} = 0$, give (Mellor, 1973)

$$\overline{u'^2} = (1 - 2\gamma_1) q^2, \quad (5.15)$$

$$\overline{v'^2} = \gamma_1 q^2 \quad (5.16)$$

and

$$\overline{w'^2} = \gamma_1 q^2, \quad (5.17)$$

where

$$\gamma_1 = \frac{1}{3} - 2 \frac{A_1}{B_1}. \quad (5.18)$$

The equality of $\overline{v'^2}$ and $\overline{w'^2}$ is, as Mellor and Yamada (1982) found, not supported by measurements. Attempting to readjust this within the model apparently introduces additional closure assumptions (Mellor and Yamada, 1982). This is pointed out here for it is the unrealistic assumption of equality between $\overline{v'^2}$ and $\overline{w'^2}$ that will be exploited further below when modifying the MYJ model.

The master length scale is defined within the model as

$$l = l_o \frac{l_s}{l_s + l_o}, \quad (5.19)$$

where

$$l_o = \alpha \frac{\int z q dz}{\int q dz}. \quad (5.20)$$

Here, α is an empirical constant set to 0.3 and the surface length scale, $l_s = \kappa z$, where κ is von Karman's constant ($= 0.4$) and z is the height above ground. Hence, given

$$\frac{\partial U}{\partial z} = \frac{u_*}{l_s}, \quad (5.21)$$

which with in addition to assuming turbulence production and dissipation are balanced, i.e.

$$\epsilon = -\frac{\partial U}{\partial z} \overline{u'w'}, \quad (5.22)$$

results, with eq. (5.8), in

$$B_1 = \frac{q^3}{u_*^3}, \quad (5.23)$$

where $-\overline{u'w'} = u_*^2$.

Given the relationship between A_1 and B_1 via eq. (5.18), then the other constants are given by Mellor and Yamada (1982) as

$$C_1 = \gamma_1 - \frac{1}{3A_1} B_1^{1/3}, \quad (5.24)$$

$$A_2 = \frac{A_1 (\gamma_1 - C_1)}{\gamma_1 \text{Pr}} \quad (5.25)$$

and

$$B_2 = \frac{B_1^{1/3} u_*^2 \overline{\theta'^2}}{\text{Pr} \overline{w' \theta'^2}}. \quad (5.26)$$

In the planetary boundary layer scheme itself (Janjić, 2002), the length scale defined by eq. (5.19) is calculated first so that eq. (5.7) can be stepped forward in time. The exchange coefficients, defined according to

$$K_{m,h} = \ell q S_{m,h} \quad (5.27)$$

are then calculated where $S_{m,h}$ are stability functions found by solving the algebraic equations, e.g. for $\overline{u'^2}$, $\overline{w'^2}$, etc (Mellor and Yamada, 1982). With $K_{m,h}$ defined, the mean variables can be diffused vertically as outlined in Janjić (1990), whereby each time-step a tendency term is then sent back to the dynamical core to be incorporated into the full equations of motion (i.e. see the momentum equation in Chapter 1).

While all this is being performed, the model constants A_1, A_2, B_1, B_2, C_1 are, as the name suggests, kept constant. For this to be possible, eq. (5.23) shows that for the purposes of calculating B_1 and hence all constants because they are interrelated, the Mellor-Yamada model is relying on inner layer similarity as discussed above. That is, it is assuming that all terms in (5.3) are constant within the surface layer (Mellor, 1973) independent of the Reynolds number. However, as shown in DeGraaff and Eaton (2000), this does not appear to be true for at least the streamwise velocity variance and hence is Reynolds number dependent. Since the constants are traditionally based on laboratory measurements (Mellor and Yamada, 1982), Reynolds number similarity is assumed as the constants are then applied in the surface layer with many more orders of magnitude of Reynolds number greater than can be measured without any great difficulty in the laboratory (Metzger et al., 2007; Marusic et al., 2010). The next section will

analyse the choices made by Mellor and Yamada (1982) and then suggest an alternative, practical strategy for their definition. The broader aim here is to enhance the calculation of TKE so that this information, along with the mean wind speed, can eventually be used in assessing wind farm power output for reasons already discussed in the opening chapter.

5.3 Determination of the closure constants

In the following section, the traditional approach for determining the closure constants by Mellor and Yamada (1982) will be reviewed. This is still relevant since the procedure has been repeated by Janjić (2002) in the more recent model version. An alternative strategy will then be proposed for the purposes of enhancing the calculation of TKE. Testing of this alternative strategy will be delayed until the next section, where results here are tested within WRF's single column model.

5.3.1 Traditional approach

Mellor and Yamada (1982) determined the magnitudes of the closure constants from classical neutrally stratified laboratory measurements (e.g. Laufer, 1954; Klebanoff, 1955) in regions where the assumption of production and dissipation apply (i.e., eq. (5.22)). For boundary layers, this is close to the wall, yet still within the logarithmic layer such that the integrated eq. (5.21), the logarithmic velocity profile, applies. For example, the figure 1 of Mellor and Yamada (1982) displaying pipe measurements for increasing Reynolds numbers according to Perry and Abell (1975) (their figure 7) is shown as an adapted version here in Fig. 5.1 (left) illustrating the hypothesised collapse (inner layer similarity, eq. (5.2)) of measurements in the region where $z_+ \sim 100$ (i.e. at the beginning of the logarithmic velocity profile region).

For the range of measurements in pipes, channels, boundary layers and homogeneous shear flows, Mellor and Yamada (1982) decided on a value for $\overline{u'^2}_+ = 3.61$, a bit lower than that found from the measurements of Perry and Abell (1975). The horizontal line in Fig. 5.1 (left) corresponds with $\overline{u'^2}_+ = 4.49$. Further selections are required for the lateral and vertical velocity variances, which by eqs. (5.16) and (5.17), are assumed to be equal, where Mellor and Yamada (1982) chose $\overline{v'^2}_+ = \overline{w'^2}_+ = 1.44$. Combining all velocity components thus gives $q_+^2 = 6.5$, which from eq. (5.23), gives $B_1 = 16.6$. By making additional assumptions for the neutral Prandtl number ($Pr = 0.8$) and the dimensionless heat flux, $\left(\frac{\overline{w'\theta'^2}}{u_+^2\theta'^2} = 0.32\right)$, eqs. (5.18) and (5.24) to (5.26) lead to

$$(A_1, A_2, B_1, B_2, C_1) = (0.92, 0.74, 16.6, 10.1, 0.08). \quad (5.28)$$

Inner layer similarity can be contrasted to the scaling proposed by Marusic et al. (1997) and Marusic and Kunkel (2003) based on the ideas of Townsend (1976) who instead write

$$\overline{u'^2}_+ = f_1(y_+,) f_2(y_+, \delta_+), \quad (5.29)$$

where δ_+ is a Reynolds number equal to $\frac{\delta u_*}{\nu}$, where δ is the outer length scale and f_1 and f_2 are functional dependencies found to match the measurements of

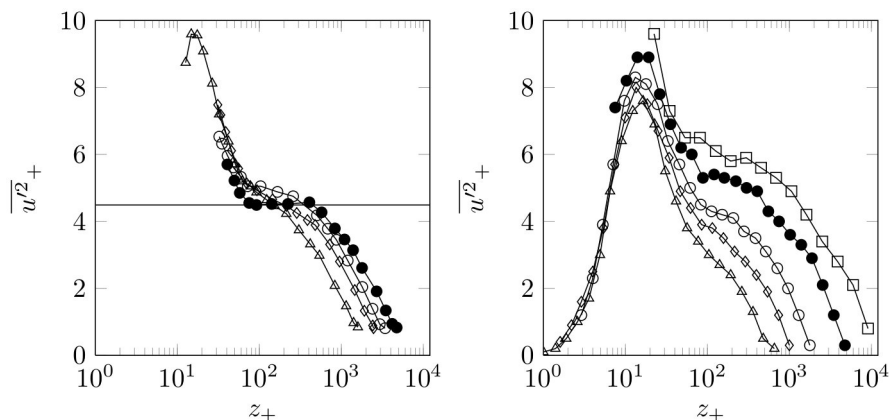


Figure 5.1: Left: Adapted from the figure 1 of Mellor and Yamada (1982) interpreting the measurements of scaled horizontal velocity fluctuations as reported by Perry and Abell (1975) (their figure 7) for different Reynolds numbers. The horizontal line corresponds with $\overline{u'^2}_+ = 4.49$. Right: Adapted from the figure 7 (top) of DeGraaff and Eaton (2000) showing measurements for a range of Reynolds numbers and a lack of an obvious choice for $\overline{u'^2}_+$.

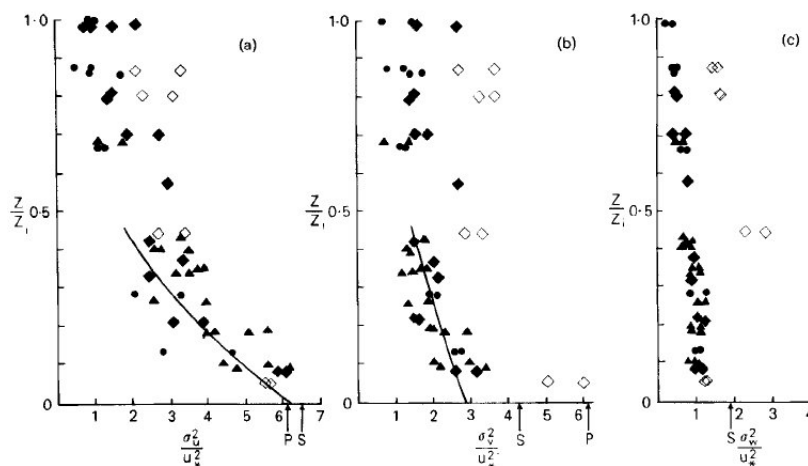


Figure 5.2: The figure 5 of Grant (1986) showing aircraft measurements of horizontal (a), lateral (b) and vertical (c) variances ($\sigma_{u,v,w}^2$) normalised by the friction velocity and plotted against the height, z which itself has been normalised by the boundary layer height, z_i . The “P” and “S” along the horizontal axis refer to the measurements of Panofsky et al. (1977) and Smith (1980), respectively. The solid lines are based on the aircraft measurements of Nicholls and Readings (1979).

DeGraaff and Eaton (2000) shown in Fig. 5.1 (right). It can be seen in Fig. 5.1 (right), in contrast to the measurements of Perry and Abell (1975) that there is no clear choice for $\overline{u'^2}_+$. Eq. (5.29) which is valid for $z_+ < 150$ and

$$\overline{u'^2}_+ = f_3(y_+, \delta_+), \quad (5.30)$$

which is valid for $z_+ > 150$ have been shown to be applicable by Kunkel and Marusic (2006) to both laboratory and atmospheric (over homogeneous desert terrain in neutral stratification) measurements.

It turns out, as demonstrated in Hutchins et al. (2009) that there has been a significant lack of spatial resolution in high Reynolds number laboratory measurements over the years that results in the sort of plots shown above in Fig. 5.1 (left). There are two competing effects in such measurements: as the Reynolds number increases, finer scales of motion carry more energy than at lower Reynolds numbers, which in order to properly measure, correspondingly requires smaller measurement probes. With insufficiently sized measurement probes, turbulent variables are underestimated with increasing Reynolds numbers which can result in an apparent collapse of normal stress profiles in inner scaling. Hence in Fig. 5.1 (left), there is unlikely a high enough Reynolds number nor a sufficient probe resolution to obtain the results shown in Fig. 5.1 (right).

In contrast to laboratory measurements at relatively low Reynolds numbers, we have the experience of neutral atmospheric boundary layers of very high Reynolds numbers, much larger than that possible in the laboratory. For example, shown in Fig. 5.2 (the figure 5 in Grant (1986)) are the aircraft observations over sea of Grant (1986) of $\overline{u'^2}_+$, $\overline{v'^2}_+$ and $\overline{w'^2}_+$ as a function of height normalised by the boundary layer height. Fig. 5.2 shows the measurements from the perspective of outer layer scaling, i.e. eq. (5.1) which are believed to collapse measurements further from the surface (Kunkel and Marusic, 2006). Also included in Fig. 5.2 are the aircraft measurements of Nicholls and Readings (1979) and surface based measurements of Smith (1980) and Panofsky et al. (1977).

Whereas Mellor and Yamada (1982) assume $\overline{u'^2}_+ = 3.61$, it is evident from Fig. 5.2 that $\overline{u'^2}_+$ in practice sits somewhere between 6 and 7, depending on the author (which could be either experimental uncertainty and/or Reynolds number effects). Therefore, one would expect that the constants chosen by Mellor and Yamada (1982) model will, depending on the boundary layer height, underpredict the TKE close to the surface given a correctly calculated friction velocity. For that reason, it will be investigated whether the TKE in the model can be simply increased and then to what degree the model constants can be modified and made functionally dependent on, e.g., the Reynolds number. For that purpose, an alternative strategy to that employed by Mellor and Yamada (1982) will be proposed in the next subsection and then tested in the single column model further below.

5.3.2 Alternative strategy to the traditional approach

Officially, the model closure constants are based on neutral laboratory measurements as described above. However in practice there are some physical constraints to how the constants can be defined. One of these constraints is governed by Monin-Obukhov similarity theory since in steady conditions, the

model can be, as will be shown below, reduced to dimensionless gradients (Mellor, 1973). There is also the issue of the critical Richardson number above which turbulence ceases and the model is constrained numerically to prevent unphysical solutions (Janjić, 2002). Both of these aspects of the model are dependent on the specification of the closure constants, which in the current version are different from that specified by Mellor and Yamada (1982). In this subsection, after introducing the model constraints, an alternative strategy to Mellor and Yamada (1982) and correspondingly Janjić (2002) will be introduced for the purposes of enhancing the TKE in the model.

5.3.2.1 Practical constraints

Dimensionless gradients A practical constraint to how the MYJ closure constants can be defined can be seen by nondimensionalising and simplifying (neglecting terms to the left of eq. (5.7)) the model equations according to Mellor (1973) and Nakanishi (2001) giving

$$\Phi_m \left[\gamma_1 - C_1 - (6A_1 + 3A_2) \frac{\zeta \ell_s}{q_*^3 \kappa z} \right] - \Phi_h \left[3A_2 \frac{\zeta \ell_s}{q_*^3 \kappa z} \right] = \frac{1}{3A_1 q_*} \frac{\kappa z}{\ell_s} \quad (5.31)$$

and

$$\Phi_h \left[\gamma_1 - (6A_1 + B_2) \frac{\zeta \ell_s}{q_*^3 \kappa z} \right] = \frac{1}{3A_2 q_*} \frac{\kappa z}{\ell_s}, \quad (5.32)$$

where

$$q_*^3 = B_1 \frac{\ell_s}{\kappa z} (\Phi_m - \zeta) \quad (5.33)$$

and reduces to eq. (5.23) in neutral stratification assuming $\ell_s = \kappa z$. As used in Chapter 2,

$$\Phi_m = \frac{\kappa z}{u_*} \frac{\partial U}{\partial z} \quad (5.34)$$

and

$$\Phi_h = \frac{\kappa z}{\theta_*} \frac{\partial \Theta}{\partial z}, \quad (5.35)$$

where $\theta_* = \overline{\theta'w'}/u_*$.

The constraint here to be demonstrated below is that increasing B_1 higher than that specified in Mellor and Yamada (1982) significantly worsens the calculation of Φ_m in stable stratification. This was one of the reasons that in the latest version, i.e. the Mellor-Yamada-Janjić model, that Janjić (2002) also chose

$$(A_1, A_2, B_1, B_2, C_1) = (0.660, 0.657, 11.878, 7.227, 0.00083), \quad (5.36)$$

which also gives $\Phi_h > \Phi_m$ in stable stratification. The value of B_1 here is 11.878 in comparison with the 16.6 in Mellor and Yamada (1982). The other reason is a significantly higher critical Richardson number obtained with (5.36) compared with the values selected by Mellor and Yamada (1982), as will be also shown below.

The unphysical behaviour of Φ_m and Φ_h in stable stratification if B_1 is too high can be demonstrated in Fig. 5.3 where B_1 has been set to 26.0 based on the measurements of Österlund (1999) and Carlier and Stanislas (2005) as shown in Table 5.1, giving

$$(A_1, A_2, B_1, B_2, C_1) = (1.733, 0.703, 26.000, 11.48, 0.135), \quad (5.37)$$

Table 5.1: Turbulence statistics from some recent laboratory boundary layer experiments by Österlund (1999) and Carlier and Stanislas (2005) and a years worth of measurements at FINO1. The magnitude of γ_1 is based on either eq. (5.15), (5.16) or (5.17) for $\overline{u'^2}$, $\overline{v'^2}$ and $\overline{w'^2}$, respectively.

Author	$\gamma_1(\overline{u'^2})$	$\gamma_1(\overline{v'^2})$	$\gamma_1(\overline{w'^2})$	$B_1 = \frac{q^3}{u_*^3}$
Österlund (1999)	0.20	0.27	0.15	26.2
Carlier and Stanislas (2005)	0.20	0.26	0.12	25.9
FINO1 (2005)	0.23	0.32	0.14	?

where $\gamma_1 = 0.2$. This is not unlike the value for γ_1 selected by Mellor and Yamada (1982) where, $\gamma_1 = 0.222$. With this set of constants, Φ_m and Φ_h have been calculated according to eqs. (5.31) and (5.32) with the result displayed as triangles in Fig. 5.3. For comparison, dimensionless gradients according to Businger et al. (1971),

$$\Phi_m = 1 + 4.7\zeta \quad (5.38)$$

and

$$\Phi_h = 0.74 + 4.7\zeta, \quad (5.39)$$

are displayed as solid lines.

Fig. 5.3 shows that the calculation of Φ_m and Φ_h are drastically over- and underestimated, respectively in stable stratification with the constants in eq. (5.37). The other cases in this figure will be explained below. The performance is also made poorer on the unstable side as can be seen in Fig. 5.4, where also after Businger et al. (1971)

$$\Phi_m = (1 - 15\zeta)^{-1/4} \quad (5.40)$$

and

$$\Phi_h = (1 - 9\zeta)^{-1/2}. \quad (5.41)$$

The existing model also underpredicts Φ_m on the unstable side, possibly because the Mellor and Yamada (1982) parametrization itself is too simple.

Critical Richardson number It can be seen in Fig. 5.3 that the constants in (5.37) give physically unrealistic dimensionless gradients for Φ_m and Φ_h . A gradient Richardson number is

$$Ri = \frac{\frac{g}{\theta} \frac{\partial \theta}{\partial z}}{\left(\frac{\partial U}{\partial z}\right)^2 + \left(\frac{\partial V}{\partial z}\right)^2}, \quad (5.42)$$

and is related to the flux Richardson number

$$Ri_f = \frac{\frac{g}{\theta} \overline{w'\theta'}}{\overline{w'u'} \frac{\partial U}{\partial z}}, \quad (5.43)$$

via

$$Ri = \frac{S_m}{S_h} Ri_f. \quad (5.44)$$

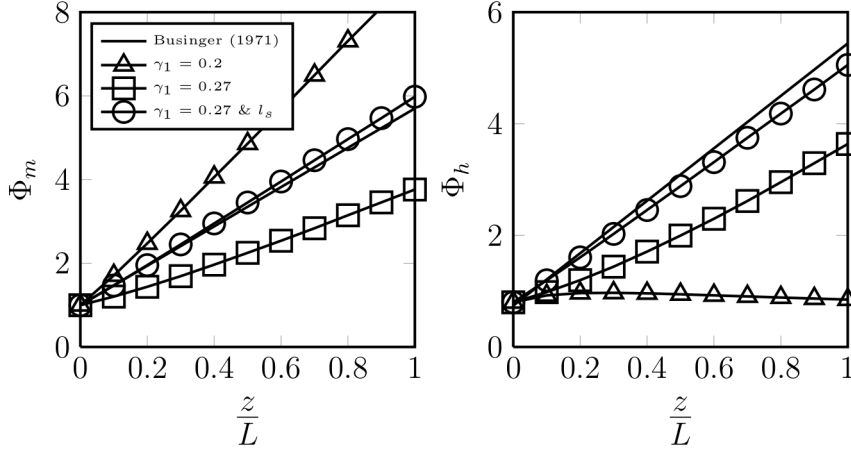


Figure 5.3: Calculation of Φ_m and Φ_h in stable stratification according to eqs. (5.31) and (5.32) for various γ_1 and surface length scale, ℓ_s as defined in the text.

When S_m and S_h are zero, then the modelled critical Richardson number gives Mellor and Yamada (1982)

$$Ri_c = \frac{\gamma_1}{\gamma_1 + \gamma_2}, \quad (5.45)$$

where γ_1 has been defined above in eq. (5.18) and $\gamma_2 = \frac{B_2}{B_1} + \frac{6A_1}{B_1}$. According to eq. (5.45), the constants in (5.37) give a critical Richardson number of 0.19, similar to that found by Mellor and Yamada (1982) for their numbers (see eq. (5.28)).

However, a more detailed analysis of the model equations by Janjić (2002) found that eq. (5.45) is rather

$$Ri_c = -\frac{a_H}{a_M}, \quad (5.46)$$

where

$$a_H = \frac{g}{\theta} [9A_1A_2^2B_1 + 9A_1A_2^2(12A_1 + 3B_2)] \quad (5.47)$$

and

$$a_M = 3A_1A_2B_1(3A_2 + 3B_2C_1 + 18A_1C_1 - B_2) + 18A^2A_2(B_2 - 3A_2). \quad (5.48)$$

Eq. (5.46) gives 0.19 again for Mellor and Yamada (1982), but for (5.37), a negative critical Richardson number of -0.423 is found, confirming the physically unrealistic behaviour illustrated in Fig. 5.3. Janjić (2002) has since put numerical constraints on the length scale, ℓ and TKE to prevent physically unrealistic solutions such as found for constants (5.37) for Richardson numbers greater than -0.423. In practice, this results in near constant exchange coefficients throughout the boundary layer (see below), and hence such a parametrization will be unsatisfactory in anticipating many of the features of a stable boundary layer (Stull, 1988). According to eq. (5.46), Janjić (2002)'s constants (eq. 5.36) give $Ri_c = 0.505$ and thus possibly advantageous over those of Mellor and Yamada (1982) in that turbulence can be produced in flows where $Ri_c > 0.19$.

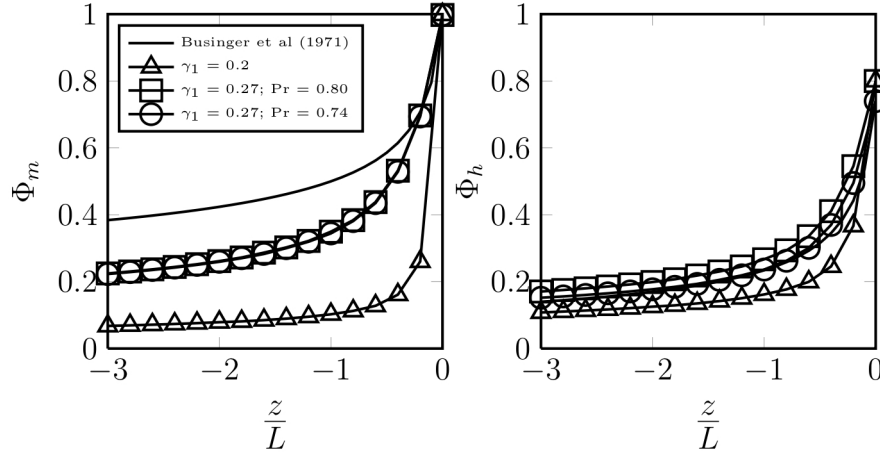


Figure 5.4: Calculation of Φ_m and Φ_h in unstable stable stratification according to eqs. (5.31) and (5.32) for various γ_1 and ℓ_s as defined in the text.

However, it has been shown in the previous chapter that the B_1 specified by Janjić (2002) will underpredict the TKE close to the surface and consequently makes it undesirable for the estimation of turbulence intensity, especially at higher wind speeds. At this juncture, one could abandon attempts to continue to work with the MYJ model and move to a more complex or even higher order scheme – thus requiring further complexity. Instead, the situation here can be rescued by focusing on the selection for γ_1 as defined above in eqs. (5.15), (5.16) and (5.17) as originally done in Mellor and Yamada (1982) and repeated in Janjić (2002).

5.3.2.2 Alternative strategy

Dimensionless gradients and surface length scale The problem with the constants in (5.37) where $B_1 = 26$ is that a specification for γ_1 ($= 0.2$) similar to Mellor and Yamada (1982) ($\gamma_1 = 0.222$) has been used and is based on the magnitude of $\overline{w'^2}_+$ defined according to eq. (5.15). Based on the yearly averaged measurements at FINO1 for the whole of 2005 stated in Table 5.2, $\gamma_1 = 0.222$ seems to have been an excellent choice. The magnitude of γ_1 based on the laboratory boundary layer measurements of Österlund (1999) and Carlier and Stanislas (2005) are also included in Tab. 5.1 as calculated according to eqs. (5.15), (5.16) and (5.17) for streamwise ($\overline{u'^2}$), lateral ($\overline{v'^2}$) and vertical ($\overline{w'^2}$) variances, respectively. It can be seen from Table 5.1 that there are some other options for γ_1 other than 0.2. This is also apparently allowable due to the lack of truth in eqs. (5.15) to (5.17), i.e. $\overline{v'^2}_+ \neq \overline{w'^2}_+$.

For reference, lateral and vertical variances for the whole of 2005 as measured at FINO1 at 40 m above sea level as a function of stability, $\frac{z}{L_L}$ (L_L is the local Obukhov length as introduced in the previous chapter) are displayed in Fig. 5.5 and compared with the LES results of Nakanishi (2001)¹ where a good agreement is evident in near neutral stratification. The agreement however is

¹Provided courtesy of M. Nakanishi

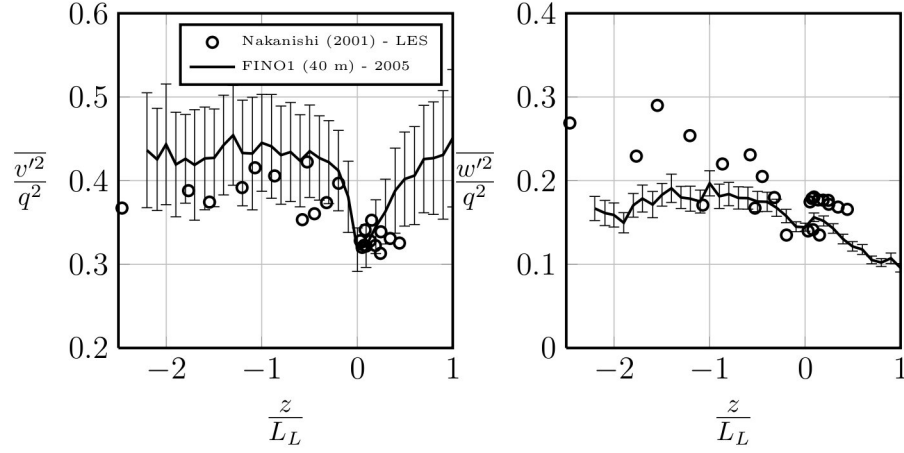


Figure 5.5: 40 m lateral and vertical variances normalised by twice the TKE, q^2 for the year 2005 at FINO1 as a function of stability. The error bars are two standard deviation width. Comparison the LES results of Nakanishi (2001) are also included.

less so away from neutrality and could be because L_L departs further from L (i.e. at the surface) as $|L|$ increases. The magnitude of γ_1 as calculated according to eqs. (5.15), (5.16) and (5.17) from the neutral variances at FINO1 in neutral stratification are displayed above in Table 5.1. It can be seen in Fig. 5.5 that $\frac{v'^2}{q^2}$ and $\frac{w'^2}{q^2}$ are most alike in neutral stratification, but are nonetheless not equal. For that reason, one appears to be within their rights to treat γ_1 as a free parameter, although according to eq. (5.18), it has a maximum of $\frac{1}{3}$ which is approached at FINO1 for $\frac{v'^2}{q^2}$ in neutral stratification.

For example, in contrast to Mellor and Yamada (1982) and Janjić (2002), γ_1 can be increased to 0.27 according to the laboratory measurements in Table 5.2 for w'^2 here giving

$$(A_1, A_2, B_1, B_2, C_1) = (0.823, 0.563, 26.000, 12.410, 0.133), \quad (5.49)$$

where $\gamma_1 = 0.27$, $Pr = 0.74$ and $\frac{w'\theta'^2}{u_*^2\theta'^2} = 0.32$. As demonstrated above with respect to Fig. 5.1, the magnitude of B_1 is uncertain due to Reynolds number effects (see eq. (5.29)) and will in practice depend on the model resolution and the Reynolds number. For example, Kunkel and Marusic (2006) measure $\overline{u'^2}_+ \rightarrow 10$ as $\frac{z}{\delta} \rightarrow 0$ over homogeneous terrain, which would require $B_1 \rightarrow 90$ to model this accurately using a very high vertical resolution². For now, let us assume $B_1 = 26$ according to Table 5.1 with the understanding that B_1 could be made Reynolds number dependent if required.

The point here however, is that in contrast to the constants in (5.37), the set of constants in (5.49) with an unconventional choice for γ_1 give an improved functional dependence of Φ_m and Φ_h in that they are now both underpredicted in stable stratification as seen by the squares in Fig. 5.3. The model can then

²TKE₊ = $\frac{1}{2}q_+^2 \approx \overline{u'^2}_+ = \frac{1}{2}B_1^2/3$.

be made to match the Businger et al. (1971) functions by using some explicit dependence of ℓ_s on stability where, for example

$$\ell_s = \kappa z (1 + c\zeta)^{-1}, \quad (5.50)$$

where c is a constant depending on the functional form of Φ_m . For example, Nakanishi (2001) uses $c = 2.7$ but other choices are possible. Fig. 5.3 shows eq. (5.50) for $c = 2.7$ in conjunction with constants (5.49) substituted into eqs. (5.31) and (5.32) as circles (labelled as $\gamma_1 = 0.27$ & ℓ_s in the legend). Here, the agreement with Businger et al. (1971) in both stable (Fig. 5.3) and unstable (Fig. 5.4) is now far better compared with above (see the triangles) and from that we could expect a more physically realistic model behaviour.

While $c = 2.7$ is explicitly from Nakanishi (2001), a dependence of ℓ_s on stability has been suggested in many forms before (Holt and Raman, 1988). A discussion of the various functional dependencies as reported in the literature in very stable stratification is given in Luhar et al. (2009) where the decision is uncertain, particularly in very stable stratification (Mahrt, 1998), but one could also chose for example

$$\Phi_m = 8 - \frac{4.25}{\zeta} + \frac{1}{\zeta^2}, \quad (5.51)$$

for $\frac{z}{L} > 0.5$ according to Carson and Richards (1978) and this function, along with

$$\Phi_m = 1 + 5\zeta \quad (5.52)$$

for $\frac{z}{L} < 0.5$ to give a smoother blend with eq. (5.51).

Many different forms for ℓ above the surface have been further proposed, where e.g. Nakanishi (2001) uses eq. (5.50) along with a buoyancy governed length scale in his more elaborate parametrization. Here however, only ℓ_s is modified for the purposes of calculating Φ_m and Φ_h to be in agreement with more acceptable functions. Sušelj and Sood (2010) also used all the suggested length scales by Nakanishi (2001) in the MYJ model but did not address the issue of the constants themselves or the magnitude of the TKE. Here in Fig. 5.3, it can be seen that a physically realistic calculation of Φ_m and Φ_h is possible by using merely eq. (5.50) and the constants selected in (5.49) using an unconventional choice for γ_1 .

Critical Richardson number and test cases The strategy here can also be extended to higher values of B_1 while keeping ℓ_s defined according to eq. (5.50), for example

$$(A_1, A_2, B_1, B_2, C_1) = (0.90, 0.45, 41.46, 14.78, 0.18), \quad (5.53)$$

where here $\gamma_1 = 0.29$, $Pr = 0.74$ and $\frac{w'\theta'^2}{u_*^2\theta'^2} = 0.32$ as before. While the definition for γ_1 (eq. (5.18)) gives a limit ($\frac{1}{3}$) to the magnitude of γ_1 , Janjić (2002)'s critical Richardson number also limits the selection of γ_1 , where in Fig. 5.6, Ri_c has been plotted against B_1 for various γ_1 . It can be seen there that the higher B_1 is, the higher γ_1 must also be for there to be a realistic critical Richardson number. This could be, for example, $Ri_c = 0.2$ (similar to Mellor and Yamada (1982)) which is displayed as the solid horizontal line in Fig. 5.6. The constants in (5.53) have been selected to correspond with $Ri_c = 0.2$ while keeping $\gamma_1 = 0.29$. In

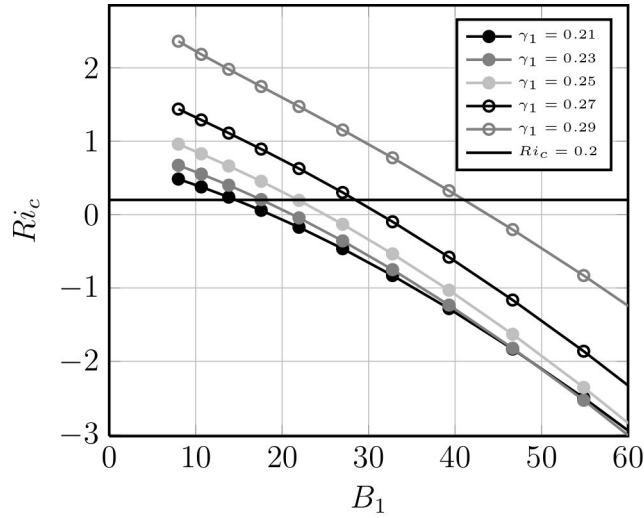


Figure 5.6: The relationship between Ri_c and B_1 as calculated from eq. (5.46) for a range of γ_1 .

principle then, the constants could be varied depending on the application or made a functional dependence themselves on some other parameter, e.g. the Reynolds number or stability.

A number of different versions using the strategy outlined above will be tested below in the single column model within WRF where according to Fig. 5.6, Ri_c can be kept constant at a magnitude of 0.2 by varying γ_1 , while using different values of c in eq. (5.50). The constants in eq. (5.53) correspond with $\gamma_1 = 0.29$ and $Ri_c = 0.2$, which is close to the Ri_c used by Mellor and Yamada (1982). For $\gamma_1 = 0.27$ and $Ri_c = 0.2$, then

$$(A_1, A_2, B_1, B_2, C_1) = (0.91, 0.54, 28.76, 13.08, 0.15), \quad (5.54)$$

and for $\gamma_1 = 0.25$,

$$(A_1, A_2, B_1, B_2, C_1) = (0.92, 0.64, 22.05, 11.98, 0.12). \quad (5.55)$$

Given the constants in (5.53), (5.54) and (5.55), c in eq. (5.50) will be 2.7, 5 and 10. Hence, in addition to the four cases presented in Table 5.2, this gives a total of 13 different model versions to be investigated below.

In Table 5.2, MYJ is the default model in WRF described in section 5.3.1 with the standard length scale formulation. MY82 are constants described in Mellor and Yamada (1982) (5.28), with the same length scale as in MYJ. MYJv2 uses the constants according to (5.49), but with the surface length scale defined by eq. (5.50), where $c = 2.7$. A higher critical Richardson number is evident for MYJ (0.51) compared with for MYJv2 (0.37). For reference here and in the simulations below, MYJg1 is also considered and corresponds with the constants in (5.37) and a critical Richardson number (-0.41) such that turbulence will only be able to be produced in convective conditions.

Before applying this new strategy on real scenarios such as that at FINO1 in the next chapter, it will first be tested in the single column model within

Table 5.2: Summary of different cases tested in the single column model below. The constants are defined in the text. Ri_c is the critical Richardson number as determined from the constants.

Case	constants	ℓ_s	B_1	γ_1	Ri_c
MYJ	eq. (5.36)	κz	11.9	0.222	0.51
MY82	eq. (5.28)	κz	16.6	0.222	0.19
MYJv2	eq. (5.49)	eq. (5.50)	26.0	0.27	0.37
MYJg1	eq. (5.37)	κz	26.0	0.20	-0.43
group1	eq. (5.55)	eq. (5.50)	22.1	0.25	0.2
group2	eq. (5.54)	eq. (5.50)	28.8	0.27	0.2
group3	eq. (5.53)	eq. (5.50)	41.5	0.29	0.2

WRF. The purpose here is not determine the optimum constants, but rather to demonstrate that a realistic physical behaviour of, in particular, the wind speed can be obtained despite making some unconventional choices. The results here will further help interpret real simulations in the next chapter.

5.4 Single Column Model Results

In the following section, the modifications to the MYJ model as detailed in Table 5.2 will be tested in the single column model (SCM) available in WRF. The single column model in WRF is based on the second GABLS (GABLS2) case study which itself is based on the CASES-99³ experiment which took place in Kansas, USA (Poulos et al., 2002). Two days from that study were chosen for the GABLS2 study on account of a strong diurnal cycle and a steady geostrophic wind, which is set to 9.5 ms^{-1} during the simulations, along with a prescribed, diurnally varying surface temperature (Svensson et al., 2011). One hundred vertical levels as opposed to the default 60 have been used in order to help resolve the lower vertical levels as results will be compared with the 50 m high main tower erected during the CASES-99 experiment⁴. As with Svensson et al. (2011), the local time period 20:00, 22/10/99 - 7:00, 24/10/99 is considered here where after this period, the actual geostrophic wind deviates substantially from the constant 9.5 ms^{-1} specified in the model.

A series of 13 simulations based on descriptions above, and in Table 5.2 will be investigated, including the original Mellor-Yamada setup (MY82) after Mellor and Yamada (1982), the current model in WRF (MYJ) after Janjić (2002) and that (MYJv2) based on some recent laboratory measurements (see Table 5.1). For an illustration of what appears to be an “unphysical” simulation, the case denoted MYJg1, which corresponds with the constants according to eq. (5.37), and hence with the triangles displayed above in Fig. 5.3, is also considered. In Fig. 5.3, the case MYJg1 appeared to significantly depart from the dimensionless gradients defined according to Businger et al. (1971). Furthermore, the critical Richardson number is negative, and hence the model is unable to produce TKE in either stable or even in weakly unstable stratification. The other 9 simulations (group1–3) correspond with the same critical Richardson number (0.2) but different magnitudes of γ_1 and c as defined above.

³Cooperative Atmospheric Surface Exchange Study-1999

⁴Measurements available online at <http://www.eol.ucar.edu/projects/cases99/>

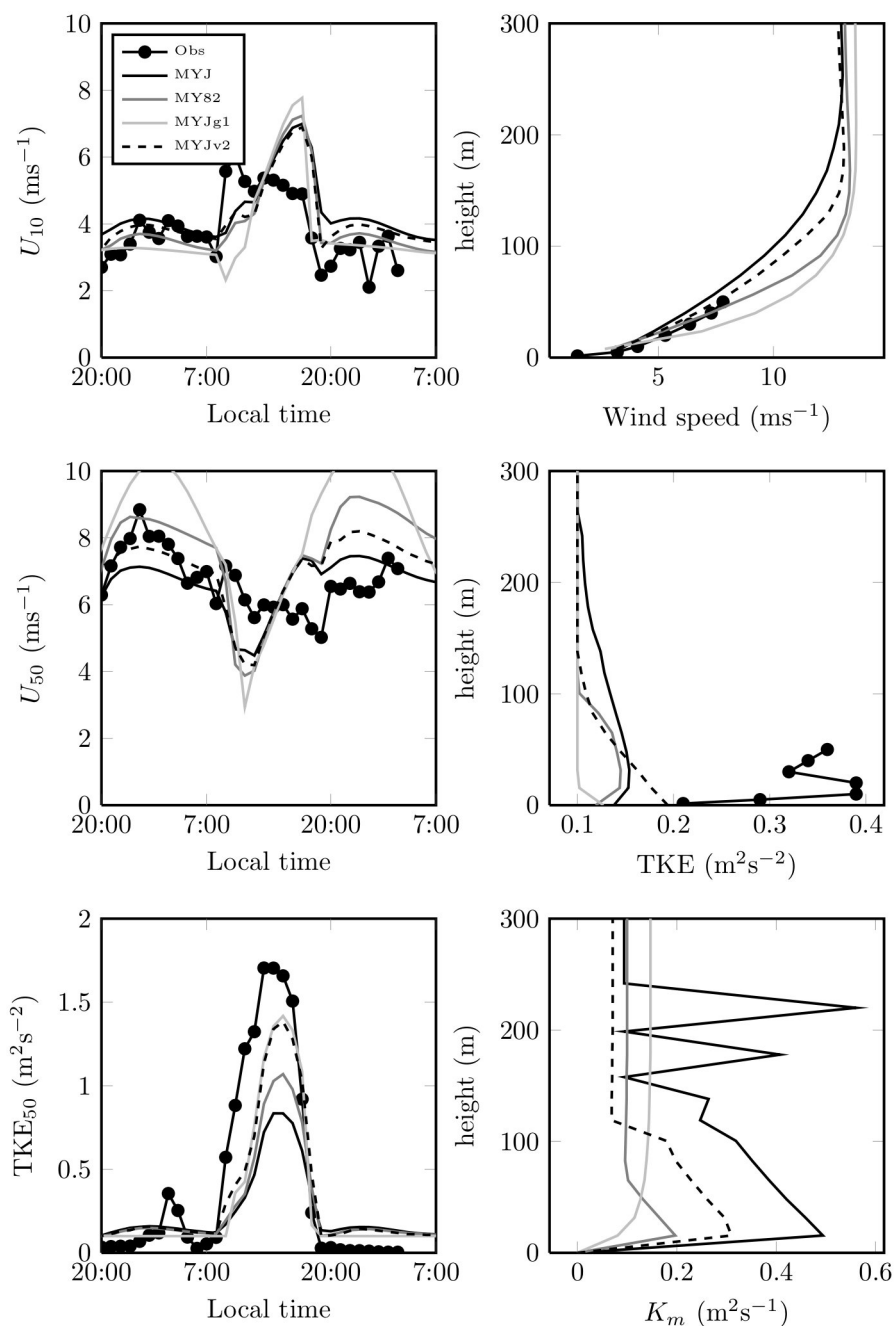


Figure 5.7: Left column: Time series of 10 and 50 m wind speeds and TKE from single column model simulations using the current MYJ model, that defined in Mellor and Yamada (1982) (MY82), an example of physical unrealistic simulation where $\gamma_1 = 0.2$ and $B_1 = 26$ (MYJg1) and an alternative MYJ versions using $\gamma_1 = 0.27$ and $B_1 = 26$ (MYJv2). Right column: The same cases as the left column showing profiles of wind speed, TKE and K_m at 3:00 local time. The observations are those taken from the main tower during the CASES-99 experiment.

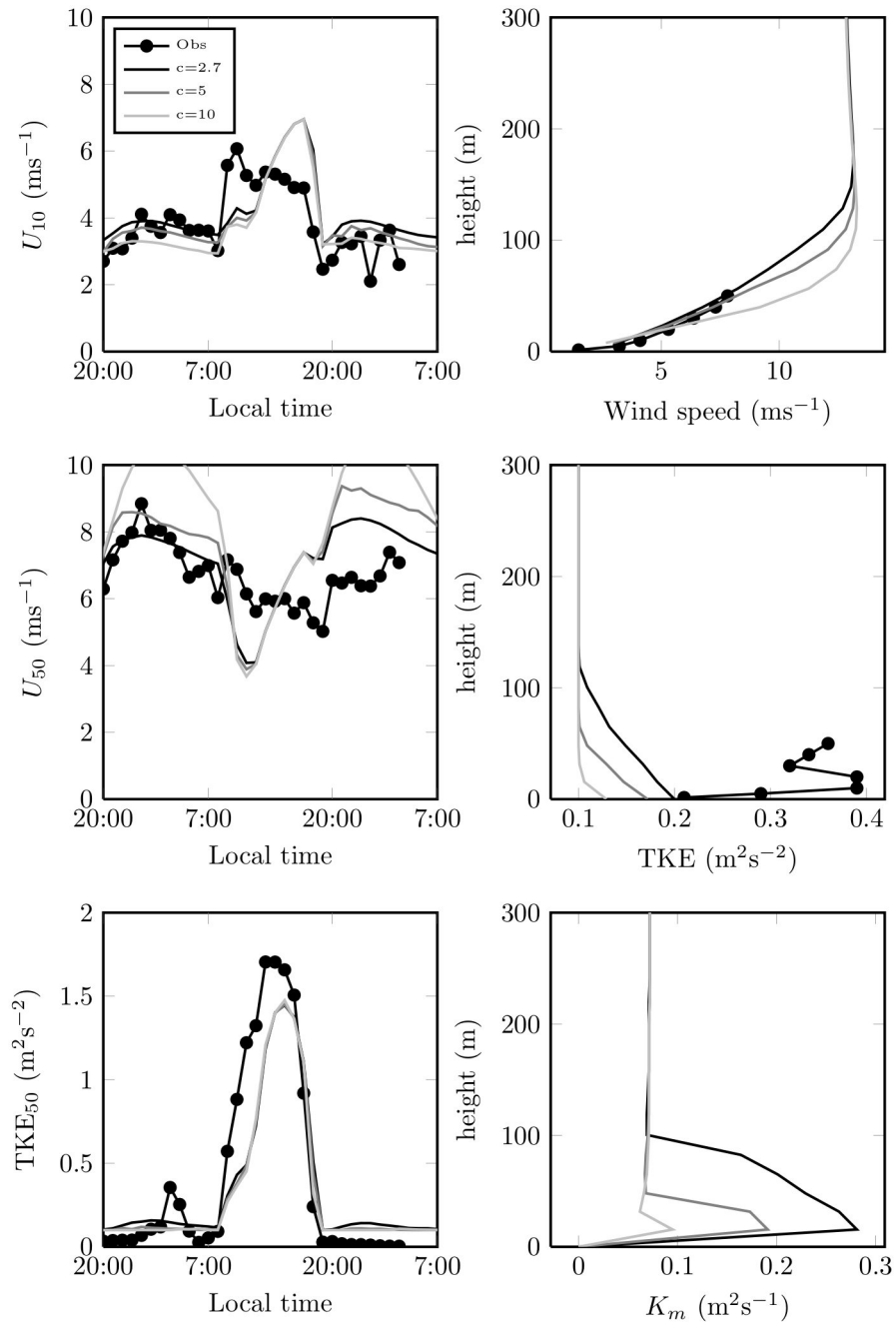


Figure 5.8: Left column: Time series of 10 and 50 m wind speeds and TKE from single column model simulations using $\gamma_1 = 0.27$. Right column: The same cases as the left column showing profiles of wind speed, TKE and K_m at 3:00 local time. The observations are those taken from the main tower during the CASES-99 experiment.

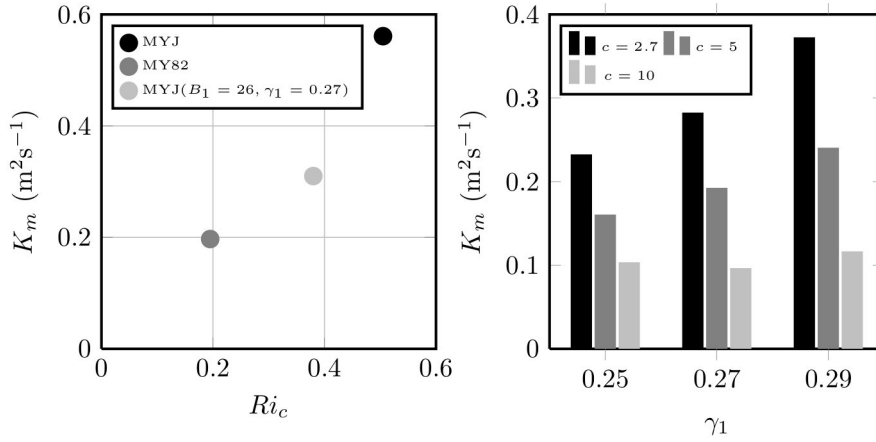


Figure 5.9: Left: The dependence of the maximum K_m throughout the boundary layer at 3:00 local time on Ri_c for MYJ, MY82 and MYJ (with $\gamma_1 = 0.27$, $B_1 = 26$ and $c = 2.7$). Right: The dependence on this same K_m on γ_1 and c at constant Ri_c .

Fig. 5.7 shows time series of 10 and 50 m wind speeds and TKE from single column model simulations using MYJ, MY82, MYJg1 and MYJv2 (left column) and wind, TKE and K_m profiles at 3:00 local time (right column). Fig. 5.8 shows the same information as Fig. 5.7, but rather $\gamma_1 = 0.27$ and different magnitudes of c have been used for $Ri_c = 0.2$. At 3:00 local time, an event of high TKE is evident in the time series and has been attributed to “advection or an instability over a deep layer” (Mahrt and Vickers, 2002). Comparing Figs. 5.7 with 5.8, the most obvious difference is evident between profiles of TKE. In these figures, it is evident that the main difference is in the vertical TKE profiles as calculated by the conventional models, MYJ and MY82, compared with MYJv2 and those in Fig. 5.8. MYJ and MY82 give a peak in the TKE above the surface, consistent with a so called “upside down boundary layer”, whose result is an elevated wind shear generated turbulence above the surface, rather than at the surface (Mahrt, 1999). The cases in Fig. 5.8 however anticipate a conventional boundary layer structure, for example after Caughey et al. (1979). The measurements also appear to give at least one peak TKE above the surface, but this structure is not resolved by any of the models.

Hence, the changes here may be less sensitive to capturing an unconventional structure of turbulence within the stable boundary layer. Practical differences in the vertical profile of exchange coefficients, K_m however appear to be minimal. The main differences are to be found in the absolute magnitude of K_m between each case. Above the boundary layer, constant exchange coefficients are to be found. The vertical oscillation of K_m towards the top of the boundary layer and above evident in Fig. 5.7 is a known phenomena that is more noticeable with a higher vertical resolution. There are methods to improve this aspect of the model (Buzzi et al., 2011), but this will not be dealt with here.

The main point of Figs. 5.7 and 5.8 is to contrast apparently unphysical behaviour (e.g. MYJg1) with physical behaviour (e.g. MYJ and MY82), and then to show that the changes suggested here can also give a physical behaviour.

For example, in Fig. 5.7 (bottom left), the 50 m TKE as calculated by MYJg1 remains constant beyond daybreak as a consequence of the negative critical Richardson number. One can compare the behaviour of MYJg1 with MYJ and MY82 in the same figure, where the TKE of MYJg1 begins to increase once the Richardson number has decreased sufficiently. As could thus be expected, the 50 m wind speeds as calculated by MYJg1 deviate significantly from the other models and the observations, especially during the night. Only when the TKE begins to be able to be produced during the day does the wind speed calculated by MYJg1 appear to match that of the other wind speeds. The MYJg1 case can then be used as reference for non-physical model behaviour. For example in Fig. 5.8, a constant of $c = 10$ in eq. (5.50) gives relatively small K_m corresponding with the sort of wind shear produced by MYJg1. The other two cases $c = 2.7$ and $c = 5$ are more consistent with the MYJ and MY82 wind shears, while at the same time giving a clearly higher TKE than either MYJ and MY82 during the day according to the time series. Hence, this was the desired effect originally sought.

In order to summarise the results for all test cases, the maximum K_m throughout the vertical layer at 3:00 is displayed in Fig. 5.9 (left) as a function of the critical Richardson number for MYJ, MY82 and MYJv2 (with $\gamma_1 = 0.27$, $B_1 = 26$ and $c = 2.7$). It is evident that there is a near one-to-one relationship between these values, MYJv2 possibly departing from this relationship due to the addition of ℓ_s . The relative effect of ℓ_s and Ri_c on K_m can be seen by comparing Fig. 5.9 (left) with Fig. 5.9 (right) where the maximum K_m is displayed again but for Ri_c kept constant and γ_1 and c varied. For constant Ri_c and c , K_m increases with γ_1 . For constant Ri_c and γ_1 , K_m decreases with c .

The point of this exercise was to demonstrate some possible advantages (and disadvantages) of making some traditionally unconventional selections for γ_1 and ℓ_s . Two practical differences relevant to wind energy applications is an increased wind shear in stable stratification compared with the standard selections, while at the same time enhancing the magnitude of the TKE in convective conditions. To determine whether these changes could manifest themselves advantageously in practice is something left to the next chapter where the approach suggested here will be tested on real cases at FINO1, including the May 2006 case presented in Chapter 4 and the high wind speed cases during 2005 considered in Chapters 2 and 3.

5.5 Conclusions

In this chapter, it was investigated whether it was possible to increase the TKE in the Mellor-Yamada-Janjić model and still produce physically realistic results. It was found that in order to get this to work practically, an alternative strategy had to be employed which involved treating certain parameters more liberally than that done by Mellor and Yamada (1982) and followed to a certain extent by Janjić (2002) in WRF. By a proper consideration for the critical Richardson number in addition to the introduction of an explicit stability dependent length scale, model estimates of dimensionless wind shear and temperature gradients, $\Phi_{m,h}$ can be made to agree more readily with commonly accepted forms.

Tests in WRF's single column model were performed to compare unrealistic model parameters having a negative critical Richardson number with more re-

alistic versions having a positive and similar critical Richardson number to that used by Mellor and Yamada (1982). Based on single column model tests, it is apparent that physically realistic wind profiles are possible using the alternative strategy described here, but with the added advantage of an enhanced magnitude of TKE. This is based on both a comparison with observations, the existing models (Mellor and Yamada, 1982; Janjić, 2002) and the unrealistic model parameters giving a negative critical Richardson number. To investigate whether these effects found here with respect to the single column model translate into enhanced wind speed profiles and the calculation of turbulence intensity by the WRF model in three dimensional simulations will be investigated in the next chapter.

Chapter 6

Applications for wind energy: Accounting for offshore roughness and turbulence intensity

6.1 Introduction

In the previous chapters, it was demonstrated that the behaviour of numerical models in calculating offshore turbulence parameters could be structured differently from current practice. In Chapters 2 and 3, the functional form of the offshore surface roughness parametrization was demonstrated to deviate from that expected according to the Charnock (1955) aerodynamic roughness parametrization, where Chapter 3 showed this to be due to the nature of the water surface. For example, the drag coefficients of two particular periods during 2005 as measured at FINO1 (January 4–10 and February 20–28) were demonstrated to give a different dependence on the wave field. Chapter 4 then showed that any precise dependence of the surface roughness on the waves will likely need to incorporate further wind-wave complexities. The nature of the wave field will thus consistently affect the performance of numerical models that neglect this aspect (e.g. WRF). From the perspective of wind energy purposes, this could be significant in the calculation of the wind speed since surface roughness that is either too high or too low will affect the magnitude of the wind at hub height, but also the reduction of wind speed behind wind turbines (Emeis and Frandsen, 1993). This reduced wind speed within wind farms will also be a function of the turbulence intensity (Elliott and Barnard, 1990) and hence the modified turbulence parametrization presented in Chapter 5 is relevant for this purpose.

In Chapter 4, a case of a stable internal boundary layer generated by warm air advection over cooler water as detected at FINO1 during May 2006 was presented. There it was demonstrated that the existing MYJ model underpredicted wind speeds and did not follow the expected functional dependence of TKE normalised by the friction velocity, i.e. TKE_+ as could be expected from

conventional stable boundary layer scaling, e.g. according to Caughey et al. (1979). In particular, it was found that the TKE would be underestimated close to the surface, i.e. as $\frac{z}{z_i} \rightarrow 0$ and overestimated as $\frac{z}{z_i} \rightarrow 1$, where z is the height above the surface and z_i is the boundary layer height. The incorrect calculation of TKE close to the surface can be attributed to the following boundary condition

$$\text{TKE}_+ = \frac{1}{2} B_1^{2/3}, \quad (6.1)$$

where B_1 is a model constant set to 11.9 by Janjić (2002), where observations suggest $B_1 \rightarrow 40$ (and higher depending on the model resolution) as $\frac{z}{z_i} \rightarrow 0$. The practical significance of this is that numerically underpredicting the turbulence intensity could affect the anticipated power output within wind farms.

Changes to the MYJ model as suggested in the previous chapter for the purposes of enhancing the calculation of TKE included an unconventional selection for the model parameter γ_1 while keeping a critical Richardson number of $Ri_c = 0.2$. This then further necessitated a modification to the surface layer length scale corresponding with

$$\ell_s = \frac{\kappa z}{\Phi_m} \quad (6.2)$$

where κ is von Karman's constant. The dimensionless wind shear for all ζ is

$$\Phi_m = 1 + c\zeta \quad (6.3)$$

(c is a constant set to 5 here), although for $\zeta > 0.5$,

$$\Phi_m = 8 - \frac{4.25}{\zeta} + \frac{1}{\zeta^2} \quad (6.4)$$

could be used according to Carson and Richards (1978), but there are a number of alternatives to this that could be applied in stable stratification (Grachev et al., 2007). The model constants as introduced in Chapter 5 to be compared with the existing MYJ model (Janjić, 2002) and the traditional version (Mellor and Yamada, 1982) (MY82) are

$$(A_1, A_2, B_1, B_2, C_1) = (0.91, 0.54, 28.76, 13.08, 0.15), \quad (6.5)$$

which gives $\gamma_1 = 0.27$. Below, this case will be labelled as “g127b128” to indicate the nominal values of g_1 and B_1 . The periods of investigation for this chapter include the stable May 2006 period (see Chapter 4), as well as the January, February and November 2005 periods as introduced in Chapters 2 and 3 where the focus was on the aerodynamic roughness length. The later periods all give high wind speeds and in general higher turbulence intensities than measured during May 2006.

The investigation of the nature of the surface roughness length scale as specified in numerical models will also be investigated during these periods. In particular in Chapter 3, a different dependence of the drag coefficient on the sea state was detected between the January and February, 2005 periods. To quickly recapitulate those results here, a correlation equation defined by

$$C_{D10m} = \left(0.03^3 + \left(\frac{H_s}{\lambda_p} \right)^3 \right)^{2/3}, \quad (6.6)$$

was developed from the asymptotic correlating method described in Churchill and Usagi (1972), where $\frac{H_s}{\lambda_p}$ is the wave steepness or the inverse aspect ratio. Eq. (6.6) is a relationship bridging two asymptotic functions, which for high aspect ratios is a constant,

$$C_{D10n}^{1/2} = 0.03 \quad (6.7)$$

and at low aspect ratios is a squared wave steepness,

$$C_{D10n} = \left(\frac{H_s}{\lambda_p} \right)^2. \quad (6.8)$$

It was found in Chapter 3 that drag coefficients measured during the January period were best described by eq. (6.6), while the February period gave drag coefficients fitting eq. (6.8). The consequences of these alternative scaling regimes are that lower drag coefficients and hence lower aerodynamic roughnesses were detected during February compared with during January.

In order to be able to incorporate these results in some form into a numerical weather prediction model, a further parametrization that can distinguish the different wave steepness scaling regimes needs to be found. Chapter 4 further shows that higher order effects such as the angle between the wind and the waves may also be important. The purpose of this chapter however is to demonstrate that a more advanced offshore surface roughness model by taking into account the work presented in Chapter 2 has the potential to further improve the calculation of offshore wind speeds. There is a belief in the literature that only a basic parametrization for offshore roughness for any particular site is required since, e.g. the constant α in Charnock's roughness parametrization, if calibrated properly, does not vary much at a particular site (Johnson et al., 1998). While this may be true at sites closer to the coast where the wave climate (and hence wave steepness) is possibly dictated to a greater extent by the depth of the water, this assumption, as will be demonstrated in this chapter may be insufficient for wind parks tending to be sited further offshore and exposed to a broader range of wind and wave climates.

For the purposes of modifying the roughness length in the WRF model, the simple linear relationships between the friction velocity and wind speed as found in Chapter 2 will be used:

$$u_* = a_1 U_{10n} + a_2, \quad (6.9)$$

and hence no wave information is required to make these work. Eq. (6.9) can be rearranged¹ and substituted into the logarithmic law so that

$$z_o = z \exp \left(\frac{-\kappa (u_* - a_2)}{a_1 u_*} \right). \quad (6.10)$$

Below, a couple of combinations of the "constants" $a_{1,2}$ will be used, but the exact numbers aren't as important as demonstrating a contrasting behaviour with the existing Charnock's parametrization in the model which uses an $\alpha = 0.018$ in

$$z_o = \alpha \frac{u_*^2}{g}. \quad (6.11)$$

¹As suggested by Ed Andreas (2010, Private communication)

In this way, while the use of these equations can not be general since they neglect the wave field, it is intended to demonstrate that accounting for the wave field in the future could lead to an improved wind speed calculation, depending on the offshore application.

To summarise, the purpose of this chapter is to demonstrate (a) that changes to the MYJ model suggested in Chapter 5 can give a physically realistic solution in three-dimensional simulations, (b) those changes can offer practical advantages over the existing scheme from the perspective of wind energy considerations and (c) a more elaborate roughness length parametrization can offer advantages over the existing one, based on the discussion carried out in Chapters 2 to 4. In the following section, results from a number of numerical simulations of the flow at FINO1 will be investigated, beginning with the May 2006 internal boundary layer introduced in Chapter 4. Results of both MYJ and roughness length simulations during the January 2005 period will then be presented, followed by February and November 2005.

6.2 Results

6.2.1 May 2006

The May 4–11, 2006 case at FINO1 corresponds with a stable internal boundary layer height $O(100\text{ m})$ as estimated previously in Chapter 4 based on the work of Mulhearn (1981) and Garratt (1987). Using this estimate of the boundary layer height and an estimate of the friction velocity, vertical profiles of TKE appeared to scale in a manner similar to that expected over land where a comparison with the curve reported by Caughey et al. (1979) yielded some correspondence. In comparison with the MYJ model, scaled profiles of TKE did not follow the expected behaviour and these are reproduced here in Fig. 6.1 in comparison with the curve reported by Caughey et al. (1979) based on their measurements of $\overline{u'^2}$ over land, where $\text{TKE}_+ = \overline{u'^2}$ has again been assumed. The periods on display during each day in Fig. 6.1 correspond with the passage warmer continental air over the cooler sea surface. Also included now in Fig. 6.1 is MY82 corresponding with the original constants defined in Mellor and Yamada (1982) (see Chapter 5). It can be seen that MY82 will tend to give a better vertical structure of TKE compared with MYJ. Close to the surface however, MY82 will nevertheless underestimate the TKE, since $B_1 = 16.6$ and hence $\text{TKE}_+ = 3.25$ at the surface.

Fig. 6.2 shows a particular alternative MYJ version labelled as “g127b128” which is based on the suggestions in the previous chapter corresponding with $\gamma_1 = 0.27$, $B_1 = 28.8$ and $\text{Ri}_c = 0.2$. Hence, $\text{TKE}_+ \rightarrow 4.7$ as $\frac{z}{z_i} \rightarrow 0$, and should give some improvement over both MYJ and MY82 closer to the surface. Further above the surface, this version can decay at a rate more consistent with the expected behaviour of the measurements compared with MYJ, but still similar with MY82. For example, during the 4th, TKE_+ as calculated by g127b128 is greater than TKE_+ as calculated by MYJ as $\frac{z}{z_i} \rightarrow 0$, but lower as $\frac{z}{z_i} \rightarrow 1$. Both MY82 and g127b128 could possibly be further improved to be more closely aligned with the FINO1 measurements, which were estimated to be near the curve taken from the measurements reported by Caughey et al. (1979) as presented in Chapter 4.

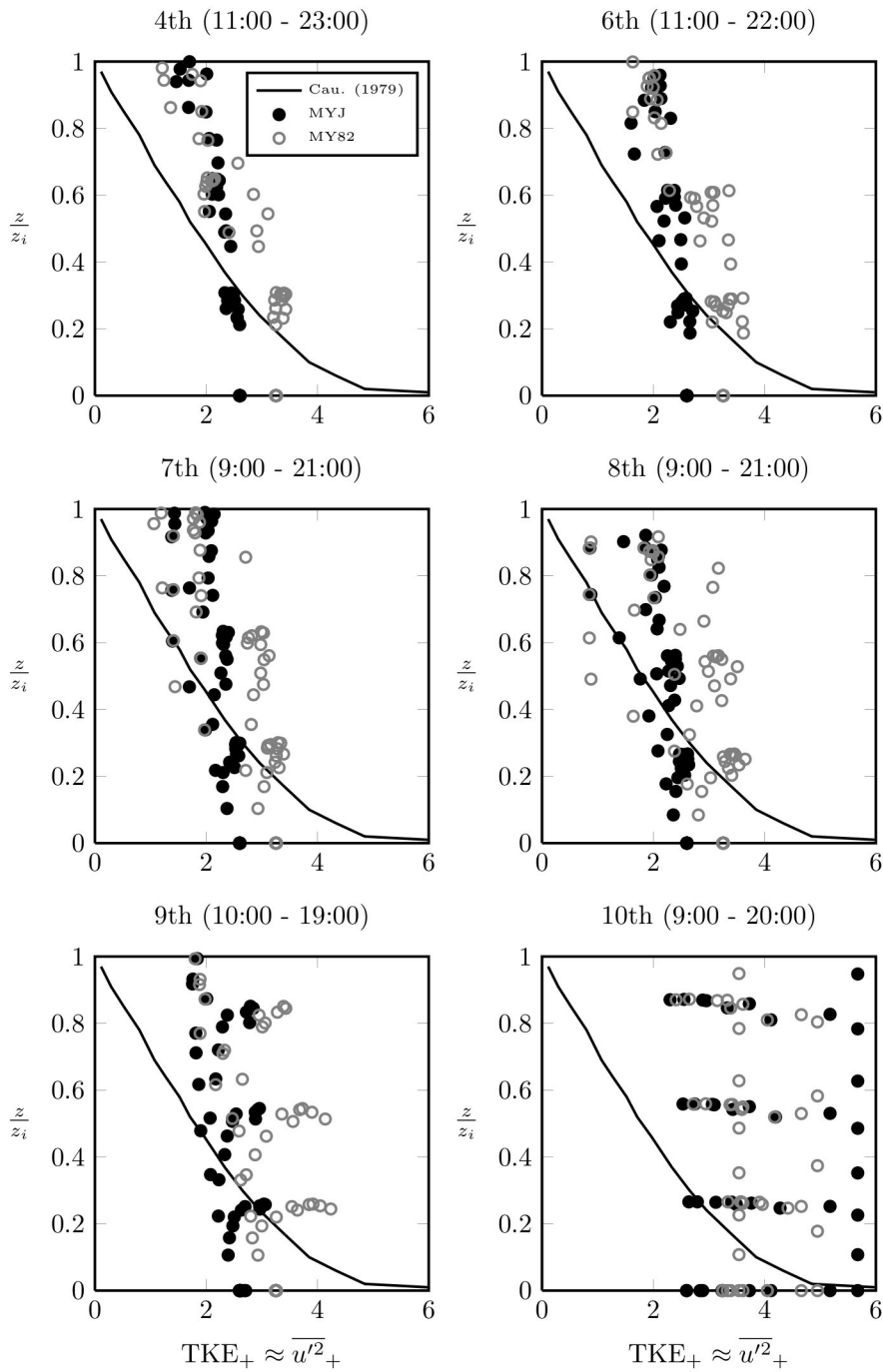


Figure 6.1: Vertical profiles of turbulent kinetic energy normalised by the friction velocity as calculated by MYJ and MY82 and compared with the curve of Caughey et al. (1979) as presented in their figure 5 (top left). The height, z has been normalised by the estimated internal boundary layer height (see Chapter 4).

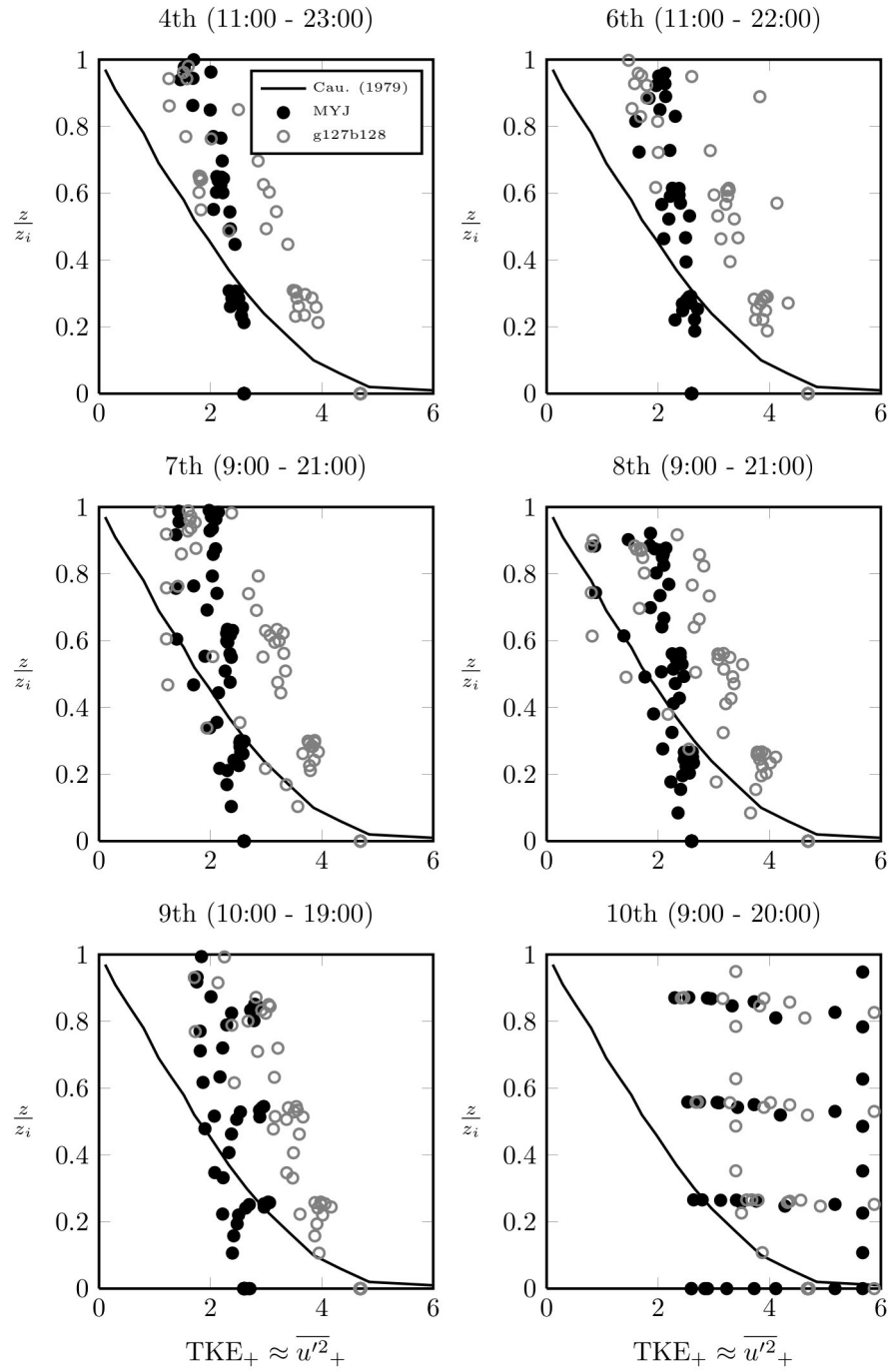


Figure 6.2: Vertical profiles of turbulent kinetic energy normalised by the friction velocity as calculated by MYJ and g127b128 and compared with the curve of Caughey et al. (1979) as presented in their figure 5 (top left). The height, z has been normalised by the estimated internal boundary layer height (see Chapter 4).

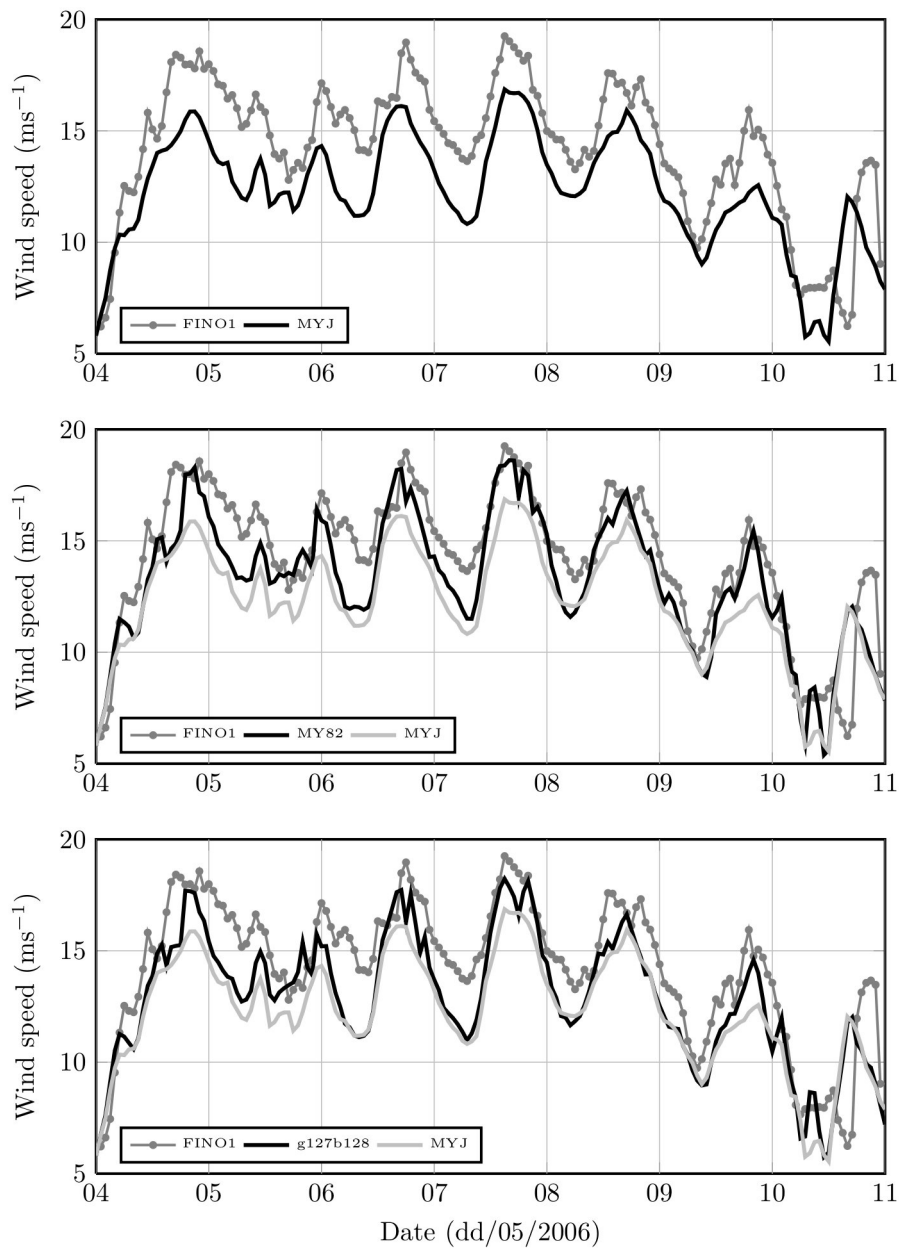


Figure 6.3: Wind speed at 80 m as calculated by MYJ (top), MY82 (middle) and g127b128 (bottom) in comparison with both MYJ and FINO1 measurements.

The consequence of the enhanced calculation of vertical profiles of TKE_+ by MY82 and g127b128 is, it can be seen from the time series displayed in Fig. 6.3, a superior calculation of the hub height (80 m) wind speed as evident in Fig. 6.3 compared with MYJ. Fig. 6.3 shows time series of the 80 m wind speed in comparison with the 80 m cup anemometer at FINO1. While the MYJ wind speed appears to underestimate the measurements consistently throughout

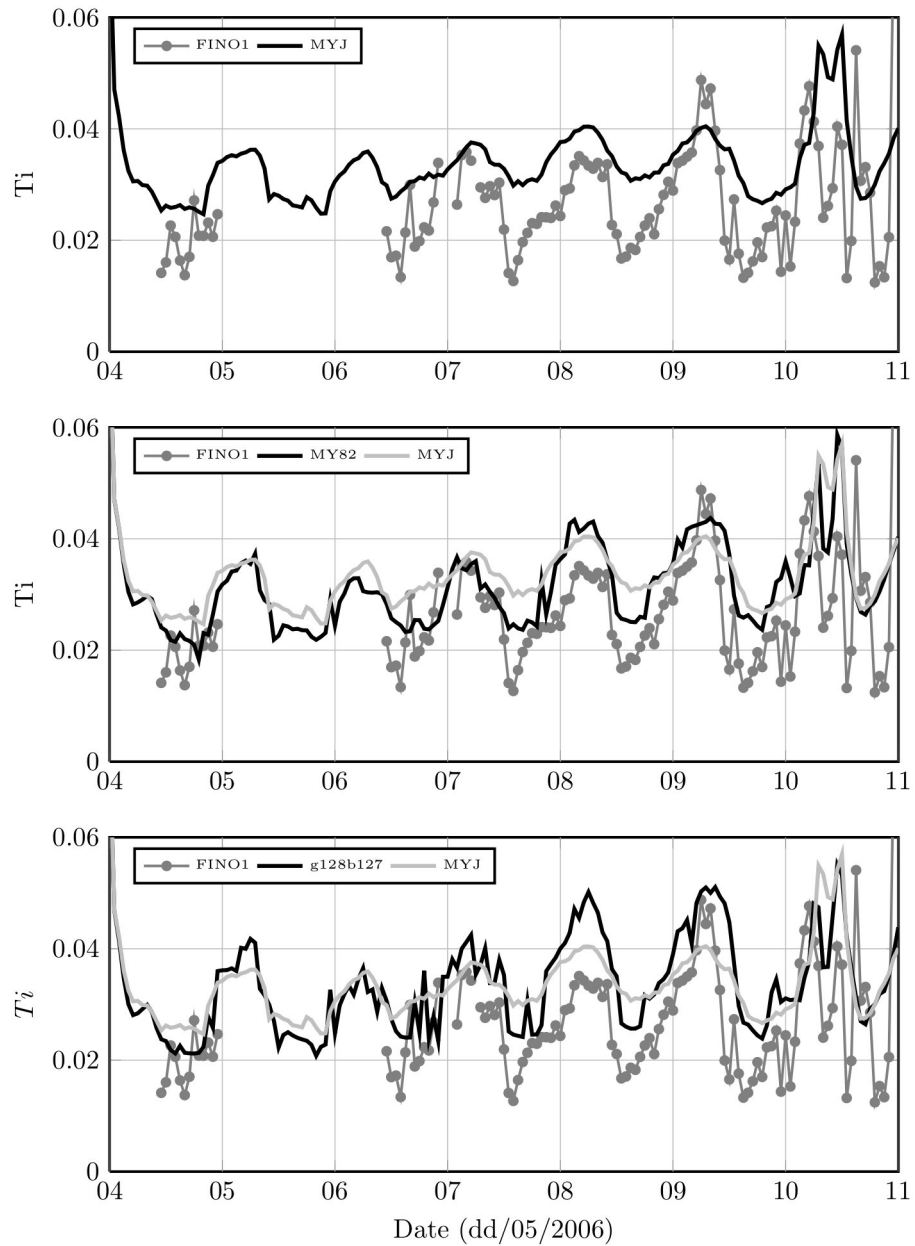


Figure 6.4: Turbulence intensity as calculated by MYJ (top), MY82 (middle) and g127b128 (bottom) in comparison with both MYJ and FINO1 measurements.

the entire period, both MY82 and g127b128 are in better agreement. However, the night time wind speeds corresponding with very low turbulence are still consistently underpredicted as particularly evident during the mornings of the 6th and the 7th. During these mornings, MY82 also gives higher wind speeds than g127b128. Wind speed, TKE and K_m profiles to be displayed below will further illustrate why wind speeds still appear to be underpredicted here.

The turbulence intensity at 80 m as calculated by MYJ, MY82 and g127b128 is displayed in Fig. 6.4 and compared with FINO1 observations. The turbulence intensity is defined as

$$Ti = \frac{\sqrt{TKE_{80}}}{U_{80}}. \quad (6.12)$$

This definition of the turbulence intensity is indicative of, although not exactly like, the one used in practice based merely on $\overline{u'^2}$ (see Chapter 4 for a comparison). The turbulence intensity is consistently over-estimated by MYJ, whereas MY82 and g127b128 are better correlated with the measurements, but nonetheless are consistently higher than the FINO1 data. This would be consistent with the scaling displayed in Figs. 6.1 and 6.2 shown above. Importantly though, the g127b128 model version is able to perform in a physically realistic manner consistent with the standard model versions, MYJ and MY82.

For example, wind speed, absolute TKE and K_m profiles during the 4th at 12:00 and 22:00 are displayed in Fig. 6.6, where these times have been presented previously in Chapter 4 demonstrating the underestimated MYJ wind shear. Here, profiles of MY82 and g127b128 have also been included and in comparison with FINO1 measurements, and both models appear to show improvement over MYJ in the calculation of wind shear and TKE profiles. The TKE as calculated by MYJ decays much more slowly with height compared with the other simulations, here at 23:00 giving a boundary layer height about 3 times higher (~ 300 m) than the measurements would suggest (~ 100 m). Because the decay rate of TKE is too low, K_m produces too much momentum exchange within the boundary layer resulting in not enough wind shear. The net effect then is that the MYJ overpredicts the TKE at about 80 m during this period and underpredicts the wind speed.

It can be demonstrated here in Fig. 6.5 that the key parameter governing the vertical structure of turbulence as calculated by the model is the critical Richardson number where wind speed and TKE profiles at 22:00 on May 4th are shown for $Ri_c = 0.51$ (i.e. MYJ), 0.37 and 0.2 (i.e. g127b128). Here it can be seen that the negative slope of TKE profiles are roughly proportional to Ri_c , where on that basis Ri_c may well be less than 0.2 according to the measurements. The oscillation of K_m with height above the boundary layer height pointed out in the previous chapter within the single column model is also evident in Fig. 6.6 for MYJ. Fig. 6.6 shows that the TKE decay rate has been characterised well by both MY82 and g127b128, with g127b128 being able to give a higher TKE closer to the surface. Since the eddy viscosity is broadly proportional to the TKE, lower K_m are calculated by both MY82 and g127b128 compared with MYJ.

The key difficulty with all models can be seen in the magnitude of TKE above the boundary layer which is constrained to $0.1 \text{ m}^2\text{s}^{-2}$ for numerical reasons, so that as a result, K_m gives a minimum of about $0.1 \text{ m}^2\text{s}^{-1}$ depending on the model constants. A non-zero K_m above the boundary layer is apparently necessary since the PBL scheme (if indeed used) handles all vertical diffusion in the WRF model (Skamarock et al., 2008). It can be seen in Fig. 6.6 however that the TKE as measured by FINO1 continues to decay below $0.1 \text{ m}^2\text{s}^{-2}$ after which the model is unable to resolve this. Instead, the model calculated TKE reaches a minimum value at the top of the boundary layer and this correspondingly affects the velocity profiles. Since the eddy viscosity is too high above the boundary

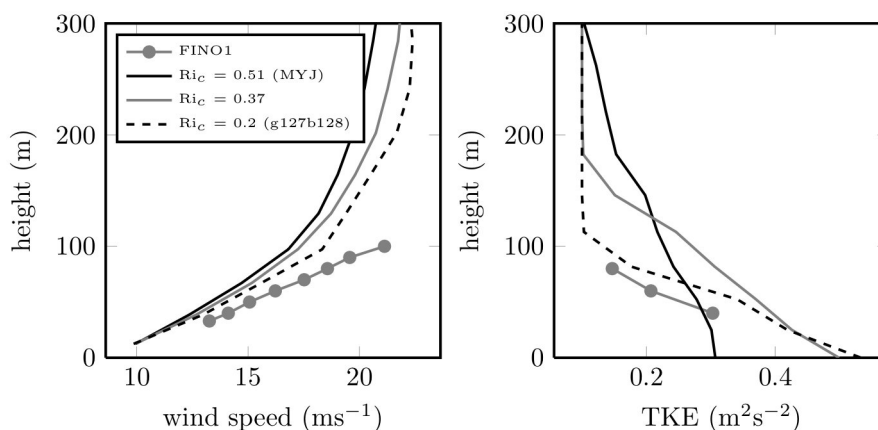


Figure 6.5: Wind speed (left) and TKE (right) profiles on May 4th at 22:00 for different critical Richardson numbers, Ri_c .

layer, there is too much vertical momentum exchange in all models and they are all unable to anticipate the wind shear beyond this point, as is particularly evident in wind speed profiles at 13:00 in Fig. 6.6 (compare top left with middle left). This is also evident, although to a lesser degree at 23:00, where lower K_m above the boundary layer height could help improve wind speed calculations further. Buzzi et al. (2011) obtained improved wind speed profiles in their single column model tests using a version of the Mellor-Yamada model in the COSMO² single column model by reducing K_m above the boundary layer and this deserves further investigation within WRF since this seems to be the principal way to improve wind speed profiles in very stable stratification from this point.

In Chapter 4, wind profiles at FINO1 were further displayed for the 6th and 8th at 15:00 and 23:00 in comparison with the MYJ results and these are now redisplayed including MY82 and g127b128 in Fig. 6.7 and Fig. 6.8, respectively. The increased wind shear given by MY82 and g127b128 with respect to MYJ is also evident in those figures. Elevated TKE maxima seem to have been calculated by MYJ and MY82 on the 6th, but consistent with the single column model in the previous chapter, g127b128 does not produce this effect. At 15:00 on the 8th, there is a gradual decay of TKE as calculated by MYJ far above the boundary layer height implied by the measurements, resulting in a broad spike of K_m in this range, but possibly had limited effect on the wind speed profiles. At this particular time, it is further evident that the correct calculation of wind speed profiles is sabotaged for all cases on account of the too high K_m above the boundary layer.

With regards to applications in wind energy, the turbulence intensity is low during this stable period compared to that expected in more neutral and unstable stratification, especially over land. For that reason, we could expect a more significant wind speed reduction within a wind farm exposed to such a flow, but depending also on the roughness length (Emeis, 2010*b*). If the MYJ model were used for some estimate of the wind speed deficit which takes into account the Ti of the undisturbed flow, then one could expect the wake wind speed to be

²<http://www.cosmo-model.org/>

overestimated based on the quicker wind speed recovery in periods of higher Ti (Elliott, 1991). Using either the original MY82 constants or a version such as g127b128 could be used to improve any estimate, although there is still room for further improvement.

However, there were further reasons for introducing this case. Firstly, to demonstrate that the changes to the MYJ model described in the previous chapter can produce physically reasonable results in a relatively complex off-shore flow, albeit one that apparently displays a conventional turbulence structure. One can compare wind speeds in Fig. 6.3 where the g127b128 wind speed appears realistic with respect to MYJ, MY82 and the measurements. Secondly, the boundary layer could be either detected or inferred approximately since the PBL height was $O(100\text{ m})$, and hence turbulence throughout a good portion of the boundary layer could be measured by FINO1. TKE profiles as output from the various models were then able to be scaled and compared with the measurements. From that, one could say in general that hub height TKEs would be overestimated by MYJ for low boundary layer heights as already seen in Fig. 6.3 and severely underestimated for conditions where the boundary layer height is much higher, such as in near neutral stratification or even in convective conditions. It is in these conditions where a much higher turbulence intensity can be found and hence where g127b128 could be expected to clearly outperform the MYJ model. For example, the January 2005 period shown in previous chapters resulted in very high wind speeds at FINO1 and this case will be investigated in the next section.

6.2.2 January 2005

The January 4–10 2005 case at FINO1 (see also previous chapters) is marked by a consistent south-westerly wind direction, weakly stable stratification and very high wind speeds including the named storm “Erwin” occurring on the 8th (Emeis and Türk, 2009). Fig. 6.9 shows WRF modelled TKE_+ for MYJ (left) and g127b128 (right) compared with the FINO1 measurements at 40, 60 and 80 m during this period and the curve from Caughey et al. (1979) as displayed above. The models have been normalised by their own calculated planetary boundary layer height here, whereas the FINO1 PBL height has been estimated from

$$z_i = 0.2 \frac{u_*}{f_c}. \quad (6.13)$$

The boundary layer height is of $O(1000\text{ m})$, and hence the FINO1 measurement heights of 40, 60 and 80 m sit approximately within the surface layer. The measurements, in correspondence with Caughey et al. (1979), thus suggest $\overline{u'^2} > 6$ as $\frac{z}{z_i} \rightarrow 0$, hence even the version g127b128 will underestimate the TKE close to the surface, but is still clearly better than MYJ.

A direct comparison between the modelled and measured hub height Ti can be seen in Fig. 6.10 for MYJ (top right), MY82 (middle right) and g127b128 (bottom right). Here it is evident that MYJ underestimates the Ti the most, followed by MY82 whereas g127b128 is the best for this case. All models give similar results for the wind speeds as evident in Fig. 6.10 (left) and are fairly good above 20 ms^{-1} . Hence it is shown here that g127b128 is able to give results consistent with the other two standard model versions in slightly stable stratification during this period on top of the agreement found above in very stable

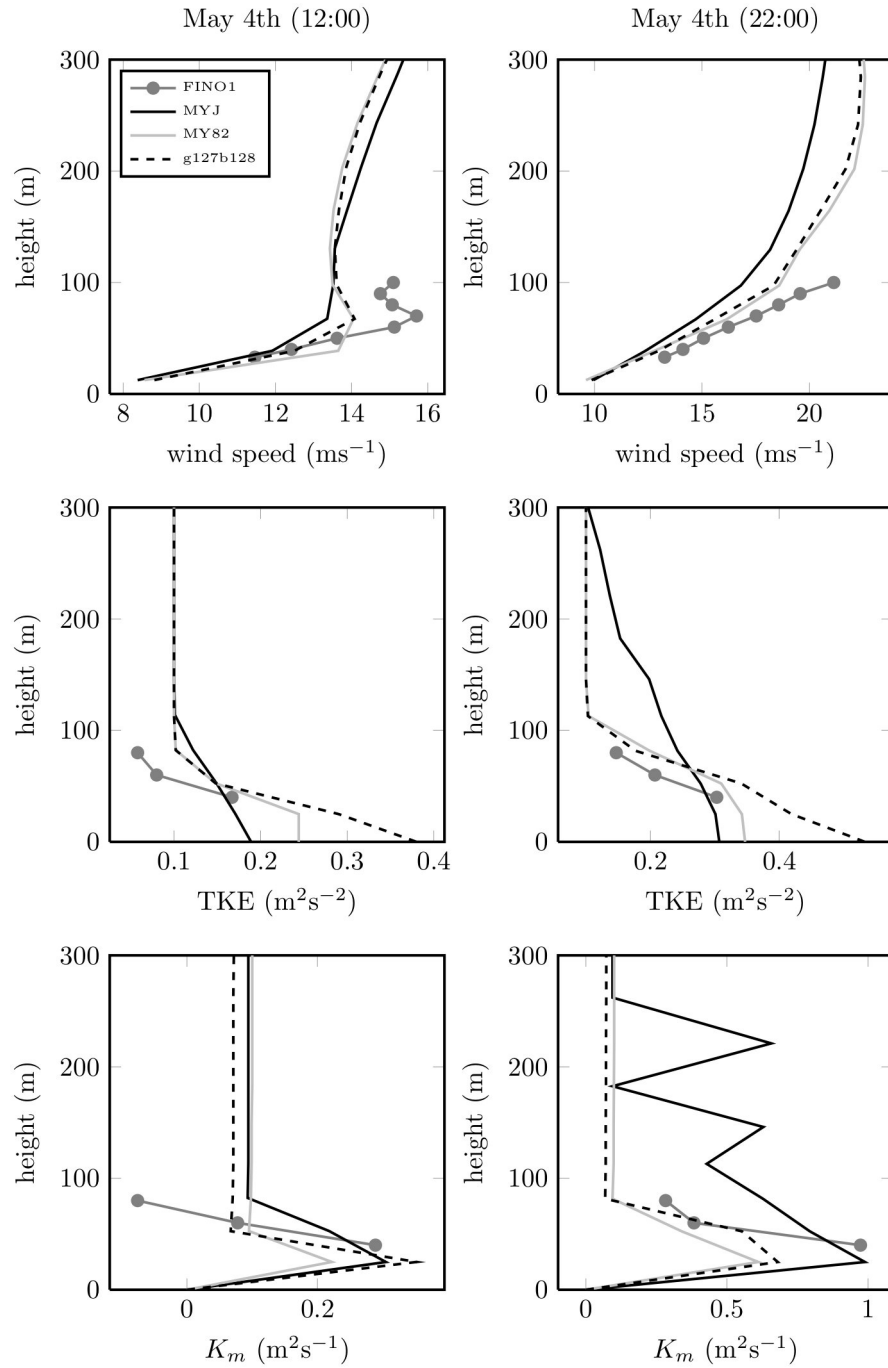


Figure 6.6: Wind speed and TKE (absolute) profiles on May 4th at 12:00 (left) and 22:00 (right) as calculated by MYJ, MY82 and g128b128 compared with FINO1 measurements.

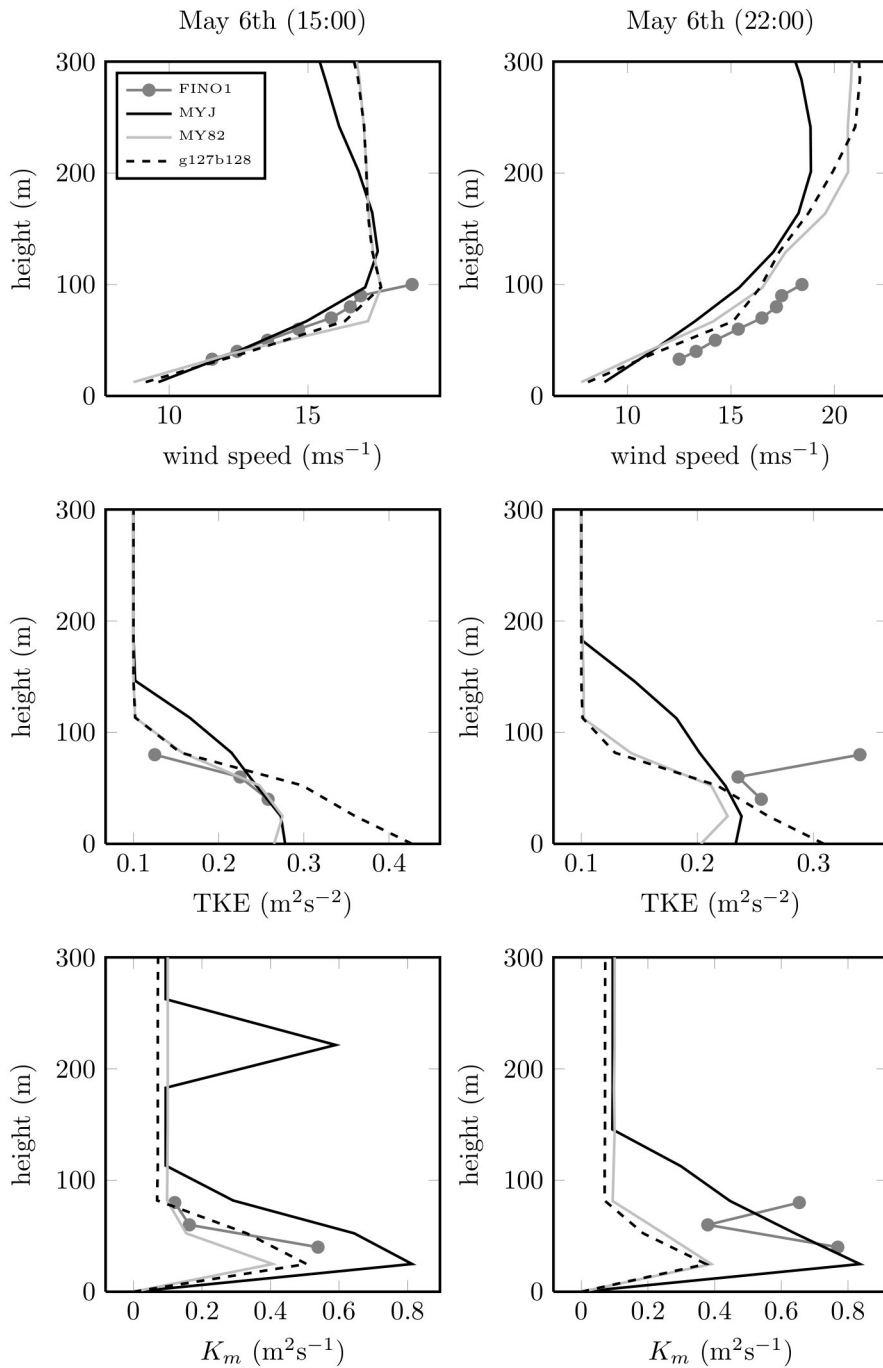


Figure 6.7: Wind speed and TKE (absolute) profiles on May 6th at 15:00 (left) and 22:00 (right) as calculated by MYJ, MY82 and g128b128 compared with FINO1 measurements.

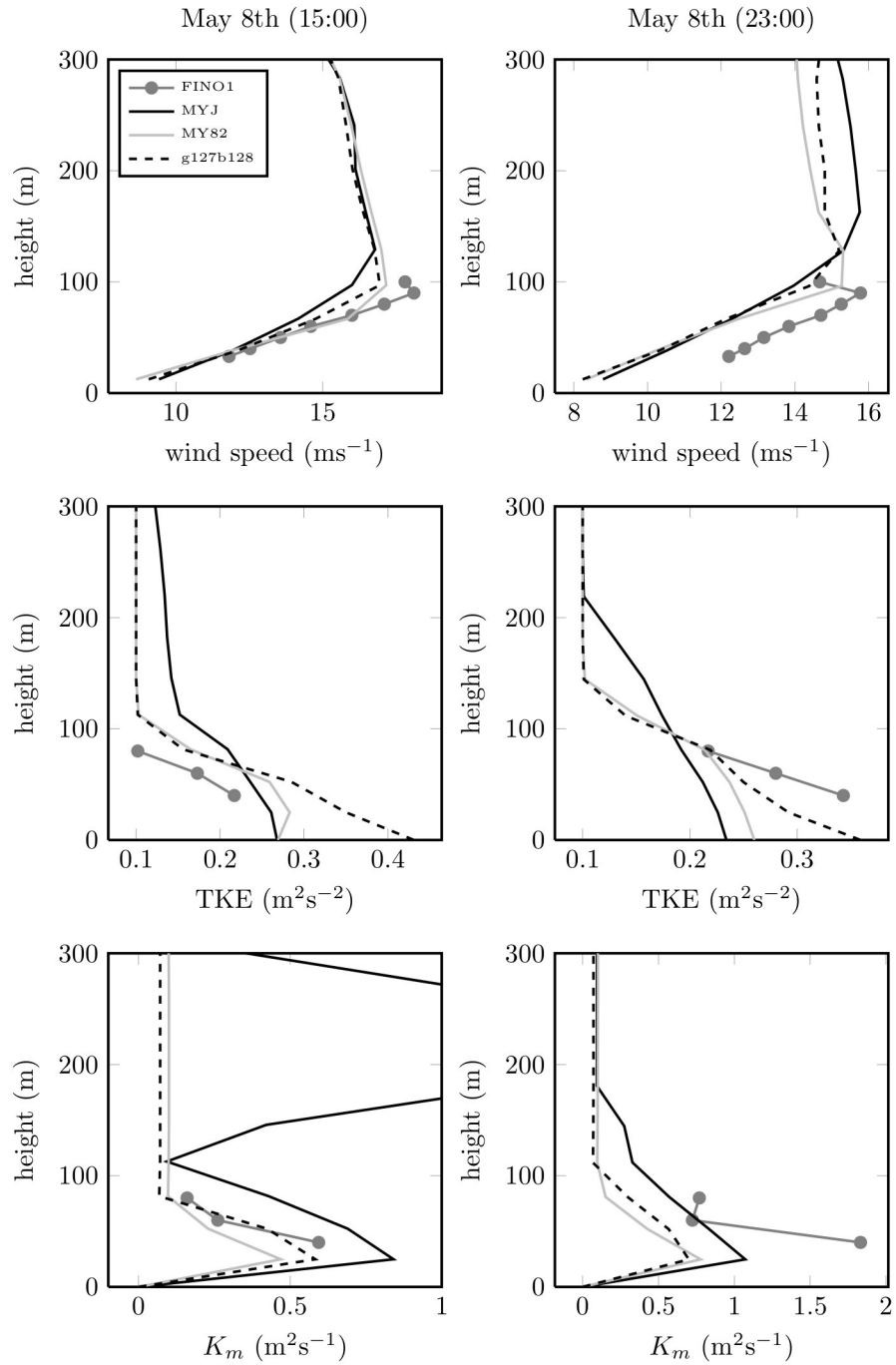


Figure 6.8: Wind speed and TKE (absolute) profiles on May 8th at 15:00 (left) and 22:00 (right) as calculated by MYJ, MY82 and g128b128 compared with FINO1 measurements.

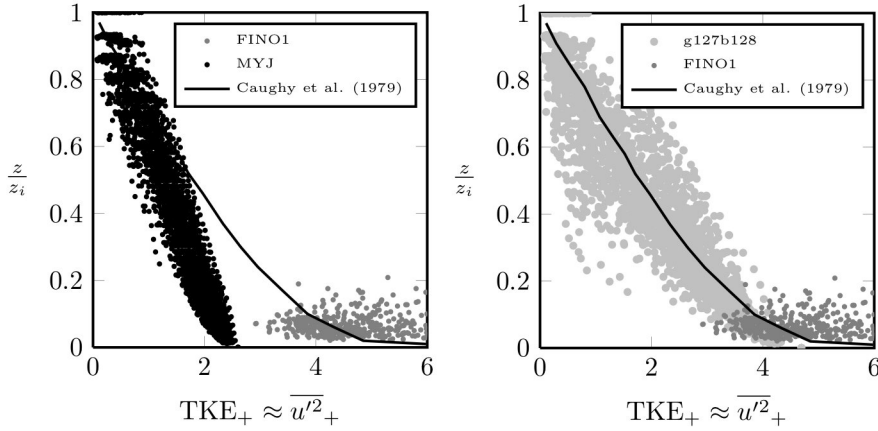


Figure 6.9: Profiles of WRF calculated TKE_+ according to MYJ (left) and g127b128 (right) as a function of the height normalised by the boundary layer height, $\frac{z}{z_i}$ in comparison with the results of Caughey et al. (1979) and the FINO1 measured TKE_+ at 40, 60 and 80 m during January 4–10, 2005.

stratification during May 2006. The advantage of g127b128 over both MYJ and MY82 though is the enhanced calculation of TKE profiles as demonstrated in Fig. 6.9 and hub height T_i as seen in Fig. 6.10.

Looking closer now at the wind speeds below 20 ms^{-1} in Fig. 6.10, it can be seen that all models appear to underpredict that measured at FINO1 at these speeds. To explore this in more detail, shown in Fig. 6.11 are average wind speed profiles during the 5th (top left), where speeds were on average less than 20 ms^{-1} and during the 7th (top right), where wind speeds were on average about 20 ms^{-1} . Fig. 6.11 also shows drag coefficients plotted as a function of one-tenth the aspect ratio (bottom left) and the wind speed (bottom right), where in both figures, points during the 5th and 7th are marked by circles and squares, respectively. Fig. 6.11 (bottom left) shows the solid black, and dashed black and gray lines displaying the aspect ratio scaling developed in Chapter 3 and restated here in the introduction. The dashed black and gray lines are the asymptotes at low and high aspect ratios defined according to a constant $C_{D10n}^{1/2}$ (eq. (6.7) and a squared wave steepness (6.8), respectively. The solid black is the smooth correlation between the two asymptotes, eq. (6.6).

In Chapter 3, it was demonstrated that this January period follows a scaling based on the smooth correlation where the January 5th and 7th measurements fall somewhat below and on top of this curve, respectively. In $C_{D10n} = f(U_{10n})$ space shown in Fig. 6.11 (bottom right), i.e. the space in which the model is basing z_o , the measurements during January the 5th happen to fall below the MYJ model (here g127b128 is used) which assumes $\alpha = 0.018$ in Charnock's roughness parametrization, eq. (6.11) and is shown by the solid black line. On the other hand, Charnock's roughness works better during the 7th where the g127b128 model passes through the cluster of C_{D10n} illustrated by the squares in Fig. 6.11 (bottom right). Referring once more back to the aspect ratio scaling in Fig. 6.11 (bottom left), it is evident that points following the solid black line, i.e. eq. (6.6), correspond with Charnock's roughness length for $\alpha = 0.018$, and

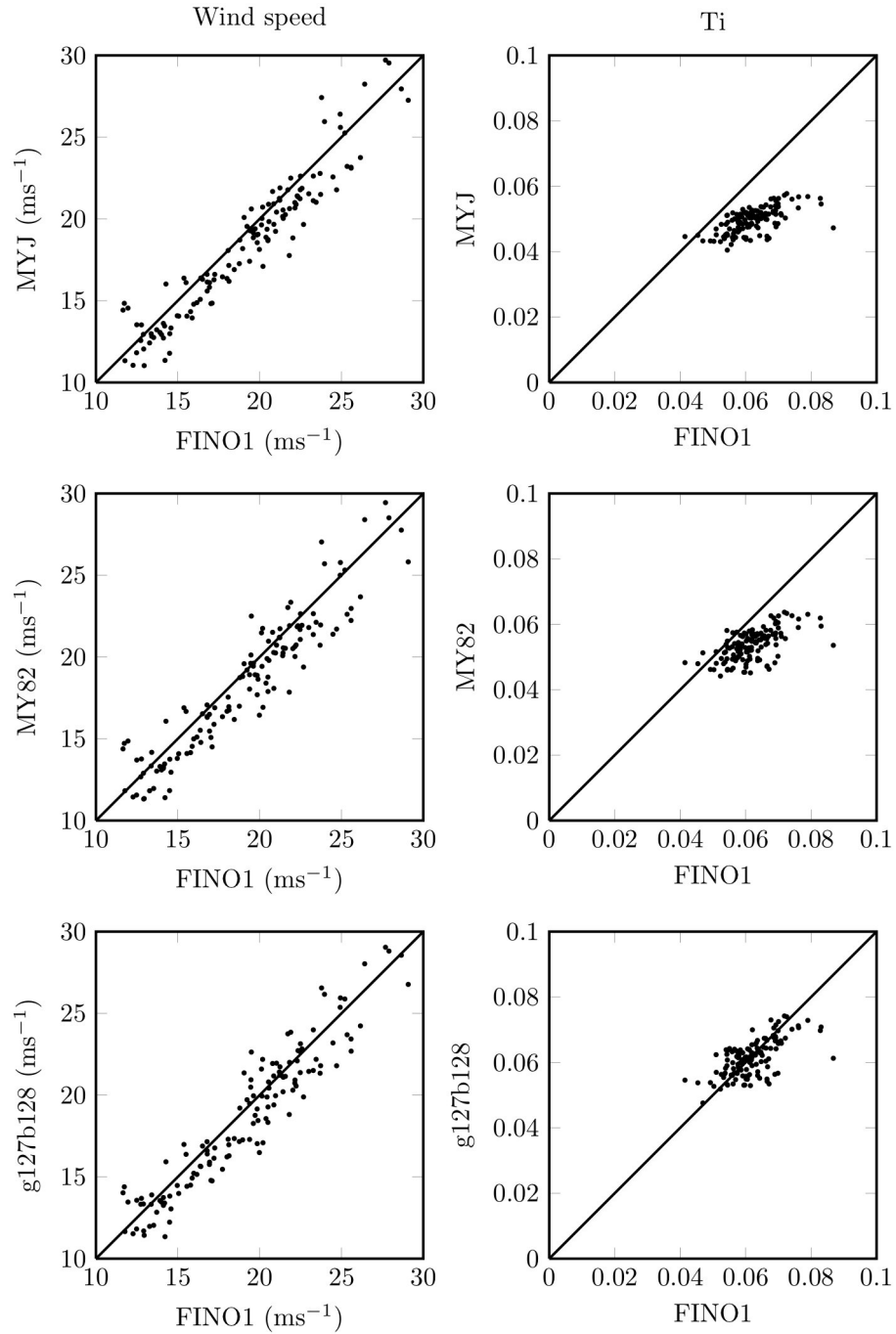


Figure 6.10: Hub height (80 m) wind speeds (left column) and turbulence intensity (right column) as measured by FINO1 in comparison with MYJ (top), MY82 (middle) and g127b128 (bottom).

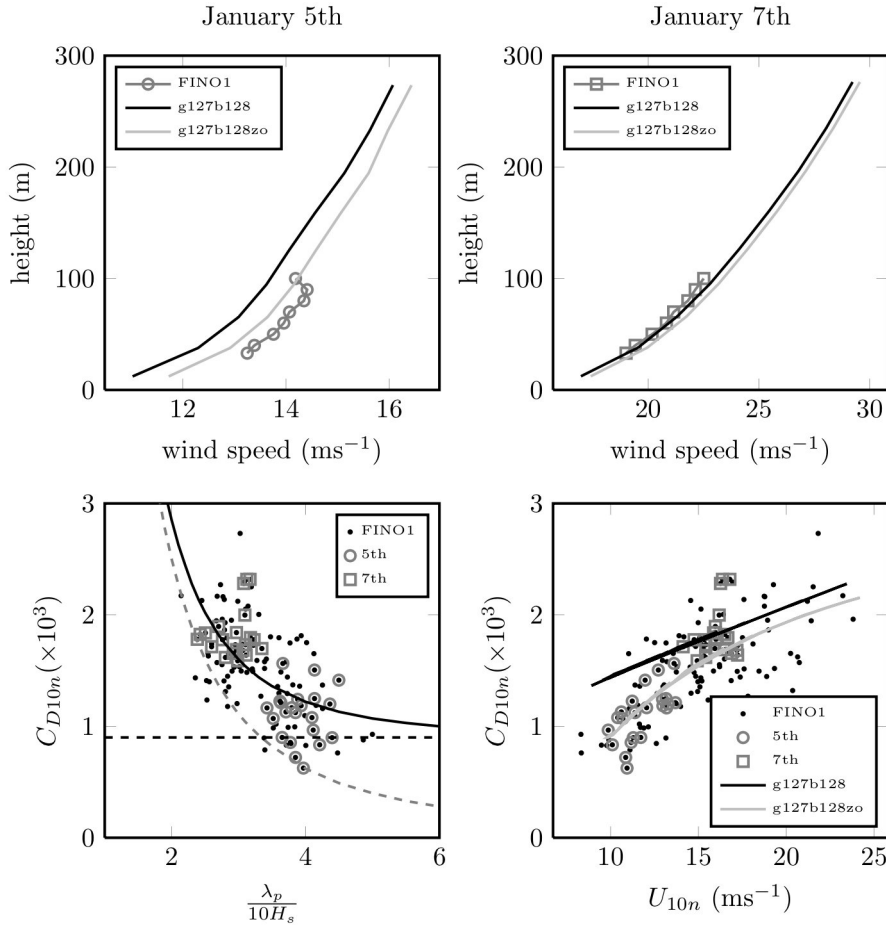


Figure 6.11: Average profiles at FINO1 during January 5th (top left) and 7th (top right) compared with MYJ and g127b128. The drag coefficient as a function of the aspect ratio (bottom left) and wind speed (bottom right) at FINO1. Highlighted in these figures are the points corresponding with the 5th (circles) and the 7th (squares). Bottom left: Solid black line is eq. (6.6); dashed black line is eq. (6.7); dashed gray line is eq. (6.8). Bottom right: The solid black line is Charnock's parametrization and the solid gray line is eq. (6.10) for $a_{1,2} = (0.058, -0.28)$.

hence the black curve in Fig. 6.11 (bottom right).

However, at FINO1 during this period, $\alpha = 0.018$ is only applicable some of the time. This result appears to be consistent with the average wind profiles where during the 5th where the wind speed is underpredicted by g127b128 whereas it is better calculated during the 7th. The case labelled as “g127b128zo” in Fig. 6.11 corresponds with the empirical linear fit to the u_* versus U_{10n} plot as demonstrated in Chapter 2 where from eq. (6.9) above, $a_{1,2} = (0.058, -0.28)$, and has been substituted into the logarithmic velocity profile, eq. (6.10). Eq. (6.10) is then used in WRF in place of Charnock's roughness, eq. (6.11). The case g127b128zo is able to better represent the wind profiles during the 5th but is

slightly worse during the 7th when Charnock works better. Importantly though, neither of these results are generally applicable since as they are neglecting any scaling with the wave steepness which can take a form defined by the correlation eq. (6.6), or the asymptotic eqs. (6.8) and (6.7), such as occurred during the February 2005 period to be considered below.

6.2.3 February 2005

Fig. 6.12 shows the high wind speed period during 20–28 February 2005 presented in previous chapters, where colder north-easterly air arrived at FINO1 resulting in convective conditions. Included in Fig. 6.12 are the 80 m wind speeds at FINO1 and calculated by MYJ (top), the 33 m wind and wave directions (middle) and the 80 m Ti at FINO1 compared with MYJ (bottom). The wind speed appears to be relatively well calculated during the first couple of days, but during the higher wind speed periods of the 22nd and the 23rd the calculation appears to be poorer. For example, Fig. 6.13 (top) shows average wind speed profiles during the 22nd and 23rd of February as calculated by the MYJ model compared with the FINO1 wind profiles. Also included in those figures is “MYJzo” which is based on the empirical fit to $u_* = f(U_{10n})$ and eq. (6.10) using $a_{1,2} = (0.046, -0.13)$.

As demonstrated in Chapter 3, this particular February period does not scale with the correlating wave steepness function eq. (6.6) as was found with the January 2005 measurements demonstrated above in Fig. 6.11 (bottom left), but with the asymptotes themselves according to eq. (6.8) at lower aspect ratios and eq. (6.7) at higher aspect ratios. This situation has been illustrated again in Fig. 6.13 (bottom left) showing eqs. (6.6), (6.8) and (6.7) as the solid black, dashed gray and black lines, respectively as in Fig. 6.11 (bottom left). The points corresponding with the 22nd and 23rd have been highlighted as the gray circles and squares, respectively, where generally they fall on the asymptote, eq. (6.8). In $C_{D10n} = f(U_{10n})$ space shown in Fig. 6.13 (bottom right), these points occur at the higher wind speed range. Also shown in Fig. 6.13 (bottom right) are curves corresponding with Charnock’s parametrization (black) as used by MYJ and $a_{1,2} = (0.046, -0.13)$ (gray) as used by MYJzo. The smooth flow regime is evident here at low wind speeds which results in an increasing C_{D10n} with decreasing wind speeds. The gray curve appears to give a smoother transition here between the smooth and rough flow regimes but the consequences of this will not be explored any further here.

This figure demonstrates that Charnock’s parametrization with a constant $\alpha = 0.018$ is generally too high during this period, while the gray curve corresponding with the constants $a_{1,2} = (0.046, -0.13)$ is better, but still possibly too high. This can only be true on average since there are some data points, as seen in Fig. 6.13 (bottom left), that nonetheless follow the correlation curve (black line) in $C_{D10n} = f\left(\frac{\lambda_p}{H_s}\right)$ space which will correspond with Charnock’s parametrization in $C_{D10n} = f(U_{10n})$ space (bottom right). However, Charnock overestimates roughness lengths at higher wind speeds during this period, the consequences being underestimated wind speeds as seen by velocity profiles in Fig. 6.13 (top) during the 22nd and 23rd. Some possible clues for the scaling with the asymptote as opposed to the correlation curve (and hence a disagreement with Charnock) can be seen by referring to the wind and wave directions

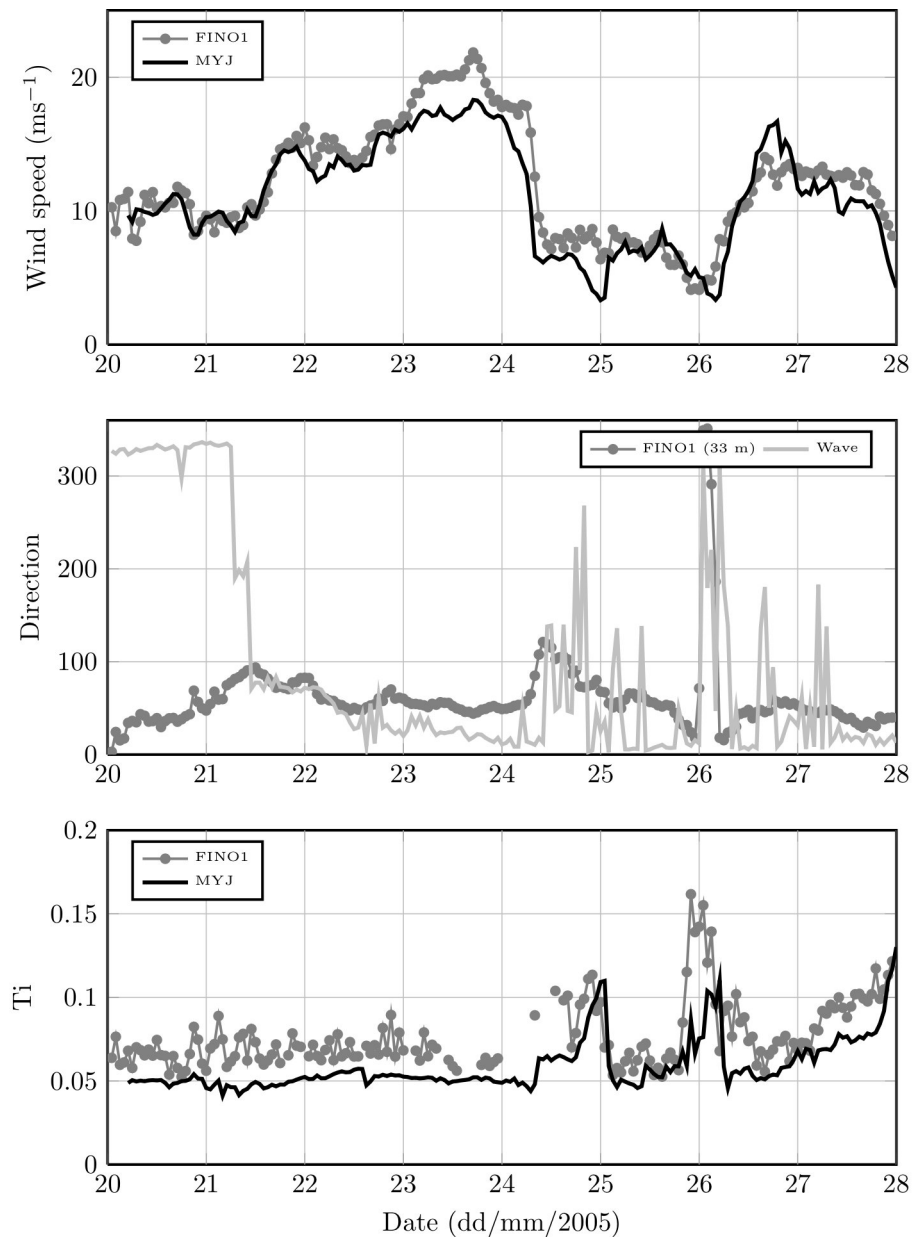


Figure 6.12: Wind speeds at 80 m (top), Wind (33 m) and wave directions (middle) and Turbulence intensity (bottom) during February 20–28, 2005.

in Fig. 6.12 (middle). It is evident for this period that wave directions were initially from the north-west, but turned rapidly to a north-easterly, a process that possibly resulted in the transport of swell towards the FINO1 platform, thus complicating the air-sea interaction process. The effect of swell on drag coefficients from the perspective of wave steepness scaling is left for a higher order analysis in the future.

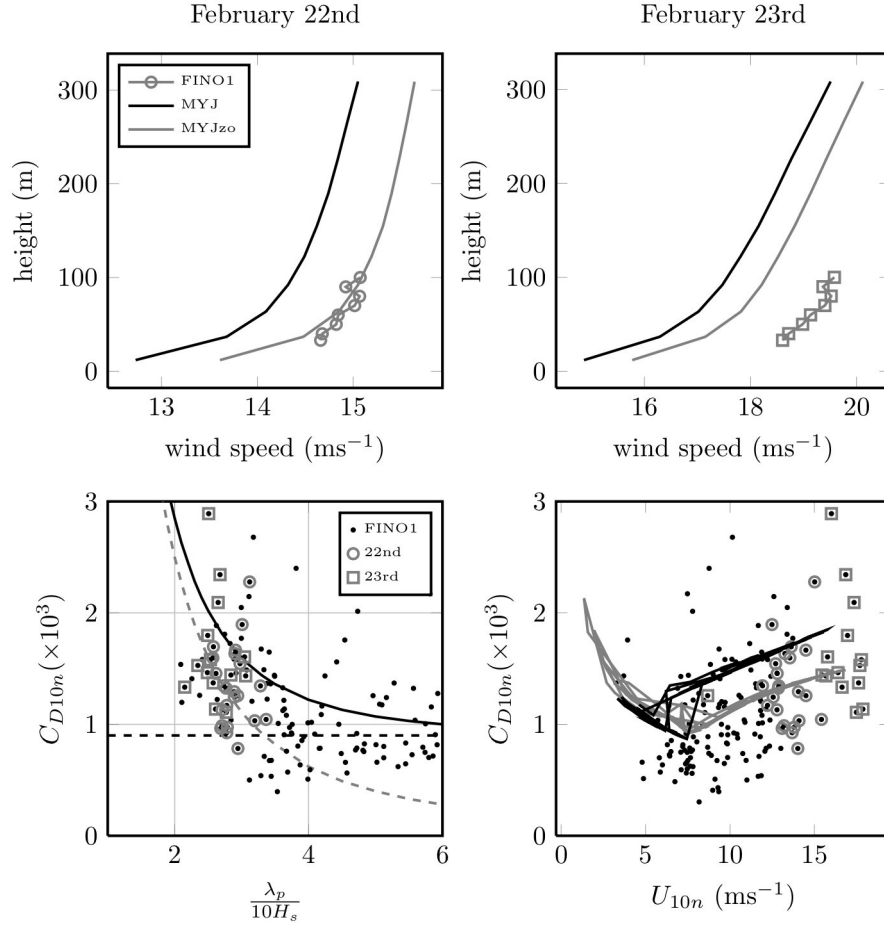


Figure 6.13: Top: Average wind speed profiles during the 22nd (left) and 23rd (right) as calculated by the standard MYJ model and compared with a modified roughness length (MYJzo) defined according to eq. (6.10), compared with average wind speed profiles at FINO1. Bottom left: Drag coefficients as a function of the aspect ratio. The solid black line is eq. (6.6); dashed black line is eq. (6.7); dashed gray line is eq. (6.8). Highlighted by circles and squares are points during the 22nd and 23rd, respectively. Bottom right: Drag coefficients as a function of wind speed. The solid black lines correspond with MYJ while the solid gray lines MYJzo.

Since neither Charnock's parametrization, nor the solution offered here with the constants $a_{1,2} = (0.046, -0.13)$ is general enough to account for the different flows potentially encountered at FINO1, further work could be done in this area to offer a more general solution. Fig. 6.13 demonstrates that if this can be made to work, an improved wind speed forecast could be possible. Since both the mean wind speed and Ti will be needed to anticipate offshore wind power within wind farms, improvement could also be gained in enhancing the calculation of turbulence intensity, where MYJ calculated turbulence intensities have been displayed in Fig. 6.14 (left). The time series in Fig. 6.12 (bottom)

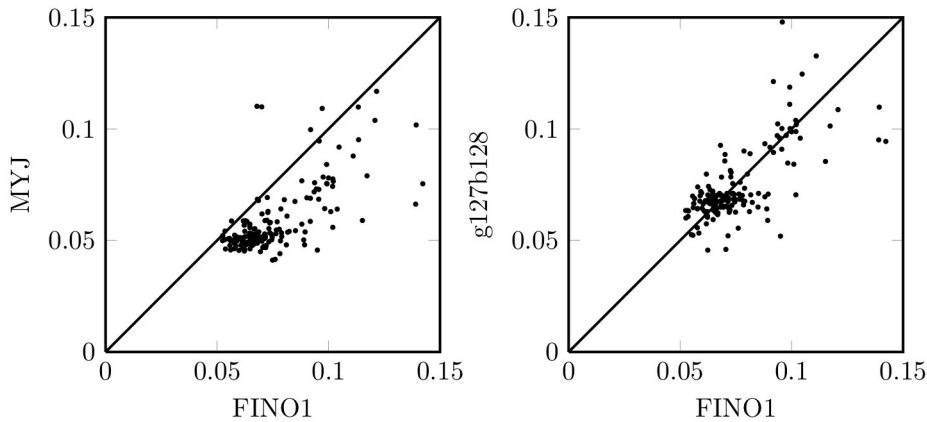


Figure 6.14: A direct comparison between the 80 m Ti as calculated by MYJ (left) and g127b128 (right) during February 20-28, 2005.

above showed that turbulence intensities are generally underpredicted during this period, except for possibly parts of the 24th and 25th. For example, this is particularly evident during the 27th when the Ti reaches 10% and wind speeds are about 13 ms^{-1} , where both these parameters have been underestimated. Some improvement in the calculation of Ti could be achieved for example, by using the modified MYJ case g127b128, where a more accurate calculation of Ti is evident compared with MYJ as displayed in Fig. 6.14 (right).

6.2.4 November, 2005

The period during November 9-16, 2005 is considered here which illustrates nicely the potential improvement in the calculation of offshore parameters if the changes suggested in this work as outlined in the introduction can be successfully implemented. Fig. 6.15 shows wind speeds at 80 m (top), wind (33 m) and wave directions (middle) and turbulence intensity (bottom) as calculated by MYJ in comparison with FINO1 measurements. Winds were predominantly from the south-west during this period which was generally unstably stratified, except for times during the 11th. It is also during the 11th when wind speeds were most accurately calculated by MYJ, compared with for example, during the 10th and the 14th.

For example, average wind speed profiles between 13:00 – 24:00 on the 11th and 14th are displayed in Fig. 6.16 (top) comparing FINO1 measurements with the MYJ model and the MYJ model (“MYJzo”) using a roughness length defined according to eq. (6.10) with $a_{1,2} = (0.046, -0.13)$ as with the February period. The wind speed profiles suggest that MYJ works better during the 11th and MYJzo works better during the 14th and the reason for this is once more explainable via drag coefficients as a function of the aspect ratio and wind speed as illustrated in Fig. 6.16 (bottom). The black points are FINO1 measurements for the entire period and the points highlighted by gray circles and squares correspond with the periods during the 11th and 14th (13:00 – 24:00), respectively. The solid and dashed lines in Fig. 6.16 (bottom left) are once more defined according to eqs. (6.6), (6.8) and (6.7) stated in the introduction of this chapter.

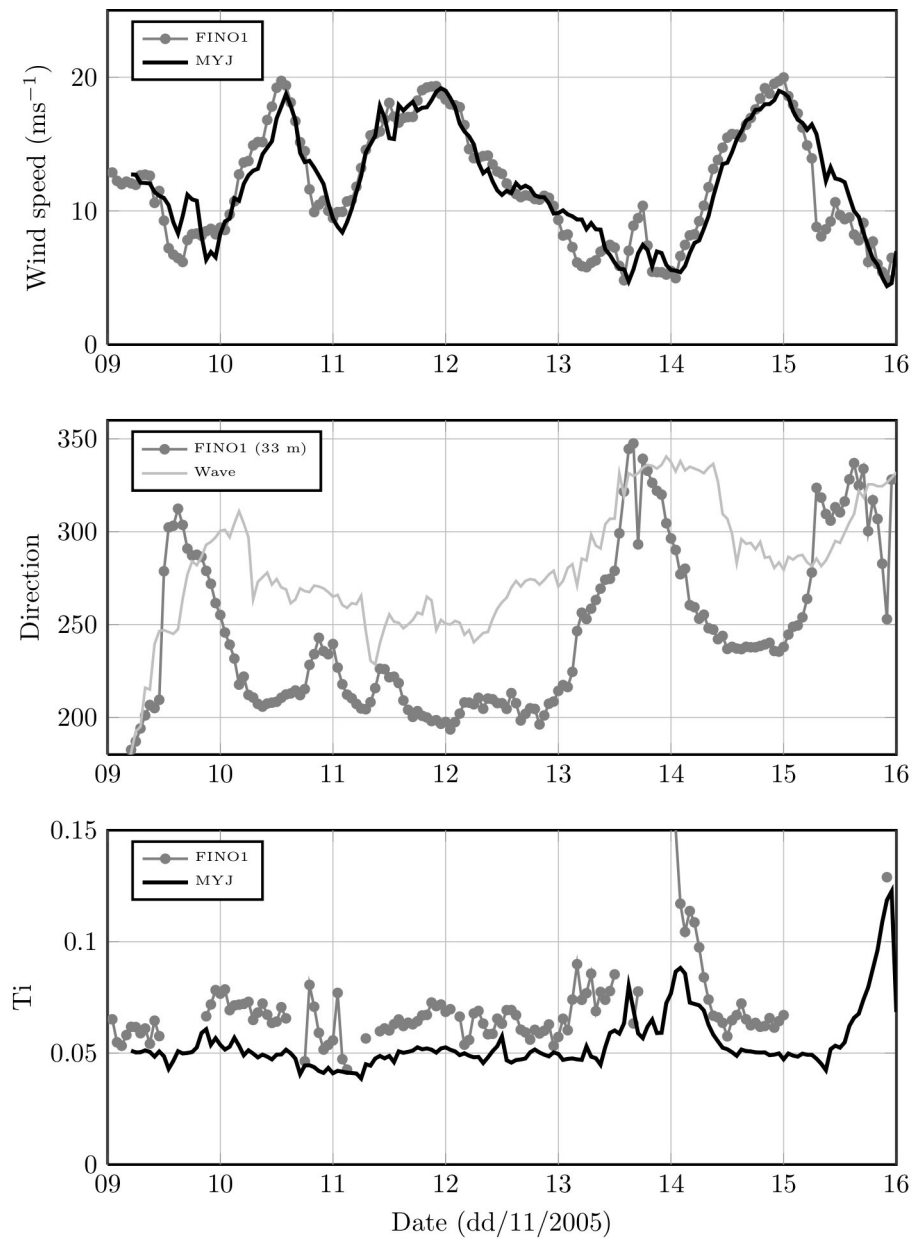


Figure 6.15: November 9-16, 2005: Wind speeds at 80 m (top), wind (33 m) and wave directions (middle) and turbulence intensity (bottom).

It can be seen that the periods during the 11th and the 14th correspond with an alternative wave steepness scaling; either according to the correlation, eq. (6.6) or the asymptotic wave steepness (6.8), respectively. The pure wave steepness scaling results in lower drag coefficients in general compared with the correlation and hence in a plot of $C_{D10n} = f(U_{10n})$, the drag coefficients during the 11th sit below those during the 14th as displayed in Fig. 6.16 (bottom

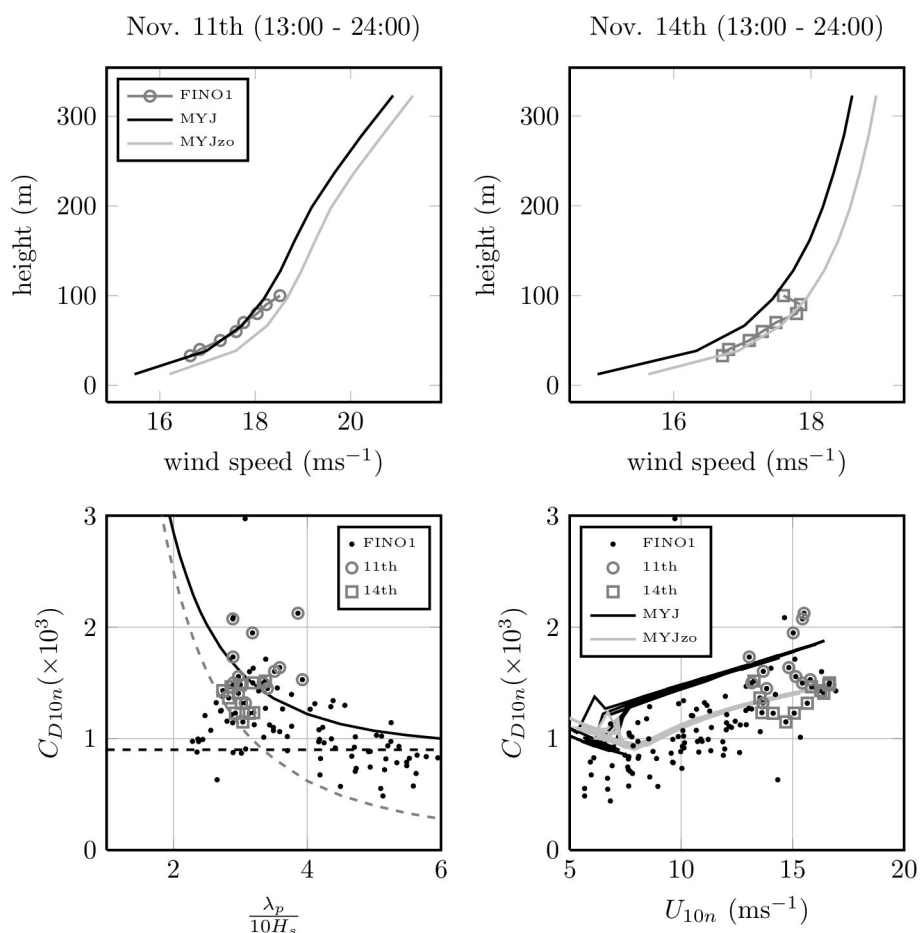


Figure 6.16: Top: Wind speed profiles for two 12 hour periods on the 11th (left) and 14th (right) November 2005 comparing profiles at FINO1 with the standard MYJ model and with a modified roughness (MYJzo) using eq. (6.10). Bottom: Drag coefficients for the entire 9-16 November period where the two 12 hour periods are highlighted as circles (11th) and squares (14th) as a function of one-tenth the aspect ratio (left) and the 10 m wind speed (right). Bottom left: The dashed and solid curves are defined in the text. Bottom right: The black and light gray curves correspond with MYJ and MYJzo, respectively.

right), despite being of the same wind speed. This will not be anticipated with standard roughness length parameterisations which are based principally on the wind speed (e.g. Fairall et al., 2003). The practical consequence of such a wind speed assumption is that the hub height wind speed is either over- or underestimated depending on the type of parametrization. For example, MYJzo gives $C_{D10n} = f(U_{10n})$ according to the light gray curve in Fig. 6.16 (bottom right) and passes through the squares indicating the 14th. However, this same curve underestimates the circles and hence during the 11th, wind speeds are overestimated in Fig. 6.16 (top left).

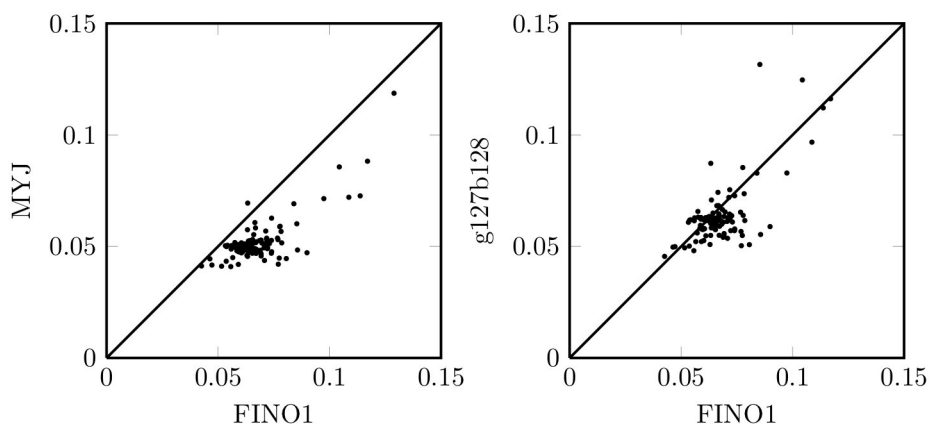


Figure 6.17: A direct comparison between the 80 m Ti as calculated by MYJ (left) and g127b128 (right) during November 9-16, 2005

It is interesting that the drag coefficients during the 11th November corresponding with times of stable stratification fit the correlation eq. (6.6), but during unstable (i.e. the rest of the period), fit better the pure wave steepness relation, eq. (6.8). Similarly, the stable January period with only a few exceptions (see chapter 3) generally scales with eq. (6.6), while the unstable February period generally scales with eq. (6.8). While there could be some latent stratification dependency within drag coefficients not accounted for in classical Monin-Obukhov similarity theory, any stratification dependency could be fortuitous as seen in wind (33 m) and wave directions above in Fig. 6.15 (middle). It can be seen that the wave direction during the 11th comes approximately from the east while during the 14th, the wave direction is fairly northerly. Similarly, the wave direction during February was predominantly from the north but easterly during January. For northerly flows, it could be possible that swell enters the North Sea via the corridor between Scotland and Norway (Geernaert et al., 1987), which is possibly what occurred during the February 2005 period shown above. There was possibly minimal swell during the more easterly 11th, and hence a more gradual transitional regime between the asymptote approximating smoothness ($C_{D10n}^{1/2} = \text{constant}$) and the asymptote describing complete roughness ($C_{D10n} = \frac{H_s^2}{\lambda_p^2}$), i.e. as indicated by the solid black curve in Fig. 6.16 (bottom left).

While a higher order analysis will be needed in order to more fully explain these issues, one can see from drag coefficients in Fig. 6.16 (bottom right) that a temporary measure could be to adopt a function as used in the case MYJzo in modelling offshore flows further from the coast or even to simply reduce Charnock's constant. However, be aware that this may result in overestimated wind speeds depending on the wave steepness as can be seen in average wind speed profiles in Fig. 6.16. In the meantime, there is some further potential improvement in the estimation of the expected power output within wind farms if undisturbed flow turbulence intensities are required. A direct comparison of turbulence intensities with FINO1 as calculated by MYJ and g127b128 is displayed in Fig. 6.17. Boundary layer heights as calculated by the model are O(500-1000

m) depending on time period and hence the hub height may sit just above the surface layer. For that reason, the standard MYJ model will consistently underpredict Ti as seen in Fig. 6.15 (bottom), while a modified MYJ version, g127b128 is able to better reproduce the measurements as seen in Fig. 6.17 (right). There it can be seen that g127b128 offers an improved calculation of Ti for the range of measurements during this period.

6.3 Conclusion

Modifications to the Mellor-Yamada-Janjić (MYJ) model as suggested in the previous chapters have been demonstrated in this chapter to offer a potential for an improved calculation in parameters of interest for wind energy applications. The modifications to some basic parameters of the Mellor-Yamada-Janjić (MYJ) boundary layer parametrization in the WRF model following tests in the single column model in the previous chapter have been demonstrated to give physically realistic results in three-dimensional simulations. Four particular periods from FINO1 as have been introduced in previous chapters (January, February and November, 2005 and May 2006) have been presented here due to their unique flow structure and high wind speeds relevant for the wind energy purposes. Two of these periods were in stable, while the other two in generally unstable stratification. The modelling strategy here which employs an alternative selection of some standard parameters as discussed in the previous chapter (i.e. in contrast to that done by Janjić (2002) and Mellor and Yamada (1982)), has been demonstrated to give an enhanced calculation of turbulence intensity. Whether this translates into a similar behaviour in parameters other than wind speed and turbulence intensity relevant to broader meteorological applications remains to be seen. At the very least, it could be useful for WRF users to switch back to the constants defined originally in Mellor and Yamada (1982) where for example during the May 2006 period, a better vertical structure of TKE as well as better represented wind profiles were detected compared with the existing version. The key difference between these two sets of constants is the critical Richardson number where the constants of Janjić (2002) continue to generate turbulence deep into the boundary layer where otherwise a rapid decay of TKE would otherwise be required during this period.

For those purely interested in enhancing the calculation of hub height turbulence intensity within the MYJ model, the strategy described in the previous section could be employed for that purpose. At FINO1 for example, setting $\gamma_1 = 0.27$ and $Ri_c = 0.2$ (giving $B_1 \approx 28$) could be a good choice there, although other options could be more optimal for other applications. At other sites, particularly onshore where there is a greater magnitude of turbulence, and/or if a higher resolution is required closer to the ground, increasing γ_1 while keeping Ri_c constant (or even reducing this) is also an option. Of most significant concern for those wanting more accurate wind speed forecasts in very stable stratification, one should look into reducing the magnitude of exchange coefficients above the boundary layer since when these are too high, insufficient wind shear within the boundary layer results. The extent to which this could degrade model performance from the perspective of numerical stability could on the other hand worsen results.

An enhanced offshore roughness length parametrization above that currently

used in WRF could also improve the calculation of wind speeds in general, with further relevance for wind energy purposes. However, the explicit dependence of the drag coefficient on the wave aspect ratio conducted based on a higher order analysis is required. Here it has been demonstrated that an enhanced calculation of the hub height wind speed will result if the roughness length parametrization takes into account the wave field unlike the currently used Charnock's parametrization. This was demonstrated using the empirical linear fits to $u_* = f(U_{10n})$ space as introduced in Chapter 2, in contrast to the non-linear dependence of u_* on U_{10n} as inferred from Charnock's parametrization. The different aspect ratio scaling introduced in Chapter 3 highlights different dependencies in $C_{D10n} = f(U_{10n})$ space not captured by conventional parametrizations. Here it is demonstrated that if the correct roughness parametrization offshore can be determined, improved wind speed profiles will result.

Chapter 7

Conclusions

The topic of calculating offshore parameters relevant for wind energy purposes as introduced in Chapter 1 has been pursued in this thesis. Concepts of similarity were either used or developed to help enhance the calculation of wind speed and turbulence intensity as expected in meteorological conditions far from the coast. These issues have not received as much attention in the past as other issues onshore for lack of observations, however with the development of offshore wind farms in the North Sea came the construction of meteorological masts such as the FINO1 tower, which has enabled work in this thesis to be undertaken. The work presented here will help improve understanding of offshore conditions and provide a framework for more progress to be made in this area.

The concept of an aerodynamic roughness length over water surfaces was introduced in Chapter 2. Roughness lengths over water surfaces are generally modelled using the classic Charnock (1955) parametrization. This parametrization is not believed to generally be valid at higher wind speeds where a rolling-off in the neutral drag coefficient, C_{D10n} as a function of the neutral 10 m wind speed is expected based on estimates in tropical cyclones. At very low wind speeds, the flow is expected to enter a smooth regime where the roughness length depends on viscosity. At intermediate regimes, the constant in Charnock's parametrization is ambiguous. This is likely because Charnock's parametrization is modelling the transitional roughness regime where complete similarity solutions are lacking. This regime broadly corresponds with wind speeds between 5 and 20 ms^{-1} . Hence, the difficulty in parametrizing the transitional roughness regime over water would be not unlike the difficulties handling this regime over well defined roughness elements over solid surfaces. Using the alternative drag law proposed in Chapter 2 based on measurements at FINO1, it can be seen that the drag coefficient levels-off at wind speeds at about 20 ms^{-1} , consistent with estimates in tropical cyclones. This is consistent with what is known over land where a constant drag coefficient and hence roughness length is found in the rough flow regime which occurs at nearly all practical wind speeds there. This also happens offshore, but it requires very high wind speeds to attain the completely rough flow regime.

To analyse these results further, a first-order scaling of C_{D10n} based on the wave field was presented in Chapter 3. By extending Toba's 3/2 power law to allow for a functional dependence of C_{D10n} on the wave field, it can be shown that

C_{D10n} scales with the squared wave steepness, $\left(\frac{H_s}{\lambda_p}\right)^2$ where H_s is the significant wave height and λ_p is the peak wave length. Pure wave steepness scaling will not be valid in the smooth flow regime since at low wind speeds, $\left(\frac{H_s}{\lambda_p}\right)^2 \rightarrow 0$, and thus so too will C_{D10n} . Instead, C_{D10n} is approximated as a constant at low wave steepnesses and an intermediate correlating equation can be used to combine the two scaling regimes. In analogy with rough and transitional flow regimes, pure wave steepness scaling is the rough flow regime and the correlation equation, $C_{D10n} = \left(0.03^3 + \left(\frac{H_s}{\lambda_p}\right)^3\right)^{2/3}$ represents a gradual transition between the smooth and rough flow regimes. It is found that C_{D10n} measured during the January 2005 period at FINO1 which demonstrated a levelling-off at high wind speeds in Chapter 2, was described better by the correlating equation. The C_{D10n} during the February 2005 period at FINO1 which demonstrated a much earlier levelling-off compared with during January 2005, scaled better with either a constant C_{D10n} at high aspect ratios (low wave steepness) and with the pure wave steepness at low aspect ratios. These results appear to be consistent with studies reported in the literature where evidence of both scaling regimes is seen, although most are in approximate agreement with the correlation equation. This equation was also tested using buoy measurements of H_s , λ_p and U_{10n} during hurricane Rita (2005), where a levelling-off of C_{D10n} is anticipated in deeper water, while a rapid increase in C_{D10n} is found in shallower water which possibly could be more consistent with storm surge modelling.

Higher order wind wave interaction was further studied in Chapter 4, where a unique case at FINO1 gave a persistent wind direction bringing dryer and warmer continental air over the still cold North Sea water. Consequently, a clear diurnal cycle not often evident offshore was detected by the FINO1 platform during this May 2006 period where time series showed diurnal cycles in wind speed, wind direction, relative humidity and temperature. The cyclic wind direction, which correspondingly orientates itself at an angle to the wave direction resulted in half day oscillations in the wave steepness, and consequently C_{D10n} . These processes were shown to broadly correlate with each other, but future work will be required to describe this in more detail where unique offshore flows such as this May 2006 period may prove useful. The nature of the flow facilitated estimation of the outer length scale using the analysis previously developed in the literature, where estimates yielded heights $O(100\text{ m})$. This implies the FINO1 tower was able to detect a relatively large vertical portion of this stable internal boundary layer. By assuming a functional form of the local friction velocities as measured during this period at FINO1, the friction velocity, u_* was further estimated. Following these assumptions, turbulent kinetic energy (TKE) measurements at FINO1 were scaled using outer layer scaling and were found to broadly agree with that found previously. In comparison with measurements, the Mellor-Yamada-Janjić (MYJ) boundary layer parametrization within the Weather Research and Forecasting (WRF) model was found to underpredict measurements close to the surface and overpredict them towards the top. The net result is an underpredicted wind speed which then led to investigations into the MYJ parametrization itself.

The MYJ parametrization was investigated in Chapter 5 where it is shown that the model closure constants are based on out-dated similarity theory and

hence are not general. There are some practical constraints to how the constants can be modified which limits the increase in the magnitude of certain parameters in practice. To get around this issue, an alternative strategy was employed which relaxes certain previously employed criteria with regards to specification of the lateral and vertical fluctuating velocities. This is apparently allowable since these are assumed to be constant within the model, an assumption not reflective of reality. The key to this strategy is to ensure a positive model critical Richardson number using the analysis of Janjić (2002) in addition to changing the surface length scale in stable stratification in order to accurately model dimensionless wind and temperature gradients. A number of different versions of closure constants and length scales were tested in the single column model in WRF where the default setup as based on the CASES-99 field study was run. In comparison with tower measurements during CASES-99, the existing MYJ parameters and those specified by Mellor and Yamada (1982), the different model versions gave realistic wind speeds at least at lower levels, with an increased TKE towards the surface. Tests in real simulations were however left to Chapter 6.

Chapter 6 was then able to demonstrate that if concepts suggested above could be effectively implemented in the WRF model, an improved calculation of wind speed and turbulence intensity by the WRF model is possible. The four particular periods at FINO1 referred to above were used to test the changes to the MYJ model and changes to the roughness length. Importantly, changes to the MYJ model (here labelled as “g127b128”) demonstrated a realistic physical behaviour during the very stable May 2006 period and the weakly stable January 2005 period based on comparisons with the existing MYJ model, the traditional Mellor and Yamada (1982) constants and measurements at FINO1. Both the Mellor and Yamada (1982) and g127b128 model versions gave better wind speeds and turbulence intensity compared with MYJ during May 2006. The key difference between Mellor and Yamada (1982) and MYJ is the critical Richardson number, whereby MYJ’s value is higher, and will continue producing turbulence beyond that suggested by FINO1 measurements. Further improvements in wind speed will need to take into account the magnitude of exchange coefficients above the boundary layer height. The g127b128 configuration further demonstrated an enhanced calculation of turbulence intensity during January, February and November, 2005 compared with MYJ which would make it ideal for those wanting to include some estimate of turbulence intensity in their wind power estimates further offshore. Different parameters using the strategy proposed in Chapter 5 could be more effective onshore. With regards to the offshore roughness length, an alternative parametrization to Charnock’s was used to demonstrate that a more complex consideration for the roughness length would be useful in enhancing wind speed estimates. Since neither approach is general in that both lack a consideration for the wave field, both will perform to varying degrees of success depending on the underlying wave field. A successful solution to this problem requiring a higher order analysis than that given here and successful implementation into the model will improve the calculation of hub height wind speeds.

Bibliography

- Amorochio, J. and Devries, J. (1980), “A new evaluation of the wind stress coefficient over water surfaces”, *J. Geophysical Res.* , Vol. 85, pp. 433–443.
- Anderson, R. (1993), “A study of wind stress and heat flux over the open ocean by the inertial-dissipation method”, *J. Phys. Oceanogr.* , Vol. 23, pp. 2153–2161.
- Andre, J. and Mahrt, L. (1982), “The nocturnal surface inversion and influence of clear-air radiative cooling”, *J. Atm. Sci.* , Vol. 39, pp. 864–878.
- Andre, J., Moor, G. D., Lacarrère, P., Therry, G. and Vachat, R. D. (1978), “Modeling the 24-hour evolution of the mean and turbulent structures of the planetary boundary layer”, *J. Atm. Sci.* , Vol. 35, pp. 1861–1883.
- Andreas, E. and Emanuel, K. (2001), “Effects of sea spray on tropical cyclone intensity”, *J. Atmos. Sci.* , Vol. 58, pp. 3741–3751.
- Andrén, A. (1990), “Evaluation of a turbulence closure scheme suitable for air-pollution applications”, *J. Appl. Meteor.* , Vol. 29, pp. 224–239.
- Banner, M. L. and Peirson, W. L. (1998), “Tangential stress beneath wind-driven air-water interfaces”, *J. Fluid Mech.* , Vol. 364, pp. 115–145.
- Banta, R. M., Pichugina, Y. L. and Brewer, W. A. (2006), “Turbulent velocity-variance profiles in the stable boundary layer generated by a nocturnal low-level jet”, *Journal of Atmospheric Sciences* , Vol. 63, pp. 2700–2719.
- Barenblatt, G. (1993), “Scaling laws for fully developed turbulent shear flows. part 1. basic hypotheses and analysis.”, *J. Fluid Mech.* , Vol. 248, pp. 513–20.
- Barthelmie, R., Frandsen, S., Rethore, P. and Jensen, L. (2007), Analysis of atmospheric impacts on the development of wind turbine wakes at the Nysted wind farm, in ‘Proceedings of the European Offshore Wind Conference’.
- Barthelmie, R. J., Grisogono, B. and Pryor, S. C. (1996), “Observations and simulations of diurnal cycles of near-surface wind speeds over land and sea”, *J. Geophys. Res.* , Vol. 1012, pp. 21327–21338.
- Barthelmie, R. and Palutikof, J. (1996), “Coastal wind speed modelling for wind energy applications”, *J. Wind Eng. Ind. Aerodyn.* , Vol. 62, pp. 213–236.
- Black, P., D’Asaro, E., Drennan, W., French, J., Niiler, P., Sanford, T., Terrill, E., Walsh, E. and Zhang, J. (2007), “Air-sea exchange in hurricanes”, *Bull. Amer. Meteor. Soc.* , Vol. 88, pp. 357–374.

- Bradshaw, P. (2000), “A note on “critical roughness height” and “transitional roughness””, *Phys. Fluids* , Vol. 12, pp. 1611–1614.
- Brandt, A. and Farrell, A. (2007), “Scraping the bottom of the barrel: greenhouse gas emission consequences of a transition to low-quality and synthetic petroleum resources”, *Climatic Change* , Vol. 84, pp. 241–263.
- Breton, S. and Moe, G. (2009), “Status, plans and technologies for offshore wind turbines in Europe and North America”, *Renewable Energy* , Vol. 34, pp. 646–654.
- Brooks, I. and Rogers, D. (2000), “Aircraft observations of the mean and turbulent structure of a shallow boundary layer over the Persian Gulf”, *Boundary-Layer Meteorol* , Vol. 95, pp. 189–210.
- Businger, J., Wyngaard, J., Iyumi, Z. and Bradley, E. (1971), “Flux-profile relationships in the atmospheric surface layer”, *J. Atmos. Sci.* , Vol. 28, pp. 181–189.
- Buzzi, M., Rotach, M. W., Holtslag, M. and Holtslag, A. A. M. (2011), “Evaluation of the COSMO-SC turbulence scheme in a shear-driven stable boundary layer”, *Meteorologische Zeitschrift* , Vol. 20, pp. 335–350.
- Carlier, J. and Stanislas, M. (2005), “Experimental study of eddy structures in a turbulent boundary layer using particle image velocimetry”, *J. Fluid Mech.* , Vol. 535, pp. 143–188.
- Carson, D. J. and Richards, P. J. R. (1978), “Modelling surface turbulent fluxes in stable conditions”, *Boundary-Layer Meteorology* , Vol. 14, pp. 67–81.
- Caughey, S., Wyngaard, J. and Kaimal, J. (1979), “Turbulence in the evolving stable boundary layer”, *J. Atm. Sci.* , Vol. 36, pp. 1041–1052.
- Charnock, H. (1955), “Wind stress on a water surface”, *Quart. J. Roy. Meteor.* , Vol. 81, pp. 639–640.
- Churchill, S. and Usagi, R. (1972), “A general expression for the correlation of rates of transfer and other phenomena”, *AIChE J.* , Vol. 18, pp. 1121–1128.
- Craig, R. (1949), “Vertical eddy transfer of heat and water vapour in stable air”, *J. Atm. Sci.* , Vol. 6, pp. 123–133.
- Csanady, G. (1974), “Equilibrium theory of the planetary boundary layer with an inversion lid”, *Boundary-Layer Meteorol* , Vol. 6, pp. 63–79.
- Csanady, G. (2001), *Air-sea interaction: Laws and Mechanisms*, Cambridge University Press.
- Cuxart, J., Holtslag, A. A. M., Beare, R. J., Bazile, E., Beljaars, A., Cheng, A., Conangla, L., Ek, M., Freedman, F., Hamdi, R., Kerstein, A., Kitagawa, H., Lenderink, G., Lewellen, D., Mailhot, J., Mauritsen, T., Perov, V., Schayes, G., Steeneveld, G.-J., Svensson, G., Taylor, P., Weng, W., Wunsch, S. and Xu, K.-M. (2006), “Single-column model intercomparison for a stably stratified atmospheric boundary layer”, *Boundary-Layer Meteorology* , Vol. 118, pp. 273–303.

- DeGraaff, D. and Eaton, J. (2000), “Reynolds-number scaling of the flat-plate turbulent boundary layer”, *J. Fluid Mech.* , Vol. 422, pp. 319–346.
- Det Norske Veritas (2010), Environmental conditions and environmental loads, recommended practice, Technical Report DNV-RP-C205.
- Devries, O. (1979), “Fluid dynamic aspects of wind energy conversion”, *NASA STI/Recon Technical Report N* , Vol. 80.
- Dobson, F., Smith, S. and Anderson, R. (1994), “Measuring the relationship between wind stress and sea state in the open ocean in the presence of swell”, *Atmos.-Ocean* , Vol. 32, pp. 237–256.
- Donelan, M. (1982), The dependence of the aerodynamic drag coefficient on wave parameters, *in* ‘In Proceedings of the First Int. Conf. on Meteorology and Air-Sea Interaction of the Coastal Zone’, pp. 381–387.
- Donelan, M. (1990), Air-sea interaction, *in* B. LeMehaute and D. M. Hanes, eds, ‘The Sea’, Wiley-Interscience, Hoboken, N.J., pp. 239–292.
- Donelan, M., Drennan, W. and Katsaros, K. (1997), “The air-sea momentum flux in conditions of wind sea and swell”, *J. Phys. Oceanogr.* , Vol. 27, pp. 2087–2099.
- Donelan, M., Haus, B., N.Reul, Plant, W., Stiassnie, M., Graber, H., Brown, O. and Saltzman, E. (2004), “On the limiting aerodynamic roughness of the ocean in very strong winds”, *Geophys. Res. Lett.* , Vol. 31, p. L18306.
- Drennan, W., Graber, H. and Donelan, M. (1999), “Evidence for the effects of swell and unsteady winds on marine wind stress”, *J. Phys. Oceanogr.* , Vol. 29, pp. 1853–1864.
- Drennan, W., Taylor, P. and Yelland, M. (2005), “Parameterizing the sea surface roughness”, *J. Phys. Oceanogr.* , Vol. 35, pp. 835–848.
- Elliott, D. and Barnard, J. (1990), “Observations of wind turbine wakes and surface roughness effects on wind flow variability”, *Solar Energy* , Vol. 45, pp. 265 – 283.
- Elliott, D. L. (1991), Status of wake and array loss research, *in* ‘21st American Wind Energy Association Conference: Windpower 1991, Palm Springs, CA, 24-27 Sep. 1991’.
- Emanuel, K. (1995), “Sensitivity of tropical cyclones to surface exchange coefficients and a revised steady-state model incorporating eye dynamics”, *J. Atmos. Sci.* , Vol. 52, pp. 3969–3976.
- Emeis, S. (2010a), “Meteorological explanation of wake clouds at Horns Rev wind farm”, *DEWI Magazine* , Vol. 37, pp. 52–55.
- Emeis, S. (2010b), “A simple analytical wind park model considering atmospheric stability”, *Wind Energ.* , Vol. 13, pp. 459–469.
- Emeis, S. and Frandsen, S. (1993), “Reduction of horizontal wind speed in a boundary layer with obstacles”, *Boundary-Layer Meteorol* , Vol. 64, pp. 297–305.

- Emeis, S. and Türk, M. (2009), “Wind-driven wave heights in the German Bight”, *Ocean Dynamics*, Vol. 59, pp. 463–475.
- EWEA (2011), Wind in our Sails - The coming of Europe’s offshore wind energy industry, Technical report, The European Wind Energy Association.
- Fairall, C., Bradley, E., Hare, J., Grachev, A. and Edson, J. (2003), “Bulk parameterization of air-sea fluxes: Updates and verification for the coare algorithm”, *J. Climate*, Vol. 216, pp. 571–591.
- Fernholz, H. and Finley, P. (1996), “The incompressible zero-pressure-gradient turbulent boundary layer: an assessment of the data”, *Prog. Aerospace Sci.*, Vol. 32, pp. 245–311.
- French, J., Drennan, W., Zhang, J. and Black, P. (2007), “Turbulent fluxes in the hurricane boundary layer. part 1: momentum flux”, *J. Atm. Sci.*, Vol. 64, pp. 1089–1102.
- Friedlingstein, P., Houghton, R. A., Marland, G., Hackler, J., Boden, T. A., Conway, T. J., Canadell, J. G., Raupach, M. R., Ciais, P. and Le Quéré, C. (2010), “Update on CO₂ emissions”, *Nature Geoscience*, Vol. 3, pp. 811–812.
- Garratt, J. (1977), “Review of drag coefficients over oceans and continents”, *Mon. Wea. Rev.*, Vol. 105, pp. 915–929.
- Garratt, J. (1987), “The stably stratified internal boundary layer for steady and diurnally varying offshore flow”, *Boundary-Layer Meteorol*, Vol. 38, pp. 369–394.
- Garratt, J. (1990), “The internal boundary layer - a review”, *Boundary-Layer Meteorol*, Vol. 50, pp. 171–203.
- Garratt, J. and Ryan, B. (1989), “The structure of the stably stratified internal boundary layer in offshore flow over the sea”, *Boundary-Layer Meteorol*, Vol. 47, pp. 17–40.
- Geernaert, G., Hansen, F., Courtney, M. and Herbers, T. (1993), “Directional attributes of the ocean surface wind stress vector”, *J. Geophys. Res.*, Vol. 98, pp. 16,571–16,582.
- Geernaert, G., Larsen, S. and Hansen, F. (1987), “Measurements of the wind stress, heat flux, and turbulence intensity during storm conditions over the north sea”, *J. Geophys. Res.*, Vol. 92, pp. 13,127–13,139.
- Grachev, A. A., Andreas, E. L., Fairall, C. W., Guest, P. S. and Persson, P. O. G. (2007), “SHEBA flux-profile relationships in the stable atmospheric boundary layer”, *Boundary-Layer Meteorology*, Vol. 124, pp. 315–333.
- Grachev, A. A. and Fairall, C. W. (2001), “Upward momentum transfer in the marine boundary layer”, *Journal of Physical Oceanography*, Vol. 31, pp. 1698–1711.
- Grachev, A., Fairall, C., Hare, J., Edson, J. and Miller, S. (2003), “Wind stress vector over ocean waves”, *J. Phys. Oceanogr.*, Vol. 33, pp. 2408–2428.

- Grant, A. L. M. (1986), "Observations of boundary layer structure made during the 1981 KONTUR experiment", *Quarterly Journal of the Royal Meteorological Society*, Vol. 112, pp. 825–841.
- Hidy, G. and Plate, E. (1966), "Wind action on water standing in a laboratory channel", *J. Fluid Mech.*, Vol. 26, pp. 651–687.
- Högström, U. (1996), "Review of some basic characteristics of the atmospheric surface layer", *Boundary-Layer Meteorology*, Vol. 78, pp. 215–246.
- Holt, T. and Raman, S. (1988), "A review and comparative evaluation of multi-level boundary layer parameterizations for first order and turbulent kinetic energy closure schemes", *Reviews of Geophysics*, Vol. 26, pp. 761–780.
- Hsu, S. (1974), "A dynamic roughness equation and its application to wind stress determination at the air-sea interface", *J. Phys. Oceanogr.*, Vol. 4, pp. 116–120.
- Hutchins, N., Nickels, T., Marusic, I. and Chong, M. (2009), "Hot-wire spatial resolution issues in wall-bounded turbulence", *J. Fluid Mech.*, Vol. 635, pp. 103–136.
- Janjić, Z. (1994), "The step-mountain eta coordinate model: Further developments of the convection, viscous sublayer, and turbulence closure schemes", *Monthly Weather Review*, Vol. 122, pp. 927–945.
- Janjić, Z. (2002), Nonsingular implementation of the Mellor-Yamada Level 2.5 scheme in the NCEP Meso model, Technical report, National Centers for Environmental Prediction, Office Note No. 437.
- Janjić, Z. I. (1990), "The step-mountain coordinate: Physical package", *Mon. Wea. Rev.*, Vol. 118, pp. 1429–1443.
- Janssen, J. (1997), "Does the wind stress depend on sea-state or not? - A statistical error analysis of HEXMAX data", *Boundary-Layer Meteorology*, Vol. 83, pp. 479–503.
- Jiménez, J. (2004), "Turbulent flows over rough walls", *Annu. Rev. Fluid Mech.*, Vol. 36, pp. 173–196.
- Johnson, H., Hojstrup, J., Vested, H. and Larsen, S. (1998), "On the dependence of sea surface roughness on wind waves", *J. Phys. Oceanogr.*, Vol. 28, pp. 1702–1716.
- Jones, I. and Toba, Y., eds (2001), *Wind Stress over the Ocean*, Cambridge University Press.
- Kenning, V. and Crowe, C. (1997), "On the effect of particles on carrier phase turbulence in gas-particle flows", *Int. J. Multiphase Flow*, Vol. 23, pp. 403–408.
- Klebanoff, P. (1955), Characteristics of turbulence in a boundary layer with zero pressure gradient, Technical Report 1247, Natl. Adv. Comm. for Aeronaut., Washington, D.C.

- Kolmogorov, A. (1942), "Equations of motion of an incompressible fluid", *Izv. Akad. Nauk. SSSR, Ser. Fiz.*, Vol. 6, pp. 56–58.
- Kotsch, W. (1977), *Weather for the mariner*, Naval institute press.
- Kühnel, D. and Neumann, T. (2010), "Adventure Offshore - RAVE Installations 2009", *DEWI Magazine*, Vol. February, pp. 64–67.
- Kunkel, G. and Marusic, I. (2006), "Study of the near-wall-turbulent region of the high-reynolds-number boundary layer using an atmospheric flow", *J. Fluid Mech.*, Vol. 548, pp. 375–402.
- Lange, B. (2007), Offshore wind power meteorology, in J. Peinke, P. Schaumann and S. Barth, eds, 'Wind Energy', Springer Berlin Heidelberg, pp. 1–6.
- Lange, B., Johnson, H., Larsen, S., Hojstrup, J., Hansen, H. and Yelland, M. (2004), "On the detection of a wave age dependency for the sea surface roughness", *J. Phys. Oceanogr.*, Vol. 34, pp. 1441–1458.
- Larsen, X., Makin, V. and Smedman, A. (2003), "Impact of waves on the sea drag: measurements in the baltic sea and a model interpretation", *The Global Atmosphere and Ocean System*, Vol. 9, pp. 97–120.
- Laufer, J. (1954), The structure of turbulence in a fully developed pipe flow, Technical Report 1174, Natl. Adv. Comm. for Aeronaut., Washington, D.C.
- Luhar, A. K., Hurley, P. J. and Rayner, K. N. (2009), "Modelling near-surface low winds over land under stable conditions: Sensitivity tests, flux-gradient relationships, and stability parameters", *Boundary-Layer Meteorology*, Vol. 130, pp. 249–274.
- Lumley, J. L. and Panofsky, H. A. (1964), *The structure of atmospheric turbulence*, Interscience Monographs and Texts in Physics and Astronomy, New York: Wiley.
- Mahrt, L. (1998), "Stratified atmospheric boundary layers and breakdown of models", *Theoretical and Computational Fluid Dynamics*, Vol. 11, pp. 263–279.
- Mahrt, L. (1999), "Stratified atmospheric boundary layers", *Boundary-Layer Meteorol.*, Vol. 90, pp. 375–396.
- Mahrt, L. and Vickers, D. (2002), "Contrasting vertical structures of nocturnal boundary layers", *Boundary-Layer Meteorol.*, Vol. 105, pp. 351–363.
- Mahrt, L. and Vickers, D. (2003), "Formulation of turbulent fluxes in the stable boundary layer", *J. Atmos. Sci.*, Vol. 60, pp. 2538–2548.
- Mahrt, L., Vickers, D., Frederickson, P., Davidson, K. and Smedman, A.-S. (2003), "Sea-surface aerodynamic roughness", *J. Geophys. Res.*, Vol. 108, p. 3171.
- Marusic, I. and Kunkel, G. (2003), "Streamwise turbulence intensity formulation for flat plate boundary layers", *Phys. Fluids*, Vol. 15, pp. 2461–2464.

- Marusic, I., McKeon, B., Monkewitz, P., Nagib, H., Smits, A. and Sreenivasan, K. (2010), “Wall-bounded turbulence flows at high reynolds numbers: Recent advances and key issues”, *Physics of Fluids*, Vol. 22.
- Marusic, I., Uddin, A. and Perry, A. (1997), “Similarity law for the stream-wise turbulence intensity in zero-pressure-gradient turbulent boundary layers”, *Phys. Fluids*, Vol. 9, pp. 3718–3726.
- Mellor, G. (1973), “Analytic prediction of the properties of stratified planetary surface layers”, *J. Atm. Sci.*, Vol. 30, pp. 1061–1069.
- Mellor, G. L. and Yamada, T. (1982), “Development of a turbulence closure model for geophysical fluid problems”, *Rev. Geophys. Space Phys.*, Vol. 20, pp. 851–875.
- Mellor, G. and Yamada, T. (1974), “A hierarchy of turbulence closure models for planetary boundary layers”, *J. Atmos. Sci.*, Vol. 31, pp. 1791–1806.
- Merzi, N. and Graf, W. H. (1988), “Wind stress over water waves: Field experiments on lake of Geneva”, *Meteorology and Atmospheric Physics*, Vol. 39, pp. 14–24.
- Metzger, M., McKeon, B. and Holmes, H. (2007), “The near-neutral atmospheric surface layer: turbulence and non-stationarity”, *Phil. Trans. R. Soc. A*, Vol. 365, pp. 859–876.
- Mohr, S. and Evans, G. (2009), “Forecasting coal production until 2100”, *Fuel*, Vol. 88, pp. 2059–2067.
- Mohr, S. and Evans, G. (2010), “Long term prediction of unconventional oil production”, *Energy Policy*, Vol. 38, pp. 265–276.
- Monin, A. and Obukhov, A. (1954), “Basic laws of turbulent mixing in the surface layer of the atmosphere”, *Tr. Akad. Nauk SSSR Geophys. Inst.*, Vol. 24, pp. 163–187.
- Moon, I.-J., Ginis, I., Hara, T. and Thomas, B. (2007), “A physics-based parameterization of air sea momentum flux at high wind speeds and its impact on hurricane intensity predictions”, *Monthly Weather Review*, Vol. 135, pp. 2869–2878.
- Mulhearn, P. (1981), “On the formation of a stably stratified internal boundary-layer by advection of warm air over a cooler sea”, *Boundary-Layer Meteorol.*, Vol. 21, pp. 247–254.
- Munson, B., Young, D. and Okiishi, T. (2002), *Fundamentals of Fluid Mechanics*, John Wiley & Sons.
- Nakanishi, M. (2001), “Improvement of the Mellor-Yamada turbulence closure model based on large-eddy simulation data”, *Boundary-Layer Meteorol.*, Vol. 99, pp. 349–378.
- Nakanishi, M. and Niino, H. (2004), “An improved Mellor-Yamada level-3 model with condensation physics: its design and verification”, *Boundary-Layer Meteorol.*, Vol. 112, pp. 1–31.

- Nakanishi, M. and Niino, H. (2006), “An improved Mellor-Yamada level-3 model: its numerical stability and application to a regional prediction of advection fog”, *Boundary-Layer Meteorol.* , Vol. 119, pp. 397–407.
- Neumann, T., Westerhellweg, A., Canadillas, B., Herklotz, K. and Outzen, O. (2010), New tasks for FINO1 - the research platform after installation of the first German offshore wind farm “alpha-ventus” and the start of “RAVE”, in ‘10th German Wind Energy Conference (DEWEK 2010) Bremen, Germany’.
- Nicholls, S. and Readings, C. J. (1979), “Aircraft observations of the structure of the lower boundary layer over the sea”, *Quarterly Journal of the Royal Meteorological Society* , Vol. 105, pp. 785–802.
- Nieuwstadt, F. T. M. (1984), “The turbulent structure of the stable, nocturnal boundary layer”, *Journal of Atmospheric Sciences* , Vol. 41, pp. 2202–2216.
- Nikuradse, J. (1933), “Strömgesetze in rauhen Röhren”, *Forschg. Arb. Ing.-Wes.* , Vol. 361, pp. 1–22.
- Österlund, J. (1999), Experimental studies of zero pressure-gradient turbulent boundary layer flow, PhD thesis, Royal Institute of Technology, Department of Mechanics,, Stockholm, Sweden.
- Outzen, O., Herklotz, K., Heinrich, H. and Lefebvre, C. (2008), “Extreme waves at FINO 1 research platform caused by storm “Tilo” on 9 November 2007”, *DEWI Magazine* , Vol. August, pp. 17–23.
- Panofsky, H. A. and Dutton, J. A. (1984), *Atmospheric turbulence. Models and methods for engineering applications.*
- Panofsky, H. A., Tennekes, H., Lenschow, D. H. and Wyngaard, J. C. (1977), “The characteristics of turbulent velocity components in the surface layer under convective conditions”, *Boundary-Layer Meteorology* , Vol. 11, pp. 355–361.
- Paulson, C. (1970), “The mathematical representation of wind speed and temperature profiles in the unstable atmospheric surface layer”, *Journal of Applied Meteorology* , Vol. 9, pp. 857–861.
- Perry, A. and Abell, C. (1975), “Scaling laws for pipe-flow turbulence”, *J. Fluid Mech.* , Vol. 67, pp. 257–271.
- Petersen, G. and Renfrew, I. (2009), “Aircraft-based observations of air-sea fluxes over Denmark Strait and the Irminger Sea during high wind speed conditions”, *Q. J. R. Meteorol. Soc.* , Vol. 135, p. DOI: 10.1002/qj.455.
- Poulos, G. S., Blumen, W., Fritts, D. C., Lundquist, J. K., Sun, J., Burns, S. P., Nappo, C., Banta, R., Newsom, R., Cuxart, J., Terradellas, E., Balsley, B. and Jensen, M. (2002), “CASES-99: A Comprehensive Investigation of the Stable Nocturnal Boundary Layer”, *Bulletin of the American Meteorological Society* , Vol. 83, pp. 555–581.
- Powell, M., Vickery, P. and Reinhold, T. (2003), “Reduced drag coefficient for high wind speeds in tropical cyclones”, *Nature* , Vol. 422, pp. 279–283.

- Raupach, M., Antonia, R. and Rajagopalan, S. (1991), "Rough-wall turbulent boundary layers", *Appl. Mech. Rev.*, Vol. 44, pp. 1–25.
- Rieder, K. (1997), "Analysis of sea-surface drag parameterisations in open ocean conditions", *Boundary-Layer Meteorology*, Vol. 82, pp. 355–377.
- Rotta, J. (1951), "Statistische Theorie nichthomogener Turbulenz", *Z. Phys.*, Vol. 129, pp. 547–572.
- Shockling, M. A., Allen, J. J. and Smits, A. J. (2006), "Roughness effects in turbulent pipe flow", *Journal of Fluid Mechanics*, Vol. 564, pp. 267–285.
- Skamarock, W. C., Klemp, J. B., Dudhia, J., Gill, D. O., Barker, D. M., Duda, M. G., Huang, X., Wang, W. and Powers, J. (2008), A Description of the Advanced Research WRF Version 3, Technical report, National Center for Atmospheric Research.
- Smedman, A. (1988), "Observations of a multi-level turbulence structure in a very stable atmospheric boundary layer", *Boundary-Layer Meteorology*, Vol. 44, pp. 231–253.
- Smedman, A., Bergström, H. and Grisogono, B. (1997), "Evolution of stable internal boundary layers over a cold sea", *J. Geophys. Res.*, Vol. 102, pp. 1091–1099.
- Smedman, A.-S., Bergström, H. and Högström, U. (1995), "Spectra, variances and length scales in a marine stable boundary layer dominated by a low level jet", *Boundary-Layer Meteorology*, Vol. 76, pp. 211–232.
- Smith, S. (1980), "Wind stress and heat flux over the ocean in gale force winds", *J. Phys. Oceanogr.*, Vol. 10, pp. 709–726.
- Smith, S., Anderson, R., Oost, W., Kraan, C., Maat, N., DeCosmo, J., Katsaros, K., Davidson, K., Bumke, K., Hasse, L. and Chadwick, H. (1992), "Sea surface wind stress and drag coefficients: The HEXOS results", *Boundary-Layer Meteorol.*, Vol. 60, pp. 109–142.
- Smith, S. and Banke, E. (1975), "Variation of the sea surface drag coefficient with wind speed", *Quart. J. R. Met. Soc.*, Vol. 101, pp. 665–673.
- Smith, S. D. (1988), "Coefficients for sea surface wind stress, heat flux, and wind profiles as a function of wind speed and temperature", *J. Geophys. Res.*, Vol. 93, pp. 15467–15472.
- Smith, S., Katsaros, K., Oost, W. and Mestayer, P. (1996), "The impact of the HEXOS programme", *Boundary-Layer Meteorology*, Vol. 78, pp. 121–141.
- Söderbergh, B., Robelius, F. and Aleklett, K. (2007), "A crash programme scenario for the Canadian oil sands industry", *Energy Policy*, Vol. 35, pp. 1931–1947.
- Stensrud, D. (2007), *Parametrization Schemes: Keys to Understanding Numerical Weather Predictional Models*, Cambridge University Press.

- Stull, R. (1988), *An Introduction to Boundary Layer Meteorology*, Kluwer Academic Publishers.
- Sullivan, P. and McWilliams, J. (2010), “Dynamics of winds and currents coupled to surface waves”, *Annu. Rev. Fluid Mech.* , Vol. 42, pp. 19–42.
- Sušelj, K. and Sood, A. (2010), “Improving the Mellor-Yamada-Janjić Parameterization for wind conditions in the marine planetary boundary layer”, *Boundary-Layer Meteorol.* , Vol. 136, pp. 301–324.
- Svensson, G., Holtslag, A., Kumar, V., Mauritsen, T., Steeneveld, G., Angevine, W., Bazile, E., Beljaars, A., de Bruijn, E., Cheng, A., Conangla, L., Cuxart, J., Ek, M., Falk, M., Freedman, F., Kitagawa, H., Larson, V., Lock, A., Mailhot, J., Masson, V., Park, S., Pleim, J., Söderberg, S., Weng, W. and Zampieri, M. (2011), “Evaluation of the diurnal cycle in the atmospheric boundary layer over land as represented by a variety of single-column models: The second gabs experiment”, *Boundary-Layer Meteorology* , Vol. 140, Springer Netherlands, pp. 177–206.
- Taylor, P. and Yelland, M. (2001), “The dependence of sea surface roughness on the height and steepness of the waves”, *J. Phys. Oceanogr.* , Vol. 31, pp. 572–590.
- Tennekes, H. (1973), *Similarity laws and scale relations in planetary boundary layers*, American Meteorological Society, chapter 5, pp. 177–216.
- Toba, Y. (1972), “Local balance in air-sea boundary processes i. on the growth process of wind waves”, *J. Oceanogr. Soc. Japan* , Vol. 28, pp. 109–121.
- Toba, Y., Iida, N., Kawamura, H., Ebuchi, N. and Jones, I. S. F. (1990), “Wave dependence of sea-surface wind stress”, *Journal of Physical Oceanography* , Vol. 20, pp. 705–721.
- Townsend, A. (1976), *The structure of turbulent shear flow*, Cambridge University Press.
- Türk, M. (2008), Ermittlung designrelevanter Belastungsparameter für Offshore-Windkraftanlagen, PhD thesis, Mathematisch-Naturwissenschaftliche Fakultät, Universität zu Köln.
- Van der Hoven, I. (1957), “Power spectrum of horizontal wind speed in the frequency range from 0.0007 to 900 cycles per hour”, *J. Meteor.* , Vol. 14, pp. 160–164.
- Warner, T. (2011), *Numerical weather and climate prediction*, Cambridge University Press.
- Wichmann, M. and Schaller, E. (1986), “On the determination of the closure parameters in higher-order closure models”, *Boundary-Layer Meteorol.* , Vol. 37, pp. 323–341.
- Wu, J. (1980), “Wind-stress coefficients over sea surface near neutral conditions - a revisit”, *J. Phys. Oceanogr.* , Vol. 10, pp. 727–740.

- Yamada, T. and Mellor, G. (1975), "A simulation of the wanga atmospheric boundary layer data", *J. Atm. Sci.* , Vol. 32, pp. 2309–2329.
- Yelland, M., Moat, B., Taylor, P., Pascal, R., Hutchings, J. and Cornell, V. (1998), "Wind stress measurements from the open ocean corrected for airflow distortion by the ship", *J. Phys. Oceanogr.* , Vol. 28, pp. 1511–1526.

Erklärung

Ich versichere, dass ich die von mir vorgelegte Dissertation selbständig angefertigt, die benutzten Quellen und Hilfsmittel vollständig angegeben und die Stellen der Arbeit – einschließlich Tabellen, Karten und Abbildungen –, die anderen Werken im Wortlaut oder dem Sinn nach entnommen sind, in jedem Einzelfall als Entlehnung kenntlich gemacht habe; dass diese Dissertation noch keiner anderen Fakultät oder Universität zur Prüfung vorgelegen hat; dass sie – abgesehen von unten angegebenen Teilpublikationen – noch nicht veröffentlicht worden ist sowie, dass ich eine solche Veröffentlichung vor Abschluss des Promotionsverfahrens nicht vornehmen werde. Die Bestimmungen der Promotionsordnung sind mir bekannt. Die von mir vorgelegte Dissertation ist von Prof. Dr. Stefan Emeis betreut worden.

Richard Foreman